# THE HIGGS WORKING GROUP:

## Summary Report

Conveners:

D. Cavalli[1], A. Djouadi[2], K. Jakobs[3], A. Nikitenko[4], M. Spira[5], C.E.M. Wagner[6] and W.-M. Yao[7]

Working Group:

K.A. Assamagan[8], G. Azuelos[9], S. Balatenychev[10], G. Bélanger[11], M. Bisset[12], A. Bocci[13], F. Boudjema[11], C. Buttar[14], M. Carena[15], S. Catani[16], V. Cavasinni[17], Y. Coadou[18], D. Costanzo[17], A. Cottrant[11], A.K. Datta[2], A. Deandrea[19], D. de Florian[20], V. Del Duca[21], B. Di Girolamo[22], V. Drollinger[23], T. Figy[24], M. Frank[25], R.M. Godbole[26], M. Grazzini[27], M. Guchait[2,28], R. Harper[14], S. Heinemeyer[8], J. Hobbs[29], W. Hollik[25,30], C. Hugonie[31], V.I. Ilyin[10], W.B. Kilgore[8], R. Kinnunen[32], M. Klute[33], R. Lafaye[34], Y. Mambrini[2], R. Mazini[9], K. Mazumdar[35], F. Moortgat[36], S. Moretti[16,31], G. Negri[1], L. Neukermans[34], C. Oleari[24], A. Pukhov[10], D. Rainwater[15], E. Richter–Was[37], D.P. Roy[35], C.R. Schmidt[38], A. Semenov[11], J. Thomas[3], I. Vivarelli[17], G. Weiglein[31] and D. Zeppenfeld[24].

[1] INFN and Physics Department Milano University, Italy.
[2] LPMT, Université Montpellier II, F–34095 Montpellier Cedex 5, France.
[3] Institut für Physik, Universität Mainz, Germany.
[4] Imperial College, London, UK.
[5] Paul Scherrer Institut, CH-5232 Villigen PSI, Switzerland.
[6] HEP Division, ANL, 9700 Cass Ave., Argonne, IL 60439 and Enrico Fermi Institute, University of Chicago, 5640 Ellis Avenue, Chicago, IL60637, USA.
[7] LBNL, One Cyclotron Road, Berkeley, CA 94720, USA.
[8] Department of Physics, BNL, Upton, NY 11973, USA.
[9] University of Montreal, Canada.
[10] SINP, Moscow State University, Moscow, Russia.
[11] LAPTH, Chemin de Bellevue, B.P. 110, F-74941 Annecy-le-Vieux, Cedex, France.
[12] Department of Physics, Tsinghua University, Beijing, P.R. China 100084.
[13] Rockefeller University, 1230 York Avenue, New York, NY 10021, USA.
[14] Department of Physics and Astronomy, University of Sheffield, UK.
[15] FNAL, Batavia, IL 60510, USA.
[16] CERN, Theory Division, CH–1211, Geneva, Switzerland.
[17] INFN and University of Pisa, Italy.
[18] University of Uppsala, Sweden.
[19] IPNL, Univ. de Lyon I, 4 rue E. Fermi, F–69622 Villeurbanne Cedex, France.
[20] Departamento de Física, Universidad de Buenos Aires, Argentina.
[21] I.N.F.N., Sezione di Torino via P. Giuria, 1 – 10125 Torino, Italy.
[22] EP Division, CERN, CH–1211 Genève 23, Switzerland.
[23] Department of Physics and Astronomy, University of New Mexico, USA.
[24] Department of Physics, University of Wisconsin, Madison, WI 53706, USA.
[25] Institut für Theoretische Physik, Universität Karlsruhe, D–76128 Karlsruhe, Germany.
[26] Centre for Theoretical Studies, Indian Institute of Science, Bangalore 560 012, India.
[27] INFN, Sezione di Firenze, I–50019 Sesto Fiorentino, Florence, Italy.
[28] The Abdus Salam International Centre for Theoretical Physics, Strada Costiera 11, I–34014 Trieste, Italy.
[29] SUNY at Stony Brook, Dept of Physics, Stony Brook, NY 11794, USA.
[30] Max–Planck–Institut für Physik, Föhringer Ring 6, D–80805 München, Germany.

[31] IPPP, University of Durham, Durham DH1 3LR, UK.
[32] HIP, Helsinki, Finland.
[33] Physikalisches Institut, Universität Bonn, Germany.
[34] LAPP, Chemin de Bellevue, B.P. 110, F-74941 Annecy-le-Vieux, Cedex, France.
[35] Tata Institute of Fundamental Research, Mumbai, 400 005, India.
[36] Physics Department Universitaire Instelling Antwerpen, Wilrijk, Belgium.
[37] Inst. of Computer Science, Jagellonian University; Inst. of Nuclear Physics, Cracow, Poland.
[38] Department of Physics and Astronomy Michigan State University East Lansing, MI 48824, USA.

*Report of the HIGGS working group for the Workshop*
*"Physics at TeV Colliders", Les Houches, France, 21 May – 1 June 2001.*

## CONTENTS

# PREFACE

In this working group we have investigated the propects for Higgs boson searches at the Tevatron and LHC and, in particular, the potential of these colliders to determine the Higgs properties once these particles have been found. The analyses were done in the framework of the Standard Model (SM) and its supersymmetric extensions as the minimal (MSSM) and next-to-minimal (NMSSM) supersymmetric extensions. The work for the discovery potential of the LHC mainly concentrated on the difficult regions of previous analyses as those which are plagued by invisible Higgs decays and Higgs decays into supersymmetric particles. Moreover, the additional signatures provided by the weak vector-boson fusion process (WBF) have been addressed and found to confirm the results of previous analyses. A major experimental effort has been put onto charged Higgs boson analyses. The final outcome was a significant improvement of the discovery potential at the Tevatron and LHC than previous analyses suggested.

For an accurate determination of Higgs boson couplings, the theoretical predictions for the signal and background processes have to be improved. A lot of progress has been made during and after this workshop for the gluon-fusion $gg \to H + (0, 1, 2jets)$ and the associated $t\bar{t}H$ production process. A thorough study of the present theoretical uncertainties of signal and background processes has been initialized, culminating in a list of open theoretical problems. A problem of major experimental interest is the proper treatment of processes involving bottom quark densities, which is crucial for some important signal and background processes. Further theoretical improvements have been achieved for the MSSM Higgs boson masses and Higgs bosons in the NMSSM.

This report summarizes our work. The first part deals with theoretical developments for the signal and background processes. The second part gives an overview of the present status of Higgs boson searches at the Tevatron. The third part analyzes invisible Higgs boson decays at the LHC and the forth part the Higgs boson search in the WBF channel. Part 5 summarizes the progress that has been achieved for $A/H \to \tau^+\tau^-$ decays in the MSSM. In part 6 the status of the Higgs boson search in $t\bar{t}H$ production is presented. Finally, part 7 describes the charged Higgs boson analyses in detail.

# A. Theoretical Developments

*S. Balatenychev, G. Bélanger, F. Boudjema, A. Cottrant, M. Carena, S. Catani, V. Del Duca, D. de Florian, M. Frank, R. Godbole, M. Grazzini, S. Heinemeyer, W. Hollik, V. Ilyn, W. Kilgore, R. Lafaye, S. Moretti, C. Oleari, A. Pukhov, D. Rainwater, DP Roy, C. Schmidt, A. Semenov, M. Spira, C. Wagner, G. Weiglein and D. Zeppenfeld*

#### Abstract

New theoretical progress in Higgs boson production and background processes at hadron colliders and the relations between the MSSM Higgs boson masses is discussed. In this context new proposals for benchmark points in the MSSM are presented. Additional emphasis is put on theoretical issues of invisible SUSY Higgs decays and multiple Higgs boson production within the NMSSM.

## 1. Higgs boson production at hadron colliders: signal and background processes[1]

### 1.1 Introduction

The Higgs mechanism is a cornerstone of the Standard Model (SM) and its supersymmetric extensions. Thus, the search for Higgs bosons is one of the most important endeavors at future high-energy experiments. In the SM one Higgs doublet has to be introduced in order to break the electroweak symmetry, leading to the existence of one elementary Higgs boson, $H$ [1]. The scalar sector of the SM is uniquely fixed by the vacuum expectation value $v$ of the Higgs doublet and the mass $m_H$ of the physical Higgs boson [2]. The negative direct search for the Higgsstrahlung process $e^+e^- \rightarrow ZH$ at the LEP2 collider poses a lower bound of $114.1$ GeV on the SM Higgs mass [3, 4], while triviality arguments force the Higgs mass to be smaller than $\sim 1$ TeV [5].

Since the minimal supersymmetric extension of the Standard Model (MSSM) requires the introduction of two Higgs doublets in order to preserve supersymmetry, there are five elementary Higgs particles, two CP-even ($h, H$), one CP-odd ($A$) and two charged ones ($H^{\pm}$). At lowest order all couplings and masses of the MSSM Higgs sector are fixed by two independent input parameters, which are generally chosen as $\tan\beta = v_2/v_1$, the ratio of the two vacuum expectation values $v_{1,2}$, and the pseudoscalar Higgs-boson mass $m_A$. At LO the light scalar Higgs mass $m_h$ has to be smaller than the $Z$-boson mass $m_Z$. Including the one-loop and dominant two-loop corrections the upper bound is increased to $m_h \lesssim 135$ GeV [6–9]. The negative direct searches for the Higgsstrahlung processes $e^+e^- \rightarrow Zh, ZH$ and the associated production $e^+e^- \rightarrow Ah, AH$ yield lower bounds of $m_{h,H} > 91.0$ GeV and $m_A > 91.9$ GeV. The range $0.5 < \tan\beta < 2.4$ in the MSSM is excluded by the Higgs searches at the LEP2 experiments [3, 4].

The intermediate mass range, $m_H < 196$ GeV at 95% CL, is also favored by a SM analysis of electroweak precision data [3, 4]. In this contribution we will therefore concentrate on searches and measurements for $m_H \lesssim 200$ GeV. The Tevatron has a good chance to find evidence for such a Higgs boson, provided that sufficient integrated luminosity can be accumulated [10]. The Higgs boson, if it exists, can certainly be seen at the LHC, and the LHC can provide measurements of the Higgs boson mass at the $10^{-3}$ level [11, 12], and measurements of Higgs boson couplings at the 5 to 10% level [13]. Both tasks, discovery and measurement of Higgs properties, require accurate theoretical predictions of cross sections at the LHC, but these requirements become particularly demanding for accurate coupling measurements.

In this contribution we review the present status of QCD calculations of signal and background cross sections encountered in Higgs physics at hadron colliders. Desired accuracy levels can be estimated by comparing to the statistical errors in the determination of signal cross sections at the LHC.

---

[1] *D. Rainwater, M. Spira and D. Zeppenfeld*

For processes like $H \to \gamma\gamma$, where a very narrow mass peak will be observed, backgrounds can be accurately determined directly from data. For other decay channels, like $H \to b\bar{b}$ or $H \to \tau\tau$, mass resolutions of order 10% require modest interpolation from sidebands, for which reliable QCD calculations are needed. Most demanding are channels like $H \to W^+W^- \to l^+l^-\not{p}_T$, for which broad transverse mass peaks reduce Higgs observation to, essentially, a counting experiment. Consequently, requirements on theory predictions vary significantly between channels. In the following we discuss production and decay channels in turn and focus on theory requirements for the prediction of signal and background cross sections. Because our main interest is in coupling measurements, we will not consider diffractive channels in the following, which are model-dependent and have large rate uncertainties [14]; potentially, they might contribute to Higgs discovery if, indeed, cross sections are sufficiently large.

## 1.2 Gluon fusion

The gluon fusion mechanism $gg \to \phi$ provides the dominant production mechanism of Higgs bosons at the LHC in the entire relevant mass range up to about 1 TeV in the SM and for small and moderate values of $\tan\beta$ in the MSSM [15]. At the Tevatron this process plays the relevant role for Higgs masses between about 130 GeV and about 190 GeV [10]. The gluon fusion process is mediated by heavy quark triangle loops and, in the case of supersymmetric theories, by squark loops in addition, if the squark masses are smaller than about 400 GeV [16], see Fig. 1.
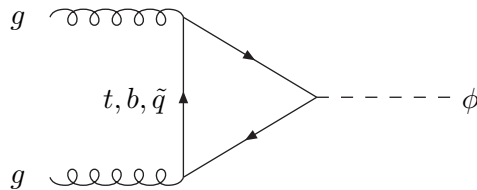


Fig. 1: *Typical diagram contributing to $gg \to \phi$ at lowest order.*

In the past the full two-loop QCD corrections have been determined. They increase the production cross sections by 10–80% [17], thus leading to a significant change of the theoretical predictions. Very recently, Harlander and Kilgore have finished the full NNLO calculation, in the heavy top quark limit [18, 19]. This limit has been demonstrated to approximate the full massive $K$ factor at NLO within 10% for the SM Higgs boson in the entire mass range up to 1 TeV [20]. Thus, a similar situation can be expected at NNLO. The reason for the quality of this approximation is that the QCD corrections to the gluon fusion mechanism are dominated by soft gluon effects, which do not resolve the one-loop Higgs coupling to gluons. Fig. 2 shows the resulting $K$-factors at the LHC and the scale variation of the $K$-factor. The calculation stabilizes at NNLO, with remaining scale variations at the 10 to 15% level. These uncertainties are comparable to the experimental errors which can be achieved with 200 fb$^{-1}$ of data at the LHC, see solid lines in Fig. 3. The full NNLO results confirm earlier estimates which were obtained in the frame work of soft gluon resummation [20] and soft approximations [21, 22] of the full three-loop result. The full soft gluon resummation has been performed in Ref. [23]. The resummation effects enhance the NNLO result by about 10% thus signaling a perturbative stabilization of the theoretical prediction for the gluon-fusion cross section.

In supersymmetric theories the gluon fusion cross sections for the heavy Higgs, $H$, and, for small $m_A$, also for the light Higgs, $h$, may be dominated by bottom quark loops for large values of $\tan\beta \gtrsim 10$ so that the heavy top quark limit is not applicable. This can be clearly seen in the NLO results, which show a decrease of the $K$ factor down to about 1.1 for large $\tan\beta$ [17]. This decrease originates from an interplay between the large positive soft gluon effects and large negative double logarithms of the ratio between the Higgs and bottom masses. In addition, the shape of the $p_T$ distribution of the Higgs
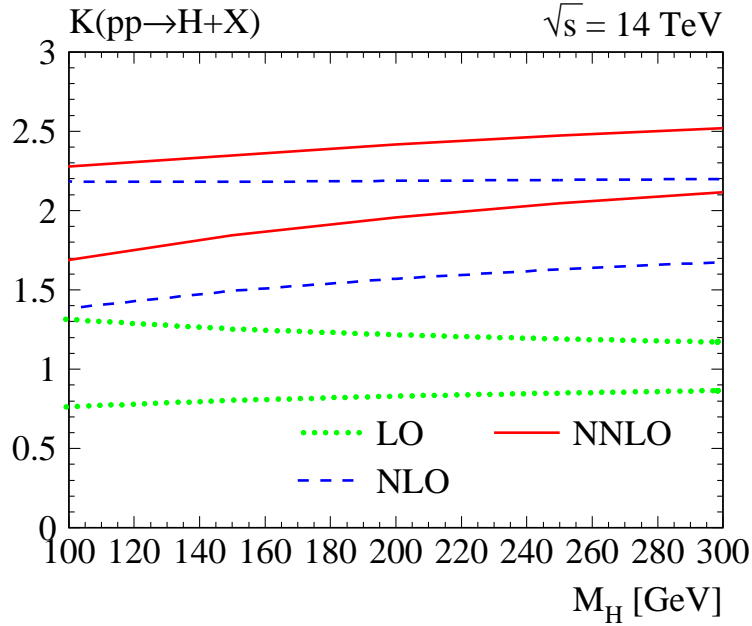
Fig. 2: *Scale dependence of the K-factor at the LHC. Lower curves for each pair are for $\mu_R = 2m_H$, $\mu_F = m_H/2$, upper curves are for $\mu_R = m_H/2$, $\mu_F = 2m_H$. The K-factor is computed with respect to the LO cross section at $\mu_R = \mu_F = m_H$. From Ref. [19].*

boson may be altered; if the bottom loop is dominant, the $p_T$ spectrum becomes softer than in the case of top-loop dominance. These effects lead to some model dependence of predicted cross sections.

Let us now turn to a discussion of backgrounds for individual decay modes.

*(i) $\phi \rightarrow \gamma\gamma$*: At the LHC the SM Higgs boson can be found in the mass range up to about 150 GeV by means of the rare photonic decay mode $H \rightarrow \gamma\gamma$ [11, 12]. The dominant Higgs decays $H \rightarrow b\bar{b}, \tau^+\tau^-$ are overwhelmed by large QCD backgrounds in inclusive searches. The QCD $\gamma\gamma$ background is known at NLO, including all relevant fragmentation effects. The present status is contained in the program DIPHOX [25]. The loop mediated process $gg \rightarrow \gamma\gamma$ contributes about 50% to the $\gamma\gamma$ background and has been calculated at NLO very recently [26]. However, a numerical analysis of the two-loop result is still missing.

Once the experiment is performed, the diphoton background can be determined precisely from the data, by a measurement of $d\sigma/dm_{\gamma\gamma}$ on both sides of the resonance peak. The NLO calculations are useful, nevertheless, for an accurate prediction of expected accuracies and for a quantitative understanding of detector performance.

*(ii) $H \rightarrow W^+W^-$*: This mode is very important for Higgs masses above $W$-pair but below $Z$-pair threshold, where $B(H \rightarrow WW)$ is close to 100%. In order to suppress the $t\bar{t} \rightarrow b\bar{b}W^+W^-$ background for $W^+W^-$ final states, a jet veto is crucial. However, gluon fusion receives sizeable contributions from real gluon bremsstrahlung at NLO, which will also be affected by the jet veto. These effects have recently been analyzed in Ref. [27], in the soft approximation to the full NNLO calculation. A veto of additional jets with $p_{Tj} > 15$ GeV, as e.g. envisioned by ATLAS [12], reduces the NNLO $K$-factor to about $K = 0.8^2$, i.e. one loses more than 60% of signal events. In addition the scale dependence of the cross section starts to grow with such stringent veto criteria. These effects need to be modeled with a NLO Monte Carlo program for $H + jet$ production in order to reach a reliable quantitative result for the signal rate. Since stop and sbottom loops are sizeable in supersymmetric theories for squark masses

---

[2]It should be noted that for this strong cut in $p_{Tj}$ the NNLO result may be plagued by large logarithms of this cut, which have to be resummed, see [23].
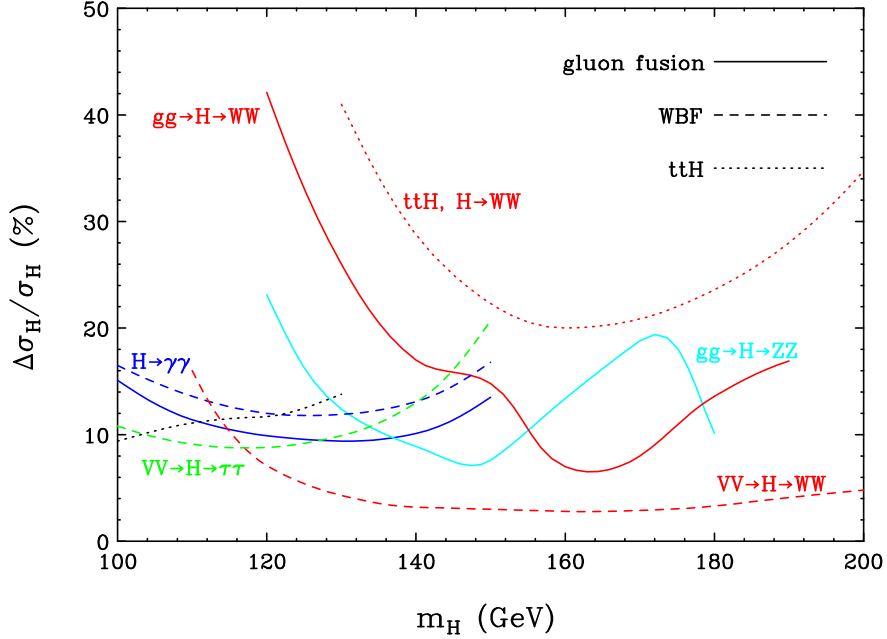
Fig. 3: *Expected relative error on the determination of $B\sigma$ for various Higgs search channels at the LHC with 200 $fb^{-1}$ of data [13]. Solid lines are for inclusive Higgs production channels which are dominated by gluon fusion. Expectations for weak boson fusion are given by the dashed lines. Dotted lines are for $t\bar{t}H$ production with $H \to b\bar{b}$ [24] (black) and $H \to W^+W^-$ [50] (red) and assume 300 $fb^{-1}$ of data.*

below about 400 GeV, their inclusion is important in these investigations.

From the perspective of background calculations, $H \to WW$ is the most challenging channel. Backgrounds are of the order of the signal rate or larger, which requires a 5% determination or better for the dominant background cross sections in order to match the statistical power of LHC experiments. In fact, the large errors at $m_H \lesssim 150$ GeV depicted in Fig. 3 ($gg \to H \to WW$ curve) are dominated by an assumed 5% background uncertainty. Clearly, such small errors cannot be achieved by NLO calculations alone, but require input from LHC data. Because of two missing neutrinos in the $W^+W^- \to l^+l^- p\!\!\!/_T$ final state, the Higgs mass cannot be reconstructed directly. Rather, only wide $(l^+l^-; p\!\!\!/_T)$ transverse mass distributions can be measured, which do not permit straightforward sideband measurements of the backgrounds. Instead one needs to measure the normalization of the backgrounds in signal poor regions and then extrapolate these, with the help of differential cross sections predicted in perturbative QCD, to the signal region. The theory problem is the uncertainty in the shape of the distributions used for the extrapolation, which will depend on an appropriate choice of the "signal poor region". No analysis of the concomitant uncertainties, at LO or NLO QCD, is available to date.

After the jet veto discussed above, the dominant background processes are $pp \to W^+W^-$ and (off-shell) $t\bar{t}$ production [11, 12]. $W^+W^-$ production is known at NLO [28] and available in terms of parton level Monte Carlo programs. In addition, a full NLO calculation including spin correlations of the leptonic $W, Z$ decays, in the narrow width approximation, is available [29]. For Higgs boson masses below the $W^+W^-(ZZ)$ threshold, decays into $WW^*(ZZ^*)$ are important [15,30]. Since hadron colliders will be sensitive to these off-shell tails, too, the backgrounds from $VV^*$ production become relevant. There is no NLO calculation of $VV^*$ background processes available so far, so that it is not clear if NLO effects will be significant in the tails of distributions needed for the Higgs search in these cases. Moreover, for $WW^*$ production the inclusion of spin correlations among the final state leptons is mandatory [31].

Top quark backgrounds arise from top-pair and $tWb$ production. Recently, a new theoretical analysis of $pp \to t^{(*)}\bar{t}^{(*)}$ has become available including full lepton correlations and off-shell effects of the final state top quarks arising from the non-zero top decay width [32]. This calculation automatically

includes $pp \rightarrow tbW$ and those contributions to $pp \rightarrow b\bar{b}W^+W^-$, which are gauge-related to $tbW$ couplings and describes the relevant tails for the Higgs search at LO. It is now necessary to investigate the theoretical uncertainties of this background. A NLO calculation of off-shell top-pair production may well be needed to reach the required 5% accuracy for extrapolation to the Higgs search region.

Other important reducible backgrounds are the $Wt\bar{t}, Zt\bar{t}, Wb\bar{b}$ and $Zb\bar{b}$ production processes. While $Vt\bar{t}$ ($V = W, Z$) production is only known at LO, the associated vector boson production with $b\bar{b}$ pairs is known at NLO including a soft gluon resummation [33]. Thus $Vb\bar{b}$ production can be considered as reliable from the theoretical point of view, while a full NLO calculation for $Vt\bar{t}$ production is highly desirable, since top mass effects will play a significant role. In addition, the background from $gb \rightarrow tH^-, g\bar{b} \rightarrow \bar{t}H^+$ has to be taken into account within the MSSM framework. The full LO matrix elements are included in the ISAJET Monte Carlo program, which can easily be used for experimental analyses.

*(iii) $H \rightarrow ZZ \rightarrow 4\ell^\pm$*: A sharp Higgs peak can be observed in the four lepton invariant mass distribution. Hence, the $ZZ \rightarrow 4\ell^\pm$ backgrounds are directly measurable in the sidebands and can safely be interpolated to the signal region.

## 1.3 $qq \rightarrow qqH$

In the SM the $WW, ZZ$ fusion processes $qq \rightarrow qqV^*V^* \rightarrow qqH$ play a significant role at the LHC for the entire Higgs mass range up to 1 TeV. We refer to them as weak boson fusion (WBF). The WBF cross section becomes comparable to the gluon fusion cross section for Higgs masses beyond $\sim 600$ GeV [15] and is sizable, of order 20% of $\sigma(gg \rightarrow H)$, also in the intermediate mass region. The energetic quark jets in the forward and backward directions allow for additional cuts to suppress the background processes to WBF. The NLO QCD corrections can be expressed in terms of the conventional corrections to the DIS structure functions, since there is no color exchange between the two quark lines at LO and NLO. NLO corrections increase the production cross section by about 10% and are thus small and under theoretical control [34, 35]. These small theory uncertainties make WBF a very promising tool for precise coupling measurements. However, additional studies are needed to assess the theoretical uncertainties associated with a central jet veto. This veto enhances the color singlet exchange of the signal over color octet exchange QCD backgrounds [36–39].

In the MSSM, first parton level analyses show that it should be possible to cover the full MSSM parameter range by looking for the light Higgs decay $h \rightarrow \tau^+\tau^-$ (for $m_A \gtrsim 150$ GeV) and/or the heavy Higgs $H \rightarrow \tau^+\tau^-$ resonance (for a relatively small $m_A$) in the vector-boson fusion processes [40]. Although these two production processes are suppressed with respect to the SM cross section, their sum is of SM strength.

For the extraction of Higgs couplings it is important to distinguish between WBF and gluon fusion processes which lead to $H + jj$ final states. With typical WBF cuts, including a central jet veto, gluon fusion contributions are expected at order 10% of the WBF cross section, i.e. the contamination is modest [41, 42]. The gluon fusion processes are mediated by heavy top and bottom quark loops, in analogy to the LO gluon fusion diagram of Fig. 1. The full massive cross section for $H + jj$ production via gluon fusion has been obtained only recently [41], while former analyses were performed in the heavy top quark limit [43]. Since stop and sbottom loops yield a sizeable contribution to the inclusive gluon fusion cross section, a similar feature is expected for $H + jj$ production. Thus, it is important to compute the effects of stop and sbottom loops in $H + jj$ gluon fusion processes, which has not been done so far.

*(i) $H \rightarrow \gamma\gamma$*: Parton level analyses show that $H \rightarrow \gamma\gamma$ decays in WBF Higgs production can be isolated with signal to background ratios of order one [36] and with statistical errors of about 15%, for 200 fb$^{-1}$ of data (see Fig. 3). Like for the inclusive $H \rightarrow \gamma\gamma$ search, background levels can be precisely determined from a sideband analysis of the data. Prior to data taking, however, full detector simulations are needed

to confirm the parton level results and improve on the search strategies.

Improved background calculations are desirable as well. In particular, the $pp \rightarrow \gamma\gamma jj$ background via quark loops (see Fig. 4) has not been calculated so far.
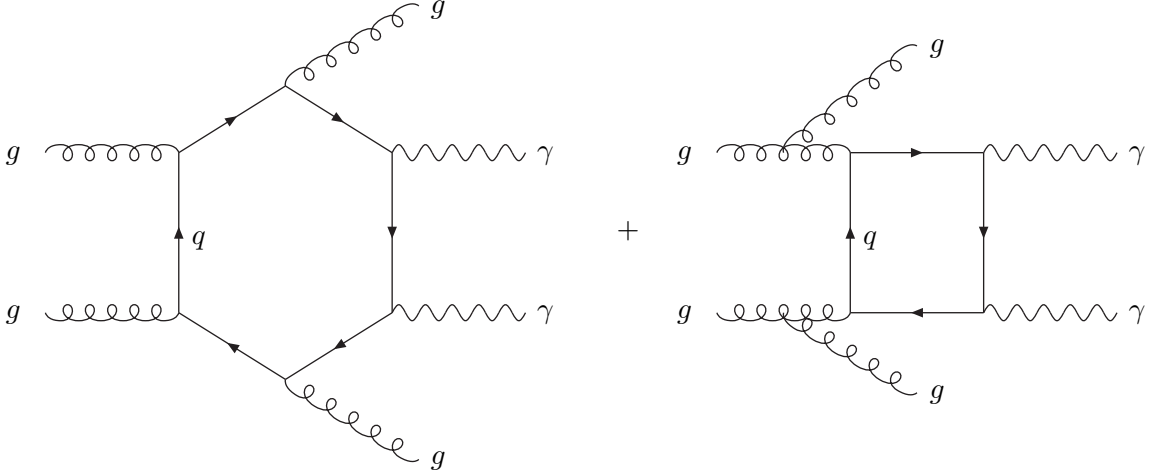


Fig. 4: *Typical diagrams contributing to $gg \rightarrow \gamma\gamma jj$ at lowest order.*

*(ii) $H \rightarrow \tau^+\tau^-$:* The observation of $H \rightarrow \tau\tau$ decays in WBF will provide crucial information on Higgs couplings to fermions [13] and this channel alone guarantees Higgs observation within the MSSM [40] and may be an important discovery channel at low pseudoscalar mass, $m_A$. Recent detector simulations [42] confirm parton level results [37] for the observability of this channel. (See Fig. 3 for parton level estimates of statistical errors.)

The $\tau^+\tau^-$-invariant mass can be reconstructed at the LHC with a resolution of order 10%. This is possible in the $qq \rightarrow qqH$ mode because of the large transverse momentum of the Higgs. In turn this means a sideband analysis can be used, in principle, to directly measure backgrounds. The most important of these backgrounds is QCD $Zjj$ production (from QCD corrections to Drell-Yan) or electroweak $Zjj$ production via WBF [37]. The (virtual) Z (or photon) then decays into a $\tau^+\tau^-$ pair. These $Zjj$ backgrounds, with their highly nontrivial shape around $m_{\tau\tau} \approx m_Z$, can be precisely determined be observing $Z \rightarrow e^+e^-, \mu^+\mu^-$ events in identical phase space regions. Theoretically the QCD $Zjj$ background is under control also, after the recent calculation of the full NLO corrections [44]. For the $\tau^+\tau^-$ backgrounds the inclusion of $\tau$ polarization effects is important in order to obtain reliable tau-decay distributions which discriminate between signal processes ($h, H \rightarrow \tau^+\tau^-$) and backgrounds. This can be achieved by linking the TAUOLA program [45] to existing Monte Carlo programs.

*(iii) $H \rightarrow WW \rightarrow \ell^+\ell^- \not{p}_T$:* The most challenging WBF channel is $H \rightarrow WW^{(*)}$ decay which does not allow for direct Higgs mass reconstruction and, hence, precludes a simple sideband determination of backgrounds. The important backgrounds [38, 39] involve (virtual) $W$ pairs, namely top decays in $t\bar{t}$+jets production, and QCD and electroweak $WWjj$ production. QCD and EW $\tau\tau jj$ production are subdominant after cuts, they are known at NLO [44], and they can be determined directly, in phase space regions for jets which are identical to the signal region and with high statistics, by studying $e^+e^-$ or $\mu^+\mu^-$ pairs instead of $\tau^+\tau^-$.

Demands on QCD calculations can be estimated by comparing the effects of systematic background errors on the measurement of the signal rate with statistical errors achievable at the LHC with 200 fb$^{-1}$ of data. Results are shown in Fig. 5 for an assumed 10% error on $\sigma(t\bar{t}$+jets), a 50% error on the QCD WWjj rate, and a 30% error on the electroweak WWjj rate. The latter two should be achievable from a LO extrapolation from signal poor to signal rich regions of phase space. A 10% error of $\sigma(t\bar{t}$+jets), on the other hand, may require a NLO calculation, in particular of the on-shell $t\bar{t}+1$ jet cross
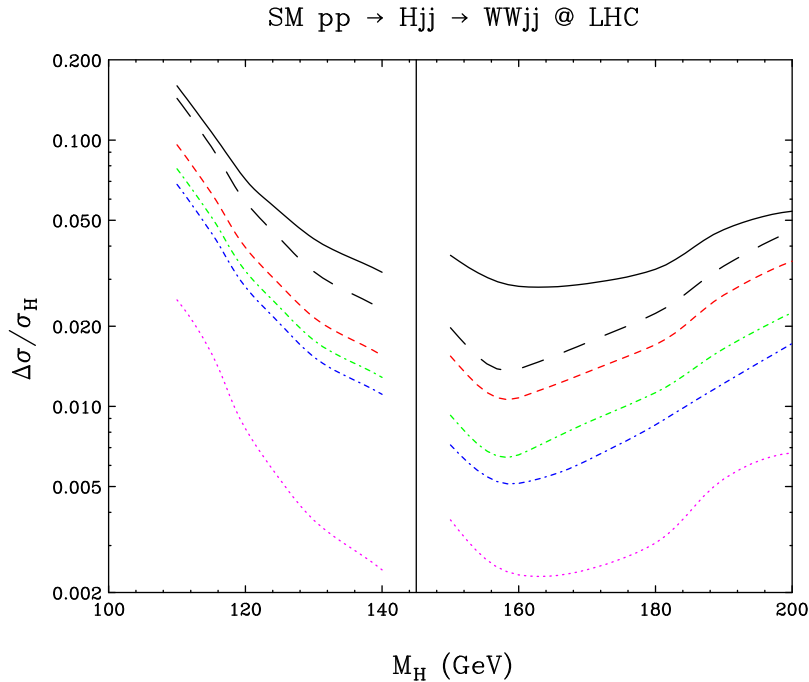
Fig. 5: *Contributions of background systematic errors $\Delta\sigma$ to a measurement of $\sigma_H = \sigma B(H \to WW)$ in WBF. Shown, from bottom to top, are the effects of a 10% uncertainty of the $\tau\tau jj$ rate (dotted line), a 50% error on the QCD WWjj rate (blue dash-dotted), a 30% error on the electroweak WWjj rate (green dash-dotted), and a 10% error on $\sigma(t\bar{t}+jets)$ (red dashes). The long-dashed line adds these errors in quadrature. For comparison, the solid line shows the expected statistical error for $200\,fb^{-1}$. The vertical line at 145 GeV separates analyses optimized for small [39] and large [38] Higgs masses.*

section which dominates the $t\bar{t}$ background. Off-shell effects have recently been studied at LO [32] and a $\mathcal{O}(20\%)$ increase of the $t\bar{t}$ background was found, which, presumably, is small enough to permit the inclusion of off-shell effects at LO only. However, a dedicated study is needed to devise optimal techniques for a reliable background determination for $H \to WW$ searches in WBF, for all major backgrounds.

*(iv) Jet veto and Jet Tagging*: Background suppression in the WBF channels relies on double forward jet tagging to identify the scattered quark jets of the $qq \to qqH$ signal and it employs a veto of relatively soft central jets (typically of $p_T > 20$ GeV) to exploit the different gluon radiation patterns and QCD scales of $t$-channel color singlet versus color octet exchange. Transverse momenta of these tagging or veto jets are relatively small for fixed order perturbative calculations of hard processes at the LHC. Thus, dedicated studies will be needed to assess the applicability of NLO QCD for the modeling of tagging jets in WBF and for the efficiency of a central jet veto in the Higgs signal. First such studies have been performed in the past at LO, for $Wjj$ or $Zjj$ events [46]. While NLO Monte Carlos for QCD $Vjj$ production are now available [44, 47], the corresponding NLO determination of electroweak $Vjj$ cross sections would be highly desirable. This would allow a comparison of calculated and measured veto efficiencies in a WBF process. These efficiencies must be known at the few percent level for the signal in order to extract Higgs couplings without loss of precision.

At present, the veto efficiencies for signal and background processes are the most uncertain aspect of WBF Higgs production at the LHC. Any improvement in their understanding, from QCD calculations, from improved Monte Carlo tools, or from hadron collider data would be very valuable.

## 1.4 $t\bar{t}\phi$ production

SM Higgs boson production in association with $t\bar{t}$ pairs plays a significant role at the LHC for Higgs masses below about 130 GeV, since this production mechanism makes the observation of $H \to b\bar{b}$ possible [11, 12, 24, 48, 49]. The decay $H \to \gamma\gamma$ is potentially visible in this channel at high integrated luminosity. For Higgs masses above about 130 GeV, the decay $H \to W^+W^-$ can be observed [50]. $t\bar{t}H$ production could conceivably be used to determine the top Yukawa coupling directly from the cross section, but this requires either assumptions about the branching ratio for $H \to b\bar{b}$, which are not justified in extensions of the SM, or observability of decay to either $\gamma\gamma$ or $W^+W^-$. Recently, the NLO QCD corrections have become available. They decrease the cross section at the Tevatron by about 20–30% [51, 52], while they increase the signal rate at the LHC by about 20–40% [51]. The scale dependence of the production cross section is significantly reduced, to a level of about 15%, which can be considered as an estimate of the theoretical uncertainty. Thus, the signal rate is under proper theoretical control now. In the MSSM, $t\bar{t}h$ production with $h \to \gamma\gamma, b\bar{b}$ is important at the LHC in the decoupling regime, where the light scalar $h$ behaves as the SM Higgs boson [11, 12, 24, 48, 49]. Thus, the SM results can also be used for $t\bar{t}h$ production in this regime.

*(i) $t\bar{t}\phi \to t\bar{t}b\bar{b}$*: The major backgrounds to the $\phi \to b\bar{b}$ signal in associated $t\bar{t}\phi$ production come from $t\bar{t}jj$ and $t\bar{t}b\bar{b}$ production, where in the first case the jets may be misidentified as $b$ jets. A full LO calculation is available for these backgrounds and will be included in the conventional Monte Carlo programs. However, an analysis of the theoretical uncertainties is still missing. A first step can be made by studying the scale dependence at LO in order to investigate the effects on the total normalization and the event shapes. But for a more sophisticated picture a full NLO calculation is highly desirable. A second question is whether these backgrounds can be measured in the experiments off the Higgs resonance and extrapolated to the signal region.

*(ii) $t\bar{t}\phi \to t\bar{t}\gamma\gamma$*: The $t\bar{t}\gamma\gamma$ final states develop a narrow resonance in the invariant $\gamma\gamma$ mass distribution, which enables a measurement of the $t\bar{t}\gamma\gamma$ background directly from the sidebands.

*(iii) $t\bar{t}\phi \to t\bar{t}W^+W^-$*: This channel does not allow reconstruction of the Higgs. Instead, it relies on a counting experiment of multilepton final states where the background is of approximately the same size as the signal [50]. The principal backgrounds are $t\bar{t}Wjj$ and $t\bar{t}\ell^+\ell^-(jj)$, with minor backgrounds of $t\bar{t}W^+W^-$ and $t\bar{t}t\bar{t}$. For the $3\ell$ channel, the largest background is $t\bar{t}\ell^+\ell^-$ where one lepton is lost. It is possible that this rate could be measured directly for the lepton pair at the $Z$ pole and the result extrapolated to the signal region of phase space. However, for $t\bar{t}Vjj$ backgrounds the QCD uncertainties become large and unknown, due to the presence of two additional soft jets in the event. Further investigation of these backgrounds is essential, and will probably require comparison with data, which is not expected to be trivial.

## 1.5 $b\bar{b}\phi$ production

In supersymmetric theories $b\bar{b}\phi$ production becomes the dominant Higgs boson production mechanism for large values of $\tan\beta$ [15], where the bottom Yukawa coupling is strongly enhanced. In contrast to $t\bar{t}\phi$ production, however, this process develops potentially large logarithms, $\log m_\phi^2/m_b^2$, in the high-energy limit due to the smallness of the bottom quark mass, which are related to the development of $b$ densities in the initial state. They can be resummed by evolving the $b$ densities according to the Altarelli–Parisi equations and introducing them in the production process [53]. The introduction of conventional $b$ densities requires an approximation of the kinematics of the hard process, i.e. the initial $b$ quarks are assumed to be massless, have negligible transverse momentum and travel predominantly in forward and backward direction. These approximations can be tested in the full $gg \to b\bar{b}\phi$ process. At the Tevatron it turns out that they are not valid so that the effective cross section for $b\bar{b} \to \phi$ has to be considered as an

overestimate of the resummed result. An improvement of this resummation requires an approach which describes the kinematics of the hard process in a better way. Moreover, since the experimental analyses require 3 or 4 $b$ tags [10–12], the spectator $b$ quarks need to have a sizeable transverse momentum of at least 15–20 GeV. Thus a resummation of a different type of potentially arising logarithms, namely $\log m_\phi^2/(m_b^2 + p_{tmin}^2)$ is necessary. This can be achieved by the introduction of e.g. unintegrated parton densities [54] or an extension of the available resummation techniques.

As a first step, however, we have to investigate if the energy of the Tevatron and LHC is sufficiently large to develop the factorization of bottom densities. This factorization requires that the transverse momentum distribution of the (anti)bottom quark scales like $d\sigma/dp_{Tb} \propto p_{Tb}/(m_b^2 + p_{Tb}^2)$ for transverse momenta up to the factorization scale of the (anti)bottom density. The transverse momentum distribu-
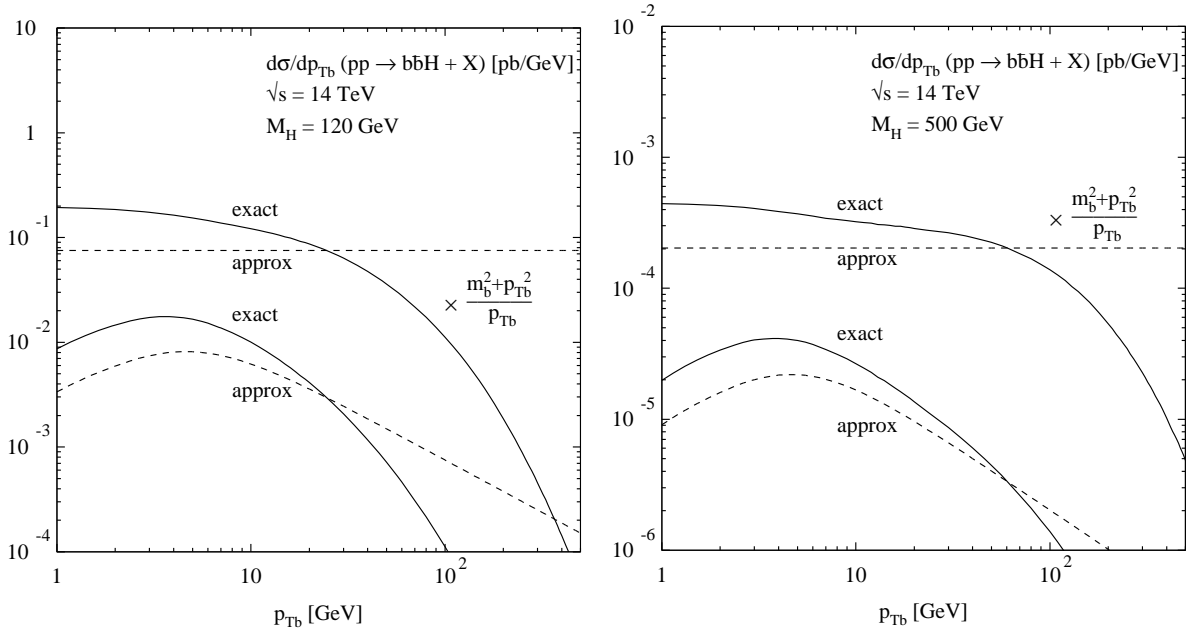


Fig. 6: *Transverse momentum distributions of the bottom quark in $b\bar{b}H$ production for two Higgs masses at the LHC. We have adopted CTEQ5M1 parton densities and a bottom mass of $m_b = 4.62$ GeV. The solid lines show the full LO result from $q\bar{q}, gg \to b\bar{b}H$ and the dashed lines the factorized collinear part, which is absorbed in the bottom parton density. The upper curves are divided by the factor $p_{Tb}/(m_b^2 + p_{Tb}^2)$ of the asymptotic behavior, which is required by factorizing bottom densities.*

tions at the LHC are shown in Fig. 6, for two different Higgs masses. The solid curves show the full distributions of the $q\bar{q}, gg \to b\bar{b}\phi$ processes, while the dashed lines exhibit the factorized collinear part, which is absorbed in the bottom density. For a proper factorization, these pairs of curves have to coincide approximately up to transverse momenta of the order of the factorization scale, which is usually chosen to be $\mu_F = \mathcal{O}(m_H)$. It is clearly visible that there are sizeable differences between the full result and the factorized part, which originate from sizeable bottom mass and phase space effects, that are not accounted for by an active bottom parton density. Moreover, the full result falls quickly below the approximate factorized part for transverse momenta of the order of $m_H/10$, which is much smaller than the usual factorization scale used for the bottom densities. We conclude from these plots that $b\bar{b}\phi$ production at the LHC develops sizeable bottom mass effects, so that the use of bottom densities in the process $b\bar{b} \to \phi$ may lead to an overestimate of the correct theoretical result due to too crude approximations in the kinematics of the hard process. The full NLO calculation of the $gg \to b\bar{b}\phi$ will yield much more insight into this problem, since the large logarithms related to the evolution of bottom densities have to appear in the NLO corrections, if the picture of active bottom quarks in the proton is correct.

## 1.6 $ZH, WH$ production

Higgsstrahlung in $q\bar{q} \to WH, ZH$ plays a crucial role for the Higgs search at the Tevatron, while it is only marginal at the LHC. At the Tevatron it provides the relevant production mechanism for Higgs masses below about 130 GeV, where $H \to b\bar{b}$ decays are dominant [10]. The NLO QCD corrections have been analyzed in the past. They are identical to the QCD corrections to the Drell–Yan processes $q\bar{q} \to W, Z$, if the LO matrix elements are replaced accordingly. QCD corrections increase the production cross sections by about 30–40% [35, 55].

The most important backgrounds at the Tevatron are $Wjj$ and in particular $Wb\bar{b}$ production. Both are known at NLO and are contained in a NLO Monte Carlo program [47]. The same applies also to the $Zjj$ and in particular $Zb\bar{b}$ backgrounds [33, 44]. In addition, the $t\bar{t}$ background is relevant.

## 1.7 Conclusions

Considerable progress has been made recently in improving QCD calculations for Higgs signal and background cross sections at hadron colliders. Noteworthy examples are the NNLO corrections to the gluon fusion cross section [19], the QCD $Zjj$ cross section at NLO [44] and the determination of full finite top and $W$ width corrections to $t\bar{t}$ and $t\bar{t}j$ production at LO [32]. These improvements are crucial for precise coupling determinations of the Higgs boson.

Much additional work is needed to match the statistical power of the LHC. Largely, QCD systematic errors for coupling measurements have not been analyzed yet. Additional NLO tools need to be provided as well, and these include NLO corrections to $t\bar{t}$ production with finite width effects and $t\bar{t}j$ production at zero top width. A better understanding of central jet veto efficiencies is crucial for the study of WBF channels. These are a few examples where theoretical work is needed. Many more have been highlighted in this review. Higgs physics at the LHC remains a very rich field for phenomenology.

## 2. Direct Higgs production and jet veto[3]

Direct Higgs production through gluon–gluon fusion, followed by the decay $H \to W^*W^*, Z^*Z^*$ is a relevant channel to discover a Higgs boson with mass $140 \lesssim M_H \lesssim 190$ GeV both at the Tevatron and at the LHC. In particular, the decay mode $W^*W^* \to l^+l^-\nu\bar{\nu}$ is quite important [10–12, 31], since it is cleaner than $W^*W^* \to l\nu jj$, and the decay rate $H \to W^*W^*$ is higher than $H \to Z^*Z^*$ by about one order of magnitude.

An important background for the direct Higgs signal $H \to W^*W^* \to l^+l^-\nu\bar{\nu}$ is $t\bar{t}$ production ($tW$ production is also important at the LHC), where $t \to l\bar{\nu}b$, thus leading to $b$ jets with high $p_T$ in the final state. If the $b$ quarks are not identified, a veto cut on the transverse momenta of the jets accompanying the final-state leptons can be applied to enhance the signal/background ratio. Imposing a jet veto turns out to be essential, both at the Tevatron [10, 56] and at the LHC [11, 12, 31], to cut the hard $b$ jets arising from this background process.

Here we study the effect of a jet veto on direct Higgs production. More details can be found in Ref. [27]. The events that pass the veto selection are those with $p_T^{\text{jet}} < p_T^{\text{veto}}$, where $p_T^{\text{jet}}$ is the transverse momentum of any final-state jets, defined by a cone algorithm. The cone size $R$ of the jets will be fixed at the value $R = 0.4$.

The vetoed cross section $\sigma^{\text{veto}}(s, M_H^2; p_T^{\text{veto}}, R)$ can be written as

$$\sigma^{\text{veto}}(s, M_H^2; p_T^{\text{veto}}, R) = \sigma(s, M_H^2) - \Delta\sigma(s, M_H^2; p_T^{\text{veto}}, R) \ , \tag{1}$$

where $\sigma(s, M_H^2)$ is the inclusive cross section, and $\Delta\sigma$ is the 'loss' in cross section due to the jet-veto procedure. The jet-vetoed cross section is evaluated by using the large-$M_{\text{top}}$ limit. At NLO (NNLO)

the calculation is performed by subtracting the LO (NLO) cross section for the production of Higgs plus jet(s) from the inclusive NLO (NNLO) result.

The NLO calculation is exact: apart from using the large-$M_{\text{top}}$ limit, we do not perform any further approximations. At the NNLO, the contribution $\Delta\sigma$ to Eq. (1) is again evaluated exactly, by using the numerical program of Ref. [57]. To evaluate the contribution of the inclusive cross section we use the recent result of Ref. [21, 22], and in particular, we rely on our approximate estimate NNLO-SVC [21]. In the following we present both NLO and NNLO numerical results for the vetoed cross section. The results are obtained by using the parton distributions of the MRST2000 set [58], with densities and coupling constant evaluated at each corresponding order. The MRST2000 set includes (approximate) NNLO parton densities.
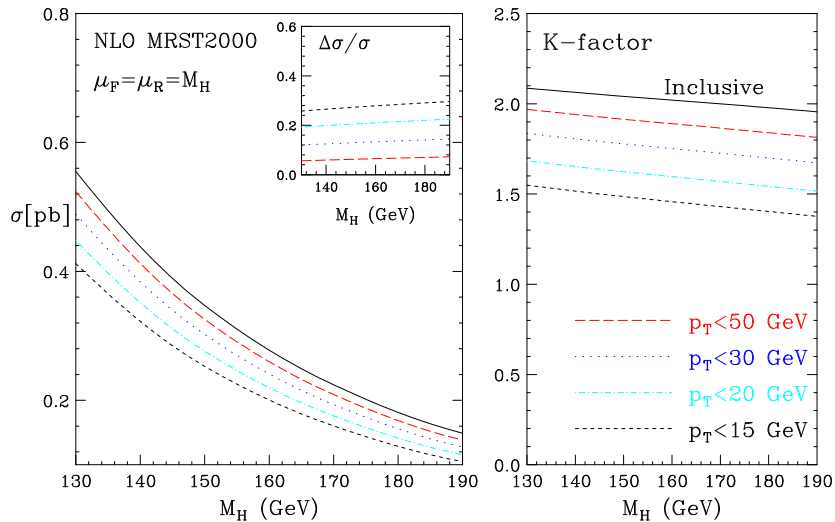


Fig. 7: *Vetoed cross section and K-factors: NLO results at the Tevatron Run II.*

We first present the vetoed cross section at the Tevatron Run II. In Fig. 7 we show the dependence of the NLO results on the Higgs mass for different values of $p_T^{\text{veto}}$ (15, 20, 30 and 50 GeV). The vetoed cross sections $\sigma^{\text{veto}}(s, M_H^2; p_T^{\text{veto}}, R)$ and the inclusive cross section $\sigma(s, M_H^2)$ are given in the plot on the left-hand side. The inset plot gives an idea of the 'loss' in cross section once the veto is applied, by showing the ratio between the cross section difference $\Delta\sigma$ in Eq. (1) and the inclusive cross section at the same perturbative order. As can be observed, for large values of the cut, say $p_T^{\text{veto}} = 50$ GeV, less than 10% of the inclusive cross section is vetoed. The veto effect increases by decreasing $p_T^{\text{veto}}$, but it is still smaller than 30% when $p_T^{\text{veto}} = 15$ GeV. On the right-hand side of Fig. 7, we show the corresponding K-factors, i.e. the vetoed cross sections normalized to the LO result, which is independent of the value of the cut. Figure 8 shows the analogous results at NNLO. In Fig. 9 we show the LO, NLO and NNLO-SVC K-factor bands, computed by varing renormalization ($\mu_R$) and factorization ($\mu_F$) scales in the range $1/2M_H < \mu_F, \mu_R < 2M_H$ and normalizing to the LO contribution at $\mu_F = \mu_R = M_H$. The calculation is done with $p_T^{\text{veto}} = 15$ GeV. Comparing Fig. 9 with the inclusive case (see Ref. [27]), we see that the effect of the veto is to partially reduce the relative difference between the NLO and NNLO results; the increase of the corresponding K-factors can be estimated to about 25%.

The results for the vetoed cross sections at the LHC are presented in Figs. 10 and 11 for $p_T^{\text{veto}} = 20$, 30, 50 and 70 GeV. At fixed value of the cut, the impact of the jet veto, both in the 'loss' of cross section and in the reduction of the K-factors, is larger at the LHC than at the Tevatron Run II. This effect can also be appreciated by comparing Fig. 12 and Fig. 9. At the LHC, the value of $p_T^{\text{veto}} = 30$ GeV is already sufficient to reduce the difference between the NNLO and NLO results to less than 10%.

The results presented above can be interpreted according to a simple physical picture. The dominant part of QCD corrections is due to soft and collinear radiation [21]. The characteristic scale of the highest transverse momentum $p_T^{\text{max}}$ of the accompanying jets is $p_T^{\text{max}} \sim \langle 1 - z \rangle M_H$, where the average
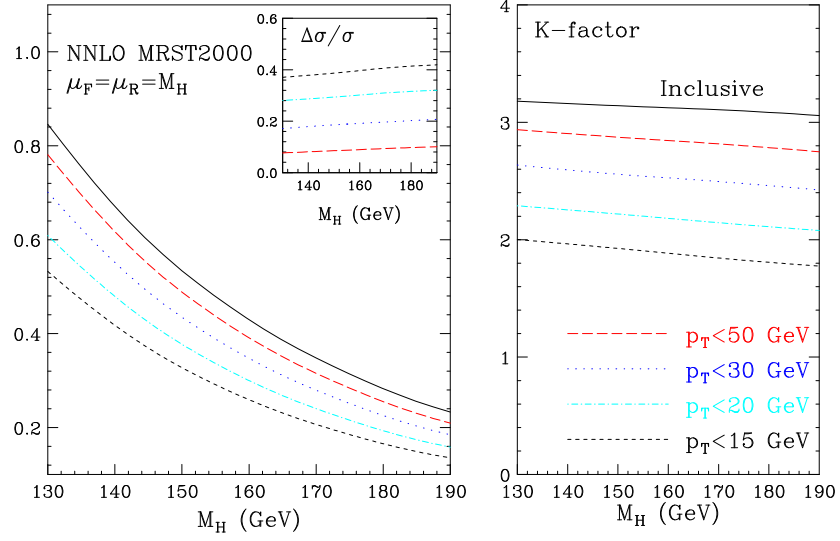
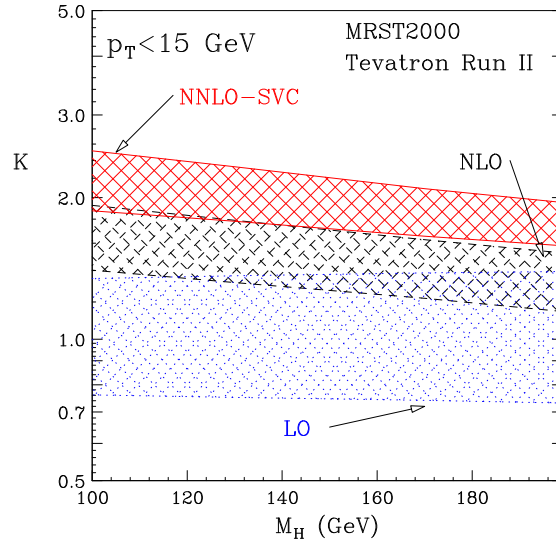Fig. 8: *Vetoed cross section and K-factors: NNLO results at the Tevatron Run II.*



Fig. 9: *K-factors for Higgs production at the Tevatron for a veto of $p_T^{veto} = 15$ GeV at LO, NLO and NNLO-SVC.*

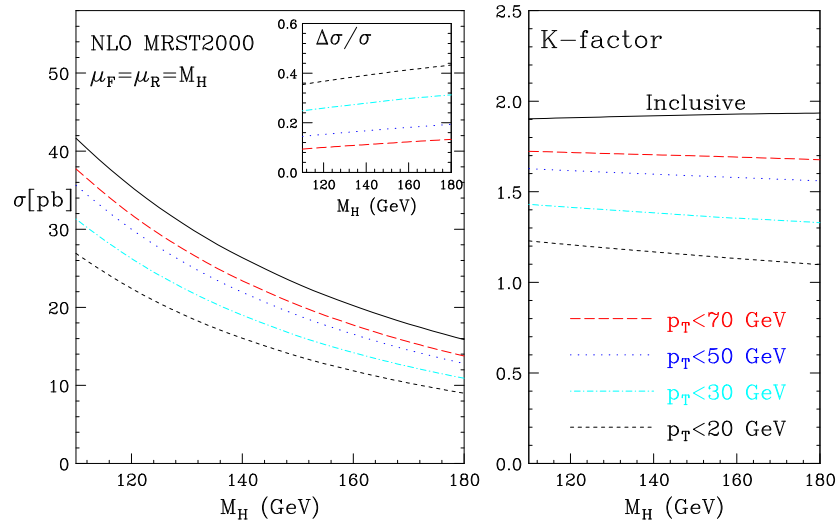

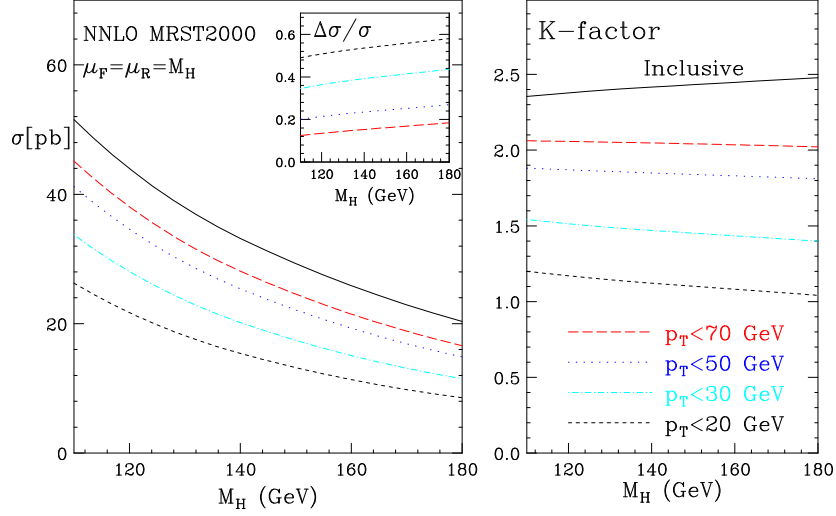Fig. 10: *Vetoed cross sections and K-factors at NLO at the LHC.*

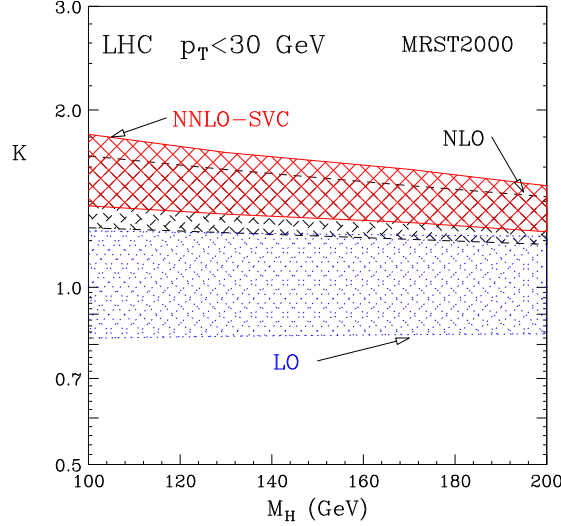Fig. 11: *Vetoed cross sections and K-factors at NNLO at the LHC.*



Fig. 12: *The same as in Fig. 9, but at the LHC and with $p_T^{cut} = 30$ GeV.*

value $\langle 1 - z \rangle = \langle 1 - M_H^2/\hat{s} \rangle$ of the distance from the partonic threshold is small. As a consequence the jet veto procedure is weakly effective unless the value of $p_T^{\rm veto}$ is substantially smaller than $p_T^{\max}$. Decreasing $p_T^{\rm veto}$, the enhancement of the inclusive cross section due to soft radiation at higher orders is reduced, and the jet veto procedure tends to improve the convergence of the perturbative series. At the LHC Higgs production is less close to threshold than at the Tevatron and, therefore, the accompanying jets are harder. This is the reason why, at fixed $p_T^{\rm veto}$, the effect of the jet veto is stronger at the LHC than at the Tevatron.

When $p_T^{\rm veto}$ is much smaller than the characteristic scale $p_T^{\max} \sim \langle 1 - z \rangle M_H$, the perturbative expansion of the vetoed cross section contains large logarithmic contributions that can spoil the convergence of the fixed-order expansion in $\alpha_{\rm S}$. Since $\langle 1 - z \rangle M_H$ is larger at the LHC than at the Tevatron, the value of $p_T^{\rm veto}$ at which these effects become visible is larger at the LHC. Whereas at the Tevatron the perturbative calculation for $p_T^{\rm veto} = 15$ GeV seems still to be reliable, at the LHC, with the same value of $p_T^{\rm veto}$, the perturbative result suggests that the effect of these logarithmic contributions is large [27].

**Note added.** After the completion of this work, the full NNLO QCD contribution to *inclusive* Higgs boson production has been computed [19]. These results influence those in the present paper through Eq. (1), since in our NNLO calculation the inclusive cross section $\sigma(s, M_H^2)$ is evaluated by using the approximate (soft-collinear) estimate (named NNLO-SVC) of Ref. [21]. We have considered the effect

of the additional hard corrections of Ref. [19] and, as expected [21, 27], we find that they are relatively small. The inclusive cross section at full NNLO is smaller than its NNLO-SVC approximation by about $5\%\,(7\%)$ at the LHC (Tevatron Run II). This correction can directly be applied to our results. For instance, the NNLO K-factors in Figs. 8, 9 and 11 can be modified as $K \to K - \Delta K$, where $\Delta K = 0.20\text{-}0.21$ at the Tevatron and $\Delta K = 0.11\text{-}0.13$ at the LHC (the variations of $\Delta K$ correspond to variations of the Higgs mass in the range considered in the Figures).

## 3.  The high-energy limit of $H + 2$ jet production via gluon fusion[4]

At the Large Hadron Collider (LHC), the main production channels of a Higgs boson are gluon fusion and weak-boson fusion (WBF) [12, 59]. The WBF process, $qq \to qqH$, occurs through the exchange of a $W$ or a $Z$ boson in the $t$ channel, and is characterized by the production of two forward quark jets [60]. Even though it is smaller than the gluon fusion channel by about a factor of 5 for an intermediate mass Higgs boson, it is interesting because it is expected to provide information on Higgs boson couplings [13]. In this respect, $H + 2$ jet production via gluon-gluon fusion, which has a larger production rate before cuts, can be considered a background; it has the same final-state topology, and thus may hide the features of the WBF process.

In Higgs production via gluon fusion, the Higgs boson is produced mostly via a top quark loop. The computation of $H + 2$ jet production involves up to pentagon quark loops [41]. However, if the Higgs mass is smaller than the threshold for the creation of a top-quark pair, $M_{\mathrm{H}} \lesssim 2M_t$, the coupling of the Higgs to the gluons via a top-quark loop can be replaced by an effective coupling [61]: this is called the *large-$M_t$ limit*. It simplifies the calculation, because it reduces the number of loops in a given diagram by one. In $H + 2$ jet production, the large-$M_t$ limit yields a good approximation to the exact calculation if, in addition to the condition $M_{\mathrm{H}} \lesssim 2M_t$, we require that the jet transverse energies are smaller than the top-quark mass, $p_\perp \lesssim M_t$ [41]. However, the large $M_t$ approximation is quite insensitive to the value of the Higgs–jet and/or dijet invariant masses. The last issue is not academic, because Higgs production via WBF, to which we should like to compare, features typically two forward quark jets, and thus a large dijet invariant mass.

In this contribution, we consider $H + 2$ jet production when Higgs–jet and/or dijet invariant masses become much larger than the typical momentum transfers in the scattering. We term these conditions the *high-energy limit*. In this limit the scattering amplitude factorizes into *impact factors* connected by a gluon exchanged in the $t$ channel. Assembling together different impact factors, the amplitudes for different sub-processes can be obtained. Thus the high-energy factorization constitutes a stringent consistency check on any amplitude for the production of a Higgs plus one or more jets.

In the high-energy limit of $H + 2$ jet production, the relevant (squared) energy scales are the parton center-of-mass energy $s$, the Higgs mass $M_{\mathrm{H}}^2$, the dijet invariant mass $s_{j_1 j_2}$, and the jet-Higgs invariant masses $s_{j_1\mathrm{H}}$ and $s_{j_2\mathrm{H}}$. At leading order they are related through momentum conservation,

$$s = s_{j_1 j_2} + s_{j_1\mathrm{H}} + s_{j_2\mathrm{H}} - M_{\mathrm{H}}^2\,. \tag{2}$$

There are two possible high-energy limits to consider: $s_{j_1 j_2} \gg s_{j_1\mathrm{H}}, s_{j_2\mathrm{H}} \gg M_{\mathrm{H}}^2$ and $s_{j_1 j_2}, s_{j_2\mathrm{H}} \gg s_{j_1\mathrm{H}}, M_{\mathrm{H}}^2$. In the first case the Higgs boson is centrally located in rapidity between the two jets, and very far from either jet. In the second case the Higgs boson is close to one jet, say to jet $j_1$, in rapidity, and both of these are very far from jet $j_2$. In both cases the amplitudes will factorize, and the relevant Higgs vertex in case 1 and the Higgs–gluon and Higgs–quark impact factors in case 2 can be obtained from the amplitudes for $q\,Q \to q\,Q\,H$ and $q\,g \to q\,g\,H$ scattering.

---

[4]*V. Del Duca, W.B. Kilgore, C. Oleari, C.R. Schmidt and D. Zeppenfeld*

**The high-energy limit $s_{j_1 j_2} \gg s_{j_1 H},\ s_{j_2 H} \gg M_H^2$**

We consider the production of two partons of momenta $p_1$ and $p_3$ and a Higgs boson of momentum $p_H$, in the scattering between two partons of momenta $p_2$ and $p_4$, where all momenta are taken as outgoing. We consider the limit in which the Higgs boson is produced centrally in rapidity, and very far from either jet, $s_{j_1 j_2} \gg s_{j_1 H},\ s_{j_2 H} \gg M_H^2$, which is equivalent to require that

$$p_1^+ \gg p_H^+ \gg p_3^+\,, \qquad p_1^- \ll p_H^- \ll p_3^-\,, \tag{3}$$

where we have introduced the light-cone coordinates $p^\pm = p_0 \pm p_z$, and complex transverse coordinates $p_\perp = p^x + i p^y$. In the limit (3), the amplitudes are dominated by gluon exchange in the $t$ channel, with emission of the Higgs boson from the $t$-channel gluon. We can write the amplitude for $q\,Q \to q\,Q\,H$ scattering in the high-energy limit as [62]

$$
\begin{aligned}
& i\,\mathcal{M}^{qq \to Hqq}(p_2^{-\nu_1}, p_1^{\nu_1} \mid H \mid p_3^{\nu_3}, p_4^{-\nu_3}) \\
&= 2s\left[g\,T_{a_1 \bar{a}_2}^c\, C^{\bar{q};q}(p_2^{-\nu_1}; p_1^{\nu_1})\right] \frac{1}{t_1} \left[\delta^{cc'} C^H(q_1, p_H, q_2)\right] \frac{1}{t_2} \left[g\,T_{a_3 \bar{a}_4}^{c'}\, C^{\bar{q};q}(p_4^{-\nu_3}; p_3^{\nu_3})\right]\,,
\end{aligned} \tag{4}
$$

where $q_1 = -(p_1 + p_2)$, $q_2 = p_3 + p_4$, $t_i \simeq -|q_{i\perp}|^2$, $i = 1, 2$, and the $\nu$'s are the quark helicities. In Eq. (4) we have made explicit the helicity conservation along the massless quark lines. The effective vertex $C^{\bar{q};q}$ for the production of a quark jet, $q\,g^* \to q$, contributes a phase factor [63]: its square is 1. The effective vertex for Higgs production along the gluon ladder, $g^* g^* \to H$, with and off-shell $g^*$ is

$$C^H(q_1, p_H, q_2) = 2g^2 M_t^2/v \cdot \left(m_{H_\perp}^2 A_1(q_1, q_2) - 2A_2(q_1, q_2)\right)\,. \tag{5}$$

The scalar coefficients of the triangle vertex with two off-shell gluons, $A_{1,2}$, are defined in terms of the form factors $F_T$ and $F_L$ of Ref. [41] as

$$A_1 = iF_T/(4\pi)^2\,, \qquad A_2 = i\left(F_T\,q_1 \cdot q_2 + F_L\,q_1^2 q_2^2\right)/(4\pi)^2\,. \tag{6}$$

We have checked analytically that the amplitude for $q\,g \to q\,g\,H$ scattering can also be written as Eq. (4), provided we perform on one of the two effective vertices $C^{\bar{q};q}$ the substitution (for the sake of illustration, we display it here for the lower vertex)

$$ig\,f^{bb'c}\, C^{g;g}(p_b^{\nu_b}; p_{b'}^{\nu_{b'}}) \leftrightarrow g\,T_{b'\bar{b}}^c\, C^{\bar{q};q}(p_b^{-\nu_{b'}}; p_{b'}^{\nu_{b'}})\,, \tag{7}$$

and use the effective vertices $g^* g \to g$ for the production of a gluon jet [63] (which contribute a phase factor as well). The same check on the (squared) amplitude for $g\,g \to g\,g\,H$ scattering has been performed numerically. Thus, in the high-energy limit (3), the amplitudes for $q\,Q \to q\,Q\,H$, $q\,g \to q\,g\,H$ and $g\,g \to g\,g\,H$ scattering only differ by the color strength in the jet-production vertex. Therefore, in a production rate it is enough to consider one of them and include the others through the effective parton distribution function [64], $f_{\text{eff}}(x, \mu_F^2) = G(x, \mu_F^2) + (C_F/C_A) \sum_f \left[Q_f(x, \mu_F^2) + \bar{Q}_f(x, \mu_F^2)\right]$, where $x$ is the momentum fraction of the incoming parton, $\mu_F^2$ is the collinear factorization scale, and where the sum is over the quark flavors.

In Fig. 13 we plot the cross section in $H + 2$ jet production at the LHC energy $\sqrt{s} = 14$ TeV, as a function of $\Delta y$, which is defined as the smallest rapidity difference between the Higgs and the jets, $\Delta y = \min(|y_{j_1} - y_H|, |y_{j_2} - y_H|)$, with the kinematical constraint $y_{j_1} > y_H > y_{j_2}$. The solid line is the exact production rate, with the amplitudes evaluated in Ref. [41]; the dashed line is the rate in the high-energy limit (3), with the amplitudes evaluated using Eqns. (4)–(7). It is apparent that the high-energy limit works very well over the whole $\Delta y$ spectrum. However, in the evaluation of the effective vertex (5), we used the exact value of the scalar coefficients $A_{1,2}$. A more conservative statement is to say that when any kinematic quantity involved in the amplitude (4) is evaluated in the limit (3), we expect the high-energy limit to represent a good approximation of the exact calculation when $\Delta y \gtrsim 2$.
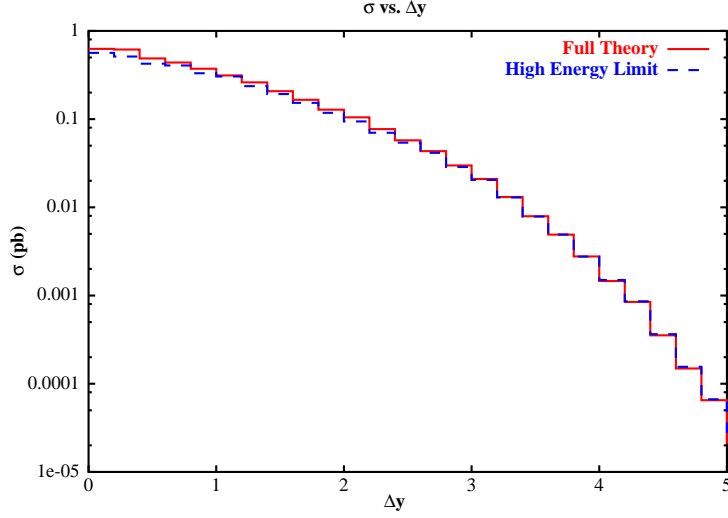
Fig. 13: Cross section in $H + 2$ jet production in $pp$ collisions at the LHC energy $\sqrt{s} = 14$ TeV as a function of $\Delta y$, with $M_{\text{H}} = 120$ GeV and $M_t = 175$ GeV. The dijet invariant mass fulfills the constraint $\sqrt{s_{j_1 j_2}} \geq 600$ GeV. The rapidity interval $\Delta y$ is defined as $\Delta y = \min(|y_{j_1} - y_{\text{H}}|, |y_{j_2} - y_{\text{H}}|)$, with the kinematical constraint $y_{j_1} > y_{\text{H}} > y_{j_2}$. The solid line is the exact production rate; the dashed line is the rate in the high-energy limit.

**The high-energy limit $s_{j_1 j_2}$, $s_{j_2 \text{H}} \gg s_{j_1 \text{H}}$, $M_{\text{H}}^2$**

Next, we consider the limit in which the Higgs is produced forward in rapidity, and close to one of the jets, say to jet $j_1$, and both are very far from jet $j_2$, *i.e.* $s_{j_1 j_2}$, $s_{j_2 \text{H}} \gg s_{j_1 \text{H}}$, $M_{\text{H}}^2$. This limit implies that

$$p_1^+ \simeq p_{\text{H}}^+ \gg p_3^+ \,, \qquad p_1^- \simeq p_{\text{H}}^- \ll p_3^- \,. \tag{8}$$

In this limit, the amplitudes are again dominated by gluon exchange in the $t$ channel, and factorize into in effective vertex for the production of a jet and another for the production of a Higgs plus a jet. For example, in the limit (8) the amplitude for $q\, g \to q\, g\, H$ scattering [41] with the incoming gluon (quark) of momentum $p_2$ ($p_4$), can be written as [62]

$$
\begin{aligned}
&i\, \mathcal{M}^{gq \to gHq}(p_2^{\nu_2}; p_1^{\nu_1}, H \mid p_3^{\nu_3}; p_4^{-\nu_3}) \\
&= 2s \left[ig\, f^{a_2 a_1 c}\, C^{g;Hg}(p_2^{\nu_2}; p_1^{\nu_1}, p_{\text{H}})\right] \frac{1}{t} \left[ig\, T_{a_3 \bar{a}_4}^c\, C^{\bar{q};q}(p_4^{-\nu_3}; p_3^{\nu_3})\right] \,,
\end{aligned} \tag{9}
$$

where $C^{g;Hg}(p_2^{\nu_2}; p_1^{\nu_1}, p_{\text{H}})$ is the effective vertex for the production of a Higgs boson and a gluon jet, $g^* g \to gH$. It has two independent helicity configurations, which we can take to be $C^{g;Hg}(p_2^-; p_1^+, p_{\text{H}})$ and $C^{g;Hg}(p_2^+; p_1^+, p_{\text{H}})$ [62]. High-energy factorization also implies that the amplitude for $g\, g \to g\, g\, H$ scattering can be put in the form (9), up to replacing the incoming quark with a gluon via the substitution (7). Likewise, the amplitude for $q\, Q \to q\, Q\, H$ scattering can be written as

$$
\begin{aligned}
&i\, \mathcal{M}^{qQ \to qHQ}(p_2^{-\nu_1}; p_1^{\nu_1}, p_{\text{H}} \mid p_3^{\nu_3}; p_4^{-\nu_3}) \\
&= 2s \left[g\, T_{a_1 \bar{a}_2}^c\, C^{\bar{q};Hq}(p_2^{-\nu_1}; p_1^{\nu_1}, p_{\text{H}})\right] \frac{1}{t} \left[g\, T_{a_3 \bar{a}_4}^{c'}\, C^{\bar{q};q}(p_4^{-\nu_3}; p_3^{\nu_3})\right] \,,
\end{aligned} \tag{10}
$$

where $C^{\bar{q};Hq}(p_2^{-\nu_1}; p_1^{\nu_1}, p_{\text{H}})$ is the effective vertex for the production of a Higgs and a quark jet, $g^* q \to qH$. There is only one independent helicity configuration, which we can take to be $C^{\bar{q};Hq}(p_2^-; p_1^+, p_{\text{H}})$, and its expression is given in Ref. [62], where an analysis of the limit (8) with the kinematic parameters of Fig. 13 can also be found.

In conclusion, we have considered $H + 2$ jet production via gluon fusion, when either one of the Higgs-jet or the dijet invariant masses become much larger than the typical momentum transfers in the scattering. These limits also occur naturally in Higgs production via WBF. We have shown that we can write the scattering amplitudes in accordance to high-energy factorization, Eqns. (4), (9) and (10). The corresponding effective vertices, whose squares are the impact factors, can be found in Ref. [62].

## 4. FeynHiggs1.2: Hybrid $\overline{\text{MS}}$/on-shell Renormalization for the MSSM Higgs[5]

### 4.1 Introduction

In this section we present an updated version of the Fortran code *FeynHiggs* [65] that evaluates the neutral $\mathcal{CP}$-even Higgs sector masses and mixing angles [7,66]. It differs from the previous version as presented in Ref. [65] by a modification of the renormalization scheme concerning the treatment of subleading terms at the one-loop level; the two-loop corrections, for which the leading contributions of $\mathcal{O}(\alpha_t\alpha_s)$ and $\mathcal{O}(\alpha_t^2)$ are implemented, are not affected. In particular, an $\overline{\text{MS}}$ renormalization for $\tan\beta$ and the field renormalization constants has been used (where the $\overline{\text{MS}}$ quantities are evaluated at the scale $m_t$). The renormalization in the new version of *FeynHiggs* does no longer involve the derivative of the $A$ boson self-energy and the $AZ$ mixing self-energy. This leads to a more stable behavior around thresholds, e.g. at $M_A \approx 2\,m_t$, and avoids unphysically large contributions in certain regions of the MSSM parameter space. Thus, the new renormalization scheme stabilizes the prediction of the masses and mixing angles in the $\mathcal{CP}$-even Higgs sector of the MSSM.

### 4.2 Renormalization schemes

At the tree-level, The MSSM Higgs boson masses $m_h$ and $m_H$ can be evaluated in terms of the SM gauge couplings and two MSSM parameters, conventionally chosen as $M_A$ and $\tan\beta$. Beyond lowest order, the Feynman-diagrammatic (FD) approach allows to obtain in principle the most precise evaluation of the neutral $\mathcal{CP}$-even Higgs boson sector, since in this way the effect of different mass scales of the supersymmetric particles and of the external momentum can consistently be included. The masses of the two $\mathcal{CP}$-even Higgs bosons are obtained in this approach by determining the poles of the $h - H$-propagator matrix, which is equivalent to solving the equation

$$[\, q^2 - m_{h,\text{tree}}^2 + \hat{\Sigma}_h(q^2) \,][\, q^2 - m_{H,\text{tree}}^2 + \hat{\Sigma}_H(q^2) \,] - [\, \hat{\Sigma}_{hH}(q^2) \,]^2 = 0, \tag{11}$$

where $\hat{\Sigma}_s, s = h, H, hH$, denote the renormalized Higgs boson self-energies. For the renormalization within the FD approach usually the on-shell scheme is applied [66]. This means in particular that all the masses in the FD result are the physical ones, i.e. they correspond to physical observables. Since eq. (11) is solved iteratively, the result for $m_h$ and $m_H$ contains a dependence on the field renormalization constants of $h$ and $H$, which is formally of higher order. Accordingly, there is some freedom in choosing appropriate renormalization conditions for fixing the field renormalization constants (this can also be interpreted as affecting the renormalization of $\tan\beta$). Different renormalization conditions have been considered, e.g. ($\hat{\Sigma}'$ denotes the derivative with respect to the squared momentum):

1. on-shell renormalization for $\hat{\Sigma}_Z, \hat{\Sigma}_A, \hat{\Sigma}'_A, \hat{\Sigma}_{AZ}$, and $\delta v_1/v_1 = \delta v_2/v_2$ [67]
2. on-shell renormalization for $\hat{\Sigma}_Z, \hat{\Sigma}_A, \hat{\Sigma}_{AZ}$, and $\delta v_i = \delta v_{i,\text{div}}, i = 1, 2$ [68]
3. on-shell renormalization for $\hat{\Sigma}_Z, \hat{\Sigma}_A$ [67], $\overline{\text{MS}}$ renormalization for $\delta Z_h, \delta Z_H, \tan\beta$ [69].

The previous version of *FeynHiggs* is based on renormalization 1, involving the derivative of the $A$ boson self-energy. The new version of *FeynHiggs*, see www.feynhiggs.de, is based on renormalization 3 (a detailed discussion can be found in Ref. [69]).

### 4.3 Numerical comparison

In this section we numerically compare the output of the previous version (based on renormalization 1) and the new version (based on renormalization 3) of *FeynHiggs*. We also show results for the recently obtained non-logarithmic $\mathcal{O}(\alpha_t^2)$ corrections [8,9] that are also included in the new version of *FeynHiggs*. The comparison is performed for the parameters of the three LEP benchmark scenarios [70]. In this way, the effect of the new renormalization and the non-logarithmic $\mathcal{O}(\alpha_t^2)$ corrections on the analysis of the LEP Higgs-boson searches can easily be read off.

---

[5]*M. Frank, S. Heinemeyer, W. Hollik and G. Weiglein*

In Figs. 14–16 we show the results in the "$m_h^{\mathrm{max}}$", "no-mixing" and "large $\mu$" scenario as a function of $M_A$ (left column) and of $\tan\beta$ (right column) for two values of $\tan\beta$ ($\tan\beta = 3, 50$) and $M_A$ ($M_A = 100, 1000$ GeV for the $m_h^{\mathrm{max}}$ and the no-mixing scenario, $M_A = 100, 400$ GeV for the large $\mu$ scenario), respectively. The solid lines correspond to the new result while the dashed lines show the old results. The dotted lines correspond to the new result including the non-logarithmic $\mathcal{O}(\alpha_t^2)$ contributions. Concerning the new renormalization scheme, in the $m_h^{\mathrm{max}}$ (Fig. 14) and the no-mixing scenario (Fig. 15) the new result is larger by $\approx$1–2 GeV for not too small $M_A$ and $\tan\beta$. For small $\tan\beta$ and large $M_A$ the enhancement can be even larger. In the large $\mu$ scenario (Fig. 16) the largest deviations appear for small $\tan\beta$ for both large and small $M_A$. While the previous prescription for the field renormalization constants leads to unphysically large threshold effects in some regions of the parameter space, which arise from the $AZ$ mixing self-energy and the derivative of the $A$ boson self-energy, no threshold kinks are visible for the result based on the new renormalization. The shift in $m_h$ of $\approx$1–2 GeV related to the modification of the renormalization prescription lies in the range of the anticipated theoretical uncertainty from unknown non-leading electroweak two-loop corrections [71]. The new $\mathcal{O}(\alpha_t^2)$ corrections can further increase $m_h$ by up to $\approx$3 GeV for large $\tilde{t}$ mixing (a detailed analysis will be presented elsewhere [72]).

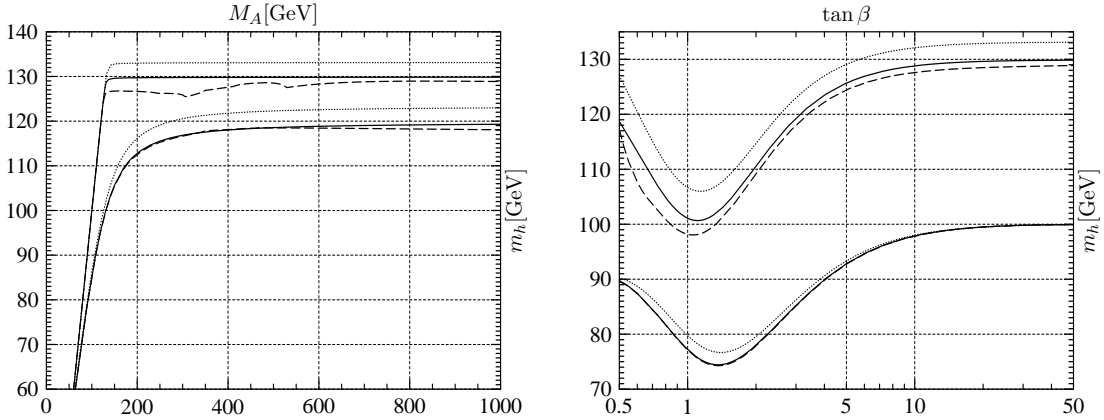The new version of *FeynHiggs* can be obtained from `www.feynhiggs.de`.



Fig. 14: The new renormalization (3, solid) and the old scheme (1, dashed) are compared in the $m_h^{\mathrm{max}}$ scenario. The dotted line shows the inclusion of the non-logarithmic $\mathcal{O}(\alpha_t^2)$ corrections. The lower curves are for $\tan\beta = 3$ (left plot) or $M_A = 100$ GeV (right). The upper curves are for $\tan\beta = 50$ (left) or $M_A = 1000$ GeV (right).
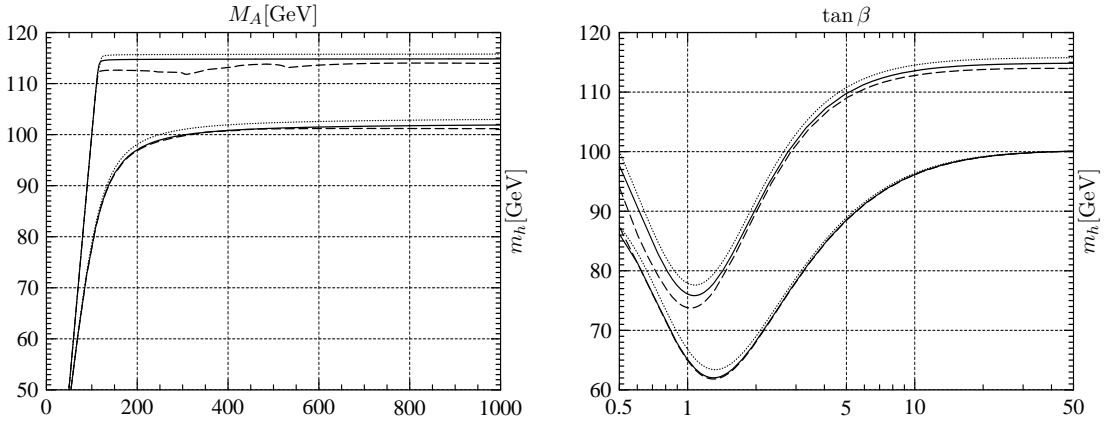


Fig. 15: The new renormalization (3, solid) and the old scheme (1, dashed) are compared in the no-mixing scenario. The dotted line shows the inclusion of the non-logarithmic $\mathcal{O}(\alpha_t^2)$ corrections. The lower curves are for $\tan\beta = 3$ (left plot) or $M_A = 100$ GeV (right). The upper curves are for $\tan\beta = 50$ (left) or $M_A = 1000$ GeV (right).

Fig. 16: The new renormalization (3, solid) and the old scheme (1, dashed) are compared in the large $\mu$ scenario. The dotted line shows the inclusion of the non-logarithmic $\mathcal{O}(\alpha_t^2)$ corrections. The lower curves are for $\tan\beta = 50$ (left plot) or $M_A = 100$ GeV (right). The upper curves are for $\tan\beta = 3$ (left) or $M_A = 400$ GeV (right).
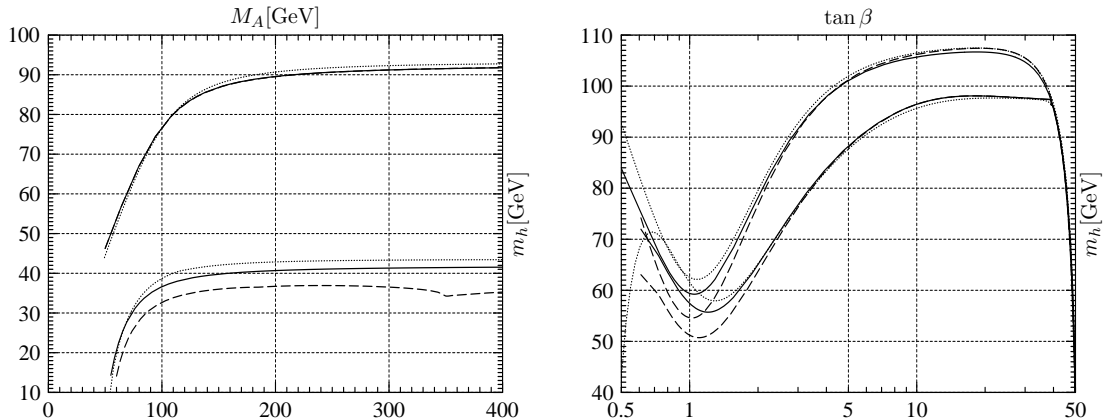
## 5. Suggestions for MSSM Benchmark Scenarios for Higgs Boson Searches at Hadron Colliders[6]

### 5.1 Introduction and theoretical basis

Within the MSSM the masses of the $\mathcal{CP}$-even neutral Higgs bosons are calculable in terms of the other MSSM parameters. The lightest Higgs boson has been of particular interest, since its mass, $m_h$, is bounded from above according to $m_h \leq M_Z$ at the tree level. The radiative corrections at one-loop order have been supplemented in the last years with the leading two-loop corrections, performed by renormalization group (RG) methods [73], by renormalization group improvement of the one-loop effective potential calculation [6], by two-loop effective potential calculations [8, 9], and in the Feynman-diagrammatic (FD) approach [7, 66]. These calculations predict an upper bound for $m_h$ of about $m_h \lesssim 135$ GeV.[7]

After the termination of LEP, the Higgs boson search has now shifted to the Tevatron and will later be continued to the LHC. Due to the large number of free parameters, a complete scan of the MSSM parameter space is too involved. Therefore at LEP the search has been performed in three benchmark scenarios [70]. Besides the $m_h^{\mathrm{max}}$ scenario, which has been used to obtain conservative bounds on $\tan\beta$ [74], and the no-mixing scenario, the large-$\mu$ scenario had been designed to encourage the investigation of flavor and decay-mode independent decay channels (instead of focusing on the $h \to b\bar{b}$ channel). The investigation of these channels has lead to exclusion bounds [4] that finally completely ruled out the large-$\mu$ scenario.

The different environment at hadron colliders implies different Higgs boson production channels and also different relevant decay channels as compared to LEP. The main production modes at the Tevatron will be $V^* \to V\phi$ ($V = W, Z, \phi = h, H, A$) and also $b\bar{b} \to b\bar{b}\phi$, while the relevant decay modes will be $\phi \to b\bar{b}$ and $\phi \to \tau^+\tau^-$ [10]. At the LHC, on the other hand, the most relevant process for a Higgs boson with $m_h \leq 135$ GeV will be $gg \to h \to \gamma\gamma$, supplemented by $t\bar{t} \to t\bar{t}h \to t\bar{t}b\bar{b}$. In order to investigate these different modes, we propose new benchmark scenarios for the Higgs boson searches at hadron colliders. Contrary to the new "SPS" benchmark scenarios proposed in Ref. [75] for general SUSY searches, the scenarios proposed here are designed specifically to study the MSSM Higgs sector without assuming any particular soft SUSY-breaking scenario and taking into account constraints only from the Higgs boson sector itself.

The tree-level value for $m_h$ within the MSSM is determined by $\tan\beta$, the $\mathcal{CP}$-odd Higgs-boson mass $M_A$, and the $Z$-boson mass $M_Z$. Beyond the tree-level, the main correction to $m_h$ stems from the $t$–$\tilde{t}$-sector, and for large values of $\tan\beta$ also from the $b$–$\tilde{b}$-sector (see Ref. [70] for our notations.) Accordingly, the most important parameters for the corrections to $m_h$ are $m_t$, $M_{SUSY}$ (in this work we

---

[6]*M. Carena, S. Heinemeyer, C.E.M. Wagner and G. Weiglein*

[7] This value holds for $m_t = 175$ GeV and $M_{SUSY} = 1$ TeV. If $m_t$ is raised by 5 GeV then the $m_h$ limit is increased by about 5 GeV; using $M_{SUSY} = 2$ TeV increases the limit by 2 GeV.

assume that the soft SUSY-breaking parameters for sfermions are equal: $M_{SUSY} := M_{\tilde{t}_L} = M_{\tilde{t}_R} = M_{\tilde{b}_L} = M_{\tilde{b}_R}$), $X_t$ ($\equiv A_t - \mu/\tan\beta$), and $X_b$ ($\equiv A_b - \mu\tan\beta$) ($A_{t,b}$ are the trilinear Higgs sfermion couplings, $\mu$ is the Higgs mixing parameter.) $m_h$ depends furthermore on the SU(2) gaugino mass parameter, $M_2$ (the U(1) gaugino mass parameter is given by $M_1 = 5/3 \, s_W^2/c_W^2 \, M_2$.) At the two-loop level also the gluino mass, $m_{\tilde{g}}$, enters the prediction for $m_h$.

It should be noted in this context that the FD result has been obtained in the on-shell (OS) renormalization scheme (the corresponding Fortran code, that has been used for the studies by the LEP collaborations, is *FeynHiggs* [65, 69]), whereas the RG result has been calculated using the $\overline{\text{MS}}$ scheme; see Ref. [76] for details (the corresponding Fortran code, also used by the LEP collaborations, is *subhpole* [73, 76]). While the corresponding shift in the parameter $M_{SUSY}$ turns out to be relatively small in general, sizable differences can occur between the numerical values of $X_t$ in the two schemes; see Refs. [8, 66, 76]. For this reason we specify below different values for $X_t$ within the two approaches.

## 5.2   The benchmark scenarios

In this section we define four benchmark scenarios suitable for the MSSM Higgs boson search at hadron colliders[8]. In these scenarios the values of the $\tilde{t}$ and $\tilde{b}$ sector as well as the gaugino masses will be fixed, while $\tan\beta$ and $M_A$ are the parameters that are varied.[9] It has been checked that the scenarios evade the LEP2 bounds [4] over a wide range of the $M_A$-$\tan\beta$-plane, where the variation should be chosen according to: $0.5 \le \tan\beta \le 50$, $M_A \le 1000$ GeV.

*(i) The $m_h^{\text{max}}$ scenario*: This scenario is kept as presented in Ref. [70], since it allows for conservative $\tan\beta$ exclusion bounds [74] (only the sign of $\mu$ is switched to a positive value.) The parameters are chosen such that the maximum possible Higgs-boson mass as a function of $\tan\beta$ is obtained (for fixed $M_{SUSY}$, and $M_A$ set to its maximal value, $M_A = 1$ TeV). The parameters are[10]:

$$m_t = 174.3 \text{ GeV}, \quad M_{SUSY} = 1 \text{ TeV}, \quad \mu = 200 \text{ GeV}, \quad M_2 = 200 \text{ GeV}, \, m_{\tilde{g}} = 0.8 \, M_{SUSY},$$

$$X_t^{\text{OS}} = 2 \, M_{SUSY} \text{ (FD calculation)}, \quad X_t^{\overline{\text{MS}}} = \sqrt{6} \, M_{SUSY} \text{ (RG calculation)}, \quad A_b = A_t . \quad (12)$$

*(ii) The no-mixing scenario*: This benchmark scenario is the same as the $m_h^{\text{max}}$ scenario, but with vanishing mixing in the $\tilde{t}$ sector and with a higher SUSY mass scale to avoid the LEP Higgs bounds:

$$m_t = 174.3 \text{ GeV}, \quad M_{SUSY} = 2 \text{ TeV}, \quad \mu = 200 \text{ GeV}, \quad M_2 = 200 \text{ GeV}, \quad m_{\tilde{g}} = 0.8 M_{SUSY},$$

$$X_t = 0 \text{ (FD/RG calculation)}, \quad A_b = A_t . \quad (13)$$

*(iii) The gluophobic Higgs scenario*: In this scenario the main production cross section for the light Higgs boson at the LHC, $gg \to h$, is strongly suppressed (see Ref. [84]). The parameters are:

$$m_t = 174.3 \text{ GeV}, \, M_{SUSY} = 350 \text{ GeV}, \, \mu = 300 \text{ GeV}, \, M_2 = 300 \text{ GeV}, \, m_{\tilde{g}} = 500 \text{ GeV},$$

$$X_t^{\text{OS}} = -750 \text{ GeV} \text{ (FD calculation)}, \quad X_t^{\overline{\text{MS}}} = -770 \text{ GeV} \text{ (RG calculation)}, \quad A_b = A_t . \quad (14)$$

*(iv) The small $\alpha_{\text{eff}}$ scenario*: Besides the channel $gg \to h \to \gamma\gamma$ at the LHC, the other channels for light Higgs searches at the Tevatron and at the LHC mostly rely on the decays $h \to b\bar{b}$ and $h \to \tau^+\tau^-$.

---

[8]Here, we will comment only on the phenomenology of the lightest $h$ boson. The couplings of the $H, A$ and $H^{\pm}$ bosons are also subject to important radiative corrections in the large tanbeta regime, see for instance ref. [77, 78]. It is customary to define the searches for these particles in terms of their tree-level couplings. Since the corrections to these couplings are strongly dependent on the value of the supersymmetry breaking parameters, a precise interpretation of these search analyses within the MSSM will demand a knowledge of the characteristic supersymmetry breaking parameters. In the case of the $h$ boson, see [79, 82] for more details.

[9] Plots that show the behavior of different Higgs production and decay channels in the four scenarios can be found at www.feynhiggs.de . The numerical evaluation is based on Refs. [80–83].

[10]Better agreement with BR($b \to s\gamma$) constraints is obtained for the other sign of $X_t$ (called the "constrained $m_h^{\text{max}}$" scenario) [78]. However, this lowers the maximum $m_h$ values by $\sim 5$ GeV.

In comparison to the Standard Model, both $hf\bar{f}$ couplings have an additional factor of $\sin\alpha_{\text{eff}}/\cos\beta$, where $\alpha_{\text{eff}}$ is the mixing angle of the neutral $\mathcal{CP}$-even Higgs sector, including radiative corrections (see e.g. Refs. [82, 83]). If $\alpha_{\text{eff}}$ is small, these two decay channels can be heavily suppressed ($h \to b\bar{b}$ can receive also large corrections from $\tilde{b}$-$\tilde{g}$ loops [81, 82]). This case is realized for large $\tan\beta$ and not too large $M_A$ (in a similar way as in the large-$\mu$ scenario [70]) for the following parameters:

$$m_t = 174.3 \text{ GeV}, \ M_{SUSY} = 800 \text{ GeV}, \ \mu = 2.5\,M_{SUSY}, \ M_2 = 500 \text{ GeV}, \ m_{\tilde{g}} = 500 \text{ GeV}$$

$$X_t^{\text{OS}} = -1100 \text{ GeV (FD calculation)}, \ X_t^{\overline{\text{MS}}} = -1200 \text{ GeV (RG calculation)}, \quad A_b = A_t. \quad (15)$$

### 5.3 Conclusions

We have presented four benchmark scenarios for the MSSM Higgs boson search at hadron colliders, evading the exclusion bounds obtained at LEP2. These scenarios exemplify different features of the MSSM parameter space, such as large $m_h$ values and significant $gg \to h$ or $h \to b\bar{b}$, $h \to \tau^+\tau^-$ suppression. In analyzing the new benchmark scenarios, it will be helpful to make use of the complementarity of different channels accessible at the Tevatron and the LHC (see e.g. Ref. [82] for details).

## 6.  The invisible SUSY Higgs and Dark Matter[11]

### 6.1  Introduction

Current limits [85] on both the Higgs and the neutralino in a general SUSY model are such that it is kinematically possible for the light Higgs to decay into the lightest neutralino. If the decay rate is substantial the Higgs will be mainly invisible, while its usual branching ratios will be dramatically reduced preventing a detection in the much studied channels at the LHC and the Tevatron. Some theoretical studies [86–88] have addressed the issue of how to hunt an invisibly decaying Higgs at a hadronic machine. For the LHC it has been suggested to use $WH/ZH$ production , $t\bar{t}h$ [87] or more recently the the $W$ fusion process [88]. The results for the latter are quite promising since for a luminosity of $100fb^{-1}$ a branching ratio into invisibles as low as $5\%$ is enough for Higgs discovery. The aim of the present report is to summarize our findings on the size of the branching ratio of the Higgs into neutralinos, taking into account the latest data from colliders as well as from cosmology.

### 6.2  MSSM parameters and $h \to \chi\chi$

For a substantial branching fraction of the Higgs into invisible to occur one needs both enough phase space for the decay as well as a large enough coupling of the Higgs to neutralinos. Considering that the present experimental and theoretical limits on the lightest MSSM Higgs implies that its mass lies in the interval $113 - 135$ GeV, the maximum LSP mass must be below $55 - 65$GeV. In models with gaugino unification where $M_1 \approx M_2/2$ , the lower limit on the chargino mass (which depends essentially on $M_2$ and $\mu$) turns into a lower limit on the neutralino mass, leaving only a small window for the Higgs into neutralinos. In fact in this type of models we found that the branching is never above 20% [89] (see also ref. [90]). For this reason we will relax the relation between $M_1$ and $M_2$ and consider these as independent parameters. In order that the coupling of the LSP to the Higgs be large, it can be shown that the LSP has to be a mixture of gaugino and Higgsino [89]. However a light LSP, which corresponds to $M_1$ small, is mostly a Bino. To have a non negligible Higgsino component implies that $\mu$ should be small as well. However $\mu$ is bounded below by the chargino mass constraint. From these arguments, we can already expect that if the Higgs invisible decay is large then the chargino and next to lightest neutralino should not be far above the present LEP limit. One also finds [89] that positive $\mu$ values lead to larger couplings. Large $\tan\beta$ values also lead to large Higgs mass and more phase space for the invisible decays, however the LSP mass increases even faster with $\tan\beta$, and we found that their coupling to

---

[11]G. Bélanger, F. Boudjema, A. Cottrant, R.M. Godbole, A. Pukhov and A. Semenov

the Higgs get smaller with increasing $\tan\beta$ [89]. Therefore the largest effect for the Higgs occurs for moderate $\tan\beta$ and we will consider $\tan\beta = 5$.

We take a model with a common scalar mass $m_0$ (defined at the GUT scale) for the SUSY breaking sfermion mass terms of both left and right sleptons of all three generations. As for the gaugino masses, we take $M_1 = rM_2$ at the weak scale. For $r < 1/3$ or so, this scheme leads to almost no running of the right slepton mass, since the contribution from the running is of order $M_1^2$, while left sleptons have an added $M_2^2$ contribution and would be "much heavier". Indeed, neglecting Yukawa couplings one has

$$
\begin{aligned}
m_{\tilde{e}_R}^2 &= m_0^2 \; + \; .88 \, r^2 M_2^2 \; - \; \sin^2\theta_W M_Z^2 \cos(2\beta) \\
m_{\tilde{e}_L}^2 &= m_0^2 \; + \; (0.72 + .22 \, r^2) M_2^2 \; - \; (.5 - \sin^2\theta_W) M_Z^2 \cos(2\beta)
\end{aligned}
\tag{16}
$$

Even with a common scalar mass squarks are much heavier than sleptons, since they receive a large contribution from the SU(3) gaugino mass. For simplicity, we then assume all squarks to be heavy (1TeV). In any case heavy squarks especially stops would be required in order to get a heavy enough light Higgs. Of course, to allow for a low $\mu$ in this scenario one needs to appropriately choose the soft SUSY Higgs scalar masses at high scale. It is important to stress that the kind of models we investigate in this report are quite plausible. The GUT-scale relation which equates all the gaugino masses at high scale need not be valid in a more general scheme of SUSY breaking. SUGRA models with general kinetic terms [94, 95], superstring models with moduli-dominated or with a mixture of moduli and dilaton fields, as well as anomaly-mediated SUSY breaking mechanisms, all lead to non-universality of the gaugino masses [96].

## 6.3 Constraints

Our scenario requires as large a Higgs mass as possible without a too large value for $\tan\beta$ . We will then only consider the MSSM in the decoupling limit with $M_A \sim 1\text{TeV}$ and choose large enough stop masses ($m_{\tilde{t}} = 1\text{TeV}$) and large mixing ($A_t = 2.4\text{TeV}$). With these parameters we have $m_h = 125\text{GeV}$ for $\tan\beta = 5$ and we are never in conflict with the lower limit on the Higgs mass $m_h > 113\text{GeV}$.

The limits on $M_1, M_2, \mu$, the key ingredients for this analysis, are set from the chargino mass limit at LEP2, $m_{\chi_1^\pm} > 103\text{GeV}$ [85]. This bound can be slightly relaxed depending on $\tan\beta$ and the sneutrino mass, however we prefer to take the strongest constraint so that our results are more robust. In addition to this, one must include the limits from LEP2 on pair production of neutralinos, as well as the limit on the invisible width of the Z. For the parameters we have studied these two constraints are weaker than the chargino mass constraint. We will also take $m_{\tilde{l}} > 96\text{GeV}$, for all sleptons $\tilde{l}$, even though the limit on the lightest stau is slightly lower [85].

Apart from the chargino mass limit, the most important constraint comes from the relic density of the LSP. In the models we are considering the LSP is *mainly* (but not totally) a bino. Since it is rather light the main annihilation channels are into the light fermions. The largest contributions are from processes involving "right-handed" sleptons since they have the largest hypercharge. In this case the relic density may be approximated as $\Omega h^2 \sim 10^{-3} m_{\tilde{l}_R}^4 / m_{\tilde{\chi}_1^0}^2$ (all masses in GeV) which imposes a strong constraint on $m_{\tilde{l}_R}$. However this approximation does not hold if the neutralino mass is such that annihilation through the $Z$ pole, $\tilde{\chi}_1^0 \tilde{\chi}_1^0 \to Z$, occurs. In this case the contribution of this channel alone is enough to bring the relic density in the relevant range irrespective of the slepton mass.

We use a new code [91] for the calculation of the relic density that tackles all $s$-channels poles, threshold effects and includes all co-annihilations channels. The program extracts all *exact* matrix elements from `CompHEP` [92] and is linked to `FeynHiggs` [7, 65] for the Higgs mass. Radiative corrections to Higgs partial widths are extracted from HDECAY [80].

Fig. 1a shows the allowed parameter space in the $M_2, \mu$ plane with $\tan\beta = 5$ and $M_1 = M_2/5$ for a light slepton, $m_0 = 100\text{GeV}$. The chargino mass limit from LEP2 is delimited by a line. It does not depend on $m_0$. The direct LEP2 limits, expectedly, cut on the lowest $\mu, M_2$ region. This is in contrast

to the relic density requirement which depends sensitively on $m_0$. We delineate three regions set by the relic density: a) the overclosure region $\Omega h^2 > .3$ which we consider as being definitely ruled out [93], b) $.1 < \Omega h^2 < .3$ which is the preferred region and c) $\Omega h^2 < .1$ where one needs other form of Dark Matter than the SUSY Dark Matter considered here. As $m_0$ increases the allowed region for the relic density shrinks. However there always remain allowed regions that correspond essentially to the pole annihilation $\tilde{\chi}_1^0 \tilde{\chi}_1^0 \to Z$ [89]. For $M_1 = M_2/10$ (Fig. 1b), the effect of the Z-pole would be seen only at much larger values of $M_2$. For $m_0 = 94$GeV, the relic density constraint leaves a sizeable allowed region, however as soon as $m_0$ increases the region allowed is restricted to the regions of parameter space where $m_\chi \approx M_z/2$.

In view of the latest theoretical calculations of the muon anomalous magnetic moment, showing consistency between the experimental limit and the SM within $1.6\sigma$ [99], all constraints that were previously thought to play an important role, (in particular the preference for light smuons) disappear in the range of parameters considered here. Finally, we note that $b \to s\gamma$ is irrelevant since the squarks and gluinos are assumed heavy and that we are choosing $\mu > 0$ anyway.

## 6.4 Results

The branching ratio into invisible due to neutralinos will be denoted by $B_{\chi\chi}$. The opening up of this channel will not have any effect on any of the Higgs production mechanisms. This is in contrast to other SUSY effects on the production and decay of the Higgs, like those due to a light stop [97]. Thus the Higgs discovery significances of the different channels at the LHC (and the Tevatron) are only affected by the reduction in the branching ratio into $b\bar{b}$ and $\gamma\gamma$. We define $R_{bb}$ ($R_{\gamma\gamma}$)as the reduction factor of the branching ratio of $h \to b\bar{b}$ ($h \to \gamma\gamma$) due to invisible compared to the same branching ratio of a standard model Higgs with the same Higgs mass. Since in the absence of light neutralinos the width of the Higgs is dominated by that into $b\bar{b}$, one has roughly $R_{bb} \sim R_{\gamma\gamma} \sim 1 - B_{\chi\chi}$. This is well supported by our full analysis and therefore we will only show the behaviour of the branching into invisible.
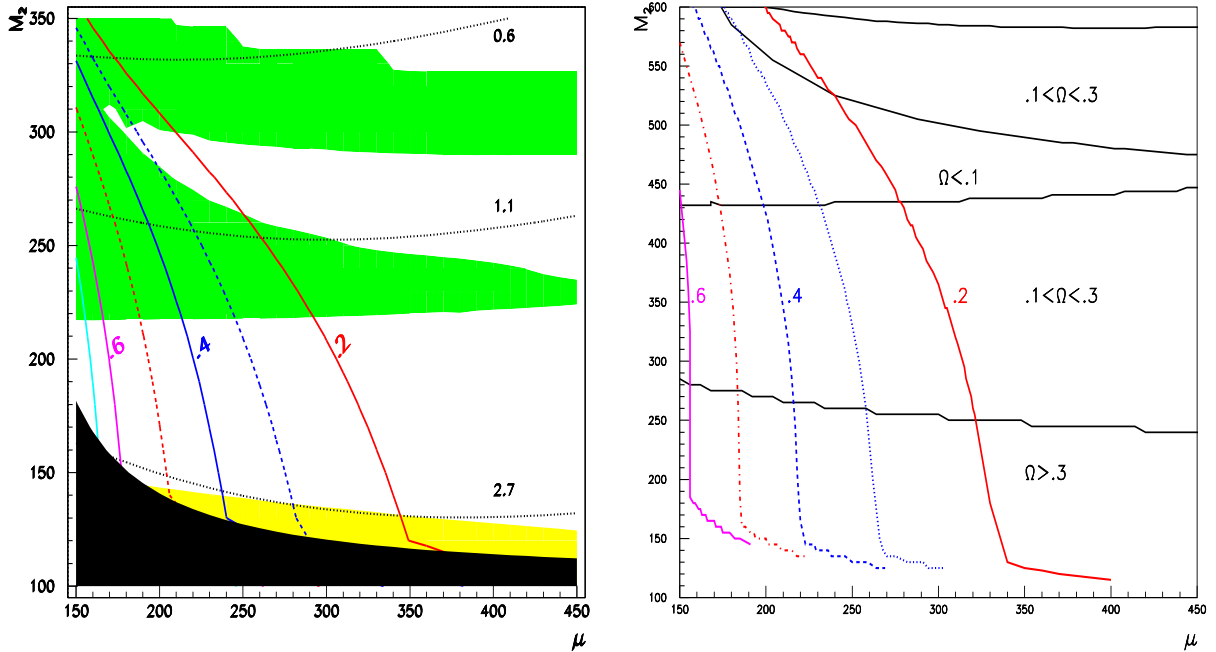


Fig. 17: *a) Contours of constant $Br_{\chi\chi}$ from .2 (far right) to .65 (far left) for $M_1/M_2 = 1/5, m_0 = 100$GeV We have also superimposed the various constraints. The black area is excluded by the chargino mass at LEP. The other shadings refer to the relic density, with the allowed region (white), the overclosure region (light grey) and the region with $\Omega < .1$ (medium grey). The dotted lines are constant $a_\mu$ lines in units of $10^{-9}$. b)Similarly for $M_1/M_2 = 1/10, m_0 = 94$GeV.*

Fig. 17a shows the different contours in the $M_2 - \mu$ plane of $B_{\chi\chi}$ for $M_1 = M_2/5$ and for a

light slepton. We see that, even after taking all constraints, we still find large branching ratio of the lightest SUSY Higgs into neutralinos. The largest branchings correspond to the smallest $\mu$ values, which as argued before maximises the Higgsino content. It is also worth stressing that even in these general models, the branching ratio into invisible is never larger than 70%. For a lower ratio $M_1 = M_2/10$, the invisible branching ratio can reach over 60% (Fig. 17b). Even in the case of heavier sleptons large branching ratio into invisible are possible although the allowed region of in the $M_2 - \mu$ plane corresponds to a narrow region around the Z pole.

We have also searched, by making a large scan over $M_1, M_2, \mu$ and $m_0$, but for fixed $\tan \beta = 5$, which minimum value of $M_1$ one can entertain. The parameters were varied in the range $10 < M_1 < 100\text{GeV}$, $100 < M_2, \mu < 500\text{GeV}$, $70 < m_0 < 300\text{GeV}$ as given by Eq. 1. We find that, in order not to have too large a relic density, $M_1$ must be above 20GeV independently of $M_2$ and $\mu$, as seen in Fig. 18. However, this is not a value that gives the largest branching into invisibles, largest values are in the range $40 < M_1 < 60$ GeV where one has both a significant Higgsino-gaugino mixing and a LSP light enough for the Higgs to decay into it. Note that this lower bound on $M_1$ is more or less independent on $\tan \beta$ [98]. We also show the relic density as a function of $M_1$. Note that one hits both the Z pole and the Higgs pole. However for the latter configurations, $B_{\chi\chi}$ is negligible.

To conclude we have found that there are regions of parameter space that give a substantial branching fraction of the lightest SUSY Higgs into invisibles that can account for the dark matter in the universe. We also find that these scenarios do not always require a very light slepton since we can obtain an acceptable amount of LSP relic density through an efficient annihilation at the $Z$ pole. However scenarios with the largest branching ratio into LSP do entail that the lightest chargino and at the least the next LSP are light enough that they could be produced at the Tevatron. The phenomenology at the Tevatron should somehow be similar to the Sugra $SU(5)$ based "24-model" which was studied in [95]. Among other things, due to the fact that one has a larger splitting between the LSP and the NLSP, as compared to the usual unified scenario, one expects an excess of events containing many isolated leptons originating, for example, from a real $Z$ coming from the decay of the NLSP. However to make definite statements about observability of these states at the Tevatron requires a thorough simulation.
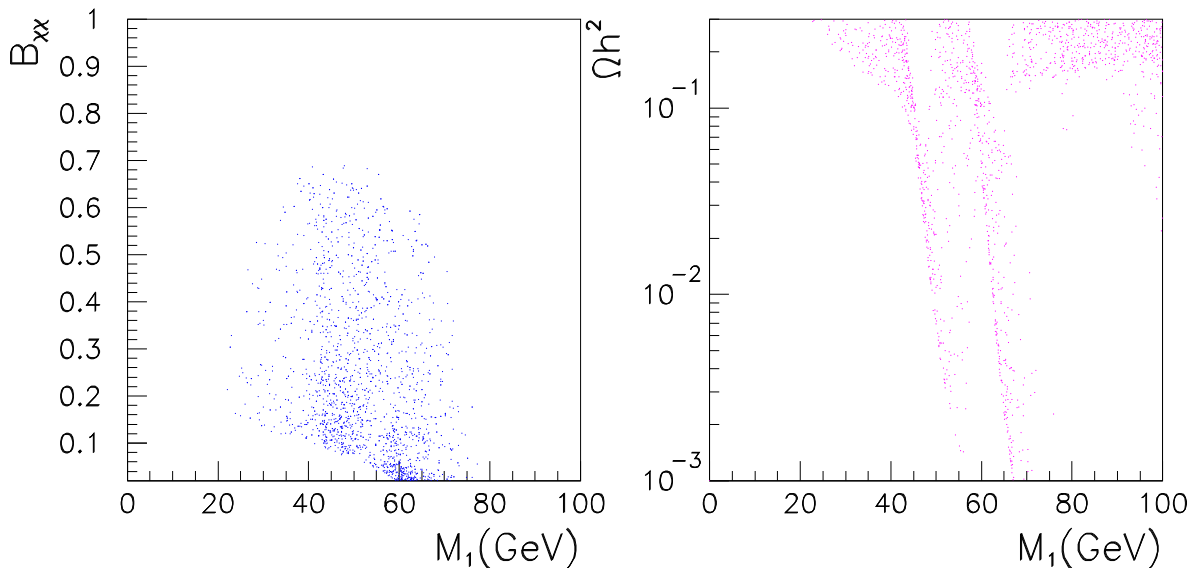


Fig. 18: *Large scan over $M_1, M_2, \mu, m_0$ for $\tan \beta = 5$. The first panel shows the branching ratio into invisibles vs $M_1$. The second panel shows the relic density as a function of $M_1$.*

## 7. Search for the invisible Higgs in the $Wh/Zh$ channel at the LHC[12]

One of the various methods to search for an invisible Higgs at the LHC is the associated production process $pp \rightarrow Wh(Zh)$ followed by the invisible decay of h is one of them. The signatures being a single lepton with large transverse momentum and missing $P_T$, from the higgs as well as from the neutrino from the W decay, and lepton pair whose mass constructs to $Z$ and missing $P_T$, for the $Wh$ and $Zh$ production respectively. A parton level study, which took into account the dominant irreducible background caused by the $WZ(ZZ)$ production followed by the invisible $Z \rightarrow \nu\bar{\nu}$ decay, had been made [87]. This had shown that that it is possible to have $S/\sqrt{B} \sim 5.9$ for the process for $m_h = 120$ GeV and 100% B.R. into the invisible channel. The issue of the reach of these channels in terms of $m_h$ and the $B(h \rightarrow \text{invisibles})$, is being revisited here.

**In the $Wh$ process**: The backgrounds relevant for this signal are: (1) The irreducible background due to the $WZ$ production followed by $Z \rightarrow \nu\bar{\nu}$. (2) $WW$ production followed by leptonic decays of both the $W$'s, one lepton being lost, due to low $P_T$ or too large a rapidity. (3) The large QCD backgrounds caused by the production of $W$ with jets which are lost. The lost jets can add on to the missing $P_T$ of the decay $\nu$ from the $W$ and thus possibly give substantial missing $P_T$. (4) Another source of background would be the $t\bar{t}$ production with their decay producing a $W$ pair with two $b$ jets. This can cause a background if the $b$ jets are lost along with one of the decay leptons. (5) $Z + \text{jets}$ production will also give a background if the jet(s) are missidentified as a lepton.

Before discussing the separation of the signal from the mentionned QCD backgrounds, we report the result of a repetition of the of the calculation of the signal and the irreducible background, with more modern parton densities. A calculation of the $Wh$ signal, using the LO formulae, with $|\eta_l| < 2.5, P_T^\ell > 100$ GeV, gives 28 fb. The irreducible $WZ$ background for the same cuts is 40 fb. The higher order corrections to the signal give rise to a moderate $K$ factor and might just compensate for lepton detection effeciencies of 70%. Thus the above numbers, though calculated from a LO formula can be considered representative. All the numbers are for $m_h = 120$ GeV and 100% B.R. into the invisible channel.

The $WW$ background mentioned in point (2) above has also been evaluated and is 9 fb. The canonical values for LHC used here for the soft and forward leptons that lost, giving rise to a final state similar to the signal are, i) a $P_T^e < 10$ GeV, ii) $P_T^\mu < 5$ GeV or $|\eta_\mu| > 2.5$, iii) $P_T^\tau < 20$ GeV. Incidentally the background also has been evaluated only at the LO.

The big discriminant between the QCD background and the signal is the hadronically quiet nature of the signal. Hence one has to tune cuts and jet vetos such that we get rid of the background at low cost to the signal. Towards this end we have to first look at the effect of the initial state radiations on the kinematical distributions in the following variables: 1) Missing $P_T$ which no longer is just the lepton $P_T$. 2) rapidity and $P_T$ of the jet with the largest $P_T$ in the event. 3) the same for the jet with the second largest $P_T$. The knowledge of 2 and 3 can help determine the vetos for the two $b$ jets that will be produced in $t\bar{t}$ process. Results of a priliminary calculation are very encouraging and suggest that with a cut on the transverse mass $M_T$ of the lepton and the missing $P_T$, as well as appropriate jet vetos, it should be possible to reduce the QCD background substantially without any harm to the signal. The last background due to $Z + \text{jets}$ has been evaluated. With a rejection factor of $10^{-5}$ against a misidentification of the jet as a lepton, this background can at the most be 1.2 fb, even for a missing $P_T$ cut of 100 GeV.

The NLO corrections to a pair of gauge bosons production [88] shows that a veto on the jet with $P_T > 50$ GeV and $\eta < 3$ reduces them to within 20% of the Born cross-section. This also gives an indication that these kinds of jet vetos will work well to reduce the background. We will have to optimise these cuts once we after taking into account the effect of the initial state radiation on the signal.

**In the $Zh$ process**: This signal in this case is of course much smaller. The possible backgrounds in this case are: (1) $ZZ$ production followed by the invisible $Z \rightarrow \nu\bar{\nu}$ decay of the $Z$. (2) $WZ$ production with leptonic decay of the $W$ lepton getting lost as outlined in the consideration of the background due

---

[12]*S. Balatenychev, G. Bélanger, F. Boudjema, R.M. Godbole, V.A. Ilyin and D.P. Roy*

to the $WW$ production in the earlier caser. This can give rise to a final state with $l^+l^-$ coming from the $Z$ decay and missing $P_T$. (3) Production of $Z + 1$ jet where the jet gets lost can also cause a small background.

In the $Zh$ case one would want to use a cut on the missing $P_T$ unlike the case of the $Wh$ signal where demanding a large $P_T$ lepton automatically guranteed a large missing $P_T$. The signal and $ZZ$ background as well as the $WZ$ background mentioned in (2) has been calculated at the parton level. The numbers are for a missing $P_T$ cut of 100 GeV, with $P_T^\ell < 20 GeV$, and $|\eta^\ell| < 2.5$. The size of the signal, $ZZ$ and $WZ$ background are about 8 fb, 21 fb and 3 fb respectively. The cut on the missing $P_T$ can be increased without harming the signal but can bring down the QCD backgrounds effectively. Again to decide on the cuts to optimise the signal, one needs to know the effect of the initial state radiation on the $Zh$ signal.These calculations are in progress.

## 8. Simulation of neutral Higgs Pair Production in PYTHIA using HPAIR Matrix Elements[13]

### 8.1 Introduction

Scalar Higgs boson pair production at LHC allows to study the trilinear Higgs self couplings in the Minimal Supersymmetric Standard Model (MSSM) scheme. In $pp$ collisions the dominating process is the gluon fusion $gg \to HH$, where $H$ can be any of $A$, $H$ or $h$. In PYTHIA those processes can be generated through the resonance channel $H \to hh$ or via $f_i \bar{f}_i \to AH$, $Ah$. But for Standard Model (SM) and MSSM scenarios with high values of $\tan \beta$ the contribution of $s$-channels becomes negligible, thus PYTHIA alone can not be used to explore this region of the parameters space where the cross section can rise above 1 pb for values of $m_A$ up to 150 GeV. At LHC measuring trilinear self couplings in production modes dominated by the gluon fusion would require a huge amount of data. Nonetheless the MSSM high $\tan \beta$ values cases are also interesting as a discovery channel, as their cross section is large enough.

This note presents the implementation of LO matrix elements calculated with HPAIR[14] into PYTHIA 6.1 [100]. This implementation will allow a more complete simulation of $hh$ production in resonance region as well as all neutral Higgs pairs in continuum production. After a brief description of the implementation steps, we will present a comparison between cross sections values obtained with PYTHIA Monte Carlo generation and those computed with VEGAS. For a more complete version of this work, refer to the ATLAS note about to be published.

### 8.2 Neutral Higgs pair production in PYTHIA

The already implemented processes into PYTHIA are $f_i \bar{f}_i \to Ah^0$ and $f_i \bar{f}_i \to AH^0$. Although those processes are dominant in most MSSM scenarios, above $\tan \beta = 30$ they contributes for only 10% of the total cross section. In those cases, the dominant process is $gg \to AA$ and all others processes contributes for 50% of the total cross section, as can be seen on figure 19. Thus for a more complete study of those scenarios we have added into PYTHIA, the following processes [101]: $gg \to h^0h^0$, $gg \to H^0h^0$, $gg \to H^0H^0$, $gg \to Ah^0$, $gg \to AH^0$ and $gg \to AA$. All processes described above were implemented in a private version of PYTHIA, as standard $2 \to 2$ PYTHIA processes. We tried to keep the modifications into PYTHIA to the minimum.

For each event tried, the kinematic is chosen by PYTHIA, taking into account resonance and continuum production in the shape of the phase space. The PYSIGH routine then call the PYHPAIR function to get the differential cross section. This differential cross section is computed with HPAIR Matrix Elements using PYTHIA parameters. Finally, the event is selected or rejected according to the PYTHIA standard Monte-Carlo procedure. In SM and MSSM large $\tan \beta$ scenarios, the Higgs width might be non negligible and Higgs particles might be produced off-shell. Thus in order to reproduce correctly the kinematic of the events, this should be taken into account.

---

[13]*R. Lafaye*
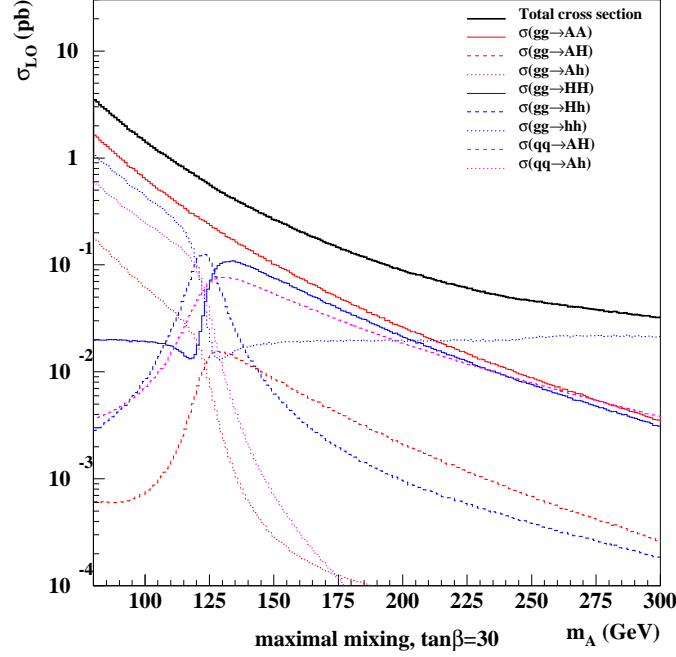[14]HPAIR is a program written by M. Spira.

Fig. 19: *Neutral Higgs pair LO cross sections as a function of $m_A$ in maximal mixing for $\tan\beta = 30$. Below the transition limit, the cross section is dominated by $AA$, $Ah$ and $hh$ production, while above $AA$, $AH$ and $HH$ dominate. The transition region is special as $A$, $H$ and $h$ have all very similar masses and all possible Higgs pairs can be produced. Higgs pair production studies can not disentangle different Higgs, as dominating processes are made of degenerated Higgs with similar masses and branching ratios.*

When $MSTP(42) = 1$ Higgs are produced off-shell by PYTHIA. Those off-shell values are then used to compute weight factors for the cross section like in $WW$ production processes. The generation of events for those cases is much slower and can sometimes leads to unphysical and very high differential cross sections. Thus, except in the purpose of studying the differences in kinematics, one should rely on on-shell bosons production.

For each off-shell Higgs the cross section is weighted by a factor $B_H^*/B_H$ from the propagators of the virtual Higgs, defined as follow:

$$B_H^* = \frac{m_H^* \Gamma_H^*}{(m_H^{*2} - m_H^2)^2 + m_H^{*2}\Gamma_H^{*2}} \ , \ B_H = \frac{m_H \Gamma_H}{(m_H^{*2} - m_H^2)^2 + m_H^2 \Gamma_H^2}$$

where $H$ can be any of $A$, $H$ and $h$. The total cross section suppression factor is then ($i = 1, 2$ denotes the two identical Higgs in the final state)

$$B_{H_1}^*/B_{H_1} \cdot B_{H_2}^*/B_{H_1} \cdot m_{H_1^*} m_{H_2^*}/m_H^2$$

### 8.3 Monte-Carlo results

The stand alone HPAIR program uses VEGAS to integrate the total cross section of Higgs pair production processes. It can also gives NLO order results with QCD corrections. Although, those corrections are not valid for $m_A$ larger than 200 GeV. As a check, one can compare cross section obtained using PYTHIA and VEGAS with the same matrix elements. Comparisons were made with 1000 VEGAS iterations and 100 PYTHIA events per bin. Most of the cross sections obtained are very similar. But unfortunately, the stand alone HPAIR code and PYTHIA have some small differences in their Higgs mass spectrum algorithms. Thus the cross section obtained might be slightly different, especially in cases where it is sensitive to the $H, h$ mass difference like for the resonance $gg \to H \to hh$ process at low $\tan\beta$.

Kinematic distributions have been investigated for the 4 $b$ final state, that is when both Higgs disintegrate to $b\bar{b}$. The most important for this final state is the $p_T$ distribution of the $b$, as current

selection algorithms ask for $b$ with a $p_T$ above 40 GeV. Furthermore, as there is no $b$-trigger in ATLAS, high $p_T$ jets will be more likely to pass the jet trigger thresholds.

First of all the distributions in $\eta$ and $p_T$ of the $b$ for the existing $gg \rightarrow H \rightarrow hh$ PYTHIA process 152 and our implemented process $gg \rightarrow hh$ process in the resonance region ($\tan\beta = 3$ and $m_A = 300$ GeV) are very similar. We then take a look at the $p_T$ distributions of the $b$ and mass resolution of the $b$ pairs for $\tan\beta = 50$ and $m_H = 150$ GeV for on-shell and off-shell Higgs bosons in the maximal mixing scenario. All Higgs pair production processes were turned on, including the already existing $f\bar{f} \rightarrow AH$ and $f\bar{f} \rightarrow Ah$. For this set of MSSM parameters, Higgs pair production are largely dominated by $A$ and $H$ pairs. The following table summarize the MSSM parameters and cross sections obtained for those processes:

| $\tan\beta$ | $m_A$ | $m_H$ (GeV) | $\Gamma_H$ | $\sigma$ (pb) | Number of events generated | Number of events tried |
|---|---|---|---|---|---|---|
| 50 | 148.9 | 150.0 | 9.1 GeV | 1.46 | 20000 | 113186 |
| 50 | 148.9 | 150.0 | 9.1 GeV | 1.45 | 20000 | 334236 |

Events were then analyzed with the ATLAS fast simulation, ATLFAST, to take into account the detector resolution. The $b$ pairs invariant mass resolution of 15 GeV is convoluted by the Higgs width of 9.1 GeV, when bosons are produced off-shell, as expected. The distribution of the $p_T$ of the jets is very similar and makes very little difference.

## 8.4   Conclusion and prospects

Higgs pair production processes have been successfully implemented in PYTHIA 6.1. Although in some rare points of the parameters space when using off-shell bosons the behavior of the matrix elements should be investigated. Neutral Higgs bosons production has two main interests [102] [103]. The first is Higgs discovery and this could be achieved through the study of the resonance production where the cross section according to NLO predictions is of the order of 2 pb or for high values of $\tan\beta$ where the cross section for $\tan\beta = 50$ can reach 30 pb. The first case as already been studied in [104] while the second is under analysis. An other interest is the reconstruction of the Higgs potential which implies the measurement of the Higgs self couplings like $\lambda_{Hhh}$. Whether this coupling can be measured for double Higgs resonance production with sufficient integrated luminosity at the LHC is under investigation.

## 9.   Multiple NMSSM Higgs boson signals at the LHC[15]

In Ref. [105] a no-loose theorem was established for the NMSSM [106], guaranteeing that the LHC will discover *at least one* neutral NMSSM Higgs boson (unless there are large branching ratios for decays to SUSY particles and/or to other Higgs bosons). Here, we try to establish the plausibility of a NMSSM scenario in which *multiple* neutral Higgs boson detection is possible at the LHC, with a number of available Higgs states in excess of those pertaining to the MSSM. Similarly to what done there, we only consider the 'direct' production channels (at the accuracy described in [107]), namely ($V = W^\pm, Z$, $Q = b, t$ and $q^{(')}$ refers to any possible quark flavour):

$$gg \rightarrow \text{Higgs (gluon} - \text{gluon fusion)}, \qquad q\bar{q}^{(')} \rightarrow V \text{ Higgs (Higgs} - \text{strahlung)}, \qquad (17)$$
$$qq^{(')} \rightarrow qq^{(')} \text{ Higgs } (VV - \text{fusion)}, \qquad gg, q\bar{q} \rightarrow Q\bar{Q} \text{ Higgs (quark associated production)}.$$

We neglect 'indirect' Higgs production via decays/bremsstrahlung off SUSY particles [108] and Higgs production in association with squarks [109].

The parameter scan performed here is somewhat different though. By using the program described of Ref. [110], we have first constrained the soft terms of the NMSSM by requiring *universality* at the
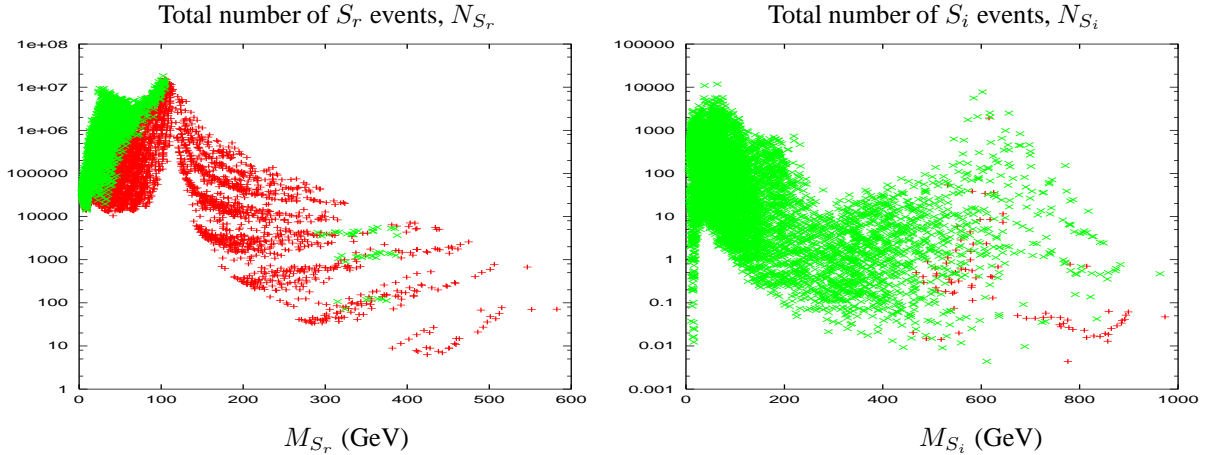
---

[15]*C. Hugonie and S. Moretti*

Fig. 20: Total number of events produced through processes (17) at the LHC after 300 fb$^{-1}$ in the NMSSM, for the CP-even singlet $S_r$ (left plot) and the CP-odd singlet $S_i$ (right plot), at LHC after 300 fb$^{-1}$. (For an explanation of the colour coding, see the text.)

GUT scale. The independent parameters of the model are then: a universal gaugino mass $M_{1/2}$, a universal mass for the scalars $m_0$, a universal trilinear coupling $A_0$, the Yukawa coupling $\lambda$ and the singlet self-coupling $\kappa$: see eqs. (2.1)–(2.2) of [105]. The (well-known) value of the $Z$-boson mass fixes one of these parameters with respect to the others, so that we end up with *four* free parameters at the GUT scale. As independent inputs characterising the NMSSM, we adopt here: $m_0/M_{1/2}$, $A_0/M_{1/2}$, $\lambda$ and $\kappa$. We then integrate numerically the Renormalisation Group Equations (RGEs) between the GUT and the weak scale and minimised the two-loop effective potential. Furthermore, we impose the current experimental bounds on (s)particle masses and couplings, especially the LEP limits on the Higgs mass vs. its coupling to gauge bosons, see [111]. Finally, we assume the existence of one neutral CP-even Higgs boson with mass 115 GeV and sufficient coupling to gauge bosons, as hinted by LEP [112].

The main result of this numerical analysis, as already pointed out in Ref. [110], is that the additional couplings appearing in the Superpotential are always small: $\lambda(\kappa) < 10^{-2}$. The mixing angles of the additional singlet states to the non-singlet sector, being proportional to these couplings, are also small and the singlet sector of the *universal* NMSSM is then quasi decoupled. (In the non-universal scenario of the previous section, the outcome was quite different: see also Ref. [105]). Hence, the neutral Higgs sector consists of a quasi pure (qp) CP-even Higgs singlet state, $S_r$, a qp CP-odd singlet, $S_i$, and the doublet sector is basically MSSM-like, apart from small perturbations of order $\sim \lambda^2$, so that results known for the Higgs sector of the MSSM are also valid in our case.

Fixing the mass of the lightest visible (non-singlet) CP-even Higgs at 115 GeV puts further constraints on the parameter space of the model: we find that $\tan\beta$ is always larger than 4, the CP-odd doublet Higgs mass $M_A$ is larger than 160 GeV and $M_{\text{SUSY}}$ is larger than 350 GeV. In this limit, the CP-even doublet states are the qp interaction eigenstates. The Higgs state with mass 115 GeV is a qp $H_u$, and the qp $H_d$ is heavy (with mass larger than 300 GeV). On the other hand, the masses of the singlet Higgs states, $S_r$ and $S_i$, can vary from a few GeV to 1 TeV. For each of the five neutral Higgs bosons of the NMSSM, we have computed the total number of events obtained by summing the rates of all production processes in (17), assuming 300 fb$^{-1}$ as integrated luminosity, at the LHC. We have plotted these rates versus the mass of the given Higgs states in Fig. 20. If, as tentative threshold of detectability of a signal, we assume 100 events, the conclusions are quite encouraging[16].

At the LHC, all three non-singlet Higgs states, $H_u$, $H_d$ and $A$, might be visible at the same time,

---

[16]However, we emphasise that this is not intended to be a definite claim of visibility, as the evaluation of such thresholds would require hadron-level simulations and detector-dependent considerations which are beyond the scope of this preliminary study.

as they are MSSM-like. In the singlet sector, $S_r$ could be visible if its mass is $\lesssim 600$ GeV and $\lambda$ is not too small. In the NMSSM, this covers most of the parameter space. Moreover, the CP-odd singlet, $S_i$, might be visible too, for an appreciable part of the parameter space (when its mass is below 200 GeV or so). To render this manifest, we have plotted in Fig. 20 the total number of events produced at the LHC with $S_r$ in the final state, $N_{S_r}$ (left plot) in green (light) when the corresponding $S_i$ state is also visible ($N_{S_i} > 100$) and in red (dark) when it is not ($N_{S_i} < 100$). Similarly, we did for $S_i$ (right plot), with green (light) when the corresponding $S_r$ is visible ($N_{S_r} > 100$) and red (dark) when it is not ($N_{S_r} < 100$).

Notice that the discovery areas of multiple Higgs boson states identified in Fig. 20 are indeed associated to the same regions of parameter space. In fact, a first glance at the total number of CP-odd singlet $S_i$ produced at the LHC might indicate that nearly all the parameter space of the model is already covered by the CP-even singlet $S_r$ search, as all the plotted points are in green (light). This is however not the case, as one can check from the left-hand plot ($N_{S_r}$ vs. $M_{S_r}$), where a lot of points are still under the 100 events threshold. The fact that one sees only green (light) points on the right-hand plot is due to the very high density of points considered, green (light) points being plotted after red (dark) ones. Hence, there are red (dark) areas, uncovered by the $S_r$ searches, behind green (light), covered, ones.

The conclusions of this preliminary study are that, although the singlet sector of the NMSSM tends to decouple from the rest of the neutral Higgs spectrum in the universal case, quasi pure singlet states could still be found at the LHC. In fact, one has to remember that a very light CP-even Higgs state is not excluded by LEP searches if its coupling to gauge bosons is small enough. Such a Higgs state could be visible at the LHC in the form of a CP-even singlet Higgs state of the NMSSM (even with rather heavy masses), alongside a (light) singlet CP-odd state. Besides, often this scenario occurs where the MSSM-like non-singlet Higgses ($H_u$, $H_d$ and $A$) should also be visible, hence making the whole neutral Higgs spectrum of the NMSSM in principle accessible at the CERN machine. (Rather similar conclusions also apply the the next-to-MSSM (nMSSM) of Ref. [113]: see [114].)

The caveat of our analysis is that we have not performed a full Higgs decay analysis in the NMSSM. One may question whether the additional Higgs states would actually be visible. For example, they would certainly couple to singlinos $- \tilde{S}$ is always the Lightest Supersymmetric Particles (LSP) in our context $-$ hence decay into the latter and thus remain undetected. This should however not be the case. In fact, the coupling of the singlet states to ordinary matter are generally stronger in comparison (of order $\lambda$, whereas those to two singlinos are $\sim \lambda^3$). So that, in the end, the main decay channels of singlet Higgs states should be those into detectable fermions and gauge bosons.

# B. Higgs Searches at the Tevatron

*A. Bocci, J. Hobbs and W.–M. Yao*

**Abstract**

Studies of the discovery reach for the SM and supersymmetric Higgs in Run II have been summarized. Combining the results from all possible decay channels, and combining the data from both experiments, with 15 fb$^{-1}$ the Tevatron experiments can exclude a SM Higgs at the masses up to about 190 GeV at 95 % C.L. or discover it up to 120 GeV at the 5$\sigma$ level. A great deal of effort remains in order to raise the performance of the accelerator and bring the detectors on line and fully operational to the level demanded by the Higgs search.

## 1. Introduction

The search for the Higgs boson and the dynamics responsible for electroweak symmetry breaking is the central goal of high energy physics today. The Tevatron luminosity increase provided by the Main Injector and Recycler, along with the upgrades of both CDF and D0 detectors, will provide unique opportunities to search for the Higgs both in the Standard Model (SM) and in supersymmetry model (SUSY). The Tevatron is expected to deliver an integrated luminosity of 2 fb$^{-1}$ in the first two years (Run IIa) and 13 fb$^{-1}$ in the subsequent years (Run IIb) until the LHC starts. Most of CDF and D0 Run IIa upgrades [115] were successfully installed in spring of 2001 and are now collecting data from $p\bar{p}$ collisions. Since the design of Run IIa upgrades is for the initial goal of 2 fb$^{-1}$ and will not survive the course of Run IIb, it is now anticipated that the Run 2b upgrades [116], and in particular the replacement for the Run 2a silicon vertex detector, are necessary to carrying out this exciting program.

## 2. Tevatron Run II SUSY/Higgs Workshop

A year long workshop on the Tevatron Run II Higgs physics was held at Fermilab during 1998, a joint venture between CDF, D0 and theory group at FermiLab. The aim is to explore the discovery sensitivities for the Standard Model and MSSM Higgs bosons in Run II at the Tevatron. The results is ultimately expressed in terms of the integrated luminosity required to either exclude the Higgs with 95% confidence level, or discover it with 3-$\sigma$ or 5-$sigma$ statistical significance at a given mass. The details can be found in the report of the Higgs Working Group of the Tevatron Run II SUSY/Higgs Workshop [10].

At the time of the Workshop, neither CDF nor D0 has had full Run II detector simulation package available. Two complementary approaches were adopted. The first approach was based on a CDF Run I detector simulation with the geometrical acceptance extended to correspond to the Run IIa CDF detector. The second approach was based purely on SHW, a simple simulation package that uses an average of the expected CDF and D0 detector performances as a set of parametrized resolutions and acceptances to perform simple reconstruction of tracking, jets, vertices and trigger objects. In addition, a multivariate analysis using neural network [117] has been pursued and leads to a potential gain of Higgs sensitivity above the conventional analysis.

Further challenges must be met in bringing the detectors online and fully operational, and in developing the techniques and understanding, particularly in $b\bar{b}$ jet-jet mass reconstruction and $b$ jet tagging, necessary to extract the small signal of the Higgs boson from the larger Standard Model background. Here, we will quote the results with reasonably optimistic projections for what we might achieve after a great deal of hard work in the coming years.
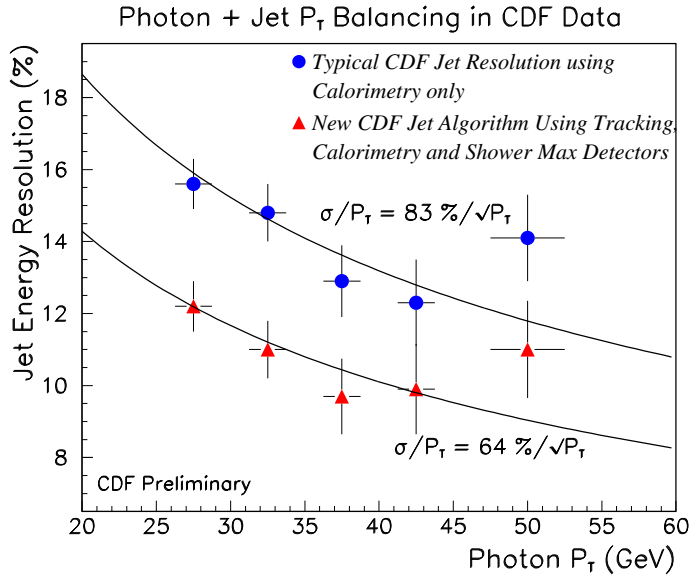
Fig. 1: Jet energy resolution as a function of jet $E_T$, comparing standard corrections based on calorimeter only with energy determination combining information from tracking, calorimetry, and shower max.

## 2.1   $b\bar{b}$ mass resolution

The $b\bar{b}$ mass resolution assumed in making these estimates is 10% in the central part of the distribution. This represents a significant improvement over the 14-15% resolution obtained in Run 1. One can improve upon the jet energy corrections by making the best possible use of all detector information, including tracking, shower max, calorimeter, and muon chambers. Figure1 shows the improvement of jet energy resolution possible by determining jet energy from an optimum combination of all jet information. A great deal of effort, presently underway, is needed to understand the jet energy corrections to the level required to attain 10% resolution. The required integrated luminosity for Higgs discovery scales linearly with this resolution.

## 2.2   $b$ tagging efficiency

The estimates of required integrated luminosity assume that the $b$ tagging efficiency and purity are essentially the same as in Run 1 in CDF, per taggable jet, shown in Figure 2. The better geometric coverage of the Run 2a and 2b silicon systems, however, is taken into account and leads to a much larger taggable jet efficiency. Unlike the Run 1 detector, the CDF Run II detector has a silicon vertex detector covering the entire luminous region, and has a 3D vertexing capability. Since the required integrated luminosity scales inversely with the *square* of the tagging efficiency (assuming constant mistagging rates), there is a potentially great improvement for developing high-efficiency algorithms for $b$-tagging. [htpb]

## 2.3   Background Systematic Studies

Most particle searches are designed to have a small background, typically only a few events. The effective fractional statistical precision of the background is of the same order as the background size, implying that (fractional) systematic errors can be rather large. Systematic uncertainties of 30% of the background are common in searches. However, the Run II Higgs search will have hundreds of background events, which come predominantly from the direct production of vector bosons plus heavy flavors, top and single top, di-boson, and QCD jets production. In some cases, the magnitude or the shape of the Standard Model backgrounds are not known at the required level of accuracy. For example, in the $\nu\bar{\nu}b\bar{b}$ channel analysis no estimates were made of the generic $b\bar{b}$ dijet background. This process has a very large cross section but tiny acceptance, and is thus not modeled reliably. In the CDF Run 1 analysis, this background was about half of the total, and estimated from the data. Uncertainties which affect the dijet mass spectrum
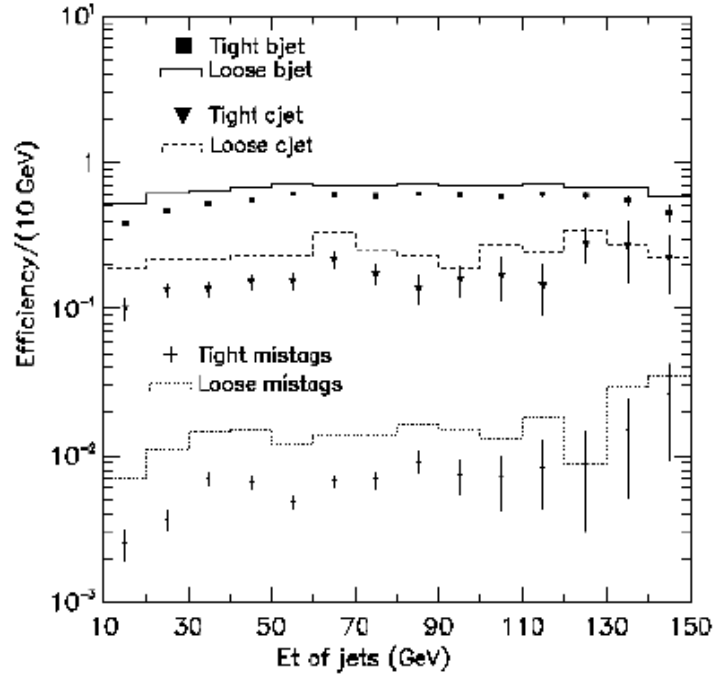
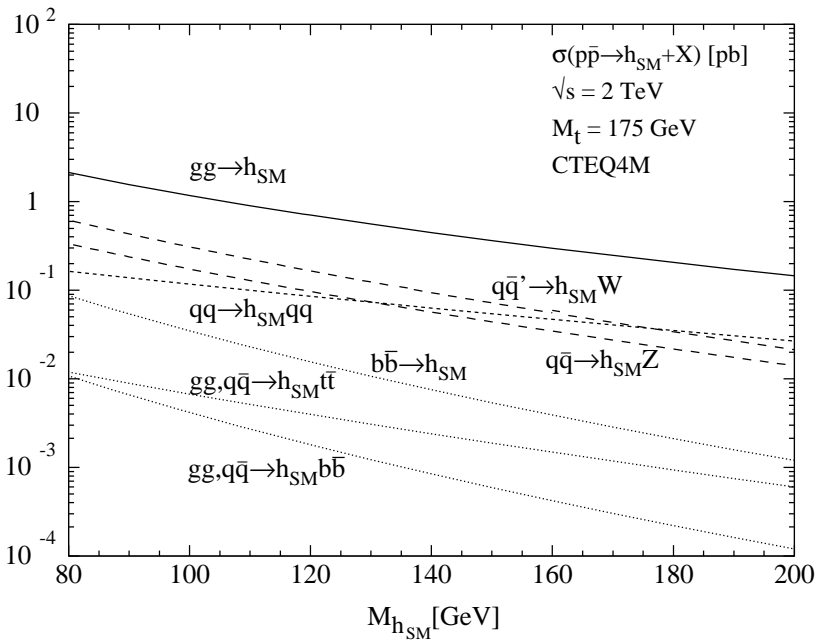Fig. 2:  b tag efficiencies as a function of jet $E_T$, determined using CDF run1 taggable jets



Fig. 3: Production cross section for Standard Model Higgs at the Tevatron as a function of Higgs mass.

Table 1: Fractional change in backgrounds to the $WH$ signal as a function of $q^2$. The result shows the fractional change of each component of the background as $q^2$ changes from the nominal to $q^2/2$ and to $2q^2$. In the average, the absolute values of percent changes for the two $q^2$ choices were used.

| Source | Percent change |
|---|---|
| $W + b\bar{b}$ | $6 \pm 1\%$ |
| $t\bar{t}$ | $1 \pm 1\%$ |
| Single top | $3.8 \pm 0.2\%$ |
| $WZ$ | $2.4 \pm 0.1\%$ |
| $WH$ signal | $0.4 \pm 0.1\%$ |

are particularly important to control because the components have different spectra. With collider data in hand, the understanding will be improved using dedicated studies and by tuning the event simulations to match collider data control samples.

The remainder of this section is an estimate, in advance of significant data taking, of the uncertainty in background estimates arising from systematic uncertainties in simulations. One of the possible sources of uncertainty has been chosen for this study. The effect from $q^2$ dependence on the background inside a mass window of $\pm 2\sigma$ around a target Higgs mass is explored. Signal and background events for the channel $p\bar{p} \rightarrow WH \rightarrow e\nu bb$ were generated using the Pythia generator and passed through the detector simulation used during the Run II SUSY/Higgs workshop. The basic event selection outlined in the SUSY/Higgs report was applied, and the acceptance within the mass window was computed. This process was repeated with the $q^2$ scale in Pythia changed to $2q^2$ and $q^2/2$, ranges commonly chosen when assessing systematic uncertainties from simulation. The results, expressed as fractional change in acceptance, are shown in table 1. Systematic effects from varying $q^2$ scale become important when the overall (fractional) uncertainty approaches 5%. As expected, the largest uncertainty comes from the steeply falling $W + b\bar{b}$ background. This is particularly important, because $W + b\bar{b}$ is the dominant component of the background.

## 3.  Standard Model Higgs

The dominant SM Higgs production at the Tevatron is gluon-gluon fusion via a heavy quark loop, giving a single Higgs produced. The Higgs can also be produced in association with a $W$ or $Z$ boson via its couplings to the vector bosons. Figure 3 shows the production cross section for various modes as a function of Higgs mass. In the range below 135 GeV Higgs mass, the decay of $b\bar{b}$ dominates, and for larger masses the decay to W pairs dominates.

In the gluon fusion case, since the Higgs decays predominantly to $b\bar{b}$ (for Higgs masses below 135 GeV), there is an overwhelming background from QCD production of $b\bar{b}$ pairs. The $WH$ and $ZH$ modes, however, have been extensively studied [10] and lead to several distinct signatures in which a Higgs signal can be observed with sufficient integrated luminosity.

### 3.1  Low-mass Higgs

For low mass ($< 135\text{GeV}$) Higgs, the most sensitive signatures arise from the leptonic decays of the $W$ and $Z$, and are denoted $\ell\nu b\bar{b}$, $\nu\bar{\nu}b\bar{b}$, and $\ell^+\ell^- b\bar{b}$. Hadronic decays of the $W$ and $Z$ lead to the $q\bar{q}b\bar{b}$ final state which suffers from large backgrounds from QCD multijet production.

In Run 1 in CDF, all four of these channels were studied, and led to limits on the Higgs cross section times branching ratio to $b\bar{b}$ as depicted in Figure 4. As the plots shown, the Run 1 limits are more than an order of magnitude above the expected Standard Model cross section. Improvements to the detector, coupled with much higher luminosity in Run II lead to the greatly enhanced sensitivity in the Standard Model search.

Maximizing the sensitivity of the search for the Higgs in these channels depends most critically
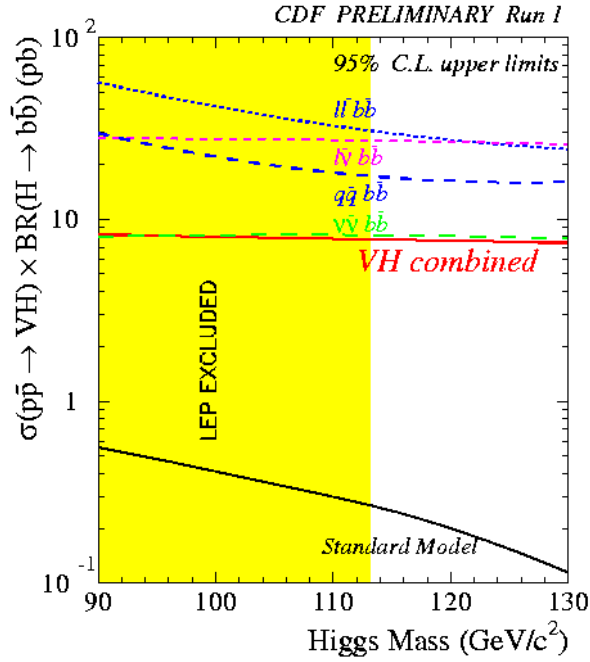
Fig. 4: Limits on SM Higgs cross section times branching ratio to $b\bar{b}$ from CDF run1.

on three things as mentioned above: attaining the best possible $b\bar{b}$ mass resolution, attaining the best possible $b$ jet tagging efficiency and purity, and attaining as large a data sample as possible.

Figure 5 shows the two $b$-tagged dijet mass distribution and Figure 6 shows the background-subtracted signal in the $\ell\nu b\bar{b}$ case, for a 120 GeV SM Higgs, combining data from both CDF and DØ representing 15 fb$^{-1}$ integrated luminosity, which clearly illustrates that even with the best resolution attainable, discovering the Higgs at Tevatron remains a major challenge.

### 3.2  High-mass Higgs

For larger Higgs masses ($> 135$ GeV), the Higgs decays predominantly to $WW^{(*)}$. Two modes have been shown to be sensitive in this mass range: $\ell\nu\bar{\ell}\bar{\nu}$ (from gluon fusion production of single Higgs) and $\ell^{\pm}\ell^{\pm}jj$ (from tri-vector-boson final states) [56]. The critical issues in these search modes are accurate estimation of the $WW$ background in the former channel and estimation of the $W/Z$+jets background in the latter.

### 3.3  Standard Model Higgs Reach in Run II

The integrated luminosity required to discover or exclude the Standard Model Higgs, combining all search channels and combining the data from CDF and D0 , is shown in figure 7. The lower edge of the bands is the nominal estimate of the Run 2 study, and the bands extend upward with a width of about 30%, indicating the systematic uncertainty in attainable mass resolution, $b$ tagging efficiency, and other parameters.

The figure clearly shows that discovering a SM (or SM-like) Higgs at the 5-sigma level requires a very large data sample: even with 15 fb$^{-1}$, the mass reach is about 120 GeV at best. A 95% CL exclusion can, however, be attained over the entire mass range 115-190 GeV with the integrated luminosity foreseen in Run 2b.

### 4.  SUSY Higgs

In the context of the minimal supersymmetric standard model (MSSM) the Higgs sector has two doublets, one coupling to up-type quarks and the other to down-type quarks and leptons. There are five physical
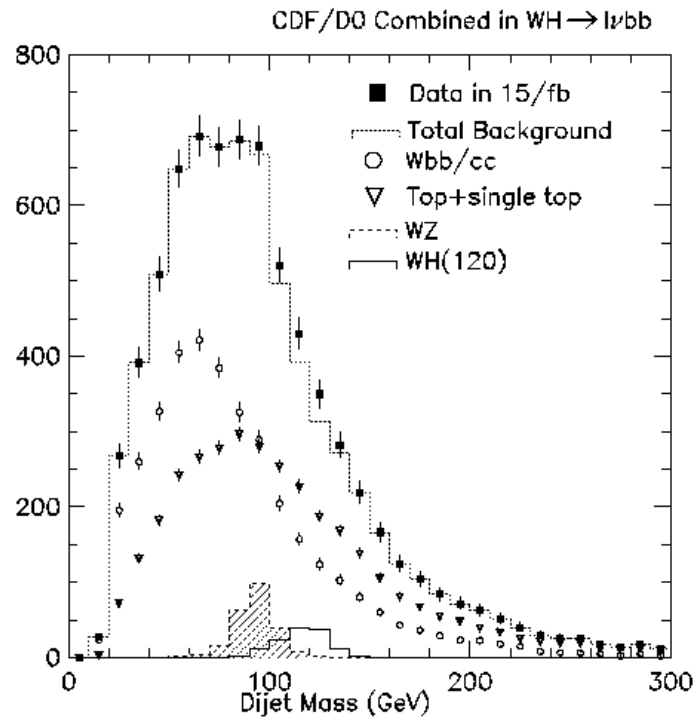
Fig. 5: Distribution of $b\bar{b}$ mass distribution in the $\ell\nu b\bar{b}$ channel, showing expected signal from 120 GeV SM Higgs, combining 15 fb$^{-1}$ of data from CDF and DØ .
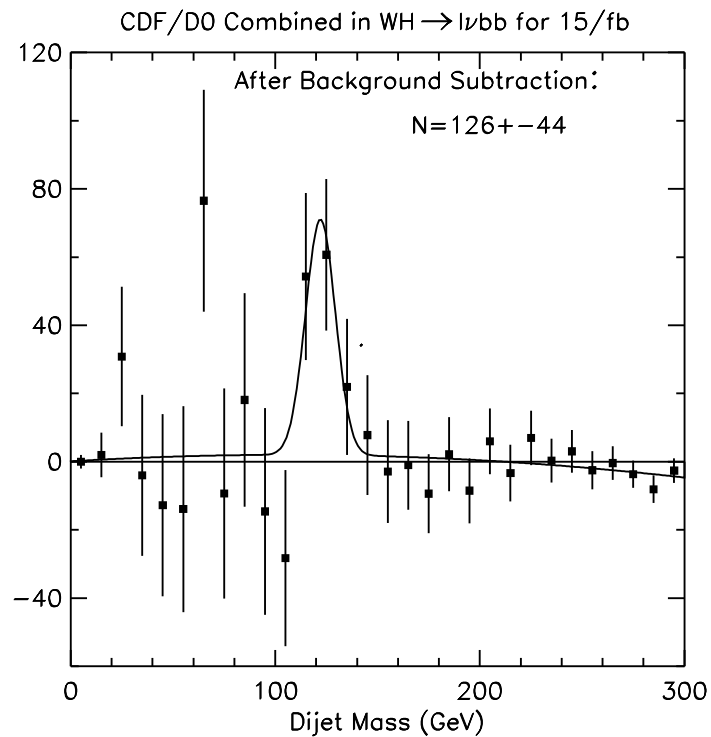


Fig. 6: Background subtracted $b\bar{b}$ mass distribution in the $\ell\nu b\bar{b}$ channel, showing expected signal from 120 GeV SM Higgs, combining 15 fb$^{-1}$ of data from CDF and DØ .
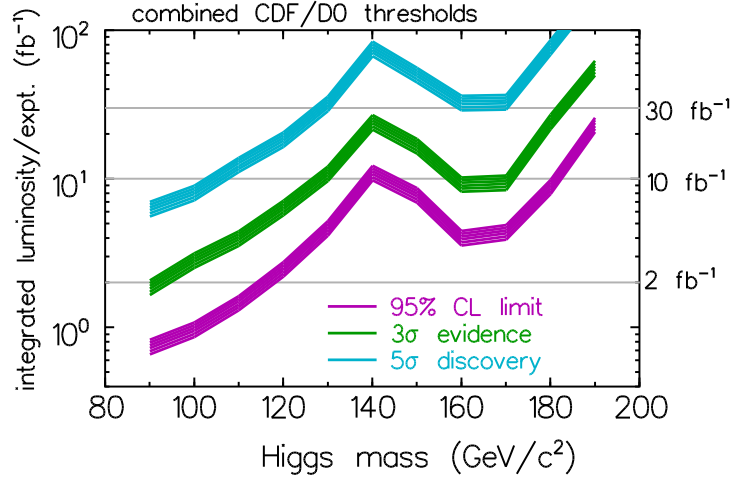
Fig. 7: The integrated luminosity required per experiment, to either exclude a SM Higgs boson at 95% CL or discover it at the $3\sigma$ or $5\sigma$ level, as a function of the Higgs mass. These results are based on the combined statistical power of both CDF and DØ and combining all search channels.
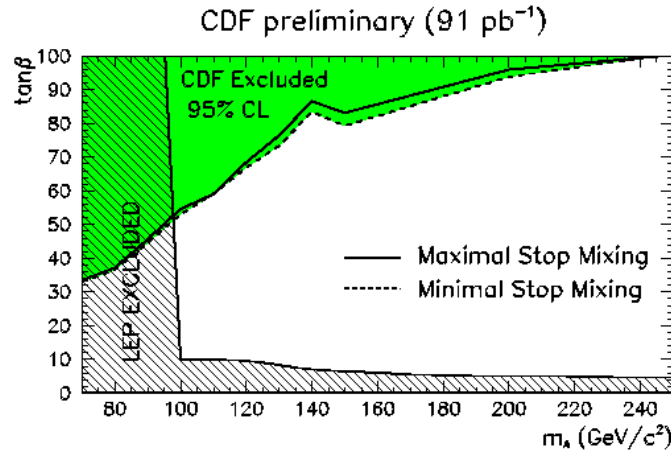


Fig. 8: CDF limits on MSSM Higgs using $b\bar{b}b\bar{b}$ final state.

Higgs boson states, denoted $h$, $A$, $H$, and $H^{\pm}$. The masses and couplings of the Higgses are determined by two parameters, usually taken to be $m_A$ and $\tan\beta$ (the ratio of the vacuum expectation value of the two Higgs doublets), with corrections from the scalar top mixing parameters.

The light scalar $h$ can appear very Standard-Model-like or nearly so over a larger range of MSSM parameter space. In this scenario the results of the search for the SM Higgs produced in the $WH$ and $ZH$ modes are directly interpretable.

More interesting is the case of large $\tan\beta$. Since the coupling of the neutral Higgses ($h/A/H$) to down-type quarks is proportional to $\tan\beta$, there is an enhancement factor of $\tan^2\beta$ for the production of $b\bar{b}\phi$, $\phi = h, A, H$ relative to the SM rate appearing in figure 3. This leads to distinct final states with four $b$ jets; if we demand that at least three of the jets be tagged, the background from QCD multijet processes is relatively small. In Run 1, CDF searched for this process, and from the null result excluded a large swath of MSSM parameter space inaccessible to LEP, as shown in figure 8.

Based on the Run 1 analysis, and taking into account the improved $b$-tagging efficiency, figure 9 shows the regions of $m_A$ versus $\tan\beta$ that the Tevatron can cover for different integrated luminosities.
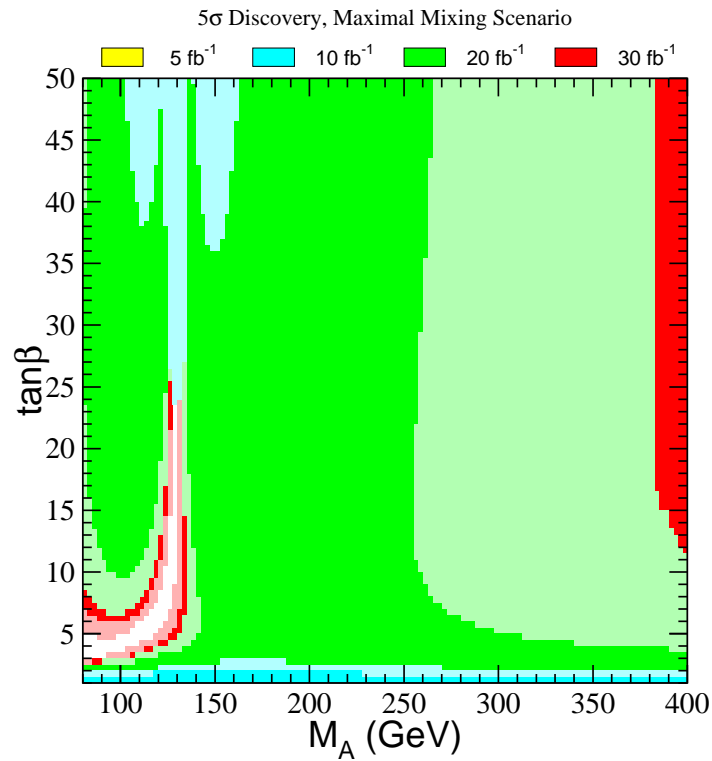
Fig. 9: Regions of MSSM Higgs parameter space where $5\sigma$ discovery is possible, using SM Higgs search results.

## 5. Conclusion

Studies of the discovery reach for the SM and supersymmetric Higgs in Run II have been summarized. Combining the results from all possible decay channels, and combining the data from both experiments, with 15 fb$^{-1}$ the Tevatron experiments can exclude a SM Higgs at the masses up to about 190 GeV at 95% C.L. or discover it up to 120 GeV at the $5\sigma$ level. A great deal of effort remains in order to raise the performance of the accelerator and bring the detectors on line and fully operational to the level demanded by the Higgs search.

# C. Experimental Observation of an invisible Higgs Boson at LHC

*B. Di Girolamo, L. Neukermans, K. Mazumdar, A. Nikitenko and D. Zeppenfeld*

**Abstract**

We present ATLAS and CMS simulation studies on the observability of an invisible Higgs boson produced via weak boson fusion at the LHC. With full and fast detector simulations we have checked the selection efficiency of the basic cuts proposed to search for such an object. The Level 1 and High Level trigger strategies for this purely jet and missing $E_T$ final state are discussed.

## 1. Introduction

Some extensions of the Standard Model (SM) exhibit Higgs bosons which can decay into stable neutral weakly interacting particles, therefore giving rise to invisible final states. In supersymmetric models, the Higgs bosons can decay with a large branching ratio into the lightest neutralinos or gravitinos in some region of parameter space [118], leading to an invisible final state if R parity is conserved. Invisible Higgs decay also happens in models with an enlarged symmetry breaking sector, *e.g.* in Majoron models [119], [120], where the Higgs disintegrates into light weakly interacting scalars. Another possibility arises in models with large extra dimensions [213]. In Randall-Sundrum type models [121], the Higgs boson can mix with the scalar radion field which then predominantly decays, invisibly, to graviton states [122]. The invisible decay of the Higgs boson is a possibility which needs to be addressed in collider searches [123].

Presently, the LEP II collaborations exclude invisible Higgs masses up to 114.4 GeV [124]. The presence of invisible Higgs decays makes much more difficult the Higgs boson search at hadron colliders. Phenomenological studies have been done on observability of the invisible Higgs in $ZH$ and $WH$ associated production [87] and $t\bar{t}H$ production [125]. Assuming that the Higgs boson is produced with SM strength, while decaying with an invisible branching fraction of $\approx 100\,\%$, associated $ZH$ production was estimated to be sensitive to Higgs masses $\leq 150$ GeV [87] at the LHC, while $t\bar{t}H$ production might extend the Higgs mass range to 250 GeV [125]. In recent work [88] it was shown that the LHC potential for the search of an invisibly decaying Higgs boson can be considerably extended by studying Higgs production via weak boson fusion. According to these parton level studies, $10\,fb^{-1}$ of data should allow to discover these particles with masses up to 480 GeV, at the $5\sigma$ level, provided their invisible branching ratio is 1. A method for background estimation directly from the data has also been proposed.

The search strategy for an invisible Higgs described in [88] heavily relies on the performance of the ATLAS/CMS calorimetry for jets and $\not{p}_T$ reconstruction as well as on a dedicated calorimeter trigger. In the study presented here we basically repeat the analysis done in [88], but with a more dedicated simulation of the detectors. We also discuss possible Level 1 and High Level triggers for the most efficient on-line selection of invisible Higgs events. The efficiency of the basic selections proposed in [88] has been checked. Below we will refer to the following cuts on the $E_T$ of tagging jets, a rapidity gap between two tagging jets, an effective mass of tagging jets ($M_{jj}$), missing transverse momentum ($\not{p}_T$) and the azimuthal angle between two jets in the transverse plane ($\phi_{jj}$) :

$$E_T^{j1,\,j2} > 40\,GeV,\ \ |\eta_j| < 5.0,\ \ |\eta_{j1} - \eta_{j2}| > 4.4,\ \ \eta_{j1}\eta_{j2} < 0, \tag{1}$$

$$\not{p}_T > 100\,GeV, \tag{2}$$

$$M_{jj} > 1200\,GeV, \tag{3}$$

$$\phi_{jj} < 1 \tag{4}$$

A mini-jet veto (no jet with $E_T > 20$ GeV in the $\eta$ gap between two tagging jets) and lepton veto (no lepton with $p_T > p_T^{cut}$) have also been used. The full set of these cuts we shall refer to, hereafter, as WBF cuts.

## 2. Trigger on invisible Higgs

A purely multi-jets plus $\not{p}_T$ final state in the invisible Higgs search requires a dedicated calorimeter trigger both at Level 1 and at High Level. Off line analysis exploits a specific feature of the two tagging jets accompanying Higgs production via weak boson fusion, in particular a big gap in rapidity between them (1). Such a requirement on the two jet topology could be applied already in on-line selections - at Level 1 and in High Level trigger (HLT). Together with a cut on calorimeter $\not{p}_T$, these cuts allow to suppress the QCD background rate down to an acceptable level of a few Hz, as will be shown later.

The Forward Calorimeters of the ATLAS/CMS detectors will play a crucial role in the on-line and off-line selections of invisible Higgs due to the presence of two forward-backward tagging jets. The acceptance of the CMS Hadron Forward (HF) calorimeter ( $3.0 < |\eta| < 5.0$) for these jets with $E_T > 30$ GeV is shown in Tab. 1, before and after cut on the rapidity gap between jets. One can see that with the rapidity gap constraint, almost 80 % of the Higgs events will have at least one tagging jet in the pseudorapidity region covered by HF.

Table 1: Acceptance (in %) of the CMS Forward Hadron Calorimeter for tagging jets ($E_T > 30$ GeV) in $qq \to qqH$.

|  | no jets in HF | one jet in HF | 2 jets in HF |
|---|---|---|---|
| no cut on $\mid \eta_{j1} - \eta_{j2} \mid$ | 49 | 45 | 6 |
| $\mid \eta_{j1} - \eta_{j2} \mid > 4.4$ | 22 | 65 | 13 |

### 2.1 Level 1 trigger

**ATLAS**: The implementation of a specific trigger for Weak Boson Fusion processes is still under discussion in ATLAS. Up to now the strategy at LVL1 is to not include a trigger on jets with $|\eta| > 3.2$. However all the information on jet energy and $\not{p}_T$ is potentially available at LVL1 for all the covered regions ($|\eta| < 4.9$).

A discussion on the implementation of a dedicated trigger for tagging jets for the studies of the WBF channels is in progress. The invisible Higgs channel has been used to demonstrate how such a trigger is fundamental for such a search and, once it is implemented, how all the WBF channels benefit of the trigger redundancy that will be important for precise cross section measurements for these channels.

Using the results obtained with the off line analysis of the invisible Higgs channel, the significance $S/\sqrt{B}$ at an integrated luminosity $L = 10$ fb$^{-1}$ has been evaluated for two different regions of the jet rapidity acceptance, finding: (a) $S/\sqrt{B} \approx 10$, if $|\eta| < 4.9$ and (b) $S/\sqrt{B} \approx 4$, if $|\eta| < 3.2$.

The LVL1 hardware in ATLAS offers the capability to recognise the jet hemisphere, therefore the data produced for the off line analysis have been analysed with the cuts enumerated in the following to evaluate the expected rate at LVL1 for the background processes: (a) 2 tagging jets; (b) $|\eta_j| < 4.9$; (c) $p_T^j > 40$ GeV; (d) $\eta_{j_1} \cdot \eta_{j_2} < 0$; (e) $\not{p}_T > 85$ GeV.

The signal efficiency has been evaluated to be about 95 % with these cuts for the events which passed off-line selections (1)-(4). Table 2 gives the rates for all the background channels and for the signal for a luminosity of $L = 10^{33}$cm$^{-2}$sec$^{-1}$ and the number of events for an integrated luminosity $\int L dt = 10$ fb$^{-1}$ (corresponding to the first year of running at LHC). These preliminary results look very promising. Further studies are going on to evaluate the errors on these numbers with a more accurate simulation of the forward region.

The trigger on the tagging jets has to be extended as much as possible in $\eta$ to preserve a good signal to noise ratio, as demonstrated by the following study. The trigger efficiency versus $\eta$ has been evaluated by measuring the ratio between $N_\eta$, the number of events at a given LVL1 acceptance $|\eta| \leq \eta_{LVL1}$, and $N_{4.9}$, the number of events when $|\eta| \leq 4.9$:

$$\epsilon(\eta) = N_\eta / N_{4.9}$$

Table 2: Expected rate and number of events for signal and backgrounds during the first year of LHC operation.

| Process | Rate (Hz) | Nr. of events |
|---|---|---|
| $H \rightarrow inv$ (120 GeV) | $6.1 \cdot 10^{-4}$ | $6.1 \cdot 10^3$ |
| Wjj | $4.0 \cdot 10^{-2}$ | $4.0 \cdot 10^5$ |
| Zjj | $2.1 \cdot 10^{-2}$ | $2.1 \cdot 10^5$ |
| QCD (100-150 GeV) | $1.9 \cdot 10^{-2}$ | $1.9 \cdot 10^5$ |
| QCD (150-200 GeV) | $3.3 \cdot 10^{-2}$ | $3.3 \cdot 10^5$ |
| QCD (200-250 GeV) | $3.5 \cdot 10^{-2}$ | $3.5 \cdot 10^5$ |
| QCD (250-300 GeV) | $2.4 \cdot 10^{-2}$ | $2.4 \cdot 10^5$ |
| QCD (300-x GeV) | $4.5 \cdot 10^{-2}$ | $4.5 \cdot 10^5$ |

In figure 1 the behaviour of $\epsilon$ versus $\eta$ is shown. It is clear from the plot that, reducing the acceptance region, the signal is strongly reduced, while a lower impact is obtained on the QCD background as well as on the $Wjj$ and $Zjj$ backgrounds.
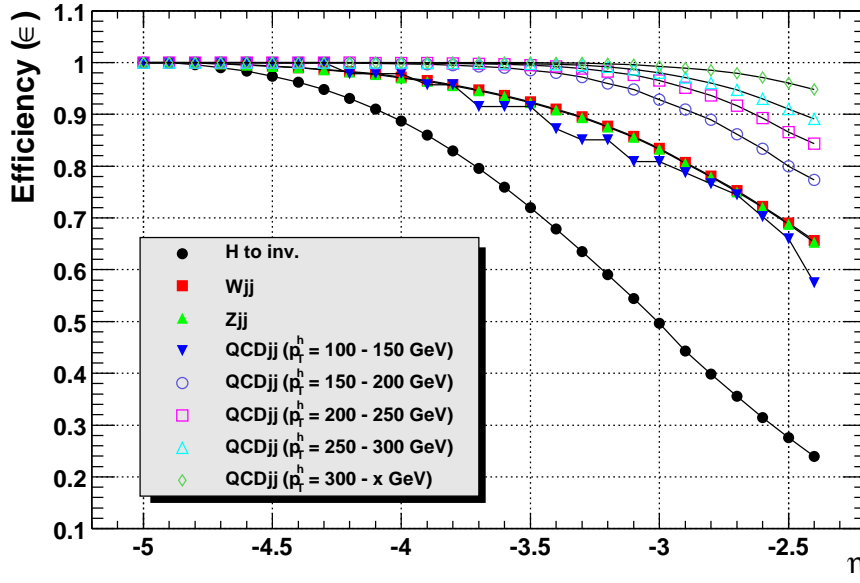


Fig. 1: Level 1 efficiency versus $\eta$ coverage of Level 1 calorimeter trigger.

**CMS**: CMS will have Jet triggers at Level 1 operating over the entire calorimeter acceptance, including Hadron Forward calorimeter [126]. The present Level 1 calorimeter trigger table includes a set of inclusive Jet triggers, missing $E_t$ (MET) trigger as well as combined Jet+MET trigger. We have found that the combined Jet+MET trigger (with Jet trigger also implemented in the HF) is the most effective for the invisible Higgs selection. At low luminosity ($L = 2 \times 10^{33} \text{cm}^{-2}\text{sec}^{-1}$), with thresholds of 70 GeV on both Jet and MET, it provides $\simeq 96$ % efficiency for the events selected with off-line cuts (1)-(4) and at an acceptable background rate of 0.6 kHz [127–129]. Such a high efficiency can be understood from Fig. 2 and Fig. 3 where transverse energy of the highest $E_t$ jet and calorimeter $\not{p}_T$ reconstructed in off-line and at Level 1 is shown for the events which passed the off-line selections (1)-(4). In the off-line reconstruction both $E_t$ of jet and $\not{p}_T$ are corrected for the effects of calorimeter non-linearity. Jet energy corrections are also applied at Level 1, while it is not foreseen to correct $\not{p}_T$ at Level 1. Due to this the Level 1 $\not{p}_T$ spectrum shown in Fig. 3 is shifted in comparison with off line $\not{p}_T$.
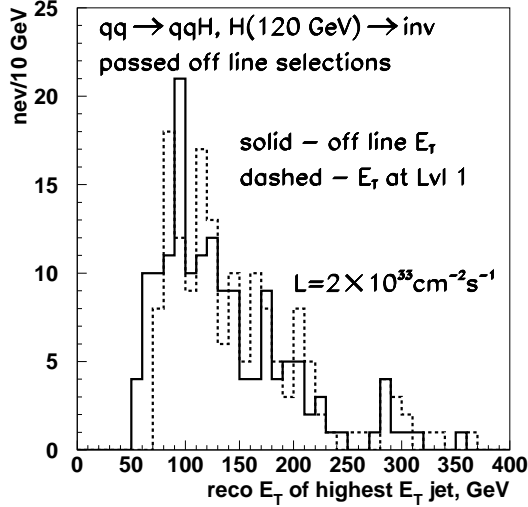
Fig. 2: Reconstructed $E_t$ of the highest $E_t$ jet for the Higgs events passing cuts (1)-(4). Solid histogram - off line reconstruction, dashed histogram - reconstruction at Level 1.
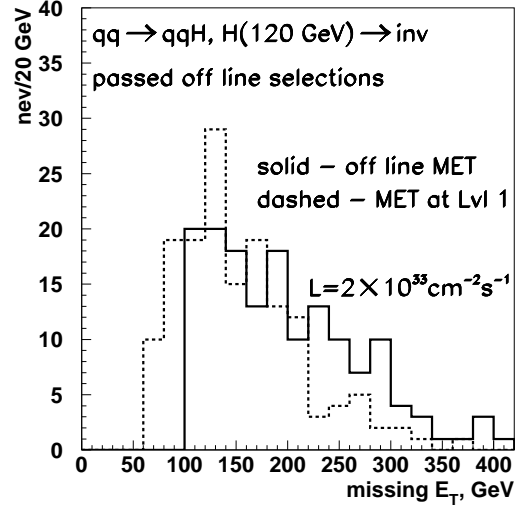
Fig. 3: Calorimeter $\not{p}_T$ reconstructed at Level 1 (dashed histogram) and off line (solid histogram) for the Higgs events passing cuts (1)-(4).

## 2.2 High Level Trigger

**CMS**: At High Level Trigger the off-line requirement (1) on the pseudorapidity gap between the two highest $E_t$ jets can be exploited together with the cut on $\not{p}_T$. Full granularity calorimeter information is available at HLT and computer farms will perform jet and $\not{p}_T$ reconstruction like in off-line analysis. In Fig. 4 the rate of QCD multi-jet events for $L = 2 \times 10^{33} cm^{-2} s^{-1}$ after cuts (1) is shown as a function of the cutoff on $\not{p}_T$. This plot has been obtained with full detector [130] and reconstruction [131] simulations processing QCD multi-jet events with $\hat{p}_t$ bins from 15-20 GeV up to 2600-3000 GeV (about 1M events). One can see that a cut on $\not{p}_T$ above 80 GeV will reduce the rate below 1 Hz.
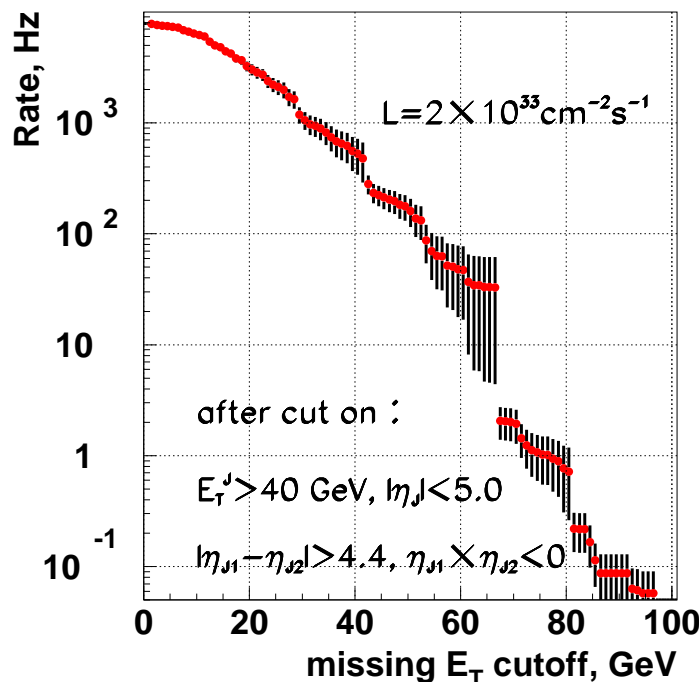


Fig. 4: QCD multi-jet background rate after cuts (1) as a function of the threshold on $\not{p}_T$.

### 3. Results of off-line analysis with detector simulation

We have performed off-line analysis, partially with full and partially with fast ATLAS/CMS detector simulation programs, using mainly the selection criteria (1)-(4) together with mini-jet veto and lepton veto. As backgrounds, QCD multi-jet production and QCD and electroweak (EW) W and Z production with more than 1 reconstructed jet have been considered. Below, we separately provide two independent ATLAS and CMS analyses.

### 3.1 CMS analysis

**Kinematics simulation**: Signal events have been generated with PYTHIA6.158 (with CTEQ5L structure functions) [100] for a SM Higgs of mass $M_H$=120 GeV, produced via weak boson fusion. All backgrounds (except QCD multi-jet production) have been simulated with LO matrix elements interfaced with PYTHIA for hadronization and additional initial and final state radiation. Colour and flavour information at the parton level is passed to PYTHIA. EW Zjj and Wjj events were generated with COM-PHEP [132] (with CTEQ5L); QCD Zjj and Wjj events (generated with CTEQ4L) were generated with MadCUP programs [133] based on the work of Ref. [134]. Loose selection criteria have been used to produce events at the parton level with tree level matrix elements:

$$p_T^j > 20 GeV, \ |\eta_j| < 5.0, \ |\eta_{j1} - \eta_{j2}| > 4.2, \ \eta_{j1}\eta_{j2} < 0, \tag{5}$$

$$M_{jj} > 900 GeV, \tag{6}$$

These events are further processed through PYTHIA. Initial cross sections (in pb) given by the matrix element calculations with these cuts are presented in Tab. 3. Cross sections include $Br(Z \to \nu\nu)$ and $Br(W \to \ell\nu)$ for three lepton generations.

Table 3: Cross sections (in pb) for backgrounds as given by LO matrix element calculations with cuts (5), (6). $Br(Z \to \nu\nu)$ and $Br(W \to \ell\nu)$ is included.

| QCD W+jj | QCD Z+jj | EW W+jj | EW Z+jj |
|---|---|---|---|
| 76.0 | 15.7 | 4.7 | 0.644 |

**Detector simulation:** Full detector simulation has been performed for the Higgs and QCD multi-jet events at $L = 2 \times 10^{33} cm^{-2} s^{-1}$ (on average 3.4 minimum bias events of PYTHIA MSEL=1 have been superimposed). One of the crucial questions of this study is a proper simulation of the tails in the $\not{p}_T$ distribution of the QCD multi-jet background. Such tails could be due to real $\not{p}_T$ from heavy quarks decays, but also due to a number of detector effects. To make confident estimates of such effects we used about 1 million QCD events, fully simulated [130] and reconstructed [131]. As mentioned already, events have been generated in different $\hat{p}_t$ bins from 10-15 GeV ($\sigma = 8.868 \times 10^{12}$ fb) up to 2600-3000 GeV ($\sigma = 11.25 fb$). However, as will be shown later, this statistics is still not enough to directly prove that the QCD background could be suppressed to an acceptable level after all cuts are applied.

The other backgrounds, QCD and EW production of Wjj and Zjj have been simulated with CMSJET [135] fast simulation with no minimum bias events superimposed.

Another key point of all searches for a light Higgs produced via weak boson fusion is the use of a mini-jet veto, namely a veto of events with additional soft ($E_T > 20$ GeV) jet(s) inside the rapidity gap between two tagging jets. The efficiency of the mini-jet veto is expected to be sensitive to detector effects like calibration, electronic noise and readout thresholds, interaction of soft particles in the tracker in front of the calorimeter, magnetic field, or pile up activity. Since we did not expect that the fast CMSJET simulation can properly reproduce some of these effects, we did not evaluate mini-jet veto efficiency from CMSJET simulation. Instead we multiply the background efficiency by $P_{surv}$ as estimated in [88]. $P_{surv}$ calculated in [136] is a probability to radiate a jet (parton) in the rapidity gap between two tagging

jets. In the parton level study of [88] it has been assumed that such jets will be reconstructed with 100 % efficiency. CMS full simulation study on soft jet reconstruction [137] shows that with a dedicated window algorithm it is possible to reconstruct 20 GeV jets at low luminosity with reasonably good purity and about 100 % efficiency. The question of the false jet suppression is still under investigation.

**Results on QCD background:** Fig. 5 shows the $\not{p}_T$ distribution of the QCD jet background (blue empty histogram) and of the Higgs signal, for $M_H$=120 GeV, (red full histogram) after cuts (1),(3). With an additional cut (4), $\not{p}_T$ for the signal events is shown as the light green histogram in Fig. 5. One observes that the tail in the background distribution goes well beyond 100 GeV. In Fig. 5 QCD events in the tail
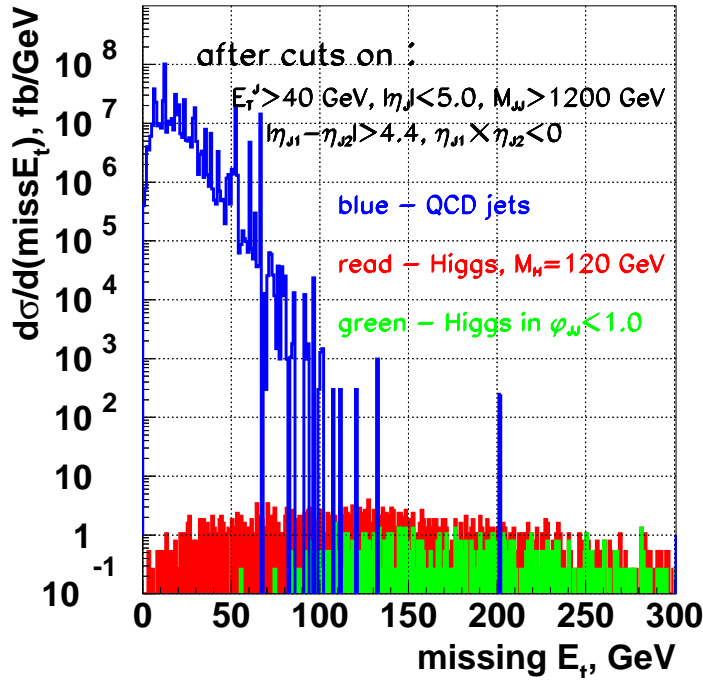


Fig. 5: $\not{p}_T$ for Higgs of $M_H$=120 GeV and QCD multi-jet background after selections (1),(3).

come from $\hat{p}_t$ bins between 300 and 600 GeV. Once the cut (4) on $\phi_{jj}$ is applied, no background event with $\not{p}_T > 100$ GeV is left. With the statistics used in the analysis, this leads to an upper limit of $\simeq$ 1 pb on the QCD background contribution which is about of 10 times higher than the signal expected after the same selections (1)-(4). The ATLAS fast simulation study (see below), which uses much higher statistics, shows that the QCD background can be suppressed to a negligible level with cuts (1)-(3) plus a cut on the minimal angle in the transverse plane between $\not{p}_T$ and a jet, or with cuts (1)-(4).

**Results on Higgs signal and QCD and EW Z+jj, W+jj backgrounds:**

Estimated cross-sections (in fb) for the Higgs and backgrounds at different steps of the event selection are shown in Tab. 4. Numbers in parentheses are the estimates obtained in [88]. Standard Model production cross-sections and Br($H \rightarrow$ invisible) = 1 are assumed.

The first row of Tab. 4 presents cross sections after cuts (1)-(3) and a veto on identified electrons (muons) for the Wjj backgrounds (including e($\mu$) from $\tau$ decay in $W \rightarrow \tau + \nu$) with $p_T^{e(\mu)} >$10 (5) GeV and $|\eta^{e(\mu)}| <$2.5. The lepton veto in [88] includes a veto on $\tau$ leptons with $p_T^\tau >$20 GeV and $|\eta^{e,\mu,\tau}| <$2.5. Here we discuss the veto on taus separately as a lepton veto or a jet veto, dependent on whether the tau decays leptonically or hadronically. Fig. 6 and Fig .7 show $\not{p}_T$ distributions for the signal and background events after cuts (1) and (3) and e, $\mu$ veto for the $Wjj$ backgrounds.

The second row of Tab. 4 presents cross-sections after mini-jet veto. As has been mentioned, the efficiency of the mini-jet veto for the backgrounds is taken from [88]. For the Wjj background with

Table 4: Cross sections in fb for the background and Higgs of $M_H$=120 GeV assuming Br($H \rightarrow$ invisible)=1 and Standard Model production cross-section for the Higgs. Numbers in parentheses are results from [88].

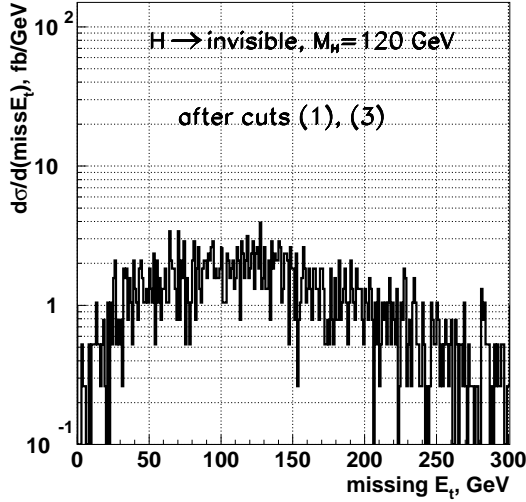| cross section, fb | Higgs | QCD $Zjj$ | QCD $Wjj$ | EW $Zjj$ | EW $Wjj$ |
|---|---|---|---|---|---|
| after cuts (1)-(3) and e($\mu$) veto for Wjj | 238(274) | 857(1254) | 1165 (1284) | 141.5(151) | 145.1(101) |
| + mini-jet veto | 180(238) | 240(351) | 237 (360) | 116(124) | 84.5 (83) |
| + $\phi_{jj} \leq 1$ | 74.7(96.7) | 48.0(71.8) | 40.0 (70.2) | 12.8(14.8) | 8.7(9.9) |



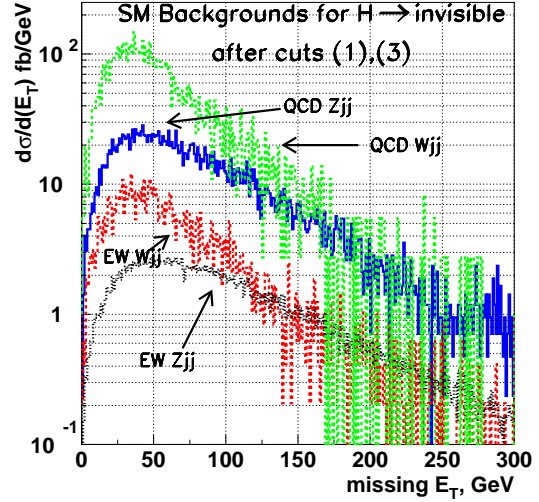Fig. 6: $\not{p}_T$ for Higgs of $M_H$=120 GeV after cuts (1), (3)



Fig. 7: $\not{p}_T$ for backgrounds after cuts (1), (3) and e($\mu$) veto for $Wjj$ background

$W \rightarrow \tau\nu$ and hadronic tau-decay, the veto on the $\tau$ jet is included in this second row. The efficiency of the $\tau$ jet veto is estimated with fast CMSJET simulation, counting events with a reconstructed energy of the $\tau$ jet greater than 20 GeV. A mini-jet veto efficiency of 0.76 for the signal is obtained from the full simulation. It is lower than the efficiency of 0.87 used in [88]. This may be due to the reconstruction of additional soft jets from minimum bias events. Since we plan to use tracker information to suppress such contributions, our estimate of the mini-jet veto efficiency for the Higgs events is conservative.

The last row of the Tab. 4 presents cross-sections after all selection cuts. Fig. 8 and Fig. 9 show $\phi_{jj}$ distributions for the Higgs and background events after cuts (1)-(3), e($\mu$) veto for Wjj background and mini-jet veto. After all selections are applied, Tab. 4 shows good agreement between our estimates and the ones obtained in [88] (except for a 40 % lower Wjj background). Our simulations therefore confirm the conclusion reached in [88]: the LHC potential in the search for an invisibly decaying Higgs boson can be considerably extended by studying the weak boson fusion channel.

## 3.2 ATLAS analysis

**Kinematics and detector simulation:** Higgs production, QCD multi-jet and QCD Zjj and Wjj production have been generated with PYTHIA6.158 [100]. QCD multi-jet events were generated with PYTHIA MSEL=1 subprocesses and for $\hat{p}_t$ in the interval 50-300 GeV, divided in bins of 50 GeV, and for $\hat{p}_t >$ 300 GeV. QCD Zjj (Wjj) backgrounds have been produced switching on the processes 15, 30 (16, 31) with $\hat{p}_t > 30$ GeV. These processes generate Z(W)+1 parton only and additional jets are produced due to initial and final state radiation (ISR, FSR) and fragmentation. Processes 123 and 124 have been used to generate Higgs production via weak boson fusion.
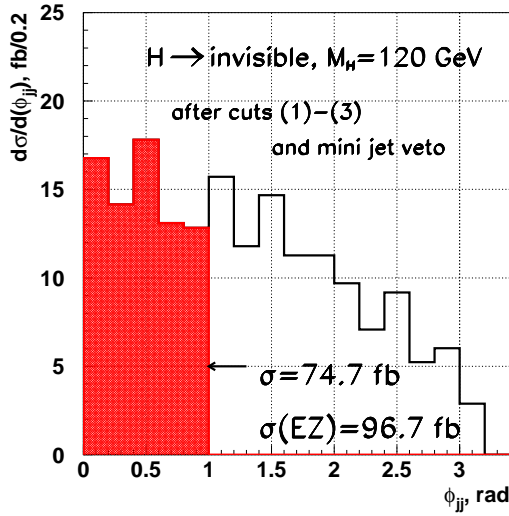
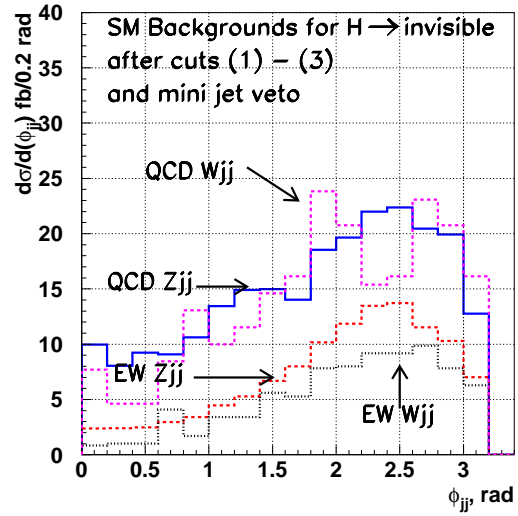Fig. 8: $\phi_{jj}$ for Higgs of $M_H$=120 GeV after cuts (1)-(3) and mini-jet veto

Fig. 9: $\phi_{jj}$ for backgrounds after cuts (1)-(3), e, $\mu$ veto for Wjj background and mini-jet veto

Fast detector simulation with the ATLFast [138] package was performed both for the signal and all backgrounds.

**QCD background rejection:** After cut (1) on the tagging jet topology, the QCD multi-jet background is about of factor $10^4$ larger than the other backgrounds. Cuts (1)-(3), mini-jet and lepton veto suppress this background to the level of QCD Wjj and Zjj backgrounds. Considerable contributions of QCD multi-jet events are still expected in the region of $\not{p}_T$ > 100 GeV, as shown in Fig. 10. The tail of the $\not{p}_T$
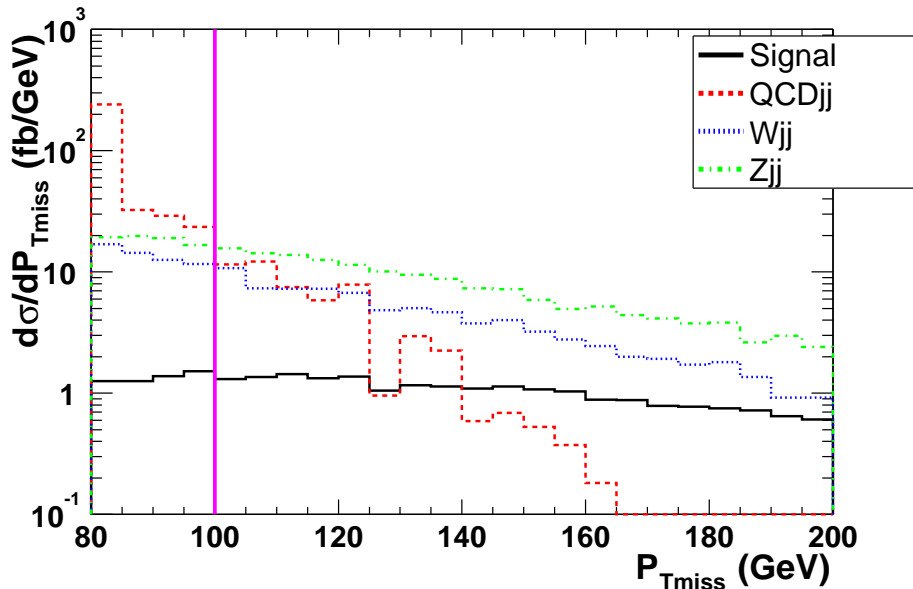


Fig. 10: Missing energy distribution after cuts (1), (3), mini-jet and lepton veto.

distribution in QCD multi-jet events is mainly due to semi-leptonic decays within jets (> 70% of b-jets). Therefore the missing energy is carried by the jet whereas it is carried by the Higgs for the signal.

An additional cut is used to ensure that the QCD multi-jet background is well under control. We define an isolation variable $I$ as the minimal angle in the transverse plane between $\not{p}_T$ and the tagging jets: $I = min(|\phi(\not{p}_T) - \phi(j_{1,2})|)$. The scatter plots in Fig. 11 show the correlation between $\phi_{jj}$ and $I$ for the signal and the different backgrounds. A cut on $I > 1$ removes 97% of the QCD multi-jet background
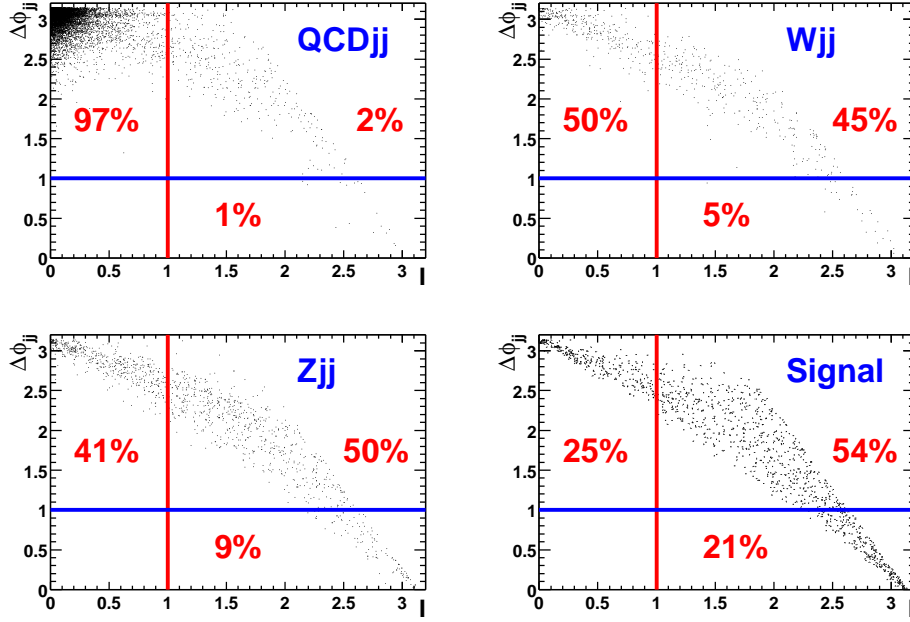
Fig. 11: Event distribution in $\phi_{jj}$ versus Isolation variable for backgrounds and signal.

at the price of a 25% loss of the signal, but it does not affect the $\phi_{jj}$ region which is important for the final counting. It may affect however, the accuracy in the prediction of the Zjj and Wjj backgrounds from the experimental data since it reduces the number of useful Zjj ($Z \to 2e$, $2\mu$) and Wjj ($W \to e(\mu) + \nu$) events by about of 40-50 % as one can see in Fig. 11. After selection of events with $I > 1$ the QCD mini-jet contribution in the region of $\not{p}_T > 100$ GeV becomes negligible as shown in Fig. 12.
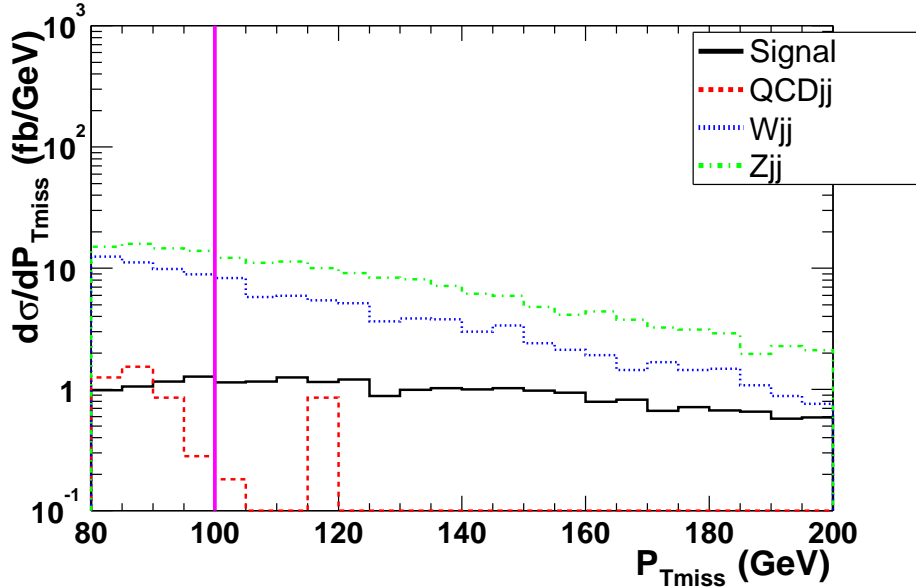


Fig. 12: Missing energy distribution after cuts (1), (3), mini-jet and lepton veto and Isolation cut.

**Higgs signal and Wjj and Zjj background estimates:** Tab. 5 presents the estimated cross-sections in fb for a Higgs of $M_H$=130 GeV and QCD Wjj and Zjj backgrounds for the different selection criteria. Standard Model Higgs production cross-section and Br($H \to$ invisible) = 1 is assumed. Lepton veto in the first row of Tab. 5 includes veto of Wjj events with lepton ($\mu$, e, $\tau$) of $p_T^{e,\,\mu,\,\tau} > 5$, 6, 20 GeV and $|\eta^{e,\,\mu,\,\tau}| <$2.5. One can see that QCD backgrounds after all cuts are about of factor 1.8 larger than in [88]. It is mainly due to the fact that the rejection factor due to the mini-jet veto obtained with this simulation is about a factor 2 smaller than the one used in [88]. The discrepancy in the signal is understood as FSR

Table 5: Cross sections in fb for the background and Higgs of $M_H$=130 GeV assuming Br($H \to$ invisible)=1 and Standard Model production cross-section for the Higgs. Numbers in parentheses are results from [88].

| cross section, fb | Higgs (130 GeV) | QCD $Zjj$ | QCD $Wjj$ |
|---|---|---|---|
| after cuts (1)-(3) and lepton veto | 187 (266) | 817 (1254) | 899 (1284) |
| + mini-jet veto | 146 (232) | 457 (351) | 451 (360) |
| + $\phi_{jj} < 1$ | 60.1 (94.3) | 132.3 (71.8) | 125.6 (70.2) |

in PYTHIA. For the QCD backgrounds it is known that PYTHIA predicts a smaller V+3jet cross section than matrix element calculations, when the hard process is simulated as V+1parton events. This might lead to an underestimate of mini-jet activity in PYTHIA. This point requires further study.

Since EW Wjj and Zjj backgrounds have not been simulated, we use the background fractions of [88] and assume that EW Wjj and Zjj events contribute $\simeq$ 20% to the total background. Tab. 6 presents cross sections in fb for the total background and for a Higgs of $M_H$=130 GeV, after all cuts including the Isolation cut. Fig. 13 shows $\phi_{jj}$ distributions for the signal and backgrounds after cuts (1)-(3), mini-jet and lepton veto and Isolation cut.

Table 6: Cross section in fb for background and Higgs of $M_H$= 130 GeV after all cuts including the Isolation cut. The EW $Vjj$ background has been estimated to contribute as 20 % of the total background and has been added.

| cross section, fb | H (130 GeV) | $Zjj$ | $Wjj$ |
|---|---|---|---|
| all cuts not including cut on $\phi_{jj} < 1$ | 130 | 446 | 428 |
| with cut on $\phi_{jj} < 1$ | 60.1 | 158. | 150.7 |
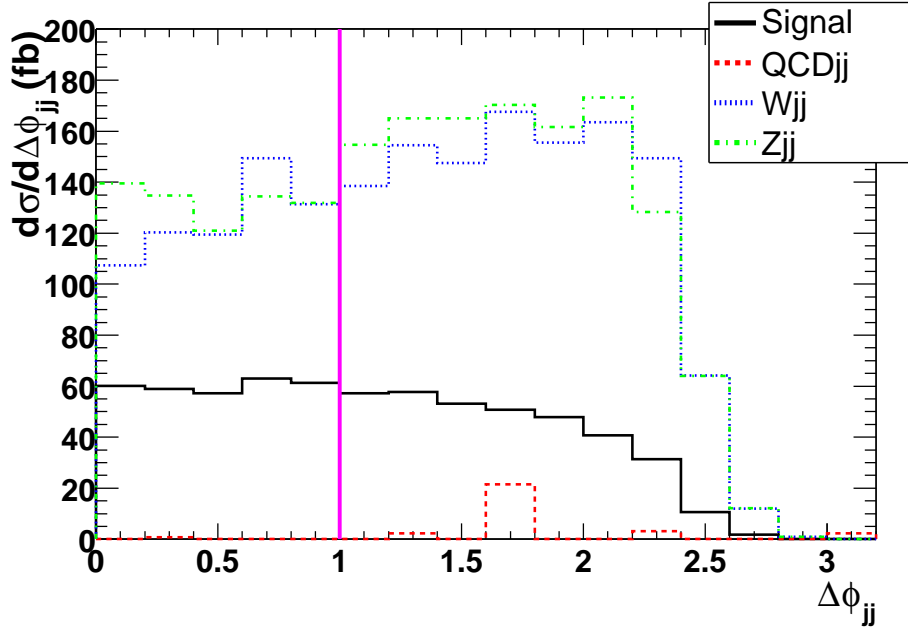


Fig. 13: $\phi_{jj}$ after cuts (1)-(3), mini-jet and lepton veto and Isolation cut

**Discovery potential:** The observation of the invisible Higgs is fully determined by the knowledge of background cross sections in the search area. At present, the leading order calculations for QCD Zjj and Wjj backgrounds lead to uncertainties of a factor of 3 to 4, depending on the renormalization scale [88]. However, these backgrounds could be directly predicted at LHC using $Z \to ll$ or $W \to l\nu$ data samples
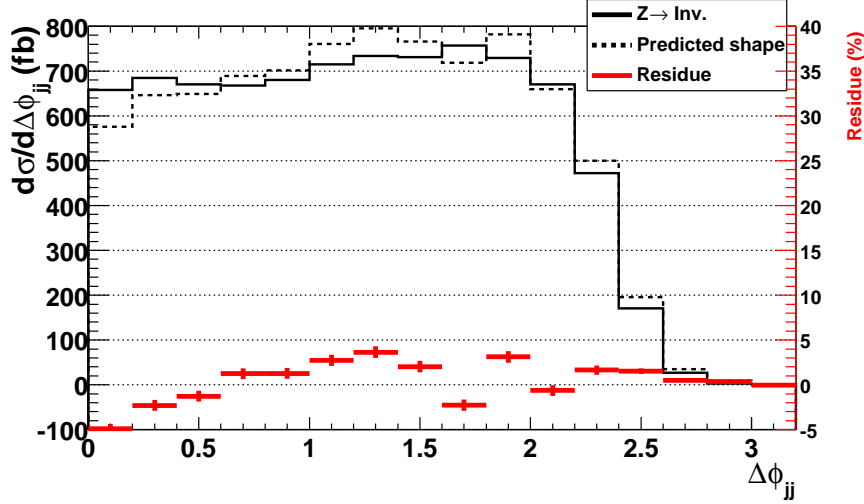
Fig. 14: $\phi_{jj}$ distribution for the QCD Zjj background (solid line) and predicted from $Z \to e^+e^-$ events (dashed line). Cross points and the right y-axis are for the residue of the two distributions, defined as $\frac{N_{Bkg}-N_{Pred}}{N_{bkg}^{tot}}$.

as proposed in [88]. Fig. 14 shows the predicted $\phi_{jj}$ distribution for the QCD Zjj background using $Z \to ee$ events. Residuals shown in this plot are defined as $(N_{Bkg} - N_{Pred})/N_{bkg}^{tot}$. Residuals indicate some pattern which is understood as the different acceptances in $\eta$ for $Z \to ee$ and $Z \to \nu\nu$ events. Moreover, the minimal lepton $p_T$ threshold to insure its observability induces a bias in the $Zjj$ prediction. Then the systematic error on the normalisation factor is $\sim 2.4\%$. At NLO these uncertainties should be negligible and they are not considered in the following.

We define the sensitivity to invisible Higgs as 1.96 standard deviations (95 % CL) from the background error which includes statistical error and the accuracy of the background prediction from the $(Z \to 2l)jj$ and $(W \to l + \nu)jj$ data. The systematic error on the background prediction is still under investigation, therefore we use the predicted accuracy of 3 % as evaluated in [88]. One should keep in mind however, that if the PYTHIA estimates of QCD Vjj cross sections with mini-jet veto are correct, then the statistics for $lljj$ and $l\nu jj$ events, which are used for the background measurement, would also be a factor 2 higher. Hence the 3% error would go down by a factor $\sqrt{2}$. Tab. 7 and Fig. 15 show the parameter

$$\xi^2 = Br(H \to invisible) \times \frac{\sigma_{(qq \to qqH)}}{\sigma_{(qq \to qqH)SM}} \qquad (7)$$

that can be probed at 95 % CL as a function of $M_H$.

Table 7: Sensitivity to the $H \to invisible$ signal for different Higgs masses. The first line is the cross section after all cuts. The two last lines give values of $\xi^2$ which can be probed at 95% CL for an integrated luminosity of 10 $fb^{-1}$ and an expected background of 310 fb without and with a 3% uncertainty on the total background.

| $M_H$ (GeV) | 110 | 120 | 130 | 140 | 150 | 200 | 250 | 300 | 400 |
|---|---|---|---|---|---|---|---|---|---|
| $\epsilon_{surv}\sigma(\phi_{jj} < 1)$ (fb) | 56.2 | 61.1 | 60.1 | 64.6 | 64.2 | 58.8 | 51.2 | 42.5 | 31.0 |
| $\xi^2$ (%) (only stat.) | 20.7 | 17.8 | 18.2 | 16.9 | 17.0 | 18.6 | 21.4 | 25.7 | 35.1 |
| $\xi^2$ (%) stat.+ 3% | 40.4 | 34.8 | 35.4 | 32.9 | 33.1 | 36.2 | 41.7 | 50.1 | 68.5 |

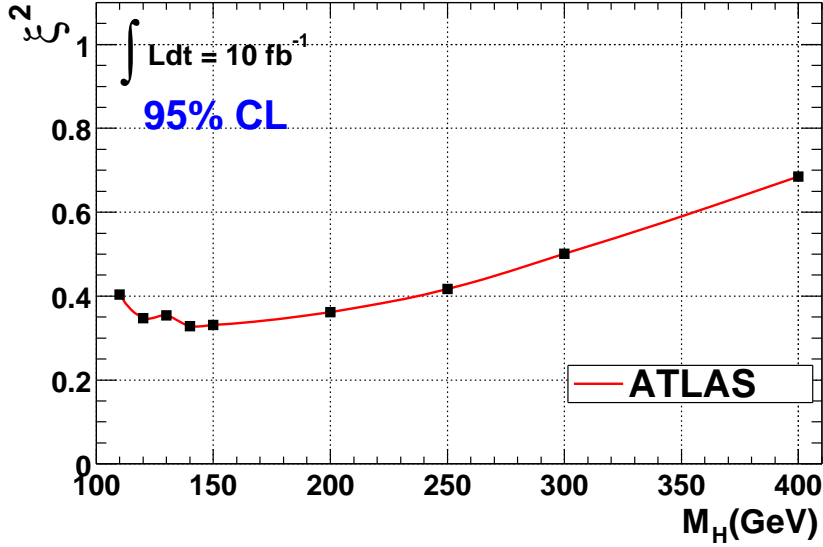We have investigated the possibility of the invisible Higgs observation in the MSSM sector. In this

Fig. 15: 95% CL sensitivity to $H \rightarrow invisible$ signal for an integrated luminosity of 10 $fb^{-1}$.

case, Higgs (h and H) production via weak boson fusion is suppressed by the factor

$$\frac{\sigma_{(qq \rightarrow qqH)MSSM}}{\sigma_{(qq \rightarrow qqH)SM}} = (g_V^{h,H})^2 \tag{8}$$

with $(g_V^h)^2 = sin^2(\alpha - \beta)$ and $(g_V^H)^2 = cos^2(\alpha - \beta)$. It means a Standard Model like production for h and a strongly suppressed production for H for large $M_A$ and $tan(\beta)$. Fig. 16 shows Higgs production cross sections via weak boson fusion for different $tan(\beta)$ values. The black line is the Standard Model cross section. The marked line is the ATLAS sensitivity assuming that $Br(H \rightarrow invisible) = 1$. The lines of different colours are production cross sections for MSSM h and H for different values of $tan(\beta)$.

In the case that gaugino mass unification is ruled out [89] and $M1/M2$=5 we have for medium $tan\beta = 5$ a large $Br(H \rightarrow \chi\chi)$ which could cause a dangerous situation for Higgs discovery at the LHC. At the decoupling limit ($M_A$=1TeV) and for large stop mixing $A_t$=2.4 TeV and large stop mass (1 TeV) the lightest Higgs mass is 120 GeV and it is produced with Standard Model cross section. Fig. 17 shows the region where the Higgs does not escape detection. For the region which is not covered by the invisible Higgs search, the Higgs boson will be detected by other decay channels.

## 4. Summary

We have presented results of two independent studies of ATLAS and CMS on the experimental observability of an invisible Higgs produced via weak boson fusion at the LHC. Background estimates in the two analyses differ substantially even though the performance of the two detectors is similar for this particular study. One of the reasons is that different MC samples are used in the analysis: purely PYTHIA ($2 \rightarrow 2$ processes) generation of W,Z plus multi-jet backgrounds vs. generation with full LO matrix elements implemented as an external process into PYTHIA. The most important reason however, which makes a difference of more than a factor of 2 between CMS and ATLAS estimates of QCD Wjj and Zjj backgrounds, is different rejection factors for the mini-jet (central jet) veto. In the CMS study, the survival probability of the mini-jet veto has been taken from analytical calculations as a multiplicative factor, while in the ATLAS study it comes from PYTHIA generation of additional soft central jets between two tagging jets and the further reconstruction of these jets with the calorimeter using the fast
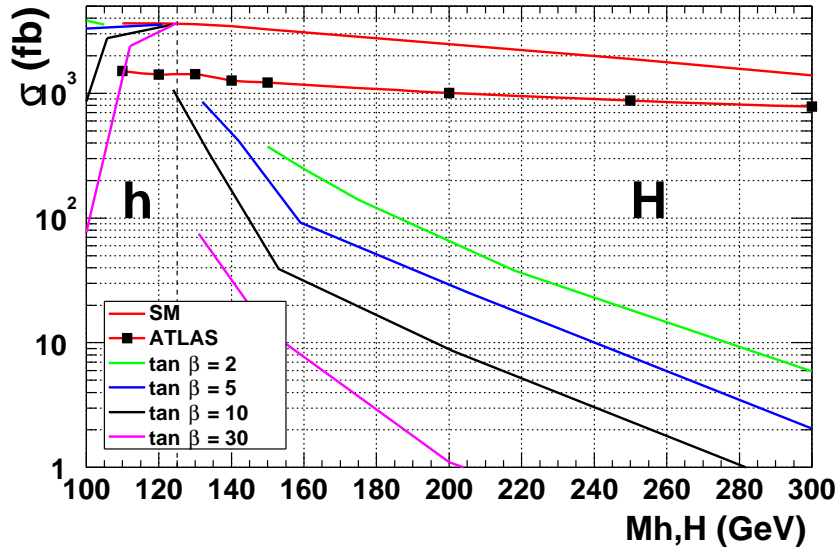
Fig. 16: Higgs production cross sections via the WBF process for different $tan(\beta)$ values. The black line is the Standard Model cross section, the marked line is the ATLAS sensitivity for $Br(H \to invisible) = 1$.
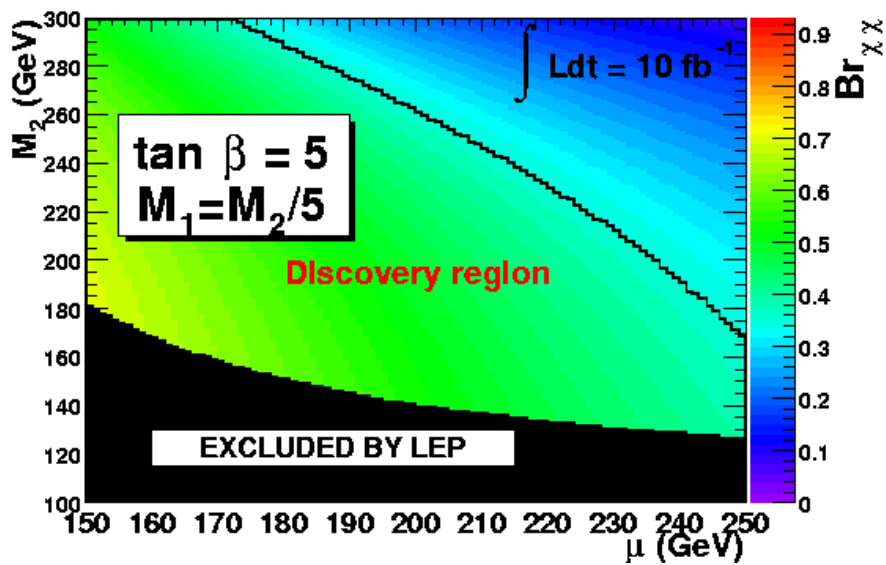


Fig. 17: Branching ratio of $H \to \chi\chi$ in the (M2,$\mu$) plane. The red line is the ATLAS limit. The black area is already excluded by LEP direct chargino searches.

detector simulation. The expected performance of mini-jet veto in weak boson fusion events requires further study, for all Higgs decay modes, not just the invisible decay considered here.

Even with the more pessimistic background estimates of the ATLAS simulations it has been shown that an invisible branching ratio of $\simeq$ 30-40 % can be probed at 95 % CL up to Higgs mass of 250 GeV with the first 10 fb $^{-1}$ of data. Fortunately, for the invisible Higgs search in the real experiment there will be the possibility to estimate Wjj and Zjj backgrounds directly from the data. In addition one can directly measure the mini-jet veto efficiency with these events.

A detailed study of the possible trigger strategy at both Level 1 and High Level trigger has now been performed. It was shown that very high trigger efficiency ($\simeq$ 95 %) for invisible Higgs can be achieved with an acceptable background rate, by making use of topological selections of the tagging jets in addition to a missing $E_T$ cutoff.

**Acknowledgements**

# D. Search for the Standard Model Higgs Boson using Vector Boson Fusion at the LHC

*G. Azuelos, C. Buttar, V. Cavasinni, D. Costanzo, T. Figy, R. Harper, K. Jakobs, M. Klute, R. Mazini, A. Nikitenko, E. Richter–Was, I. Vivarelli and D. Zeppenfeld*

**Abstract**

The weak boson fusion process has been suggested and discussed recently as a discovery process for a Standard Model Higgs boson in the intermediate mass range $m_H < 2m_Z$ at the LHC. The additional jets in the forward region of the detector and the requirement of low jet activity in the central region allow for a significant background rejection. In the present paper the analyses for the $H \to WW^{(*)}$ and the $H \to \tau\tau$ decay modes have been performed using a more realistic simulation of the expected performance of the LHC detectors. The results obtained confirm both the large discovery potential in the $H \to WW^{(*)}$ decay channel and the sensitivity to Higgs boson decays into $\tau$-pairs, which is important for the determination of the Higgs boson coupling to fermions.

## 1. Introduction

The search for the Higgs boson is one of the primary tasks of the experiments at the *Large Hadron Collider* (LHC). It has been established in many studies over the past years [11, 12] that a Standard Model Higgs boson can be identified with a high significance over the full mass range of interest, from the lower limit set by the LEP experiments of 114.1 GeV [3] up to about 1 TeV.

At the LHC the production cross section for a Standard Model Higgs boson is dominated by gluon-gluon fusion. The fusion of vector bosons radiated from initial state quarks represents the second most important contribution to the production cross section. The relative contribution depends on the Higgs boson mass. In the intermediate mass range vector boson fusion amounts to about 20% of the total production cross section and becomes more important with increasing mass. However, for this production mode additional event characteristics can be exploited to suppress the large backgrounds. In these events the Higgs boson is accompanied by two jets in the forward region of the detector originating from the initial quarks from which the vector bosons are emitted. Another feature of the vector boson fusion process is the lack of color exchange between the initial state quarks, which leads to suppressed jet production in the central region. This is in contrast to most background processes, where color flow in the t-channel appears. Jet tagging in the forward region of the detector together with a veto of jet activity in the central region are therefore useful tools to enhance the signal to background ratio. These techniques have so far been applied in the search for heavy Higgs bosons [12].

The observation of the Standard model Higgs boson at the LHC in the vector boson fusion channels in the intermediate mass range has first been discussed in Refs. [36] and [38] for the $H \to \gamma\gamma$ and $H \to WW^{(*)}$ decay modes and in Ref. [37] for the $H \to \tau\tau$ decay mode. In the framework of the *Les Houches workshop* the analyses for the $WW^{(*)}$ and $\tau\tau$ decay modes have been repeated using more realistic simulations of the performance of the LHC detectors, including forward jet tagging and jet veto efficiencies. In the present study the performance at low LHC luminosity, i.e. $\mathcal{L} = 10^{33}$ cm$^{-2}$sec$^{-1}$, is addressed, and the discovery potential is evaluated for integrated luminosity values up to 30 fb$^{-1}$, which are expected to be reached during the first years of operation.

## 2. Signal and Backgrounds

The cross sections for the vector boson fusion process have been calculated using the programme *VV2H* [139]. Although next-to-leading order calculations are available [34], leading order cross sections have

been used. The size of the QCD corrections amounts to about 10% and is thus small. Another reason for this approach is the consistency with the background estimates, for which NLO cross section calculations are not available for all relevant processes. The Higgs branching ratios have been calculated using the programme *HDECAY* [80]. The values for the total cross section for the vector boson fusion process as well as the cross sections times branching ratios for the $H \to WW^{(*)}$ and $H \to \tau\tau$ decay mode are given in Table 1 as a function of the Higgs boson mass. They have been computed using the CTEQ5L structure function parametrization [140].

Table 1: *Total vector boson fusion production cross sections $\sigma(qqH)$ and $\sigma \cdot BR(H \to WW^{(*)})$ and $\sigma \cdot BR(H \to \tau\tau)$ as a function of the Higgs boson mass.*

| $m_H$ | (GeV) | 120 | 130 | 140 | 150 | 160 | 170 | 180 | 190 |
|---|---|---|---|---|---|---|---|---|---|
| $\sigma(qqH)$ | (pb) | 4.36 | 4.04 | 3.72 | 3.46 | 3.22 | 3.06 | 2.82 | 2.64 |
| $\sigma \cdot BR(H \to WW^{(*)})$ | (fb) | 531 | 1127 | 1785 | 2370 | 2955 | 2959 | 2620 | 2054 |
| $\sigma \cdot BR(H \to \tau\tau)$ | (fb) | 304 | 223 | 135 | 64.4 | 11.9 | 2.8 | 1.6 | 1.0 |

The following background processes are common to all channels considered, as described in more detail in Ref. [38]:

- *$t\bar{t}$ production:* due to the appearence of two b-jets, $t\bar{t}$ events contribute already at leading order to the background, if the two b-jets fulfill the identification criteria of the two tag jets.
- *QCD WW background:* the continuum production of W-pairs, where two or more tag jet candidates arise from parton emission.
- *Electroweak WW background:* pair production of $W$ bosons via t-channel vector boson exchange. Due to the similarity to the signal process the rejection of this particular background is expected to be much harder than for the QCD type backgrounds.
- *QCD Drell-Yan $Z/\gamma^* + jet$ production*, with $Z/\gamma^* \to ee, \mu\mu$ and $\tau\tau$.
- *Electroweak $\tau\tau$ production:* tau pair production via a t-channel weak boson exchange.

Table 2: *Cross sections times leptonic branching ratios ($W \to l\nu$, $l = e, \mu$ and $\tau$) for the major background processes.*

| process | $p_T$-cutoff | cross-section |
|---|---|---|
| $t\bar{t}$ | | 55.0 pb |
| QCD $WW + jets$ | | 16.7 pb |
| $Z/\gamma^* + jets$, $Z/\gamma^* \to \tau\tau$ | $> 10$ GeV | 1742.0 pb |
| EW $WW + jets$ | | 81.6 fb |
| EW $\tau\tau + jets$ | | 170.8 fb |
| $Z/\gamma^* + jets$, $Z/\gamma^* \to ee/\mu\mu$ | $> 10$ GeV | 3485.0 pb |
| $ZZ$ | | 37.8 pb |
| $H \to ZZ$ | | 0.26 - 2.5 pb |

The signal processes and all background processes except the electroweak WW and $\tau\tau$ background have been generated using the PYTHIA 6.1 Monte Carlo event generator [100]. The Drell-Yan $Z/\gamma^* + jet$ background has been generated using matrix element calculations for $q\bar{q} \to Zg$ and $qg \to Zq$ with a $P_T$ cutoff of the outgoing quark or gluon of 10 GeV. A summary of the major background processes and the relevant cross sections multiplied by the branching ratio $BR(W \to l\nu)$, where $l = e, \mu$ and $\tau$ are listed in Table 2. In the PYTHIA simulation initial and final state radiation (ISR and FSR) and fragmentation have been switched on, thereby allowing for a study of the jet activity in the central detector region due to radiation. The CTEQ5L parametrization [140] of the parton distribution functions has

been used in the generation of all signal and background processes. To take the spin correlations in tau decays properly into account, tau decays have been modelled using the TAUOLA $\tau$ decay library [45]. The two electroweak processes, which are not included in PYTHIA, have been generated by interfacing the matrix element calculation of Ref. [38] to PYTHIA, which was then used to perform the parton showering, including initial and final state radiation [142]. The $W + jet$ background which is relevant for the $H \rightarrow WW^{(*)} \rightarrow l\nu\,jj$ decay channel has been generated using the matrix elements from the VECBOS Monte Carlo [141], interfaced to PYTHIA. The fast simulation packages ATLFAST [138] and CMSJET [135] of the ATLAS and CMS detectors have been used to perform the detector simulation.

### 3. Experimental Issues in the Search for the Vector Boson Fusion Process

**Trigger aspects:** all channels considered in the following have leptons ($e$ or $\mu$) in the final state and can be triggered by either the single or the di-lepton trigger. It has been assumed that full trigger efficiency can be reached for a single electron or muon for $P_T$ values above 25 GeV or 20 GeV respectively. The corresponding threshold values for the lepton pair triggers are 15 GeV (for $e$) and 10 GeV (for $\mu$).

**Lepton Identification:** it has been assumed that leptons ($e$ and $\mu$) can be identified in the pseudorapidity range, $|\eta| < 2.5$, with an efficiency of 90%. Hadronically decaying taus can be identified over the same range of pseudorapidity. The tau reconstruction efficiency is correlated with the rejection against QCD jets and the results obtained in detailed simulation studies [11, 12] have been used.

**Jet Tagging:** from the signal production process it is expected that the two tag jets are reconstructed with a sizeable $P_T$ in opposite hemispheres and have a large separation in pseudorapidty. In case where there is no further hard initial or final state radiation the transverse momentum of the tagging jets should be balanced by the transverse momentum of the Higgs boson.

In the present study the two tag jets are searched over the full calorimeter coverage of the detectors ($|\eta| < 4.9$). For all jets a calibration has been applied which corrects the jet energy on average back to the original parton energy. After calibration the jet with the highest $P_T$ in the positive and negative region of pseudorapidity is considered as the tag jet candidate. Detailed studies have shown [143] that this choice of the tag jets has a high efficiency for a correct tag jet identifiction. Since the tag jets originate from quarks in the incoming proton it is unlikely that they are b-jets. Consequently a b-jet veto has been applied in the pseudorapidity range of the detectors, where b-jet tagging is available, i.e. $|\eta| < 2.5$. In this procedure a b-tagging efficiency of 60% has been assumed with a corresponding efficiency of about 99% for a light quark or gluon jet not to be b-tagged [12].

An important question is how well the tag jets can be identified at the LHC in the presence of pile-up. To answer this question a full GEANT simulation of the performance of the ATLAS detector in which also pile-up effects have been considered, has been performed [144]. In this study it has been demonstrated that tag jets can be reliably reconstructed in the ATLAS detector and that the fast simulation package of the ATLAS detector provides a sufficiently good description of the tagging efficiency. Differences between the fast and full simulation have been found in the transition regions between different calorimeters and at very forward rapidities. The ratio between the efficiency for reconstructing a jet with $P_T$ above 20 GeV as determined in the full and fast simulation has been parametrized as a function of $P_T$ and $\eta$ and has been used to correct the fast simulation results accordingly [144].

**Jet Veto Efficiencies:** at the LHC, jets in the central region can also be produced by pile-up events. In the full simulation study [144] it has been found that after applying a threshold cut on the calorimeter cell energies of 0.2 GeV at low and 1.0 GeV at high luminosity, that fake jets from pile-up events can be kept at a low level, provided that $P_T$ thresholds of 20 GeV at low and 30 GeV at high luminosity are used for the jet definition.

## 4. The $H \to WW^{(*)}$ decay mode

In this Section the analyses of the $H \to WW^{(*)}$ channels is briefly described. The acceptance cuts proposed in Ref. [38] have been used as a starting point. Finally a multi-variate optimisation has been performed to find the best combination of values for the cuts [143] for Higgs boson masses in the range between 150 and 170 GeV. The cuts found in this optimization have also been used to get a first estimate of the discovery significance outside this mass range. The signal significance may still be improved, if the cut optimization is done as a function of mass, in particular for lower Higgs boson masses.

### 4.1 Di-lepton final states: $H \to WW^{(*)} \to l\nu l\nu$

As discussed already previously [12, 38] a large rejection against the $t\bar{t}$ and the $WW$ backgrounds is obtained by exploiting the anti-correlation of the W spins from the decay of the scalar Higgs boson [31]. Background from real taus from $Z + jet$ production with $Z \to \tau\tau$ can be rejected if the tau momenta and thereby the $\tau\tau$ invariant mass can be reconstruced in the collinear approximation [38]. Due to the high $P_T$ of the Z boson in $Z + jet$ events it can be assumed that the neutrinos in the tau decays are emitted in the direction of the visible charged leptons. From the lepton momenta and the $P_T^{miss}$ vector the fractions $x_{\tau_1}$ and $x_{\tau_2}$ of the $\tau$ energy carried by each lepton and thereby the $\tau\tau$ invariant mass $m_{\tau\tau}$ can be reconstructed. For decays of real $\tau$'s values of $x_{\tau_{1,2}}$ in the range $0 < x_{\tau_{1,2}} < 1$ are expected. The background from $Z/\gamma^*$ Drell-Yan production in association with jets can be efficiently rejected by a cut on the reconstructed transverse mass $m_T(ll\nu)$ of the di-lepton and neutrino system, defined as $m_T(ll\nu) = \sqrt{2P_T^{ll} P_T^{miss} \cdot (1 - cos\Delta\phi)}$, where $\Delta\phi$ is the angle between the di-lepton vector and the $P_T^{miss}$ vector in the transverse plane.

In the event selection the following cuts have been applied:

- Two isolated leptons with $P_T > 20$ GeV and $|\eta| < 2.5$;
- Two tag jets with $P_T^1 > 40$ GeV, $P_T^2 > 20$ GeV and $\Delta\eta_{tags} = |\eta^1_{tag} - \eta^2_{tag}| > 3.8$;
  in addition it has been required that the leptons are reconstructed within the pseudorapidity gap spanned by the two tag jets: $\eta^{min}_{tag} < \eta_{l_{1,2}} < \eta^{max}_{tag}$;
- Lepton Angular Cuts: $\Delta\phi_{ll} \leq 1.05, \quad \Delta R_{ll} \leq 1.8, \quad cos\theta_{ll} \geq 0.2$
  $$M_{ll} < 85 \text{ GeV}, \quad P_T(l_{1,2}) < 120 \text{ GeV},$$
  where $\Delta\phi_{ll}$ is the azimuthal separation between the leptons, $cos\theta_{ll}$ is the cosine of the polar opening angle, $\Delta R_{ll}$ is the separation in $\eta - \phi$ space, and $M_{ll}$ is the invariant mass of the di-lepton system.
- Real tau rejection: events are rejected, if $x_{\tau_1}, x_{\tau_2} > 0.0$ and
  $M_Z - 25 \text{ GeV} < M_{\tau\tau} < M_Z + 25 \text{ GeV}$;
- Invariant mass of the two tag jets: $M_{jj} > 550$ GeV;
- Transverse momentum balance: $|\vec{P}_T^{tot}| < 30$ GeV.
  If no hard initial or final state gluons are radiated, it is expected that the transverse momentum of the Higgs boson is balanced by the transverse momentum of the two tag jets, such that an upper cut on the modulus of the vector
  $$\vec{P}_T^{tot} = \vec{P}_T^{l,1} + \vec{P}_T^{l,2} + \vec{P}_T^{miss} + \vec{P}_T^{j,1} + \vec{P}_T^{j,2}$$
  can be used to reject background.
- Jet veto: no jets with $P_T > 20$ GeV in the pseudorapidity range $|\eta| < 3.2$;
- $Z/\gamma^*, Z/\gamma^* \to \tau\tau$ rejection: $m_T(ll\nu) > 30$ GeV.

The additional background contributions for the signal from same-flavour leptons, of which the the ee- and $\mu\mu$-Drell-Yan backgrounds are the dominant ones, can be efficiently rejected by tightening the di-lepton mass cut and by introducing a $P_T^{miss}$ cut:

- $M_{ll} < 75$ GeV and $P_T^{miss} > 30$ GeV.

Table 3: *Accepted signal (for $m_H = 160$ GeV) and background cross sections in fb for the $H \to WW \to e\mu$ channel after the application of successive cuts. For the signal the contributions via the vector boson fusion and the gluon fusion channel are given separately. The last two lines give the final numbers if the contributions from $W \to \tau\nu \to l\nu\nu\ \nu$ are added for both the $e\mu$ and the $ee/\mu\mu$ final states.*

| | signal (fb) | | background (fb) | | | | | |
| | VV | gg | $t\bar{t}$ | $WW + jets$ | | $Z/\gamma^* + jets$ | | total |
| | $m_H$=160 GeV | | | EW | QCD | EW | QCD | |
|---|---|---|---|---|---|---|---|---|
| Lepton acceptance | 25.3 | 107.4 | 5360 | 12.9 | 513.7 | 3.56 | 12589 | 18479 |
| + Forward Tagging | 10.7 | 2.35 | 186.4 | 7.79 | 1.37 | 1.04 | 125.8 | 322.4 |
| + Lepton angular cuts | 6.99 | 1.46 | 22.0 | 0.47 | 0.12 | 0.40 | 22.7 | 45.7 |
| + Real $\tau$ rejection | 6.69 | 1.44 | 21.0 | 0.42 | 0.12 | 0.06 | 3.54 | 25.1 |
| + Inv. mass $M_{jj}$ | 5.30 | 0.89 | 12.5 | 0.42 | 0.05 | 0.06 | 2.54 | 15.6 |
| + $P_T^{tot}$ | 4.56 | 0.63 | 2.71 | 0.33 | 0.04 | 0.05 | 1.77 | 4.90 |
| + Jet veto | 3.82 | 0.45 | 0.72 | 0.31 | 0.03 | 0.04 | 1.16 | 2.26 |
| + $M_T$-cut | 3.71 | 0.42 | 0.69 | 0.30 | 0.03 | 0.01 | 0.03 | 1.06 |
| $H \to WW^{(*)} \to e\mu + X$ incl. $\tau \to e, \mu$ contribution | 4.14 | 0.46 | 0.71 | 0.33 | 0.03 | 0.01 | 0.03 | 1.11 |
| $H \to WW^{(*)} \to ee/\mu\mu + X$ incl. $\tau \to e, \mu$ contribution | 3.89 | 0.43 | 0.64 | 0.33 | 0.02 | 0.01 | 0.15 | 1.15 |

The acceptance for a Higgs boson with a mass of 160 GeV and for the backgrounds after the application of successive cuts is summarized for the $e\mu$ final state in detail in Table 3. In addition to the signal from the vector boson fusion also contributions from the gluon gluon fusion process $gg \to H \to WW^{(*)}$ where the two tag jets are produced from initial and final state radiation, have been found to contribute to the final signal rate.

All numbers given in the upper part of Table 3 come from direct decays into electron and muon final states. Di-leptons can, however, also be produced via cascade decays of tau leptons, for example, $W \to \tau\nu \to l\nu\bar{\nu}\ \nu$. These contributions have also been calculated and have been added to the accepted signal and background cross sections. An increase of about 10% for the cross sections has been found. Due to the softer $P_T$ spectra of leptons from tau decays this contribution is smaller than the one expected from a scaling of branching ratios. The final acceptance including the contributions from $\tau$ cascade decays, is also given for the sum of the $ee$ and $\mu\mu$ final states. Due to the additional cuts the signal acceptance is slightly lower than in the $e\mu$ case.

It has to be pointed out that the numbers for the dominant $t\bar{t}$ background given in Table 3 have been obtained from the PYTHIA parton shower simulation. An independent estimate of that background has been made by using tree level matrix element calculations for $t\bar{t} +\ 0, 1$, and $2 - jets$. In order to avoid double counting when adding the three contributions the procedure proposed in Ref. [38], to define three distinct final state jet topologies, has been adopted. For $t\bar{t} + 0$ jets, only the two b-jets are considered as tag jet candidates. Initial and final state radiation in these events may lead to a rejection of the event due to the jet veto. A distinctively different class is defined by those $t\bar{t}+ 1$ jet events where the final state light quark or gluon gives rise to one tag jet and one of the two b-jets is identified as the other tag jet. Finally, a third class is defined where in $t\bar{t} + 2$ jet events the final state light quarks or gluons are identified as tag jets.

Using this procedure the total $t\bar{t}$ background in the $e\mu$ channel has been estimated to be 1.65 fb, which is about a factor of 2.3 higher than the PYTHIA prediction. The largest contribution has been found to arise from events where one tag jet originates from a b-jet and the second one from an emitted parton. In the following estimate of the signal significance, a conservative approach is taken and this number is assumed for the $t\bar{t}$ background.

After all cuts a large signal to background ratio can be reached, which leads to an impressive

discovery potential for a Higgs boson with a mass around 160 GeV in this channel. It has to be pointed out that even if the larger $t\bar{t}$ background estimate is taken, the signal to background ratio is much better than in the $gg \rightarrow WW^{(*)}$ channel considered so far [12, 145]. Therefore, the final signal significance is much less affected by systematic uncertainties on the background. Similar to the situation in the $gg \rightarrow WW^{(*)}$ channel no mass peak can be reconstructed. Evidence for a signal has to be extracted from an excess of events above the sum of the backgrounds, for example, in the transverse mass spectrum.

Following the discussion in Ref. [38] the transverse mass of the Higgs boson has been calculated as

$$M_T = \sqrt{(E_T^{ll} + E_T^{\nu\nu})^2 - (\vec{p}_T^{\,ll} + \vec{p}_T^{\,miss})^2}.$$

where

$$E_T^{ll} = \sqrt{(P_T^{ll})^2 + m_{ll}^2} \qquad E_T^{\nu\nu} = \sqrt{(P_T^{miss})^2 + m_{ll}^2}.$$

The corresponding distribution is shown in Fig. 1 for Higgs boson signals of 140 GeV and 160 GeV above the total background.
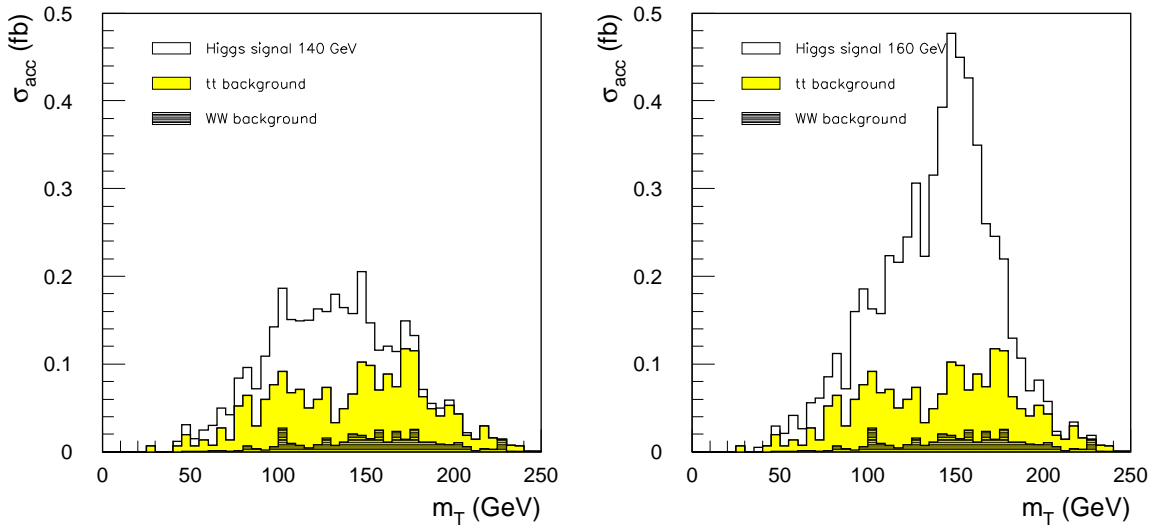


Fig. 1: *Distributions of the transverse mass $M_T$ for Higgs boson signals of 140 GeV (left) and 160 GeV (right) above the total background after all cuts are applied. The accepted cross sections $\sigma_{acc}$ (in fb/5 GeV) including all efficiency and acceptance factors are shown in both cases. The number of events observed in the detector is obtained by multiplying with the integrated luminosity.*

It should be noted that in the present study numbers for signal and background have been found which are somewhat different from the numbers quoted in the original parton level study of Ref. [38]. A detailed comparison between both simulations has been performed and the main differences have been understood. One reason for a reduced signal efficiency observed in the present study is a lower lepton acceptance. In addition, the efficiency for reconstructing the tag jets is found to be lower. Both are related to effects from initial and final state gluon radiation. They lead to a degraded lepton isolation as well as to non-Gaussian tails in the jet response which can not be fully corrected in jet calibration procedures. However, the main conclusions of Ref. [38], that the search for vector boson fusion in the intermediate mass range at the LHC has a large discovery potential for a Standard Model Higgs boson in the $H \rightarrow WW^{(*)}$ decay channel are confirmed.

## 4.2 The $l\nu$-jet-jet channel

It has also been investigated whether the larger branching ratio of the W-bosons into quark pairs can be used and the process $qq \rightarrow qqH \rightarrow qqWW^{(*)} \rightarrow qq\ l\nu\ jj$ can be identified above the larger backgrounds, in particular the $W + jet$ background. This process has already been established as a discovery channel for a heavy Higgs boson [12] in the vector boson fusion process, but has so far not been considered in the intermediate mass region.

The final signal rate in this channel is expected to be much lower than the corresponding numbers in the di-lepton channel [146]. However, a possible observation of a Higgs boson with a mass around 160 GeV can be confirmed in this channel for higher integrated luminosities around 30 fb$^{-1}$. It must be stressed that very hard cuts on the $P_T$ and on the invariant mass of the forward tag jets, as well as on the separation $\Delta R$ between the lepton and the jets from the W-decay are necessary to extract the signal above the large backgrounds. These extreme cuts might also lead to larger systematic uncertainties on the background prediction.

## 4.3 Discovery potential as a function of mass

The analyses outlined above have been performed in the full range of Higgs boson masses from 110 to 190 GeV. The expected numbers of signal and background events expected in the transverse mass interval $50 < M_T < m_H + 40$ GeV are given in Table 4 for integrated luminosities of 5 and 30 fb$^{-1}$, respectively, for the three $WW^{(*)}$ channels considered. The interval of transverse mass has been chosen to maximize the signal to background ratio. For signal events about 98% of all events are contained in that interval. For the estimate of the signal significance the more conservative matrix element estimate of the $t\bar{t}$ background has been used.

Table 4: *Expected signal and background rates for the three $WW^{(*)}$ decay channels as a function of $m_H$ assuming an integrated luminosity of 5 fb$^{-1}$ and 30 fb$^{-1}$ (for the $l\nu jj$ channel). In addition, the signal significances are given for an integrated luminosity of 5 and 30 fb$^{-1}$. They have been computed using Poisson statistics and assuming a systematic uncertainty of 5% on the background.*

| $m_H$ | (GeV) | 110 | 120 | 130 | 140 | 150 | 160 | 170 | 180 | 190 |
|---|---|---|---|---|---|---|---|---|---|---|
| $H \rightarrow WW^{(*)} \rightarrow e\mu + X$ | | | | | | | | | | |
| Signal | (5 fb$^{-1}$) | 0.4 | 1.8 | 4.8 | 8.4 | 13.9 | 22.7 | 21.6 | 16.9 | 12.7 |
| Background | (5 fb$^{-1}$) | 5.2 | 6.0 | 7.0 | 8.0 | 8.3 | 9.1 | 9.3 | 9.4 | 9.8 |
| Stat. significance | (5 fb$^{-1}$) | - | - | 1.5 | 2.5 | 3.9 | 5.8 | 5.5 | 4.4 | 3.4 |
| Stat. significance | (30 fb$^{-1}$) | - | 1.5 | 3.9 | 6.9 | 11.1 | 17.3 | 16.3 | 12.6 | 9.3 |
| $H \rightarrow WW^{(*)} \rightarrow ee/\mu\mu + X$ | | | | | | | | | | |
| Signal | (5 fb$^{-1}$) | 0.3 | 1.6 | 4.4 | 7.9 | 13.2 | 21.5 | 20.4 | 16.6 | 11.6 |
| Background | (5 fb$^{-1}$) | 5.2 | 5.9 | 6.9 | 7.6 | 8.0 | 8.6 | 8.8 | 8.9 | 9.2 |
| Stat. significance | (5 fb$^{-1}$) | - | - | 1.4 | 2.4 | 3.8 | 5.6 | 5.3 | 4.4 | 3.2 |
| Stat. significance | (30 fb$^{-1}$) | - | 1.6 | 3.9 | 6.7 | 10.8 | 16.9 | 15.8 | 12.8 | 8.8 |
| $H \rightarrow WW^{(*)} \rightarrow l\nu\ jj + X$ | | | | | | | | | | |
| Signal | (30 fb$^{-1}$) | - | - | 4.5 | 7.5 | 10.5 | 24.0 | 24.0 | 18.0 | 15.0 |
| Background | (30 fb$^{-1}$) | - | - | 6.0 | 6.0 | 6.0 | 18.0 | 18.0 | 18.0 | 18.0 |
| Stat. significance | (30 fb$^{-1}$) | - | - | 1.5 | 2.4 | 3.3 | 4.6 | 4.6 | 3.5 | 3.0 |

The signal significances, expressed in the equivalent number of Gaussian standard deviations, have been calculated using Poisson statistics and assuming an integrated luminosities of 5 and 30 fb$^{-1}$ and a systematic uncertainty of 5% on the background. A $5\sigma$ discovery can be claimed for 5 fb$^{-1}$ for $m_H = 150 - 185$ GeV if the $e\mu$ and $ee/\mu\mu$ channels are combined. For an integrated luminosity of 30 fb$^{-1}$ the discovery range increase to $m_H = 130 - 190$ GeV.

Table 5: *Accepted signal (for $m_H = 120$ GeV) and background cross sections in fb for the $H \to \tau\tau \to e\mu$ channel after the application of all cuts for both the $e\mu$ and the sum of the $ee$ and $\mu\mu$ channels. For the signal the contributions via the vector boson fusion and the gluon fusion channel are given separately.*

| | signal (fb) | | $t\bar{t}$ | background (fb) | | | | Total |
|---|---|---|---|---|---|---|---|---|
| | VV | gg | | $WW + jets$ | | $\tau\tau + jets$ | | |
| | $m_H$=120 GeV | | | EW | QCD | EW | QCD | |
| $H \to \tau\tau \to e\mu$ | 0.23 | 0.01 | 0.02 | 0.01 | 0.0 | 0.02 | 0.04 | 0.09 |
| $H \to \tau\tau \to ee/\mu\mu$ | 0.24 | 0.02 | 0.05 | 0.01 | 0.0 | 0.04 | 0.08 | 0.17 |

## 5. The $H \to \tau\tau$ decay mode

In the following searches for $H \to \tau\tau$ decays using the double leptonic decay mode, $qqH \to qq \, \tau\tau \to qq \, l^+\nu\bar{\nu} \, l^-\bar{\nu}\nu$ and the lepton-hadron decay mode $qqH \to qq \, \tau\tau \to qq \, l^\pm\nu\nu \, had \, \nu$, are described. Due to the $\tau\tau$ final state the $Z + jet$, $Z \to \tau\tau$ background contributes to the irreducible background and constitues the principal background for $H \to \tau\tau$ decays at low Higgs boson masses. The main points of the analyses are briefly summarized in the following subsections. For details the reader is referred to Refs. [147] and [148].

## 5.1 Di-lepton final states: $H \to \tau\tau \to l^+l^- P_T^{miss} + X$

The di-lepton final state is characterized by two tag jets in the forward regions of the detector, two leptons in the central region and missing transverse momentum. The following cuts have been applied to select $e\mu$ final states:

- Two isolated leptons with $P_T(e) > 15$ GeV and $|\eta_e| \leq 2.5$ and
  $P_T(\mu) > 10$ GeV and $|\eta_\mu| \leq 2.5$;
- Two tag jets with $P_T^1 > 50$ GeV, $P_T^2 > 20$ GeV and $\Delta\eta_{tags} = |\eta_{tag}^1 - \eta_{tag}^2| \geq 4.4$.
  In addition, it has been required that the leptons are reconstructed within the pseudorapidity gap spanned by the two tagging jets: $\eta_{tag}^{min} < \eta_{l_{1,2}} < \eta_{tag}^{max}$;
- Missing transverse momentum: $P_T^{miss} > 50$ GeV;
- Invariant mass of the two tag jets: $M_{jj} > 700$ GeV;
- Jet veto: no jets with $P_T > 20$ GeV in the pseudorapidity range defined by the two tag jets $\eta_{tag}^{min} < \eta_j^{veto} < \eta_{tag}^{max}$;
- Azimuthal separation $\Delta\phi_{jj}$ between the tag jets: $\Delta\phi_{jj} < 2.2$.
  This cut is applied to reduce the electroweak $Zjj$ background, for which back-to-back jets are preferred [88].
- Separation $\Delta R_{e\mu}$ in $\eta - \phi$ space between the two leptons: $\Delta R_{e\mu} < 2.6$;
- Real tau reconstruction: $x_{\tau_1}, x_{\tau_2} > 0$ and $x_{\tau_1}^2 + x_{\tau_2}^2 < 1$;
- Mass window around the Higgs boson mass: $m_H - 10$ GeV $< m_{\tau\tau} < m_H + 15$ GeV.

For $ee$ and $\mu\mu$ final states the additional background from Z decaying into $ee$ or $\mu\mu$ is efficiently rejected by requiring in addition: $m_{ll} < m_Z - 15$ GeV.

The results are summarized for both the $e\mu$ and the sum of the $ee$ and $\mu\mu$ channel in Table 5, where the accepted cross sections for the signal with $m_H = 120$ GeV and the background contributions are given after the application of all cuts. After $\tau$ reconstruction the signal to background ratio is still much smaller than 1. This situation is drastically changed after the application of the mass cut around the Higgs boson mass. Due to the reconstructed Higgs boson mass the sidebands can be used for the determination of the absolute level of the background.

The distribution of the reconstructed $\tau\tau$ invariant mass is shown in Fig. 2 (left) for the sum of the $e\mu, ee$ and $\mu\mu$ channels for a Higgs boson signal of 120 GeV above the background assuming an
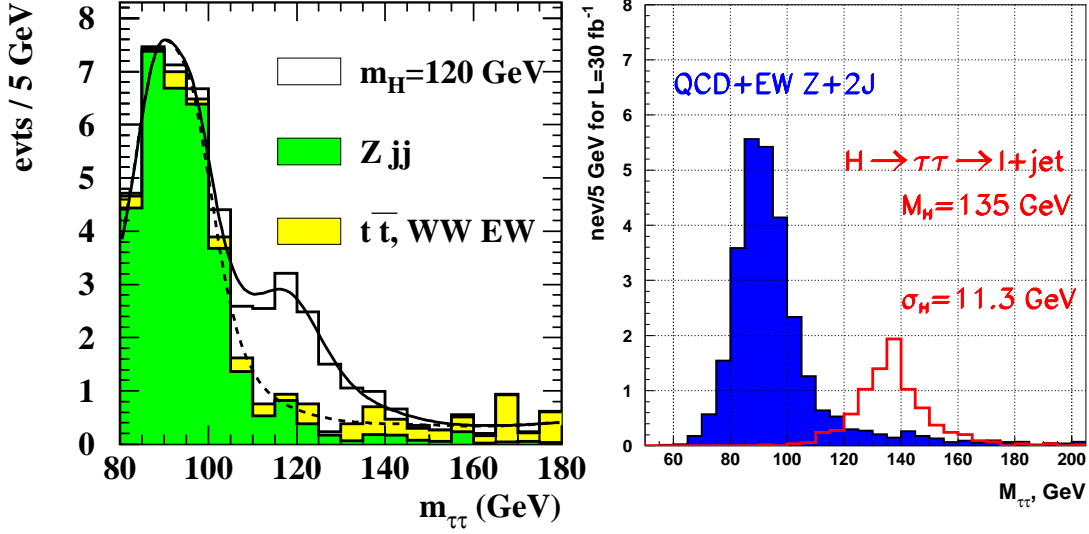
integrated luminosity of 30 fb$^{-1}$ .



Fig. 2: *left: The reconstructed $\tau\tau$ invariant mass for a Higgs boson signal of 120 GeV in the ll-channel above all backgrounds after application of all cuts except the mass window cut. right: The reconstructed $\tau\tau$ invariant mass for a Higgs boson signal of 135 GeV in the $(l - had)$-channel compared to the QCD plus electroweak $Z + jj$ ($Z \to \tau\tau \to l + had$ backgrounds after application of all cuts except the mass window cut. In both cases the signal and background numbers are shown for an integrated luminosity of 30* fb$^{-1}$.*

The analysis has been performed for Higgs boson masses in the range from 110 to 150 GeV. The expected numbers of signal and background events and the statistical significance for a Higgs boson discovery expressed in terms of Gaussian standard deviations are given in Table 6 for an integrated luminosity of 30 fb$^{-1}$ .

Table 6: *Expected signal and background rates and statistical significance for the three $\tau\tau$ decay channels as a function of $m_H$ assuming an integrated luminosity of 30* fb$^{-1}$ *.*

| $m_H$ (GeV) | 110 | 120 | 130 | 140 | 150 |
|---|---|---|---|---|---|
| $H \to \tau\tau \to e\mu\, P_T^{miss}$ | | | | | |
| Signal (30 fb$^{-1}$ ) | 7.7 | 7.0 | 5.1 | 3.3 | 1.5 |
| Background (30 fb$^{-1}$ ) | 7.0 | 2.6 | 2.3 | 1.9 | 1.5 |
| Stat. significance (30 fb$^{-1}$ ) | 2.4 | 3.2 | 2.5 | 1.8 | - |
| $H \to \tau\tau \to ee/\mu\mu\, P_T^{miss}$ | | | | | |
| Signal (30 fb$^{-1}$ ) | 9.2 | 7.2 | 5.7 | 3.1 | 1.5 |
| Background (30 fb$^{-1}$ ) | 10.5 | 5.2 | 3.8 | 3.1 | 2.3 |
| Stat. significance (30 fb$^{-1}$ ) | 2.4 | 2.6 | 2.3 | 1.4 | - |

## 5.2 The lepton-hadron decay mode: $H \to \tau\tau \to l^{\pm}\nu\nu\, had\, \nu$

The $l - had$ decay mode of the $\tau\tau$ final state has also been studied using a fast simulation of the CMS detector [135]. The backgrounds considered in this study are QCD and electroweak production of $Z + jj$ ($Z \to \tau\tau \to l + \tau$-jet) and $W + 3j$ ($W \to e(\mu) + \nu$). As in the previous studies, the $b\bar{b} + jj$ background it expected to be small [37]. QCD $Z + jj$ production has been generated using the lowest order matrix element provided by the authors of Ref. [37] interfaced to PYTHIA. The electroweak $Z + jj$ production has been simulated with COMPHEP [132], again interfaced to PYTHIA. The $W + 3j$ events have been produced with PYTHIA which may lead to an underestimate of this background cross-section.

For the present study the jet veto efficiency has not yet been evaluated in a full detector simulation and the survival probability as determined in Ref. [38] has been used to account for the acceptance of the jet veto cut. In Ref. [38] the jet veto efficiency was found to be 0.87 for signal events and background from electroweak production and 0.28 for QCD type backgrounds. In addition, it has been assumed that the jets are reconstructed with full efficiency. Results based on a full simulation of the CMS detector have shown that a reconstruction of low $P_T$ jets around 20 GeV is possible with a high efficiency in a low luminosity scenario. For the identification of the hadronic tau with the calorimeter and the tracker information an efficiency of 0.32 has been used. Using these criteria a probability of 0.0019 is obtained for mis-identifying jets as hadronic $\tau$'s.

In the event selection the following cuts are applied:

- One isolated lepton with $P_T > 15$ GeV and $|\eta| \leq 2.4$;
- One hadronic tau jet with $P_T > 30$ GeV and $|\eta| \leq 2.4$;
- Two tag jets with $\Delta\eta_{tags} = |\eta_{tag}^1 - \eta_{tag}^2| \geq 4.4$.
  In addition, it has been required that the lepton and the tau-jet are reconstructed within the pseudorapidity gap $\eta_{tag}^{min} + 0.7 < \eta_{l,\tau-jet} < \eta_{tag}^{max} - 0.7$;
- Invariant mass of the tag jets: $M_{jj} > 1000$ GeV;
- Transverse mass $m_t(l, P_T^{miss}) := \sqrt{2P_T^l P_T^{miss}(1 - cos\Delta\phi)} < 30$ GeV;
- Tau reconstruction: $0 < x_{\tau_l} < 0.75, \ 0 < x_{\tau_h} < 1$;
- Mass window: $|m_{\tau\tau} - m_H| < 15 \ GeV$.

The number of signal events for $m_H$=135 GeV and the number of different background events expected after all selections for an integrated luminosity 30 $fb^{-1}$ are given in Table. 7. The errors quoted result from the statistical uncertainty of the Monte Carlo data samples. For comparison the number of events estimated in Ref. [37] are also shown in the second row of the table.

Table 7: *Number of signal ($m_H = 135$ GeV) and background events in the $l - had$ channel expected after all selections for an integrated luminosity 30 $fb^{-1}$*

| Higgs, $M_H$=135 GeV | QCD Z+jj | EW Z+jj | W+3j |
|---|---|---|---|
| 6.7±0.3 | 0.63±0.10 | 0.74±0.08 | 0.14±0.05 |
| 6.2 (from Ref. [37]) | total background from Ref. [37] is 1.1 | | |

The number of signal and the total number of background events expected after all selections for different Higgs boson masses in the range between 115 and 145 GeV and assuming an integrated luminosity 30 $fb^{-1}$ are shown in Tab. 8.

Table 8: *Expected signal and background rates and statistical significance for the l-had $\tau\tau$ decay channels as a function of $m_H$ assuming an integrated luminosity of 30 fb$^{-1}$.*

| $m_H$ | (GeV) | 115 | 125 | 135 | 145 |
|---|---|---|---|---|---|
| $H \to \tau\tau \to lhad \ P_T^{miss}$ | | | | | |
| Signal | (30 fb$^{-1}$) | 12.6 | 9.9 | 6.7 | 3.6 |
| Background | (30 fb$^{-1}$) | 5.5 | 2.3 | 1.5 | 1.1 |
| Stat. significance | (30 fb$^{-1}$) | 4.1 | 4.5 | 3.7 | 2.4 |

The reconstructed $\tau\tau$ invariant mass for the QCD and EW $Z + jj$ ($Z \to \tau\tau \to l + \tau$-jet) backgrounds and for a Higgs boson with $m_H$=135 GeV is shown in Fig. 2 (right). The distributions are normalised to the expected number of events after all cuts, except the mass window cut, for an integrated luminosity of 30 $fb^{-1}$.

## 6. Conclusions

The discovery potential for the Standard Model Higgs boson in the intermediate mass range has been studied using the vector boson fusion process. It has been demonstrated that the LHC experiments have a large discovery potential in the $H \to WW^{(*)} \to l^+l^- P_T^{miss}$ channel. The additional signature of tag jets in the forward and of a low jet activity in the central region of the detector allow for a significant background rejection, such that a better signal to background ratio than in the inclusive $H \to WW^{(*)}$, which is dominated by gluon gluon fusion process, is obtained. As in the inclusive case, only the transverse mass of the Higgs boson can be reconstructed and a signal has to be claimed from an excess of events above the background. Due to the larger signal to background ratio in the search for the fusion process the signal sensitivity is less affected by systematic uncertainties on the background prediction. The present study shows that the ATLAS and CMS experiments at the LHC would be sensitive to a Standard Model Higgs boson in this decay channel in the mass range between 150 and 185 GeV with data corresponding to an integrated luminosity of 5 fb$^{-1}$ only.

In addition, it has been shown that in the low mass region for $m_H < 140$ GeV the LHC experiments are also sensitive to the $\tau\tau$ decay mode of the Standard Model Higgs boson, if the characteristics of the vector boson fusion are exploited. However, a discovery in this final state would require an integrated luminosity of about 30 fb$^{-1}$ and a combination of the $l-l$ and $l-had$ decay modes. The measurement of the $\tau$ decay mode is particularly important for a measurement of the Higgs boson coupling to fermions.

The present study confirms the results published earlier [36–38], that the search for vector boson fusion in the intermediate mass range at the LHC has a large discovery potential over the full range from the lower limit set by the LEP experiments up to $2\, m_Z$, where the high sensitivity $H \to ZZ \to 4\, l$ channel takes over.

# E. Study of the MSSM channel $A/H \rightarrow \tau\tau$ at the LHC

*D. Cavalli, R. Kinnunen, G. Negri, A. Nikitenko and J. Thomas*

**Abstract**

Sudies both from ATLAS and CMS with fast and full detector simulation have shown that the discovery potential of the $A/H \rightarrow \tau\tau$ channel in the MSSM is large in the $m_A$ range from $\sim$100 GeV to $\sim$1 TeV already with 30 fb$^{-1}$ collected at low LHC luminosity ($10^{33}$ cm$^{-2}$s$^{-1}$). The results of these studies, in particular for the lepton-hadron and the hadron-hadron final decay channels, are presented here. The question of the trigger for the hadron-hadron final state that is a very important issue for this purely hadronic final state process is also discussed here.

## 1. Introduction

In the minimal supersymmetric extension of the Standard Model (MSSM), two Higgs doublets are required, resulting in 5 physical states, referred to as H$^+$, H$^-$, h (neutral lighter scalar), H (neutral heavier scalar) and A (neutral pseudoscalar). At tree level their masses can be computed in terms of only two parameters, typically $m_A$ and $tan\beta$ (the ratio of the vacuum expectation values of the two doublets).

The MSSM H $\rightarrow \tau\tau$ and A $\rightarrow \tau\tau$ rates are strongly enhanced with respect to the SM case over a large region of the parameter space.

A/H can be produced via two different mechanisms. For low values of $tan\beta$, the $gg \rightarrow A/H$ (direct production mode - Fig. 1) rates are dominant and significantly larger than in the SM case. For large values of $tan\beta$, the production is dominated by $gg, q\bar{q} \rightarrow b\bar{b} \ A/H$, $gg \rightarrow b\bar{b} \ A/H$ is largely dominant between the two at the LHC, (associated b$\bar{b}$ production mode- Fig. 2).

For $m_A >$ 150 GeV, the H and A bosons are degenerated in mass, so the signal rates in the $\tau\tau$-channel can be added, whereas a more complicated procedure depending on the experimental resolution and on the mass difference $m_H$-$m_A$ has to be applied for $m_A <$ 150 GeV [149]. Higgs-boson masses below 120 GeV have not been considered in this channel because of the large resonant background from Z $\rightarrow \tau\tau$ decays.

For high $tan\beta$ values A and H couple dominantly to the heaviest lepton and to the heaviest down-type quark; the branching ratio of A/H is $\sim$ 90% into b$\bar{b}$ and $\sim$ 10% into $\tau\tau$.

Including the decay of the $\tau$ leptons, the three possible final states are:

- the lepton-lepton ($e\mu$) channel, with a branching ratio (BR) of 6.3%;
- the lepton-hadron channel, with $BR = 46\%$;
- the hadron-hadron channel, with $BR = 41\%$.

The lepton-lepton channel has been studied in the low $m_A$ region ($<\sim$500 GeV) both in ATLAS [149] and CMS [166]: compared to the lepton-hadron channel it turns out to provide a worse sensitivity
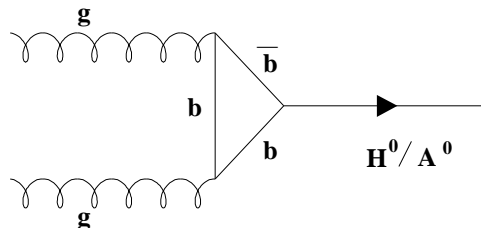
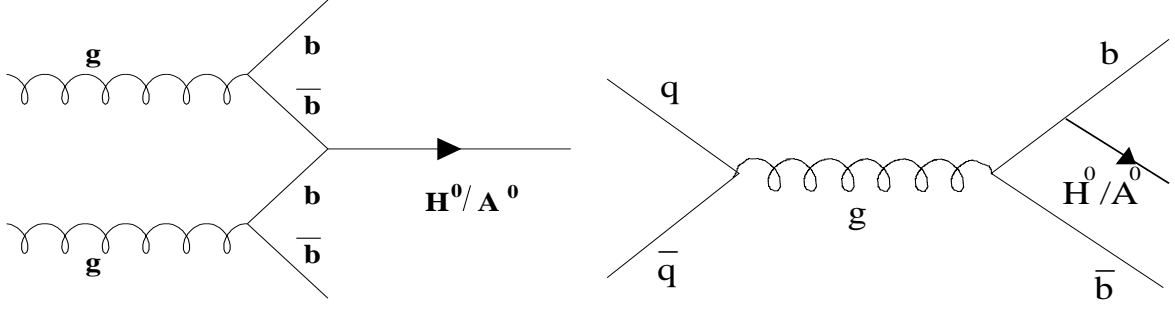

Fig. 1: Direct A/H production mode.

Fig. 2: Associated b$\overline{\text{b}}$ A/H production modes.

to a possible signal, due to both its lower rate and the less favourable kinematics of the $\tau$-decay. CMS is studying the possibility to use the impact information to reduce the backgrounds in this channel.

The lepton-hadron channel has been studied in the low $m_A$ region both in ATLAS [12] [150] and CMS [169]. In this channel the application of $\tau$-jet identification strongly reduces the jet-background from various sources. In ATLAS the $m_A$ region studied has been recently extended to $\sim$1 TeV [150] with promising results.

The hadron-hadron channel has been studied in CMS [162] and recently in ATLAS [151] in the higher $m_A$ region ($>\sim$ 500 GeV). The leptonic decay channels include a trigger lepton which allows for an efficient background reduction; in the hadron-hadron channel the purely hadronic final states compete with QCD jets, so it is difficult to maintain the trigger rates acceptable and it is also difficult to find criteria to reduce the huge QCD background. To exploit fully the 2 $\tau$-jet final states, especially in the very low ($\sim$ 200 GeV) mass range, an efficient hadronic $\tau$ trigger has been developed in CMS based on Level-1 calorimeter selection, Level-2 electromagnetic calorimeter isolation [163] and a Level-3 tracking (isolation) [164].

The search strategy for all channels is based on kinematical cuts, $\tau$-jet identification (for the channels where at least one $\tau$ decays hadronically) and the recontruction of the $\tau\tau$ invariant mass $m_{\tau\tau}$, so it relies on two very important detector performance requirements. One important feature of the A/H $\rightarrow \tau\tau$ analysis is in fact the possibility to reconstruct the invariant $\tau\tau$ mass. The energies of the two $\tau$'s are evaluated from the energies of the $\tau$ decay products, assuming that they have the same direction of the $\tau$-parent; the neutrino energies are obtained solving a system containing the two $p_T^{miss}$ components. Therefore, it is crucial to have a very good $p_T^{miss}$ resolution. For the channels where at least one $\tau$ decays to hadrons, a very good $\tau$-jet identication is also crucial, to have the possibility to reject the huge jet-background from different sources.

## 2. ATLAS Results

### 2.1 Event Generation, A/H Production Cross-Sections and Branching Ratios to $\tau\tau$

The signal and background events were generated with the PYTHIA 6.152 Monte Carlo event generator. The CTEQ5L parametrisation of the structure functions was used. The fast ATLAS detector simulation was used [138].

The direct A/H production (from $gg \rightarrow A/H \rightarrow \tau\tau$) cross-section is calculated using the program HIGLU [155], based on the results of [17]. The associated b$\overline{\text{b}}$ A/H cross-section is calculated using the program HQQ, which calculates the production cross-section of Higgs bosons via $gg, q\overline{q} \rightarrow$b$\overline{\text{b}}$ $A/H$ according to the results presented in [156]. The MSSM Higgs sector is implemented in the approximate two-loop RGE approach of [73]. The program HDECAY is used to calculate the total decay widths and the branching ratios [80]. The cross-sections calculated at leading order (LO) are used here. The direct A+H production cross-sections and the associated b$\overline{\text{b}}$ A+b$\overline{\text{b}}$ H cross-sections, both multiplied by
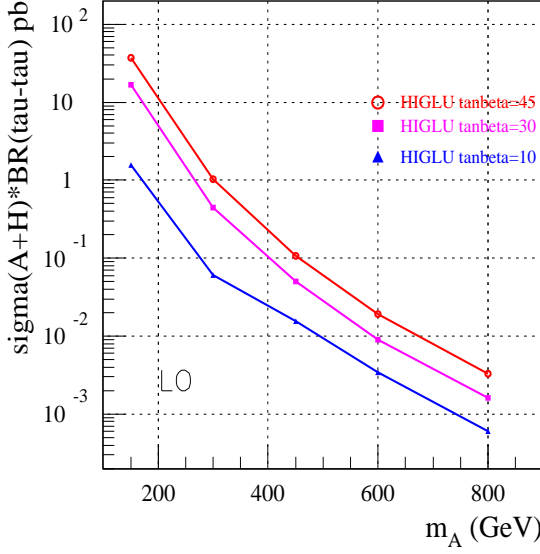
Fig. 3: Direct A/H production cross-section times BR($A/H \to \tau\tau$) as a function of $m_A$ for different $tan\beta$ values.

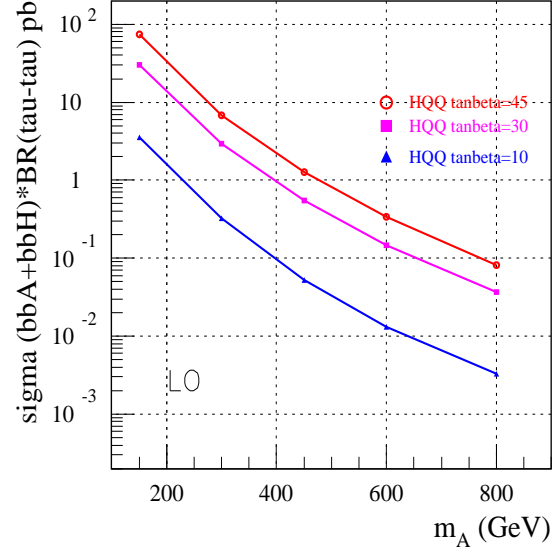Fig. 4: Associated b$\bar{\text{b}}$ A/H production cross-section times BR($A/H \to \tau\tau$) as a function of $m_A$ for different $tan\beta$ values.

the BR($A/H \to \tau\tau$), are shown in Fig. 3 and in Fig. 4 respectively, for three different $tan\beta$ values. For large values of $tan\beta$, the production is dominated by the associated production mode, moreover, for a fixed $tan\beta$ value, the ratio between the associated and direct production increases as $m_A$ increases.
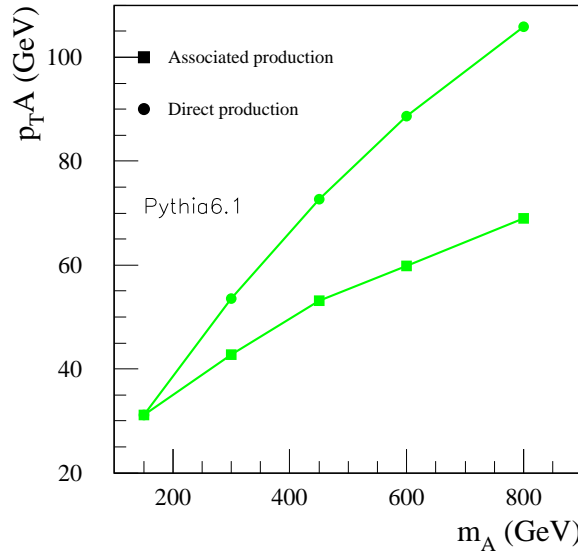


Fig. 5: Average $p_T$(A/H) as a function of $m_A$ in direct and associated production in PYTHIA6.1

There are differences in the event topology and kinematics between the events from the two different production processes:

- there are b-jets in b$\bar{\text{b}}$ A/H events
- the $p_T$ distribution of the generated A/H is different. As can be seen from Fig. 5, the average $p_T$A is larger in direct production for masses larger than 150 GeV.

It must be underlined that the theoretical uncertainty for both the computation of cross-section and simulation of events for the b$\bar{\text{b}}$ associated production is still large [157].

## 2.2 $\tau$-jet identification, $p_T^{miss}$ resolution and the reconstructed $m_{\tau\tau}$ resolution in ATLAS

An excellent *$\tau$-jet identification performance* to suppress the huge jet-background from various sources is necessary for the A/H $\to \tau\tau$ study for the channels where at least one $\tau$ decays hadronically. In ATLAS the $\tau$-jet identification/jet-rejection has been studied with full detector simulations of signal and background events [152]. The criteria to identify a hadronic jet as a $\tau$-jet are based on both calorimeter and tracker information.

In the $p_T$ region 30-150 GeV, the requests are (here called TDR criteria because they were used to obtain the results reported in in the ATLAS Physics Performance Technical Design Report (TDR) [12]):
- $R_{em} < 0.07$, where $R_{em}$ is the jet radius computed using only the e.m. cells contained in the jet;
- $\Delta E_T^{12} < 0.1$, where $\Delta E_T^{12}$ is the difference between the transverse energies contained in cones of size $\Delta R = 0.2$ and 0.1, normalised to the total jet transverse energy $E_T$;
- $N_{tr} = 1$, where $N_{tr}$ is the number of reconstructed charged tracks with $p_T > 2$ GeV pointing to the cluster.

With these cuts the *$\tau$-jet identification efficiency* ($\epsilon_\tau$) is $\sim 25\%$ for $\tau$'s from $m_A$=150 GeV ($< p_T^{\tau-jet} > \sim 50$ GeV) and the $jet - rejection$ goes from $\sim 170$ to $\sim 1700$ for jets in $30 < p_T < 150$ GeV, depending on the $p_T$ and on the jet type (light quark, gluon, b-jet). With the same criteria an $\epsilon_\tau \sim 40\%$ for $m_A$=800 GeV ($< p_T^{\tau-jet} > \sim 200$ GeV) and a $jet - rejection \sim 2500$ against QCD jets with $p_T > 150$ GeV can be achieved. In Fig. 6 the $\tau$-jet identification efficiency as a function of $m_A$ is shown, while in Fig. 7 the jet-efficiency is shown as a function of the jet $p_T$. The $\tau$-jet identification criteria
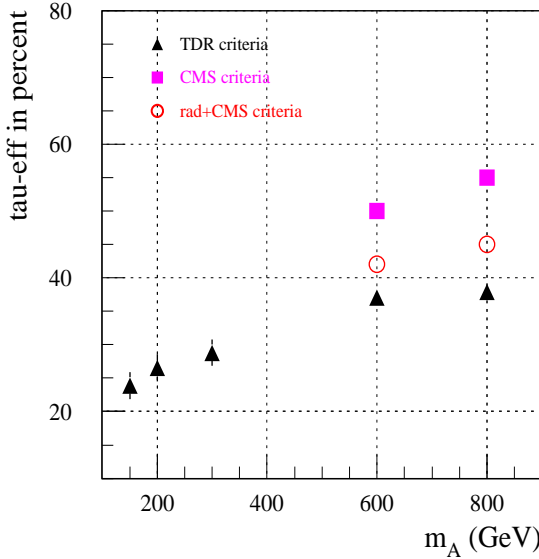


Fig. 6: Efficiency of the $\tau$-identification criteria for $\tau$'s from A $\to \tau\tau$ decays as a function of $m_A$.
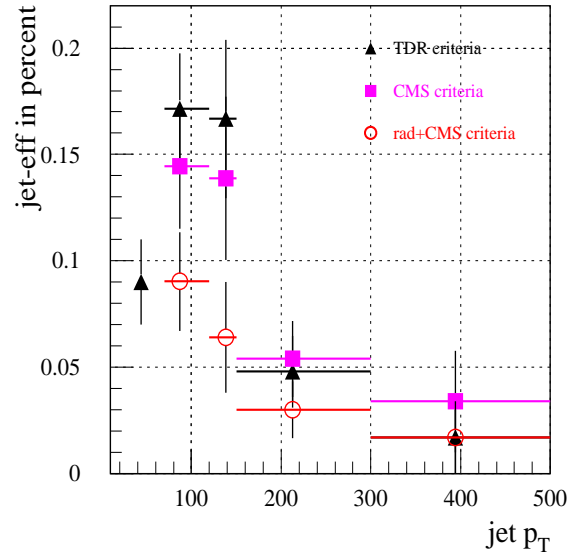
Fig. 7: Efficiency of the $\tau$-identification criteria in QCD jet events as a function of $p_T^{jet}$.

were optimized for the high $m_A$ and $p_T$(>150 GeV) [150] combining the Atlas TDR criteria and the criteria used by CMS in [162]. Asking for:
- $R_{em} < 0.12$
- CMS cuts

    - 1 isolated track with $p_T$>40 GeV within $\Delta R$<0.1 from the jet axis

    - track isolation: no other track with $p_T$>1 GeV in a cone of $\Delta R$=0.4

an $\epsilon_\tau \sim 45\%$ ($\epsilon_\tau \sim 55\%$ - only CMS criteria) for $\tau$'s from $m_A$=800 GeV can be achieved and the jet-rejection can be significantly improved to $\sim 3500$ ($\sim 2000$ - only CMS criteria) for QCD jets with $p_T$>150 GeV.

However, the jet-efficiencies are still determined with large errors: a larger statistics of fully simulated events containing jets is still needed to complete this study.

Moreover a very good $E_T^{miss}$-*resolution performance* for the reconstruction of the $\tau\tau$ mass is required for the $A \to \tau\tau$ channel study. Crucial for a good $p_T^{miss}$ resolution [153] are the calorimeter coverage until $|\eta|<5$, $p_x^{miss}$ and $p_y^{miss}$ have to be reconstructed from all calorimeters cells (in clusters and outside the clusters), a careful calorimeter calibration and intercalibration is necessary and finally a careful choice of electronic noise cutoff has to be made (only cells with $E_T > 1.5\sigma(noise)$ are kept).

In this way, the $p_T^{miss}$ resolution in ATLAS is found to be:

$$\sigma(p_T^{miss}) = 0.46 * \sqrt{\Sigma E_T}$$

where $\Sigma E_T$ is the total transverse energy in the calorimeters expressed in GeV.

This formula is valid at low luminosity and it takes into account both the coverage effect and the energy resolution. At high luminosity, there is a strong degradation of the $p_T^{miss}$ resolution (about a factor of 2 worse) due to the pile-up as described in the TDR [12].

The invariant mass of the $\tau$-pair in $A/H \to \tau\tau$ can be reconstructed in the collinear approximation that the directions of the two neutrino systems from each $\tau$-decay coincide with the ones of the measured $\tau$-decay products and under the condition that the $\tau$-decay products are not back-to-back:

$$m_{\tau\tau} = \sqrt{2(E_1 + E_{\nu_1})(E_2 + E_{\nu_2})(1 - cos\theta)}$$

where $E_1$, $E_2$ are the energies of the measured $\tau$-decay products, $E_{\nu_1}$, $E_{\nu_2}$ are the energies of the two neutrino systems and $\theta$ is the angle between the directions of the measured $\tau$-decay products. $E_{\nu_1}$ and $E_{\nu_2}$ are obtained by solving a system containing the two $p_T^{miss}$ components. The measurement uncertainties on $p_x^{miss}$, $p_y^{miss}$ combined with the assumption on the directions of the decay-products often result in unphysical negative solutions for the neutrino energies, in that case the $A$ mass cannot be reconstructed.

The mass resolution $\sigma(m_{\tau\tau})$ is proportional to $\sigma(p_T^{miss})/|sin(\Delta\phi(p_1p_2))|$, therefore both the $p_T^{miss}$ resolution and the $\Delta\phi$ separation between the charged $\tau$-decay products are important in the $\tau\tau$ mass reconstruction [154].

The reconstructed $m_{\tau\tau}$ resolution has been compared for the three different final states (after having applied a cut on the lepton $p_T > 24$ GeV and on the $\tau$-jet $p_T > 40$ GeV - the dependence of the mass resolution on the $p_T$ cutoffs is weak - and the cut $\Delta\phi < 165°$) (see Fig. 8) and it is found to
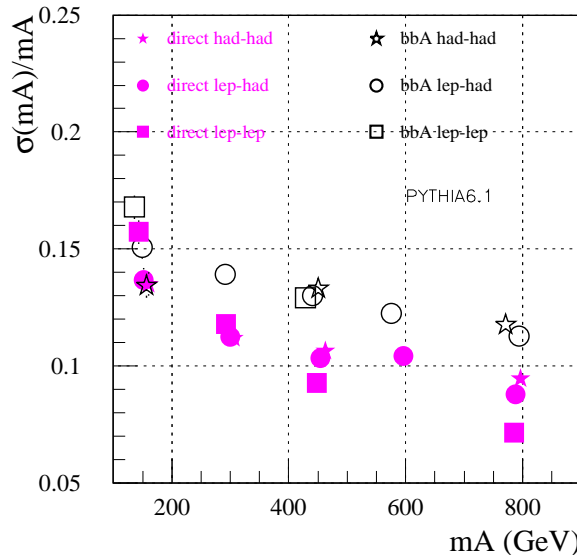


Fig. 8: Relative reconstructed $m_{\tau\tau}$ resolution as a function of A mass.

be comparable, as it is expected on the base of the $p_T^{miss}$ resolution, shown in Fig. 9, and the $\Sigma E_T$ in calorimeters, shown in Fig. 10.
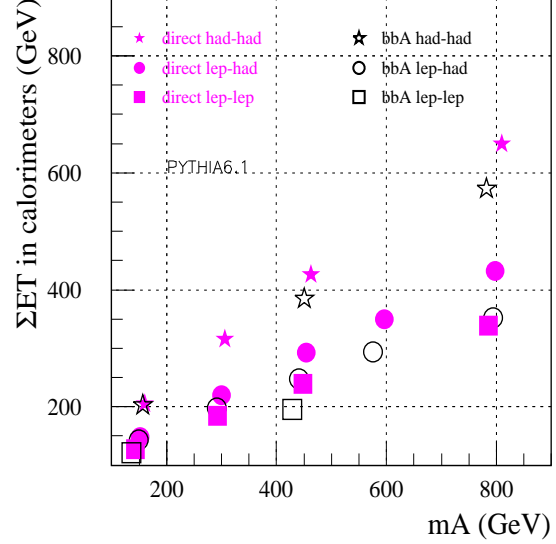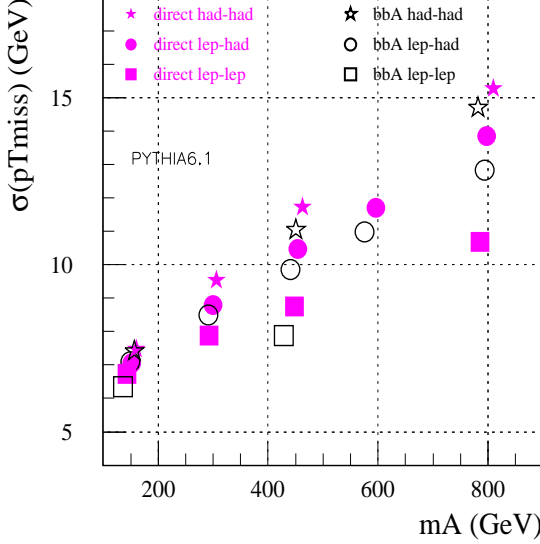


Fig. 9: $p_T^{miss}$ resolution in A events as a function of A mass.



Fig. 10: $\Sigma E_T$ in calorimeters in A events as a function of A mass.

The reconstructed mass resolution is systematically worse for the associated production events. In the associated production events in fact the average $p_T$ of the generated A is lower with respect to the direct A production and the difference increases with $m_A$ (see Fig. 5). This implies that in $b\overline{b}\,A$ events the two $\tau$'s from the $A$ tend to be more back to back, with two important consequences that are a lower acceptance of the $\Delta\phi$ cut and a final worse solution of the system giving the neutrino energies and consequently a lower efficiency in the mass reconstruction and a worse resolution. At $m_A$=450 GeV the relative $\sigma(m_{\tau\tau})$ is $\sim 10\%$ and $\sim 13\%$ respectively for direct and associated production with an overall efficiency of the $\Delta\phi$ cut and of the request of positive solutions for the neutrino energies of $\sim 30\%$ and $\sim 20\%$.

## 2.3   The lepton-hadron channel analysis in ATLAS

The irreducible backgrounds for this channel are $t\overline{t} \rightarrow bW^+\overline{b}W^- \rightarrow b\overline{b}\,lep\,\tau$ and $Z/\gamma^* \rightarrow \tau\tau$ , the reducible backgrounds are $t\overline{t} \rightarrow bW^+\overline{b}W^- \rightarrow b\overline{b}\,lep\,had$, $W \rightarrow lep$ +jets and $b\overline{b} \rightarrow lep\,had$.

The analysis criteria (*Standard A analysis*) are:
- $p_T^{lepton} > 24$ GeV (40 GeV for $m_A$>500 GeV) and $|\eta|^{lepton} < 2.5$;
- Isolation of the trigger lepton (which rejects leptons from $b\overline{b}$ by a factor 100 for a 90% efficiency for isolated leptons);
- $m_T(lepton - p_T^{miss}) < 25\ GeV$ (against the backgrounds containing W), where $m_T(lepton - p_T^{miss})$ is the transverse mass of the lepton-neutrino system;
- $p_T^{miss} > 18$ GeV (40 GeV for $m_A$>500 GeV);
- $E_T^{jet} > 40$ GeV (80 GeV for $m_A$>500 GeV), $|\eta|^{jet} < 2.5$       ($\tau$-Candidate);
- $\Delta\phi(jet - lepton)$ in $100° - 165°$;
- $m_{\tau\tau}$ in the window $m_A \pm \Delta M$ ($\Delta M = 1.5\sigma_{m_{\tau\tau}}$).

Each event is weighted using the $\tau$-jet identification factor for the $\tau$-jet candidate (see section 2.2).

Due to the topological and kinematical differences in the direct and associated events, two different analyses, one optimized for the direct production process, the other one optimized for the associated production are performed with the following criteria:
- *Direct analysis:*

• zero b-jet tagged (against $t\bar{t}$ and $b\bar{b}$ backgrounds);

• all cuts of the *Standard A analysis* ($\tau$-jet identification, kinematic and mass cuts).

- *Associated analysis:*

• 1 b-jet tagged (against $Z$ and W+jets backgrounds);

• number of non b-jets < 3 (against $t\bar{t}$ backgrounds);

• cuts of *Standard A analysis* ($\tau$-jet identification, kinematic and mass cuts) *except the cut on* $\Delta\phi(jet - lepton)$, to not reduce too much the signal acceptance.

To choose the b-jets, a b-tagging efficiency of 60%, with a corresponding rejection of 100 against other jets and of 10 against c-jets has been randomly applied.

The dominant background selected by the direct analysis arises from W+jets, which have the largest production cross-section and from the $Z \to \tau\tau$ at the lower masses. The analysis optimized for the associated production rejects much better W+jets and $Z \to \tau\tau$ backgrounds and the $t\bar{t}$ background becomes dominant.

Having the opposite request to have or not to have a b-jet tagged, the two analyses are not correlated, so, after having applied them separately to both signal samples (direct and associated A production) and to background events, the significances can be combined.

The results at lower masses have been compared to the results reported in the TDR and they have been found to be in reasonable agreement [150]. The differences observed are due to the different PYTHIA version, to the use of fast instead full simulation and to the use of different cross-sections values for signals and backgrounds.

At the higher masses ($m_A > 500$ GeV), the analysis is performed only on the events from the $b\bar{b}$ A production channel, due to the complete dominance of that production mode (see section 2.1).

Despite the low production cross-section and the low acceptances of the analysis ($\sim 0.5\%$ for $m_A$=800 GeV) the backgrounds are strongly reduced (the total background for $m_A$=800 GeV is $\sim$4.6 events, dominated by $t\bar{t}$ background, in 30 fb$^{-1}$).

Figure 11 shows the distribution of $m_{\tau\tau}$ after the analysis cuts (except the mass cut) for associated signal events at $m_A$=800 GeV for $tan\beta$=45 and for the main backgrounds normalized to the expected event number for an integrated luminosity of 30 fb$^{-1}$.
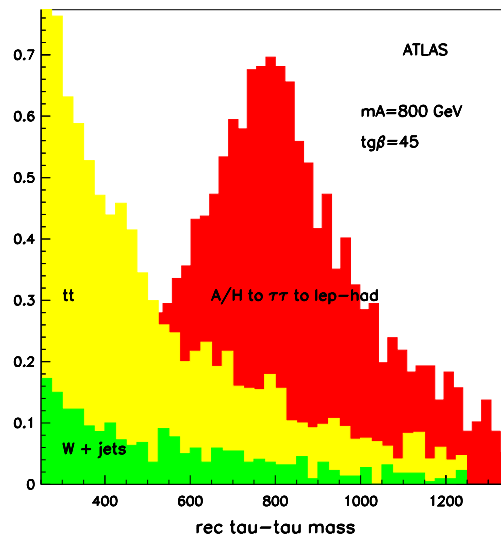


Fig. 11: Reconstructed $m_{\tau\tau}$ in the lepton-hadron channel after the analysis cuts for $m_A$=800 GeV for $tan\beta$=45 and for the $t\bar{t}$ and W+jets backgrounds (plotted separately) assuming an integrated luminosity of 30 fb$^{-1}$.

## 2.4 The hadron-hadron channel in ATLAS: trigger study and analysis

Due to the very low production cross-section of the $A/H$ especially in the higher mass region between 0.5 and 1 TeV, the trigger acceptance for the signal needs to be excellent; on the other hand, the signature of the signal with only hadronic decays is similar to QCD-background.

In the first level trigger, the total rate of Jet and $\tau$ triggers is dominated by 2-jet QCD-background, which has to be controlled by appropriately high settings of the $E_T$ thresholds for jet triggers [161]. However, these settings also reduce the acceptance of the trigger for the hadron/hadron channel of the $A/H$ decay. A high input acceptance of the trigger for A $\rightarrow \tau\tau \rightarrow$ hadron $-$ hadron signal events can be achieved by using combined Jet+$E_T^{miss}$ and $\tau$+$E_T^{miss}$ triggers.

The fast trigger simulation ATL1CT [158] [159] interfaced to the fast ATLAS simulation program has been used for the study. The following trigger types are of relevance for the hadron-hadron channel:

- Jet + $E_T^{miss}$ (Threshold: $E_T^{jet} >$ 50GeV, $E_T^{miss} >$ 50GeV)
- $\tau$ + $E_T^{miss}$ (Threshold: $E_T^{\tau} >$ 20GeV, $E_T^{miss} >$ 30GeV)
- Single Jet ($E_T^{jet} >$ 180GeV)
- Three Jet ($E_T^{jet} >$ 75GeV)
- Four Jet ($E_T^{jet} >$ 55GeV)

The threshold settings on the cluster $E_T$ of the jets and $\tau$'s are set to accept 90 % of the jets with the $E_T$ value given in the trigger menu, which is identified with the $E_T$ value in the reconstruction [159]. The isolation criteria of the $\tau$ trigger are set to fixed values of 2 GeV for the electromagnetic and 4 GeV for hadronic trigger towers [160].

The total acceptance in the Level-1 trigger is determined by the number of events accepted by at least one of the trigger types. This is equivalent to a logical *OR*. Many events are accepted by more than one trigger.

The input acceptance of the Level-1 trigger for signal events $m_{A/H} = 450, 600$ and $800$ GeV for the individual trigger types listed above and their combination (*OR*) are shown in Fig. 12. For $m_{A/H} = 800$ GeV, an input acceptance of 76.6 % is reached using fixed isolation thresholds in the $\tau$ trigger. Using an alternative scheme of a dynamic isolation in the $\tau$ trigger (electromagnetic trigger towers: 4 % of cluster energy, hadronic: 8 % of cluster energy), this value can be improved to 80.6 % [151]. The total trigger rate was evaluated being $\sim 1.4$ kHz, which fits well within the limitations of the Level-1 trigger menu [160].

The influence of the trigger acceptance on the discovery contour, however, is given by the combination of the trigger acceptance and the offline analysis, discussed after.

Since the associated production is dominant for high masses, the expected signal event signature of the hadron-hadron channel consists of two high-$p_T$ $\tau$'s in hadronic decay with two b-jets. Backgrounds for this channel are 2-jet QCD, $t\bar{t}$, W+jets and Z+jets events. The analysis uses event weighting, where the two jets with the highest $p_T$ are considered as '$\tau$ candidates', while b-tagging is used for all other jets, where one of the two expected b-jets is requested to be tagged. Using this method, background events are not rejected by the requests on the number of $\tau$'s and b-jets, but weighted accordingly, therefore background rate estimates can also be given for channels with extremely low acceptance, especially 2-jet background from QCD and also $t\bar{t}$. The $\tau$ identification described in Sec. 2.2 is used to derive the $\tau$ acceptance factors for each $\tau$ candidate. The $\tau$ identification is assumed to be $\epsilon_\tau = 55\%$ and the corresponding jet rejection is used for the other jets. The b-jet tagging efficiency is here assumed being $\epsilon_b = 70\%$.

The following cuts have been applied:

- Two jets in the event with $p_T > 100$ GeV and $|\eta| < 2.5$ ($\tau$ candidates);
- No lepton (e, $\mu$) with $p_T > 10$ GeV;
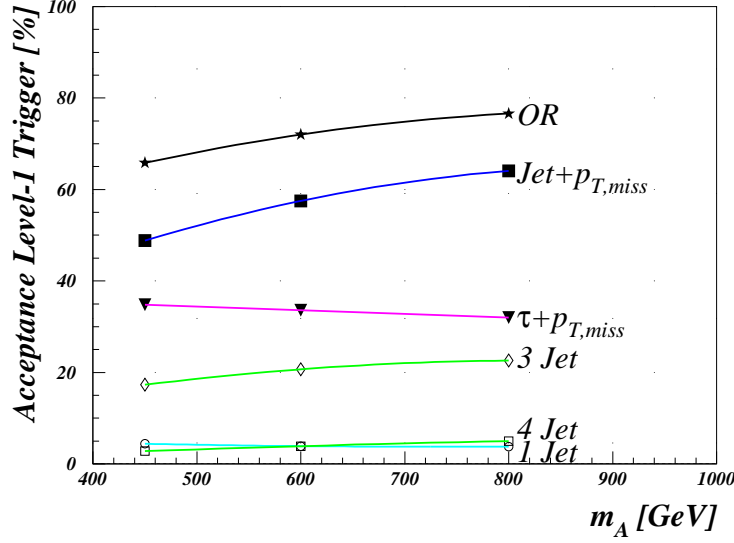- Not more than 4 jets in $|\eta| < 3.2$ with $p_T > 20$ GeV;
- at least one b-jet tagged ;

Fig. 12: Level-1 trigger input acceptance for Signal $m_{A/H}$ = 450, 600 and 800 GeV: total acceptance by all Jet and $\tau$-triggers (*OR*), and acceptances of each separate trigger.

- $p_T^{miss} > 65$ GeV;
- $\Delta\phi$ between $\tau$ candidates in $145° - 175°$;
- transverse mass cut: $m_T < 50$ GeV (minimum of $m_T(\tau_1, p_T^{miss})$ and $m_T(\tau_2, p_T^{miss})$);
- $m_{\tau\tau}$ in the window $m_A \pm \Delta M$ ($\Delta M = 1.5\sigma_{m_{\tau\tau}}$).

Some cuts lower the acceptance of signal events significantly, especially the $p_T^{miss}$ cut and b-tagging, however, those cuts are necessary to suppress the background channels efficiently. The acceptance of the analysis cuts for $m_A$=800 GeV is $\sim 0.6\%$ and the total background is $\sim 5.4$ events, with dominance of $t\bar{t}$ (2.2 events) followed by Z (0.8 events) and 2-jet QCD background in 30 fb$^{-1}$ [151].

Figure 13 shows the distribution of $m_{\tau\tau}$ after the cuts (except the mass cut) for the events at $m_A$=800 GeV for $tan\beta$=50 and for the main backgrounds normalized to the expected event number for an integrated luminosity of 30 fb$^{-1}$.

In Fig. 14 the reconstructed $m_{\tau\tau}$ is shown for $m_A$=600 GeV in the A $\rightarrow \tau\tau \rightarrow$ hadron $-$ hadron full simulated events, after the $p_T^{jet} > 50$ GeV and $\Delta\phi < 165°$ cutoffs.

The combined acceptance of the Level-1 trigger and offline analysis for the hadron-hadron channel have been studied. The acceptance after all cuts for events passing the trigger conditions are evaluated to be $92.5\%, 95.6\%$ and $95.3\%$ respectively for $m_A$=450, 600 and 800 GeV. Especially for high $m_A$, the acceptance is very good due to the similarity of the kinematic cuts used in the Level-1 trigger and offline analysis; both require large values of $E_T^{miss}$ and jets/$\tau$'s with high $p_T$.

## 2.5 Combinations of the lepton-hadron and the hadron-hadron channels in ATLAS

For higher mass values, the results from the lepton-hadron and from the hadron-hadron channels can be combined to improve the signal significance.

In Table 1, the discovery $tan\beta$ values (giving a $5\sigma$ significance) are reported for the two channels separately and combined. The extended discovery contour plot is given in Fig. 15 in the $tan\beta$ logarithmic scale and with a linear $tan\beta$ scale in Fig. 16.

## 3. CMS Results
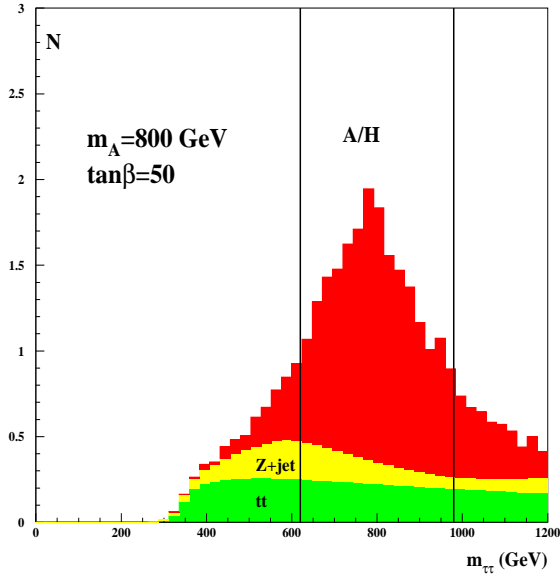
Fig. 13: Reconstructed $m_{\tau\tau}$ in the hadron-hadron channel after the analysis cuts for $m_A$=800 GeV for $tan\beta$=50 and for the $t\bar{t}$ and Z backgrounds assuming an integrated luminosity of 30 fb$^{-1}$.
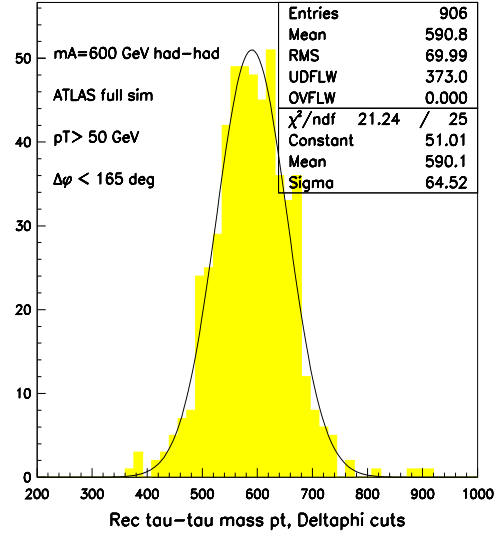


Fig. 14: Reconstructed $m_{\tau\tau}$ for signal events with $m_A$=600 GeV in the hadron-hadron channel in full ATLAS detector simulation.

Table 1: Discovery $tan\beta$ values in ATLAS ($5\sigma$ confidence).

| $m_A$ (GeV) | lepton-hadron | hadron-hadron | combined |
|---|---|---|---|
| 450 | 20.7 | 22.1 | 19.0 |
| 600 | 32.9 | 30.0 | 25.2 |
| 800 | 50.0 | 45.0 | 41.4 |
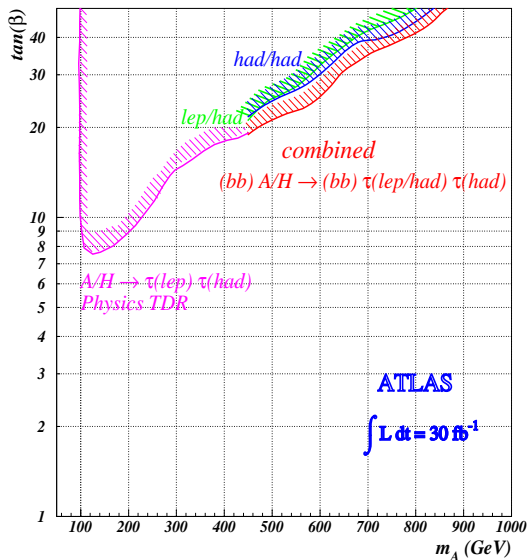


Fig. 15: Discovery contour curves for the A/H $\rightarrow \tau\tau$ channel in the ($m_A$,$tan\beta$) plane in ATLAS for an integrated luminosity of 30 fb$^{-1}$.
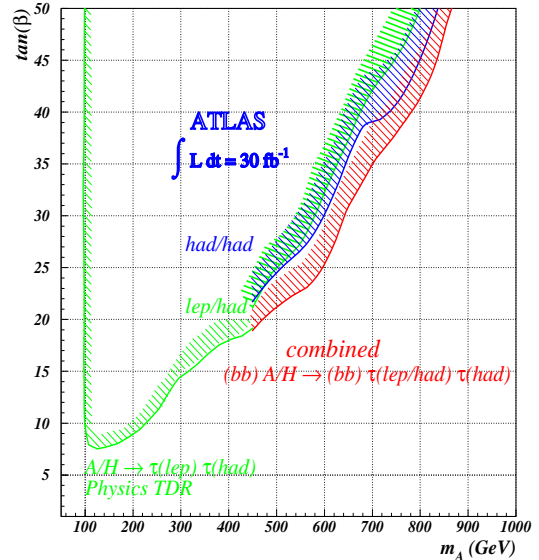


Fig. 16: Discovery contour curves for the A/H $\rightarrow \tau\tau$ channel in the ($m_A$,$tan\beta$) plane in ATLAS for an integrated luminosity of 30 fb$^{-1}$ shown using a linear scale for $tan\beta$.

Fig. 17: Efficiency of QCD background and Higgs signal at High Level trigger when the size of the pixel isolation cone is varied.

### 3.1 $A, H \to \tau\tau \to 2\,\tau\,jets$ in CMS

$A, H \to \tau\tau$ with $2\,\tau\,jet$ hadronic final states have been shown to extend significantly the SUSY Higgs discovery reach into the large mass (600 - 800 GeV) range [162]. To exploit fully the $2\,\tau\,jet$ final states - especially in the low ($\sim$ 200 GeV) mass range - an efficient hadronic $\tau$ trigger has been developed based on Level-1 calorimeter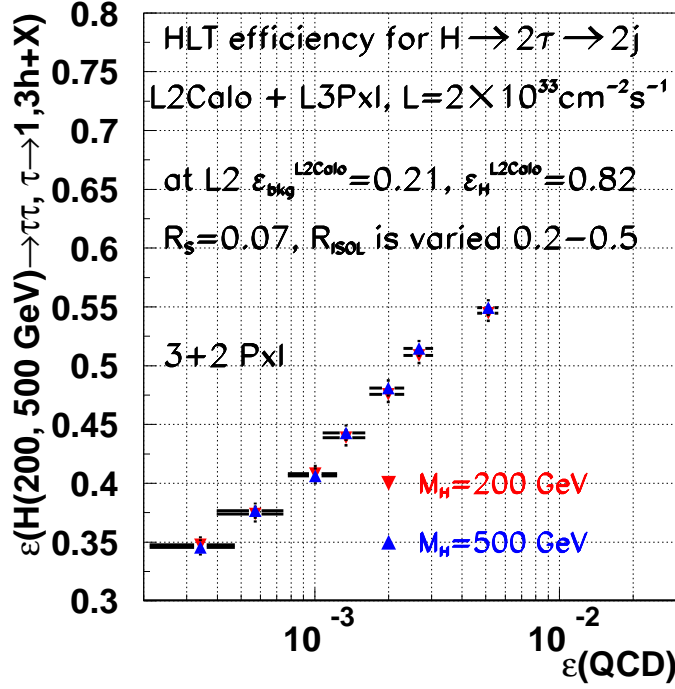 selection, Level-2 electromagnetic calorimeter isolation [163] and a Level-3 tracking (isolation) using only the pixel detector information [164].

Level-1 calorimeter single or double Tau trigger with thresholds of 80 and 65 GeV for $L = 2 \times 10^{33} cm^{-2} s^{-1}$ selects $A, H \to \tau\tau \to 2\tau$-jet events useful for off-line analysis with an efficiency of about 0.9 while giving an output QCD background rate of about 6 kHz. A further reduction of the QCD background rate by a factor $\sim 10^3$ is possible at the High Level trigger path (Level-2 calorimeter and Level-3 Pixels) with an efficiency of $\sim 40\%$ for the signal at $m_H = 200$ and 500 GeV [165] as one can see in Figure 17. Even better performance is expected using the regional tracking option of the CMS High Level trigger once the CPU performance is proven to be satisfactory.

For the off-line $\tau$ identification the tracker information is used. The fast simulation of the CMS detector [135] is used to study the signal to background ratios. The track reconstruction efficiency evaluated with full simulation of CMS tracker is included as a function of $p_t$ and $\eta$ for the track. The $\tau$ jet candidate ($E_t > 60$ GeV) is required to contain a hard ($p_t >40$ GeV) charged track within $\Delta R < 0.1$ around the calorimeter jet axis. Around this leading track in a cone of $\Delta R < 0.03$ two other tracks with $p_t > 1$ GeV are accepted to include the 3-prong $\tau$ decays. This narrow cone with one or three hard tracks is required to be isolated demanding that no track with $p_t > 1$ GeV is found in the surrounding larger cone of $\Delta R < 0.4$. The efficiency for this $\tau$ selection is 7.2% for $m_A = 200$ GeV and 34% for $m_A = 500$ GeV. Accepting the 3-prong decays in the narrow cone of $\Delta R < 0.03$ increases the event rate for $A, H \to \tau\tau \to 2\,\tau\,jets$ in the high mass range ($m_A = 500$ GeV) by $\sim 1.7$ but also degrade significantly the QCD rejection factor for hard QCD jets. Figure 18 shows the rejection factor against the QCD jets for the 1/3 prong selection a function of $E_t$ jet compared to the one prong selection with one hard ($p_t >40$ GeV) charged track within $\Delta R(jet, track) < 0.1$. Optimization is still needed for the low mass range

for more efficient selection mainly by increasing the size of the narrow cone.

A further suppression can be obtained exploiting the $\tau$ lifetime using a $\tau$ vertex reconstruction or impact parameter measurement or a combination of them. A full simulation study indicates that an additional rejection factor of $\sim 5$ against the 3-prong QCD jets and an efficiency of $\sim 70\%$ for the $\tau$ jets can be obtained with $\tau$ vertex reconstruction [167]. Promising results are also obtained from the impact parameter method in the channel $A, H \to \tau\tau \to \ell^+\ell^- + X$ using full simulation combining the impact parameter measurements for the two leptons from $\tau$ decays to reduce the backgrounds with $W \to \ell\nu$ and $Z \to \ell\ell$ decays [166].
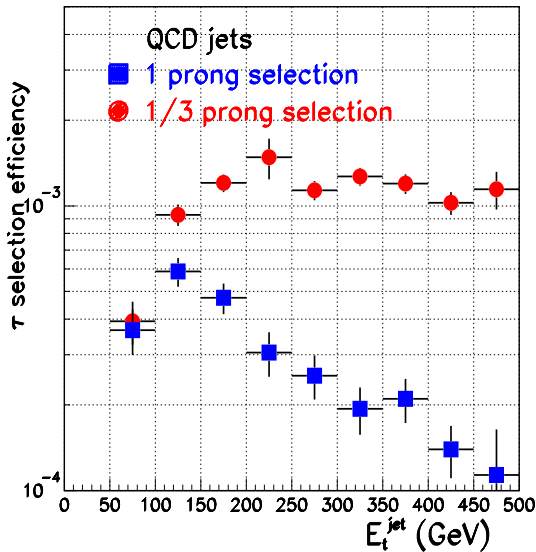


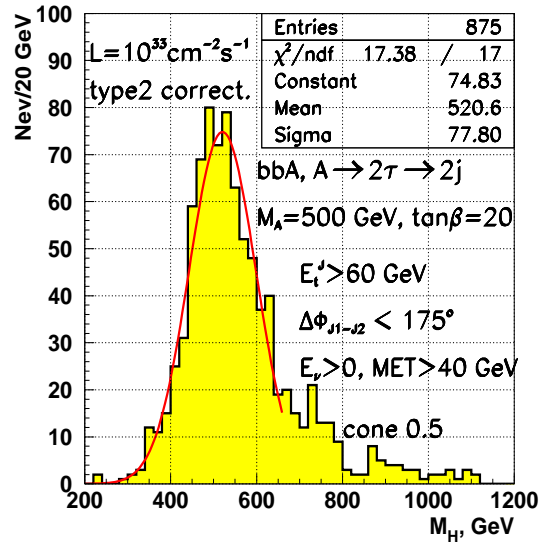Fig. 18: Rejection factor against the QCD jets as a function of $E_t^{jet}$ for the 1 and 1/3 prong $\tau$ selection.

Fig. 19: Reconstructed Higgs mass for $b\bar{b}$, $H \to \tau\tau \to 2\,\tau\,jets$ with $m_H = 500$ GeV.

The resolution of the reconstructed Higgs mass and even more so the mass reconstruction efficiency in $A, H \to \tau\tau$ events is very sensitive to the $E_t^{miss}$ measurement. The absolute value of $E_t^{miss}$ is relatively small in these events making the mass reconstruction and background reduction with a cut in $E_t^{miss}$ a difficult task. Figure 19 shows the Higgs mass reconstructed with full simulation for $b\bar{b}A$, $A \to \tau\tau \to 2\,\tau\,jets$ with $m_A = 500$ GeV and $tan\beta = 20$ [168]. The resolution of the reconstructed Higgs mass is 14.5% for $m_A = 200$ GeV and 14.9% for $m_A = 500$ GeV and the corresponding reconstruction efficiencies are 37% and 36%, respectively (including $\Delta\phi < 175°$ cut and requiring positive neutrino energies). This confirms the earlier results of the fast simulation study [162].

The large $Z, \gamma^* \to \tau\tau$ background can be reduced efficiently only with b-tagging in the associated production processes $b\bar{b}H_{SUSY}$. The associated b-jets are soft and uniformly distributed over $|\eta| < 2.5$. Nevertheless, a study with full simulation shows that a b-tagging efficiency of $\sim 34\%$ per jet can be obtained for the signal events with a mistagging rate less than 1% for $Z + jets$ events [166]. Requiring one tagged b-jet reduces efficiently also the QCD background thus improving significantly the signal visibility. Figure 20 shows the signal for $m_H = 500$ GeV and $tan\beta = 25$ superimposed on the total background with b-tagging. The missing transverse energy $E_t^{miss}$ plays a major role in the Higgs mass reconstruction as discussed above. However, a cut in $E_t^{miss}$ does not improve significantly the mass resolution and therefore, in order to retain the signal statistics, is not used in this study. Figure 21 shows the expected discovery reach for for 30 $fb^{-1}$ assuming a maximal stop mixing scenario [70, 79]. The expectations for other important MSSM Higgs discovery channels in CMS [170] and the exclusion region from LEPII [4] are also shown in the figure. The $A, H \to \tau\tau$ channels are found to be insensitive for stop mixing, the SUSY scale and for the sign of the Higgsino mass parameter $\mu$ for high enough $tan\beta$ ($\gtrsim 10$). A systematic study of the $A, H \to \tau\tau$ with $\ell^+\ell^-$, $lepton + \tau\,jet$ and $2\,\tau\,jet$ final states is presently in progress in CMS including full simulation of the hadronic $\tau$ trigger, $\tau$ identification, $\tau$

tagging with impact parameter and vertex reconstruction, Higgs mass reconstruction and b-tagging in the associated production channels.
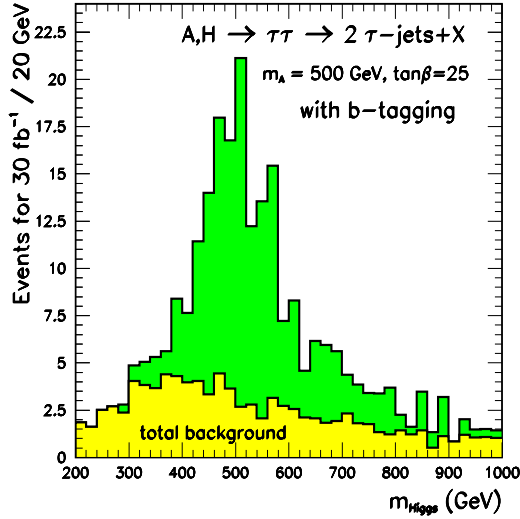


Fig. 20: Higgs mass for $H \to \tau\tau \to 2\,\tau\,jets$ with $m_H$ = 500 GeV and $tan\beta$=25 superimposed on the total background for 30 $fb^{-1}$. One tagged b-jet is required.
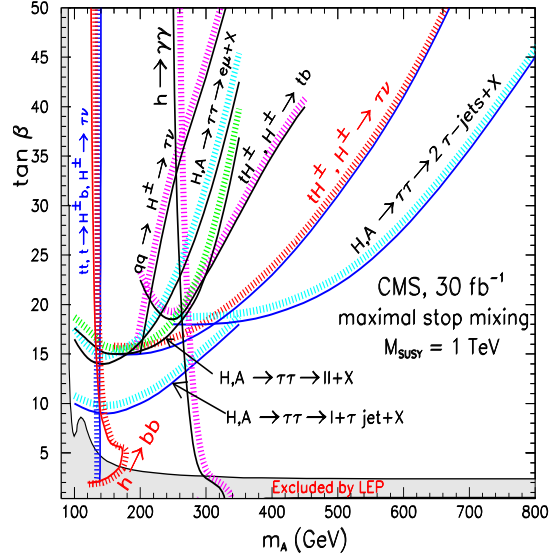


Fig. 21: Expected $5\sigma$ discovery reach for the MSSM Higgs bosons in CMS in the maximal mixing scenario for $30\,fb^{-1}$ as a function of $m_A$ and $tan\beta$. The shaded area is excluded by LEP [4].

## 4. Conclusions

The LHC discovery potential for A/H $\to \tau\tau$ has been studied in ATLAS and CMS in the three different final decay channels at low luminosity ($10^{33}$ cm$^{-2}$s$^{-1}$) in the $m_A$ range from ∼100 GeV until ∼1 TeV.

- at lower masses ($<$∼500 GeV), the lepton-lepton and lepton-hadron channels have been studied in both experiments; the lepton-hadron gives the best sensitivity. To study the hadron-hadron channel also in the lower mass range, CMS is developing an efficient hadronic $\tau$ trigger (Level-1 + High Level trigger).

- at higher masses, for large $tan\beta$ values the $A$ production is dominated by $b\bar{b}$ A. In this mass range the hadron-hadron channel can be studied because it is possible to reject the huge QCD background with kinematical cuts and $\tau$-jet identification. The trigger is a very important point for this purely hadronic channel and it has been studied in the two experiments. The lepton-hadron channel has been also studied in ATLAS in the high $m_A$ region giving promising results; the combination of the hadron-hadron and lepton-hadron channels improves the discovery potential.

The expected $5\sigma$-discovery contour curves for the combined $A/H \to \tau\tau$ signal show that a signal should be observed over a large region of the ($m_A$,$tan\beta$) plane, with $m_A$ up to ∼ 1 TeV assuming an integrated luminosity of 30 fb$^{-1}$.

At high $m_A$ (∼0.5-∼1 TeV) the $A/H \to \tau\tau$ channel should be observable for $tan\beta$ values greater than ∼ 25. This is an important result because the $A/H \to \tau\tau$ channel is up to now the only one giving access to this high $m_A$ region.

Studies are still in progress, both on the experimental and on the theoretical sides, to improve the results presented here.

### Acknowledgments

# F. Searching for Higgs Bosons in $t\bar{t}H$ Production

*V. Drollinger*

### Abstract

Higgs boson production in association with $t\bar{t}$ pairs with the subsequent decay into $l^{\pm}\nu q\bar{q}b\bar{b}b\bar{b}$ is analyzed including all relevant background processes. Excellent $b$-tagging performance and a good mass resolution turn out to be the most important components for a successful analysis. The top Yukawa coupling can be determined with an accuracy of about 17% in this process, provided the branching ratio of $H \rightarrow b\bar{b}$ is known with a sufficient accuracy. Finally, a first estimate of the potential size of higher order corrections to the $t\bar{t}b\bar{b}$ background is given.

## 1. Introduction

If the Higgs boson is lighter than $130\,GeV/c^2$, it decays mainly to a $b\bar{b}$ pair. To observe the Higgs boson at the LHC, the $t\bar{t}H^0$ channel turns out to be the most promising channel among the Higgs production channels with $H^0 \rightarrow b\bar{b}$ decay [171]. In this study, we discuss the channel $t\bar{t}H^0 \rightarrow l^{\pm}\nu q\bar{q}b\bar{b}b\bar{b}$ (Figure 1), where the Higgs Boson decays to $b\bar{b}$, one top quark decays hadronically and the second one leptonically. The relevant signal and background cross sections at the LHC ($\sqrt{s_{pp}} = 14\,TeV$) and particle masses used in the simulation are listed in Table 1.. This is the first set of signal and background processes

Table 1: *CompHEP [92] cross sections for signal and background relevant for the $t\bar{t}H^0 \rightarrow l^{\pm}\nu q\bar{q}b\bar{b}b\bar{b}$ channel, calculated with parton density function CTEQ4l [172]. The branching ratio of the semileptonic decay mode (one $W^{\pm}$ decays to quarks the other $W^{\pm}$ decays leptonically, where only decays to electrons or muons are taken into account) is 29% (not included in the cross sections of this table) and $m_{W^{\pm}} = 80.3427\,GeV/c^2$.*

| LO cross sections | | | masses | | |
|---|---|---|---|---|---|
| $\sigma_{t\bar{t}H^0} \times BR_{H^0 \rightarrow b\bar{b}}$ | $=$ | 1.09 - 0.32 $pb$ | $m_{H^0}$ | $=$ | 100 - 130 $GeV/c^2$ |
| $\sigma_{t\bar{t}Z^0}$ | $=$ | 0.65 $pb$ | $m_{Z^0}$ | $=$ | 91.187 $GeV/c^2$ |
| $\sigma_{t\bar{t}b\bar{b}}$ | $=$ | 3.28 $pb$ | $m_b$ | $=$ | 4.62 $GeV/c^2$ |
| $\sigma_{t\bar{t}jj}$ | $=$ | 507 $pb$ | $m_t$ | $=$ | 175 $GeV/c^2$ |

completely calculated at LO for the $t\bar{t}H^0$ channel. The hard processes are generated with CompHEP and then interfaced to PYTHIA, where the fragmentation and hadronisation are performed [92]- [100]. The combined package CompHEP-interface-PYTHIA includes all features of a pure PYTHIA simulation, such as initial sate radiation, final state radiation, multiple interactions and underlying event. After the final state has been obtained, the CMS detector response is simulated, with track and jet reconstruction with parametrisations FATSIM [175] and CMSJET [135], obtaining in this way tracks, jets, leptons (the electron or muon reconstruction efficiency is assumed to be 90%; taus are not considered here) and missing transverse energy. These parametrisations have been obtained from detailed simulations based on GEANT.

## 2. Reconstruction

From Figure 1 we expect to find events with one isolated lepton, missing transverse energy $E_T^m$ and six jets (four $b$-jets and two non-$b$-jets), but initial and final state radiation are sources of additional jets. So the number of jets per event is typically higher than six. On the other hand, not all six quarks of the hard process can be always recognised as individual jets in the detector, in which case it is impossible to reconstruct the event correctly - even if there are six or more jets.
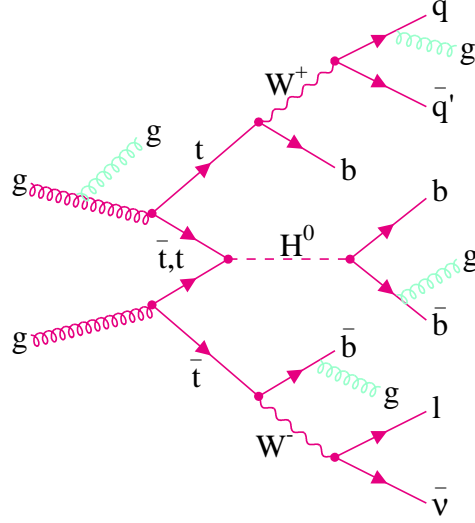
Fig. 1: *Example of a $pp \to t\bar{t}H^0 \to l^{\pm}\nu q\bar{q}b\bar{b}b\bar{b}$ signal event. The LO process is drawn in red. HO events include gluon radiation (light green) in addition. The expected final state consists of one isolated lepton, missing transverse energy, four b-jets and two (or more) non-b-jets.*

For the reconstruction of resonances it is necessary to assign the $n$ jets of an event to the corresponding quarks of the hard process. In general, and ignoring information on $b$-jets, the number of possible combinations $N$ is given in Table 2 as a function of the number of jets per event. We obtain $N$ for the case, when the masses of the Higgs boson, both top quarks and the hadronically decaying W boson are reconstructed. The nominal mass of the leptonically decaying W boson, together with $E_T^m$ and the lepton four momentum, is used to calculate two solutions of the longitudinal momentum of the neutrino $p_Z(\nu)$ which is needed for the mass reconstruction of the leptonically decaying top.

Table 2: *Number of jets per event $n$ and the corresponding number of possible combinations $N$. If there are more than a dozen jets, only the twelve with highest $E_T$ are considered.*

| $N = \binom{n}{6} \times 6! \times \frac{1}{2} \times \frac{1}{2} \times 2 \ = \binom{n}{6} \times 360$ | | | | | | |
|---|---|---|---|---|---|---|
| $n \ =$ | 6 | 7 | 8 | 9 | 10 | 11 | 12 |
| $N \ =$ | 360 | 2520 | 10080 | 30240 | 75600 | 166320 | 332640 |

Good mass resolution and the identification of $b$-jets is essential to reduce the number of wrong combinations in the event reconstruction. A good mass resolution can be obtained when the energy and direction of each reconstructed jet agree as closely as possible with the quantities of the corresponding parent quark. This can be achieved with jet corrections as described in [176] and [177]. For $b$-tagging we use the $b$-probability functions which depend on impact parameters of tracks and leptons inside the jets. They are determined using $t\bar{t}$ six jet events, as described in [171]. The identification of $b$-jets is even more important for efficient background suppression.

Figure 2 shows the invariant mass distributions of the reconstructed resonances of $t\bar{t}H^0 \to l^{\pm}\nu q\bar{q}b\bar{b}b\bar{b}$ events in the case of an ideal reconstruction: after the "preselection" and the calculation of $p_Z(\nu)$ (see later on) each quark of the hard process is matched with exactly one jet, the closest one in $R = \sqrt{\phi^2 + \eta^2}$ if $\Delta R(q,j) < 0.3$ and if the jet energy is closer than $\pm\,30\,\%$ to the parent quark energy. The mean values and widths of the top and W mass distributions are used to define likelihood functions used in the selection procedure described in the following.

### ◇ **Preselection**

Events are selected if there is an isolated lepton ($e^{\pm}$ or $\mu^{\pm}$ with $p_T > 10\ GeV/c$ within the tracker acceptance; no other track with $p_T > 1\ GeV/c$ in a cone of 0.2 around the lepton) and at least six jets ($E_T > 20\ GeV$, $|\eta| < 2.5$).

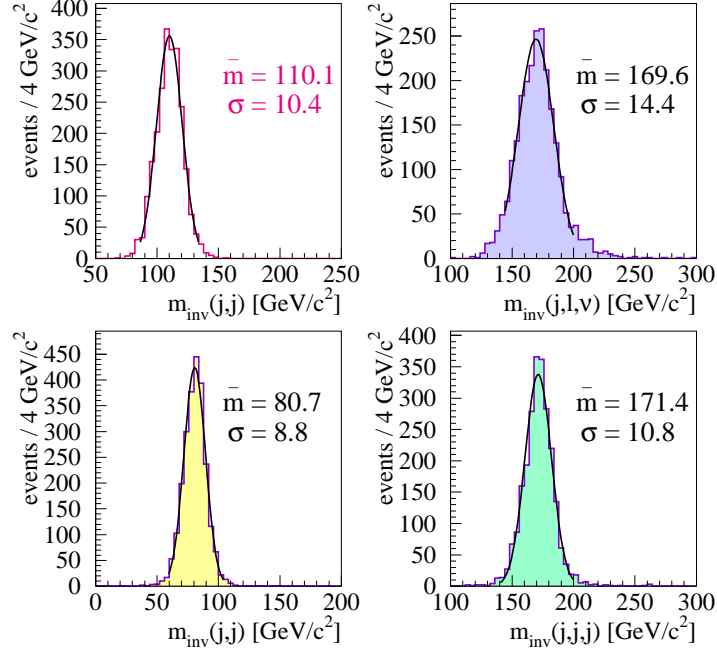Fig. 2: *Invariant resonance masses of the $t\bar{t}H^0 \to l^{\pm}\nu q\bar{q}b\bar{b}b\bar{b}$ signal: Higgs boson, leptonic top, hadronic top and hadronic $W^{\pm}$. The leptonic $W^{\pm}$ is not reconstructed but its nominal mass is used to calculate $p_Z(\nu)$. The generated masses are: $m_{H^0} = 115 \, GeV/c^2$, $m_t = 175 \, GeV/c^2$ and $m_{W^{\pm}} = 80.3427 \, GeV/c^2$.*

◇ **Event Configuration**

In order to be able to reconstruct the Higgs mass, we have to find the correct event configuration among all possible combinations listed in Table 2. The best configuration is defined as the one which gives the highest value of an event likelihood function (1) which takes into account $b$-tagging of four jets, anti-$b$-tagging of the two jets supposed to come from the hadronic $W^{\pm}$, mass reconstruction of $W^{\pm}$ and the two top quarks, and sorting of the $b$-jet energies.

$$\mathbf{L\_EVNT} = \prod_{i=1,4} P_b(b_i) \times \prod_{i=1,2} [1 - P_b(q_i)] \times \prod_{i=W^{\pm},t,\bar{t}} e^{-0.5 \times [\frac{m_i - \bar{m_i}}{\sigma_i}]^2} \times f[E_b(t,\bar{t}) - E_b(H^0)] \quad (1)$$

◇ **Jet Combinations**

Events with more than six jets can contain gluon jets from final state radiation, which are not yet used in the analysis. The combination of these jets with the correct quark jets can improve the event reconstruction further. The additional jets are combined with the decay products of both top quarks if they are closer than $\Delta R(j,j) < 1.7$, if the corresponding mass is closer to the expected value of Figure 2. If there are still jets left, they are considered as Higgs decay products and are combined with the closest of the corresponding two $b$-jets, if $\Delta R(j,j) < 0.4$.

◇ **Event Selection**

Three likelihood functions: for resonances ($L\_RESO > 0.05$), $b$-tagging ($L\_BTAG > 0.50$), and kinematics ($L\_KINE > 0.2$) are used to reduce the fraction of background events. Finally, the events are counted in a mass window around the expected Higgs mass peak ($m_{inv}(j,j)$ in $\bar{m} \pm 1.9 \, \sigma$ ; $\bar{m}$ and $\sigma$ are obtained from mass distributions as shown in Figure 2 with various generated Higgs masses).

The overall efficiency for a triggered event to be finally selected is 1.3% for $t\bar{t}H^0$ ($m_{H^0} = 115$ $GeV/c^2$), 0.2% for $t\bar{t}Z^0$, 0.4% for $t\bar{t}b\bar{b}$ and 0.003% for $t\bar{t}jj$ events. This shows that the reducible background is reduced very effectively. In addition, there is little combinatorial background left (see Figure 3) with this reconstruction method.
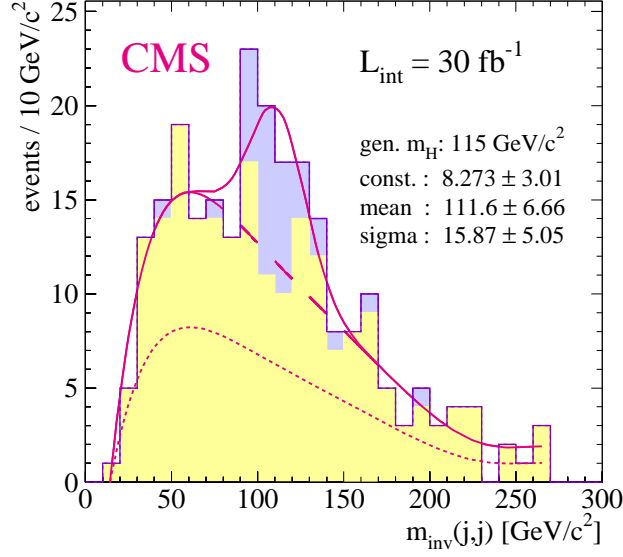
Fig. 3: *Simulated invariant mass distribution of signal (dark shaded, $m_{H^0} = 115\ GeV/c^2$) plus background for $L_{int} = 30$ $fb^{-1}$. The dashed curve is obtained from the fit of the background without signal, the solid line describes the fit of signal plus background. The small dashed line corresponds to the LO background contribution.*

## 3. SM Results

After the whole reconstruction and event selection procedure, it turns out that the irreducible background (with four real $b$-jets) is dominant. Even the $t\bar{t}jj$ background, where only two $b$-jets from the top decays are generated in the hard process, is dominated by events with four real $b$-jets. This is possible after the fragmentation of PYTHIA: e.g. $gg \to t\bar{t}gg \to l^{\pm}\nu q\bar{q}b\bar{b}gb\bar{b}$ with one $b\bar{b}$ pair coming from $g \to b\bar{b}$ (gluon splitting). In this case the final state consists of nine partons or leptons which is one more than expected at LO and is therefore considered as HO (in this case NLO) process. Together with the number of $t\bar{t}b\bar{b}$ events (considered as LO) we obtain an intrinsic k-factor $k_{t\bar{t}q\bar{q}} = 1.9$ for all $t\bar{t}q\bar{q}$ events as indicated in Figure 3. (For the full $m_{H^0} = 115\ GeV/c^2$ selection we get 23 events from "$t\bar{t}b\bar{b}$" and 20 events from "$t\bar{t}jj$" with four real $b$-jets plus 6 events with two real and two false $b$-tags. The total number for the non resonant background amounts to 49 events, whereas the corresponding number from the PYTHIA $t\bar{t}$ process with additional jets from fragmentation is only 24 events.) In case of the $t\bar{t}H^0$ signal additional $b$-jets from fragmentation cannot enhance the signal, but rather complicate the reconstruction of the correct invariant mass, the Higgs mass, in the end.

The signal to background ratio $S/B$, the significance $S/\sqrt{B}$ for $L_{int} = 30\ fb^{-1}$, the integrated luminosity $L_{int}$ required for a significance of five or more and the precision on the top Higgs Yukawa coupling $y_t$ for $L_{int} = 30\ fb^{-1}$ are shown in Figure 4 as a function of the generated Higgs mass: $S/B$ is around 50% and an relatively low integrated luminosity is sufficient to discover the Higgs boson in this channel with a significance above five. An integrated luminosity $L_{int} = 100\ fb^{-1}$ would be enough to explore all points considered in Figure 4 up to a Higgs mass of $130\ GeV/c^2$. If we assume a known branching fraction of the decay $H^0 \to b\bar{b}$, it is possible to determine the precision of $y_t$ with accuracy of about 17%. Apart from these results, the Higgs mass can be determined from the Gaussian fit of the final mass distribution (see Figure 3) with a precision of better than 6% for $L_{int} = 30\ fb^{-1}$.

## 4. Conclusions

From our present understanding, it is experimentally possible to observe the $t\bar{t}H^0 \to l^{\pm}\nu q\bar{q}b\bar{b}b\bar{b}$ channel. Most important for a successful analysis are excellent $b$-tagging performance and a good mass resolution. The effects of event pile up still have to be investigated.

From theoretical point of view, the first complete LO simulation has been performed for signal and
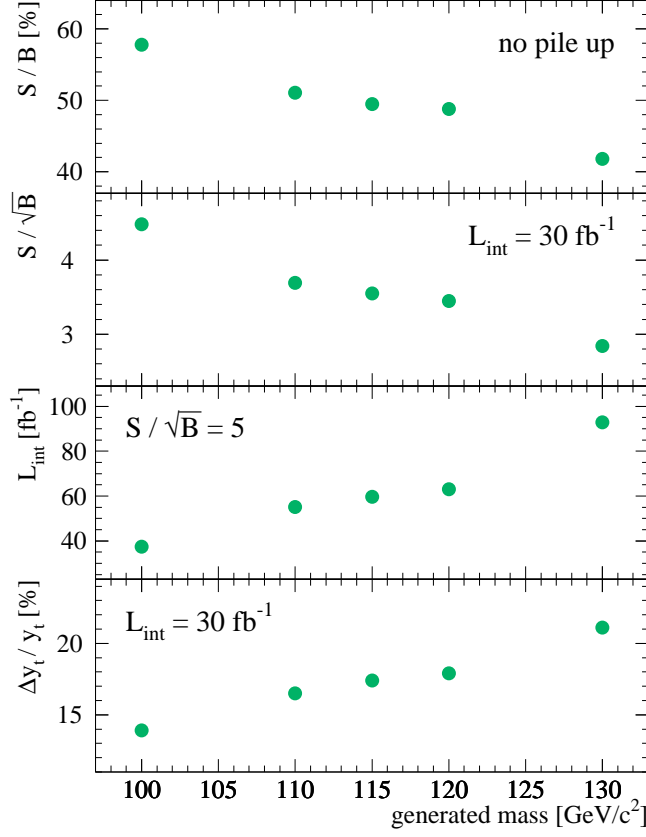
Fig. 4: $S/B$, $S/\sqrt{B}$, $L_{int}$ (required for $S/\sqrt{B} = 5$) and $\Delta y_t/y_t$ versus generated Higgs mass in the SM. All results are based on CompHEP cross sections calculated at LO; from the fragmentation with PYTHIA an intrinsic k-factor $k_{t\bar{t}q\bar{q}} = 1.9$ for $t\bar{t}q\bar{q}$ background events is included.

background. After the K-factor for the signal has been calculated (see Ref. [51]), the main uncertainty in this channel is background cross section at HO, because our first estimate gives a factor of almost two.

### Acknowledgments

## A  Comparison of $t\bar{t}b\bar{b}$ Events

Table 3: CompHEP (ISR and FSR included) PYTHIA (default) comparison of $t\bar{t}b\bar{b}$ background: the cross sections do not include any branching fractions (all decays are allowed). All four $b$-quarks are required to be within $|\eta| < 2.5$ and additional the $b$-quarks of the top decays have to satisfy $p_T(b_{top}) > 15\ GeV/c$. The $p_T(b_{glu})$ cut for both $b$-quarks not coming from the top decay is varied.

| $p_T$ Cuts | CompHEP | PYTHIA | CompHEP / PYTHIA |
|---|---|---|---|
| $p_T(b_{glu}) > 15\ GeV/c$ | $\sigma = 2407\ fb$ | $\sigma = 2927\ fb$ | 0.82 |
| $p_T(b_{glu}) > 30\ GeV/c$ | $\sigma = 1123\ fb$ | $\sigma = 1189\ fb$ | 0.94 |
| $p_T(b_{glu}) > 50\ GeV/c$ | $\sigma = 512\ fb$ | $\sigma = 431\ fb$ | 1.19 |
| $p_T(b_{glu}) > 100\ GeV/c$ | $\sigma = 116\ fb$ | $\sigma = 53\ fb$ | 2.19 |
| $p_T(b_{glu}) > 200\ GeV/c$ | $\sigma = 13\ fb$ | $\sigma = 2\ fb$ | 6.73 |
| $p_T(b_{glu}) > 300\ GeV/c$ | $\sigma = 3\ fb$ | $\sigma = 0\ fb$ | —- |

# G. Studies of Charged Higgs Boson Signals for the Tevatron and the LHC

*K.A. Assamagan, M. Bisset, Y. Coadou, A.K. Datta, A. Deandrea, A. Djouadi, M. Guchait, Y. Mambrini, F. Moortgat and S. Moretti*

**Abstract**

Two Higgs doublet models are a viable extension to the Standard Model (SM) and can be incorporated into supersymmetry (SUSY). In such models, electroweak symmetry breaking leads to five Higgs particles, three neutral and a charged pair. We discuss various analyzes of the charged Higgs boson, carried out in the context of the Minimal Supersymmetric extension of the Standard Model (MSSM) and also in models with singlet neutrinos in large extra dimensions. Specific studies for the Large Hadron Collider (LHC) and the Tevatron are presented.

## 1. Introduction

The Higgs sector of the MSSM contains five physical states, two of which are charged, $H^{\pm}$, and the other three are neutral ($h^0$, $H^0$, and $A^0$) [2,178]. Searches for the charged Higgs boson have been carried out at LEP and at the Tevatron: at LEP 2, a lower bound of 78.6 GeV has been set on the charged Higgs boson mass independent of the $H^{\pm} \to \tau^{\pm}\nu_{\tau}$ branching ratio (BR) [179]. At the Tevatron, CDF and DØ performed direct and indirect searches for the charged Higgs boson, and excluded the low and high $\tan\beta$ regions up to $\sim 160$ GeV [180].

The sensitivity of the ATLAS and CMS detectors at the LHC to the discovery of the charged Higgs boson has been investigated in detail [11, 12]. Some of these studies have been carried out as particle-level event generation in PYTHIA, HERWIG and ISAJET [100,181,182], at $\sqrt{s} = 14$ TeV, with the detector resolutions and efficiencies parameterized in ATLFAST [138] and in CMSJET [135] from the full detector simulations. Some of the LHC studies assume that the mass scale of supersymmetric partners of ordinary matter is above the charged Higgs boson mass so that charged Higgs boson decays into supersymmetric partners are forbidden. The main production processes considered in these studies are the gluon fusion mechanism, $gg \to tbH^{\pm}$ and the $2 \to 2$ process $gb \to tH^{\pm}$ shown in Figure 1. A central value of 175 GeV is used for the top-quark mass. The decay channel $H^{\pm} \to \tau^{\pm}\nu_{\tau}$ has been stud-
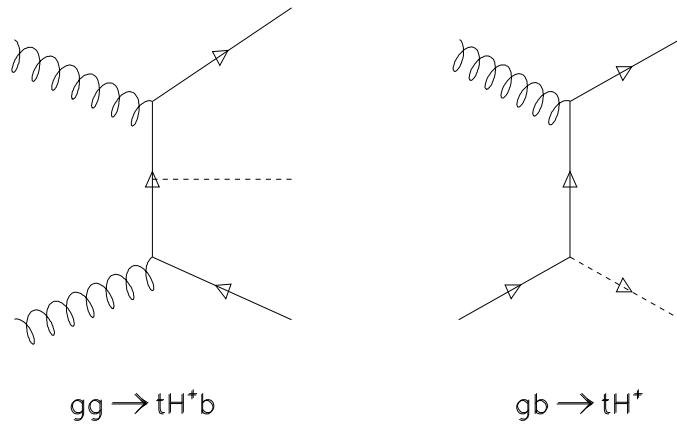


$$gg \to tH^+b \qquad\qquad gb \to tH^+$$

Fig. 1: The charged Higgs boson production at the LHC through the $2 \to 3$ process, $gg \to tbH^{\pm}$ and the $2 \to 2$ process, $gb \to tH^{\pm}$. The inclusive cross section is the sum of both contributions after the subtraction of the common terms.

ied extensively for ATLAS for $m_{H^\pm} < m_t$, and the signal appears as an excess of $\tau$ leptons [183]. The channel $H^\pm \to W h^0$ is only relevant in a tiny range of MSSM parameter space although it constitutes a unique test for MSSM and may be sensitive to the singlet extension to MSSM, i.e., NMSSM [184, 185]. $H^\pm \to tb$ and $H^\pm \to \tau^\pm \nu_\tau$ are the dominant decay channels of the charged Higgs boson in most of the parameter space. In the $H^\pm \to tb$ channel, upwards of 5-$\sigma$ discovery can be achieved above the top-quark mass in the low and high $\tan \beta$ regions up to $\sim$400 GeV [186]. $H^\pm \to \tau^\pm \nu_\tau$ extends the discovery reach to high Higgs boson masses and to lower $\tan \beta$ values in the high $\tan \beta$ region as seen in Figure 2. However, in the low $\tan \beta$ region, the $\tau^\pm \nu_\tau$ channel offers no sensitivity for the charged Higgs
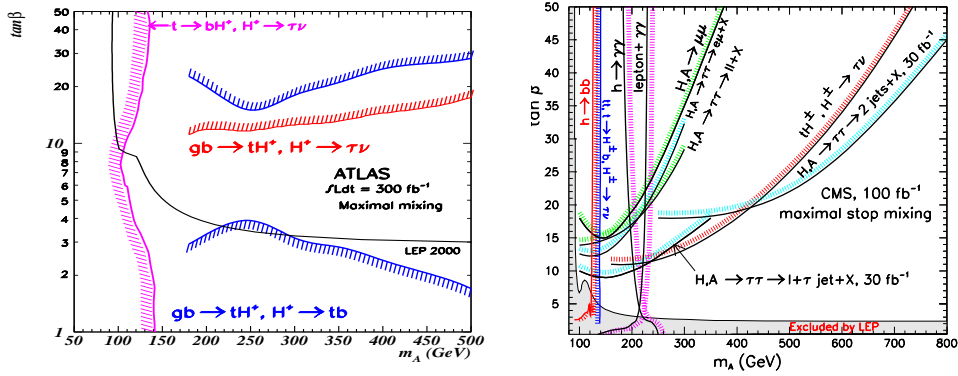


Fig. 2: The ATLAS 5-$\sigma$ discovery contour of the charged Higgs boson for an integrated luminosity of 300 fb$^{-1}$ (left plot); the CMS 5-$\sigma$ discovery contour of the MSSM Higgs bosons for 100 fb$^{-1}$ of luminosity (right plot). Below the top-quark mass, the charged Higgs boson is produced from top decay and the $\tau^\pm \nu_\tau$ channel provides coverage for most $\tan \beta$ below $\sim$160 GeV. Above the top-quark mass, the $tb$ channel covers the low and the high $\tan \beta$ regions while the $\tau^\pm \nu_\tau$ channel extends the discovery reach to high Higgs boson mass and to lower $\tan \beta$ in the high $\tan \beta$ region.

boson discovery as the $H^\pm \to \tau^\pm \nu_\tau$ branching vanishes [187]. Further studies are needed to cover the remaining areas of the 5-$\sigma$ discovery contour of Figure 2:

- The lack of sensitivity in the intermediate $\tan \beta$ region is due to the fact that the charged Higgs boson coupling to SM fermions is proportional to

$$H^+(m_t \cot \beta \bar{t} b_L + m_b \tan \beta \bar{t} b_R),\tag{1}$$

  the square of which goes through a minimum at $\tan \beta = \sqrt{m_t/m_b}$. The studies of charged Higgs boson production from SUSY cascades and charged Higgs boson decays to SUSY particles might help cover this region.

- The gap in the $m_A$ axis around $m_A = 160$ GeV corresponds to the transition region where, for the correct description of the charged Higgs boson production and decay mechanisms, it is mandatory to use the production process $gg \to tbH^\pm$ which includes not only $gg \to t\bar{t}$ with $t \to bH^\pm$, but also the Higgs-strahlung mechanism and the relative interferences [188].

- The discovery reach could be extended to high Higgs boson masses by studying the process $gg \to tbH^\pm$ with $H^\pm \to tb$ and tagging all the four b-jets in the spectrum [189].

Recent studies which attempt to cover these remaining regions of the parameter space are presented along with the observability of charged Higgs boson signals in models with singlet neutrinos in large extra dimensions and the prospects for the determination of the charged Higgs boson mass and $\tan \beta$ at the LHC.

## 2.   H$^{\pm}$ Mass and $\tan\beta$ Determination at the LHC

In this section, we discuss the expected precisions on the charged Higgs boson mass and $\tan\beta$ measurements at the LHC — above the top-quark mass — in the $H^{\pm} \to \tau^{\pm}\nu_{\tau}$ and $H^{\pm} \to tb$ channels. Details of this analysis can be found in [190].

### 2.1   Motivation

The detection of a charged Higgs boson signal would constitute an irrefutable proof for physics beyond the SM. The subsequent determination of the charged Higgs boson parameters such as the mass, the decay width, the spin, the rates in the various decay channels and the couplings to SM and SUSY particles will be necessary not only to establish that the observed particle is indeed consistent with a charged scalar boson but also to identify the actual scenario that is realized. The measurements of the charged Higgs boson mass and $\tan\beta$ will be essential to the determination of the charged Higgs boson properties.

### 2.2   H$^{\pm}$ Mass Determination in H$^{\pm} \to \tau^{\pm}\nu_{\tau}$

This channel does not offer the possibility for the observation of a resonance peak above the background, only the transverse Higgs boson mass can be reconstructed because of the neutrino in the final state. The background comes from single top $W^{\pm}t$, and $t\bar{t}$ productions with one $W^{\pm} \to \tau^{\pm}\nu_{\tau}$. Thus, the transverse mass is kinematically constrained to be less than the $W^{\pm}$ mass while in the signal the upper bound is the charged Higgs boson mass. Furthermore, the distributions of one-prong hadronic decays of $\tau^{\pm}$'s,

$$
\begin{aligned}
\tau^{\pm} &\to & \pi^{\pm}\nu_{\tau} & \quad (11.1\%) \\
\tau^{\pm} &\to & \rho^{\pm}(\to \pi^{\pm}\pi^0)\nu_{\tau} & \quad (25.2\%) \\
\tau^{\pm} &\to & a_1^{\pm}(\to \pi^{\pm}\pi^0\pi^0)\nu_{\tau} & \quad (9.0\%),
\end{aligned}
\tag{2}
$$

are sensitive to the polarization state of the $\tau$-lepton [191, 192]. In fact, it is to be noted that the spin state of $\tau^{\pm}$'s coming from $H^{\pm}$- and $W^{\pm}$-boson decays are opposite (neglecting leptonic mass effects, as we did here). This is true for the case of one-prong decays into both $\pi^{\pm}$'s and longitudinal vector mesons, while the transverse component of the latter dilutes the effect and must be somehow eliminated by requiring that 80% of the $\tau$-jet (transverse) energy is carried away by the $\pi^{\pm}$'s, i.e.:

$$
R = \frac{p^{\pi^{\pm}}}{p_T^{\tau}} > 0.8.
\tag{3}
$$

Ultimately, the polarization effect leads to a significantly harder momentum distribution of charged pions from $\tau$-decays for the $H^{\pm}$-signal compared to the $W^{\pm}$-background, which can then be exploited to increase the signal-to-background ratios and the signal significances [187, 193]. Indeed the background is relatively small as shown in Figure 3 where the transverse mass

$$
m_T = \sqrt{2p_T^{\tau}\not{p}_T(1 - \cos\Delta\phi)},
\tag{4}
$$

is reconstructed from the visible $\tau$-jet and the missing energy. As a result, although there is no resonance peak in this channel, the charged Higgs boson mass can be extracted from the transverse mass distribution with a relatively good precision. For the mass determination in this channel, we use the likelihood method described in [194], which we summarize as follows:

- Suppose we wish to estimate the expected precision $\delta m_0$ on a Higgs boson reference mass $m_0$. We generate samples of events with charged Higgs boson masses $m_k = m_0 + k \times \delta m$ and for each $m_k$ we calculate the probability density function $P_k(m)$ from the reconstructed transverse mass distribution of a charged Higgs boson with mass $m_k$. For example, for a charged Higgs boson reference mass $m_0 = 250$ GeV, we generate signal events at charged Higgs boson masses $m_k = 230, 235, 240, 245, 250, 255, 260, 265$ and $270$ GeV.
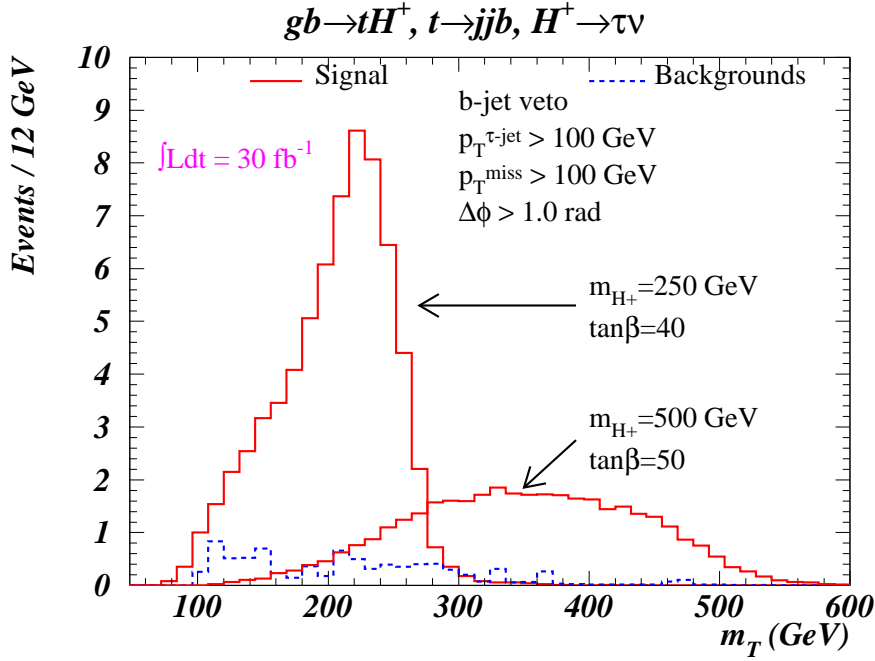
Fig. 3: The reconstruction of the transverse charged Higgs boson mass in $H^\pm \to \tau^\pm \nu_\tau$ for $m_{H^\pm} = 250$ and 500 GeV. The background is relatively small in this channel. The discovery reach is limited to high $\tan\beta$ but extended to higher mass compared to the $tb$ channel.

- Assuming $N_0$ is the expected number of events — signal and background — corresponding to the reference mass $m_0$, we draw randomly $N \equiv N_0 + \delta N_0$ masses $m_j$ from each distribution $P_k(m)$ ($\delta N_0$ is the statistical error on $N_0$). For each $m_k$, we calculate the likelihood function $\mathcal{L}_k = \Sigma_{j=1}^N \log(P_k(m_j))$. The differences $\Delta\mathcal{L}_k = \mathcal{L}_0 - \mathcal{L}_k$ show a minimum around $m_0$, where a parabolic fit is performed to get the actual expected value of $m_0$. This exercise can be repeated many times within the statistical error $\delta N_0$ and the distribution of the expected values, so obtained, of $m_0$ would be a Gaussian whose mean is the reconstructed mass and whose standard deviation is the statistical precision on the reconstructed mass.

- Three main sources of systematic uncertainties are included in the mass determination: the shape of the background, the background rate and the energy scale. The background shape becomes more significant at lower Higgs boson masses where there is more overlap between signal and background. To include this effect, we assumed a linear variation of the background shape, from $-10\%$ to $+10\%$ between the minimum and the maximum of the transverse mass distribution. Another source of systematic uncertainty is the rate of the backgrounds. It is expected that the background rate ($W^\pm t$ and $t\bar{t}$) could be known to 5% [194]. Therefore, to take this effect into account, we increase the background rate by 5% while at the same time we decrease the signal by 5%. Finally, we also include the scale uncertainty: 1% for jets and 0.1% for photons, electrons and muons. The overall precisions on the charged Higgs boson mass determination, including the systematic uncertainties, are shown in Table 1 and Figure 4.

## 2.3 $H^\pm$ Mass Determination in $H^\pm \to tb$

In the $tb$ channel, the full invariant mass can be reconstructed although this channel suffers from the irreducible $t\bar{t}b$ background and the signal combinatorial background [186]. The determination of the mass

can be done using the likelihood method described above or by fitting the signal and the background. In the latter case, one assumes that the background shape and normalization can be determined by fitting outside the signal region, thus, the systematic uncertainties include only the scale uncertainty. We assume a Gaussian shape for the signal and an exponential for the background and fit signal+background including the statistical fluctuations and the scale uncertainty. Both methods are in agreement on the mass determination. The results are shown in Table 1 and Figure 4.

Table 1: The overall precisions on the mass determination are better in the $\tau\nu$ channel than in the $tb$ channel. This is due to the fact that the latter suffers from large $t\bar{t}b$ and signal combinatorial backgrounds ($\mathcal{L} = 100$ fb$^{-1}$).

| $m_{H^\pm}$ (GeV) | $H^\pm \to \tau^\pm \nu_\tau$ | | $H^\pm \to tb$ | |
|---|---|---|---|---|
| | $<m>$ | $\delta m$ | $<m>$ | $\delta m$ |
| 225.9 | 225.9 | 2.9 | 226.9 | 1.8 |
| 271.1 | 271.0 | 3.9 | 270.1 | 10.1 |
| 317.8 | 319.7 | 5.9 | 320.2 | 11.3 |
| 365.4 | 364.9 | 8.1 | 365.4 | 12.1 |
| 413.5 | 414.8 | 8.0 | 417.4 | 17.6 |
| 462.1 | 460.7 | 10.6 | 465.9 | 24.1 |
| 510.9 | 511.4 | 15.7 | | |

## 2.4 Determination of $\tan\beta$

$\tan\beta$ can be obtained by measuring the signal rate in the $\tau^\pm\nu_\tau$ channel where the backgrounds are relatively low. The main systematic error would come from the knowledge of the luminosity, whose uncertainty is taken conservatively to be 10%. The error in the rate measurement can be estimated as [195]

$$\frac{\Delta(\sigma \times BR)}{\sigma \times BR} = \sqrt{\frac{S+B}{S^2} + \left(\frac{\Delta\mathcal{L}}{\mathcal{L}}\right)^2}, \tag{5}$$

where $S$ and $B$ are the numbers of signal and background events respectively. The uncertainty on $\tan\beta$ is computed as

$$\Delta\tan\beta \simeq \Delta(\sigma \times BR)\left[\frac{d(\sigma \times BR)}{d\tan\beta}\right]^{-1}. \tag{6}$$

The production cross-section for $gb \to tH^\pm$ and the branching ratio of $H^\pm \to \tau^\pm\nu_\tau$ above the top-quark mass can be written respectively as [2]

$$\sigma(gb \to tH^\pm) \propto m_t^2 \cot^2\beta + m_b^2 \tan^2\beta, \tag{7}$$

and

$$BR(H^\pm \to \tau^\pm\nu_\tau) \simeq \frac{m_\tau^2 \tan^2\beta}{3(m_t^2 \cot^2\beta + m_b^2 \tan^2\beta) + m_\tau^2 \tan^2\beta}. \tag{8}$$

Using the relations (7) and (8), the rate in the $\tau^\pm\nu_\tau$ channel at large $\tan\beta$ is obtained as:

$$\sigma \times BR \propto \tan^2\beta. \tag{9}$$

From the Equations (6) and (9), we get

$$\frac{\Delta\tan\beta}{\tan\beta} = \frac{1}{2}\frac{\Delta(\sigma \times BR)}{\sigma \times BR}. \tag{10}$$

The expected uncertainties on $\tan\beta$ determination from the measurement of the rate in the $H^\pm \to \tau^\pm\nu_\tau$ channel are shown in Table 2 and Figure 4.

Table 2: The overall precisions on $\tan\beta$ determination in the $H^\pm \to \tau^\pm\nu_\tau$ channel for $\mathcal{L} = 30$, 100 and 300 fb$^{-1}$, and for $m_{H\pm} = 250$ GeV.

| $\tan\beta$ | $\Delta\tan\beta/\tan\beta$ (%) | | |
|---|---|---|---|
| | 30 fb$^{-1}$ | 100 fb$^{-1}$ | 300 fb$^{-1}$ |
| 20 | 15.4 | 10.6 | 7.4 |
| 25 | 12.2 | 8.7 | 6.5 |
| 30 | 10.5 | 7.7 | 6.1 |
| 35 | 9.1 | 7.0 | 5.7 |
| 40 | 8.4 | 6.6 | 5.6 |
| 45 | 7.7 | 6.6 | 5.5 |
| 50 | 7.3 | 6.1 | 5.4 |
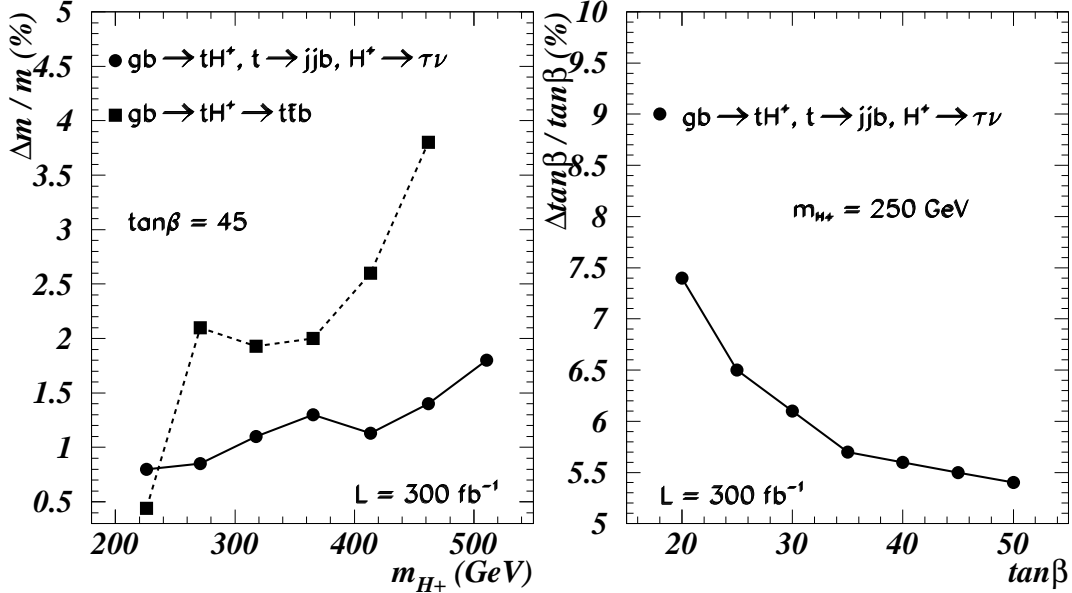


Fig. 4: The expected overall precision on the charged Higgs boson mass and on $\tan\beta$ measurements, as a function of the charged Higgs boson mass (left plot) and $\tan\beta$ (right plot) respectively. For the mass determination, the $H^\pm \to \tau^\pm\nu_\tau$ channel gives better precisions than $H^\pm \to tb$ except at low $m_{H\pm}$. In addition, $H^\pm \to \tau^\pm\nu_\tau$ allows for the determination of $\tan\beta$ by measuring the rate in this channel.

## 2.5 Conclusions

In the $\tau^\pm\nu_\tau$ channel, there is no resonance peak, only the transverse mass is reconstructed. A likelihood method is used to estimate the expected precisions on the mass measurements. The systematic effects include the background shape, the background rate and the energy scale. The overall relative precision in this channel ranges from 1.3% at $m_{H\pm} = 226$ GeV to 3.1% at $m_{H\pm} = 511$ GeV for an integrated luminosity of 100 fb$^{-1}$. At 300 fb$^{-1}$, the precision improves to 0.8% at $m_{H\pm} = 226$ GeV and 1.8% at $m_{H\pm} = 511$ GeV.

The $tb$ channel offers a resonance peak with a large background from $t\bar{t}b$ and the signal combinatorial. It is possible to use the likelihood method for the mass determination in this channel. Alternatively,

a fit of the signal and background can be performed provided the background shape and normalization can be determined by fitting outside the signal region. Results from both methods are in agreement. The relative precision in this channel ranges from 0.8% at $m_{H^\pm} = 226$ GeV to 5.2% at $m_{H^\pm} = 462$ GeV for 100 fb$^{-1}$. For 300 fb$^{-1}$, the precision improves to: 0.5% at 226 GeV and 3.5% at 462 GeV.

In either channel, the overall uncertainties are dominated by the statistical errors. The $\tau\nu$ channel offers better precisions on the charged Higgs boson mass determination than the $tb$ channel, except at low $m_{H^\pm}$ where the $\tau^\pm\nu_\tau$ channel suffers from a much reduced cut efficiency.

$\tan\beta$ can be measured in the $H^\pm \to \tau^\pm\nu_\tau$ channel (by measuring the rate) where the background is relatively low and the discovery reach is extended to high masses compared to $H^\pm \to tb$. Assuming a 10% uncertainty on the luminosity, the relative precision on $\tan\beta$ ranges from 15.4 to 7.3% for $\tan\beta = 20$ to 50, at low luminosity. For an integrated luminosity of 300 fb$^{-1}$, the precision improves to: 7.4% at $\tan\beta = 20$ to 5.4% at $\tan\beta = 50$.

## 3. $H^\pm$ Boson in the Threshold Region

In this section, we discuss charged Higgs boson analyzes in the threshold region, i.e., for $m_{H^\pm} \sim m_t$, taking into account the correct description of the charged Higgs boson production and decay mechanism in this region.

### 3.1 Motivation

In the MSSM, the LEP 2 limits on the mass of the lightest Higgs boson convert directly (see [2]) into a lower bound on the charged Higgs boson mass (at least, at low $\tan\beta$, say, around 3): $m_{H^\pm}^2 \approx m_{W^\pm}^2 + m_{h^0}^2 \gtrsim (140 \text{ GeV})^2$ [196]. Whereas the charged Higgs boson mass region just above this value is theoretically well understood, the description of the so-called (top) 'threshold region', $m_{H^\pm} \sim m_t$, requires careful considerations when it comes to $H^\pm$ production and decay in the context of a Monte Carlo (MC) simulation, as explained below. The main production mode of $H^\pm$ scalars with mass strictly below the top-quark mass, $m_{H^\pm} < m_t$, is the decay of the top (anti)quarks themselves, the latter being produced via QCD in the annihilation of gluon-gluon and quark-antiquark pairs. So far, standard MC programs, such as PYTHIA, HERWIG and ISAJET [100, 181, 182], have accounted for this process through the usual procedure of factorizing the production mode, $gg, q\bar{q} \to t\bar{t}$, times the decay one, $\bar{t} \to \bar{b}H^-$, in the so-called Narrow Width Approximation (NWA). However, this description fails to correctly account for the production and decay phenomenology of charged Higgs bosons when their mass approaches or exceeds that of the top-quark, hence undermining the ability of experimental analyzes in pinning down the real nature of these particles (if not detecting them altogether).

This is particularly a pressing issue at the Tevatron Run 2 [188], as the collider reach in $m_{H^\pm}$ dips precisely into the threshold region [198]. Here, the use of the $2 \to 3$ hard scattering process $gg, q\bar{q} \to t\bar{b}H^-$ [199], in place of the 'factorization' procedure [200], is mandatory, as one can clearly see from Figure 5 where the discrepancies in the shape and normalization come from the Higgs-strahlung mechanism and the relative interferences as mentioned earlier.

Also differential distributions can strongly be affected by an approximated modeling of the production and decay process in the threshold region, as one can appreciate from Figure 6. Here, differences are clearly sizeable also for the top quark. However, in this case one should expect the impact to be marginal, as this particle is actually unstable and since its three-body decay products are subject to the effect of usual detector resolution uncertainties. In contrast, this is no longer true for the bottom quark, which fragments directly into hadrons. Besides, the availability of the newly implanted silicon vertex detector may render the tagging of $b$-quarks a crucial ingredient in detection strategies of charged Higgs bosons at Run 2, pretty much along the same lines as established at the LHC [189].
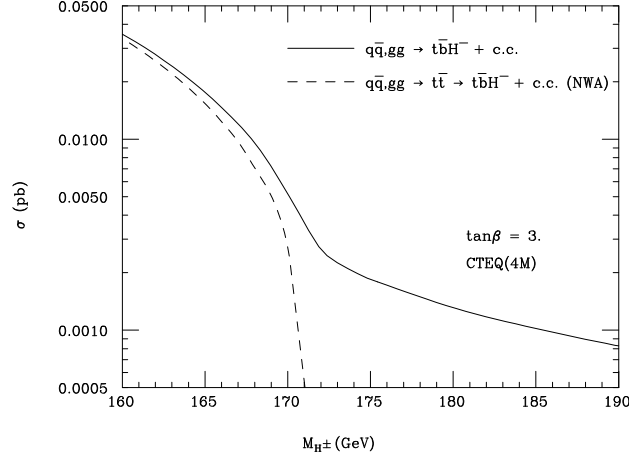
Fig. 5: Cross section for $gg, q\bar{q} \to t\bar{b}H^-$ and $gg, q\bar{q} \to t\bar{t} \to t\bar{b}H^-$ in NWA, at the Tevatron with $\sqrt{s} = 2$ TeV, as a function of $m_{H^\pm}$ for a representative value of $\tan\beta$ (the kinematical effects discussed are the same irrespective of the latter). Hereafter, charge conjugated rates are always included. Besides, both top and bottom quark masses in the Higgs boson Yukawa couplings are non-running and set to 175 and 4.25 GeV, respectively. CTEQ4M [197] is used for the Parton Distribution Functions (PDFs), with scale $m_{H^\pm}$.
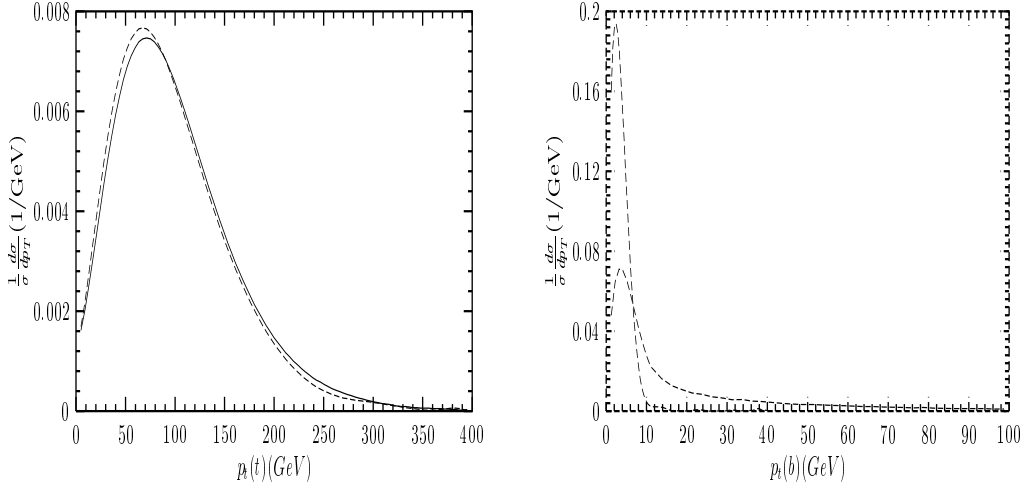


Fig. 6: Transverse momentum distributions of the final state quarks in $gg, q\bar{q} \to t\bar{b}H^-$ (solid) and $gg, q\bar{q} \to t\bar{t} \to t\bar{b}H^-$ (dashed) in NWA, at Tevatron with $\sqrt{s} = 2$ TeV, for $m_{H^\pm} = 170$ GeV. Again, the actual $\tan\beta$ value is irrelevant.

## 3.2 Analysis

If one looks at the most promising (and cleanest) charged Higgs boson decay channel, i.e., $H^\pm \to \tau^\pm \nu_\tau$ [201], while reconstructing the accompanying top quark hadronically, the prospects of detection are rather good. This is made clear in Table 3. Even if one neglects the tagging of the $b$-quarks in the final state, the final results are very different between the full process and the NWA. In Table 3, we have reported the signal and dominant (irreducible) background rates (that is, from $gg, q\bar{q} \to t\bar{b}W^- + $ c.c. events, yielding the same final state as the signal) after the following sequence of cuts:

1. Tau-jets are selected if they satisfy the criteria: $p_T^\tau > 15$ GeV and $|\eta^\tau| < 2.5$.
2. We require $p\!\!\!/_T > 20$ GeV, since the presence of neutrinos from $H^-$ decays and invisible decay

products of $\tau$'s (mainly $\pi^0$'s) implies that a significant fraction of the transverse momentum goes undetected.

3. Quark-jets are selected by imposing $p_T^j > 20$ GeV and $|\eta^j| < 2.5$. We require at least one of these to be tagged as a $b$-jet.

4. We demand that two un-tagged jets have an invariant mass around $m_{W^\pm}$, e.g., $|m_{q\bar{q}'} - m_{W^\pm}| <$ 10 GeV and that the $b$-jet in combination with the other two un-tagged jets produces an invariant mass close to $m_t$, e.g., $|m_{bq\bar{q}'} - m_t| < 15$ GeV.

5. We require that the reconstructed transverse mass, Equation (4), be above the $W^\pm$-boson mass: $m_T > m_{W^\pm} \approx 80$ GeV.

The $\tau$'s can be tagged as narrow jets in their 'one-prong' hadronic decay modes — see the relations (2) — which represent 90% of the hadronic decay rate and about 50% of the total. This distinguishing feature is in contrast to the typical appearance of quark- and gluon-jets, which yield 'multi-prong' hadronic topologies in the detectors, typical of QCD backgrounds of the form $W^\pm$ + jets and $Z^0$ + jets.

Table 3: The signal rates (in fb) for the process $q\bar{q}, gg \to t\bar{b}H^-(\to \tau^-\bar{\nu}_\tau)$, at Tevatron with $\sqrt{s} = 2$ TeV, for representative values of $m_{H^\pm}$ and $\tan\beta$, after all cuts described in the text. The corresponding rate of the background is 0.22 fb independent of $m_{H^\pm}$.

| $m_{H^\pm}$ (GeV) $\downarrow$ / $\tan\beta \to$ | 3 | 6 | 40 |
|---|---|---|---|
| 150 | 6 | 3 | 52 |
| 160 | 2.8 | 1.5 | 22 |
| 170 | .4 | 0.25 | 3.5 |
| 175 | .13 | .08 | 1.42 |
| 180 | .067 | .061 | 1.09 |

### 3.3 Conclusions

In the end, despite the fact that one should more realistically expect both signal and background rates to be further reduced by a factor of 4 or so ($\tau$-identification efficiencies are estimated to be of order 50% [202], similarly for the tagging of any $b$-jet [198]), the final message that emerges is that the chances of extracting the $H^\pm \to \tau^\pm \nu_\tau$ signal after 15 fb$^{-1}$ of luminosity at the Tevatron Run 2 are rather good for $m_{H^\pm}$ up to 180 GeV or so at large $\tan\beta$, while being negligible at low to intermediate $\tan\beta$ values. Conclusions would obviously be drastically different in the NWA scenario, if one recalls Figure 5.

The situation can be improved even further by taking advantage of the $\tau$ polarization effects as explained above. In this respect, the enforcement of the constraint (3) reduces the background by a factor of 5, while costing to the signal only a modest — in comparison — 50% suppression (for any charged Higgs boson mass in the usual interval between 160 and 190 GeV).

Although we have relied here on a parton-level analysis, it is clear that its main features would remain valid even in presence of fragmentation/hadronization effects. In fact, work is currently ongoing in order to include the latter, as well as a more realistic detector simulation, to emulate the real potential of the Tevatron experiments, by exploiting the mentioned $2 \to 3$ description of the $H^\pm$ production dynamics and the spin correlations in $\tau$-decays, as they are now both available in version 6.4 [203] of the HERWIG event generator (the latter also through an interface to TAUOLA [45]).

The problematic is very similar at the LHC, if anything more complicated. In fact, at the CERN hadron collider, the above $2 \to 3$ reaction is dominated by the $gg$-initiated subprocesses, rather than by $q\bar{q}$ annihilation, as is the case at the Tevatron. This means that a potential problem of double counting arises in the simulation of $t\bar{b}H^-$ + c.c. events at the LHC, if one considers that Higgs-strahlung can also be emulated through the $2 \to 2$ process $bg \to tH^-$ + c.c. The difference between the two descriptions is
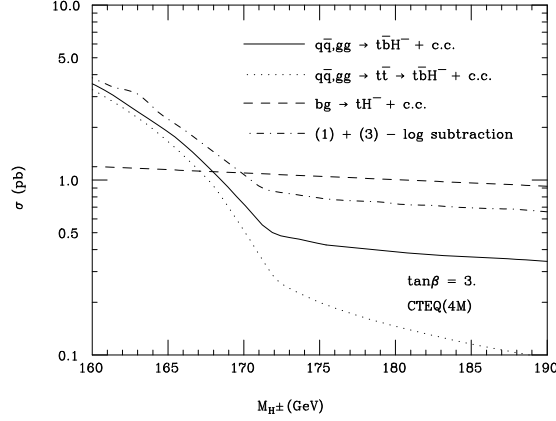
Fig. 7: Cross section for $gg, q\bar{q} \to t\bar{b}H^-$; $gg, q\bar{q} \to t\bar{t} \to t\bar{b}H^-$ with finite top-quark width; $bg \to tH^-$ and the combination of the first and the last, at the LHC with $\sqrt{s} = 14$ TeV, as a function of $m_{H^\pm}$ for a representative value of $\tan\beta$.

well understood, and a prescription exists for combining the two, through the subtraction of a common logarithmic term: see Refs [204–207]. Figure 7 summarizes all the discussed issues in the context of the LHC. The $2 \to 3$ process is available in HERWIG and detailed simulations of the $\tau^\pm \nu_\tau$ channel at the CERN hadron collider are now possible also for the threshold region, as already done for other mass intervals [185–187, 190, 193, 206].

## 4.  H$^\pm$ Boson in Large Extra Dimensions

In this section, we discuss the LHC sensitivity to the charged Higgs boson discovery in the channel $H^- \to \tau_L^- \nu$ in models with singlet neutrinos in large extra dimensions. The observation of such a signal would provide a distinctive evidence for these models since in the standard two Higgs doublet model type II, $H^- \to \tau_L^- \nu$ is completely suppressed. Details of this analysis can be found in [209].

### 4.1  Motivation

In models where extra dimensions open up at the TeV scale, small neutrino masses can be generated without implementing the seesaw mechanism [210]. These models postulate the existence of $\delta$ additional spatial dimensions of size $R$ where gravity and perhaps other fields freely propagate while the SM degrees of freedom are confined to (3+1)-dimensional wall (4D) of the higher dimensional space. The true scale of gravity, or fundamental Planck scale $M_*$, of the $(4 + \delta)$D space time is related to the reduced 4D Planck scale $M_{Pl}$, by $M_{Pl}^2 = R^\delta M_*^{\delta+2}$, where $M_{Pl} = 2.4 \times 10^{18}$ GeV is related to the usual Planck mass $1.2 \times 10^{19}$ GeV $= \sqrt{8\pi}M_{Pl}$. Since no experimental deviations from Newtonian gravity are observed at distances above 0.2 mm [211], the extra dimensions must be at the sub-millimeter level with $M_*$ as low as few TeV and $\delta \geq 2$.

The right handed neutrino can be interpreted as a singlet with no quantum numbers to constrain it to the SM brane and thus, it can propagate into the extra dimensions just like gravity [86]. Such singlet states in the bulk couple to the SM states on the brane as right handed neutrinos with small couplings – the Yukawa couplings of the bulk fields are suppressed by the volume of the extra dimensions. The interactions between the bulk neutrino and the wall fields generate Dirac mass $m_D$ terms between the wall fields and all the Kaluza-Klein modes of the bulk neutrino:

$$m_D = \frac{\lambda}{\sqrt{2}} \frac{M_*}{M_{Pl}} v, \tag{11}$$

where $\lambda$ is a dimensionless constant. The mixing between the lightest neutrino with mass $m_D$ and the heavier neutrinos introduces a correction $N$ to the Dirac mass such that the physical neutrino mass $m_\nu$ is $m_\nu = m_D/N$, where

$$N \simeq 1 + \sum_{\vec{n}}^{|\vec{n}|<M_*R} \left( \frac{m_D R}{\vec{n}} \right)^2 , \tag{12}$$

$\vec{n}$ is a vector with $\delta$ integer components counting the number of states and the summation is taken over the Kaluza-Klein states up to the fundamental scale $M_*$. The sum over the different Kaluza-Klein states can be approximately replaced by a continuous integration. As shown in Table 4, small neutrino masses, $m_\nu$, can be obtained consistent with atmospheric neutrino oscillations [212]. The spectrum of many

Table 4: The parameters used in the current analysis of the signal with the corresponding polarization asymmetry. In general, $H^-$ would decay to $\tau_L^-$ and $\tau_R^-$, $H^- \to \tau_R^- \bar{\nu} + \tau_L^- \psi$, depending on the asymmetry. For the decay $H^- \to \tau_R^- \bar{\nu}$ (as in MSSM), the asymmetry is $-1$. The signal to be studied is $H^- \to \tau_L^- \psi$.

|  | $M_*$ (TeV) | $\delta_\nu, \delta$ | $m_{H^\pm}$ (GeV) | $\tan \beta$ | $A_{LR}$ | $m_\nu$ (eV) |
|---|---|---|---|---|---|---|
| Sig.-1 | 2 | 4,4 | 219.9 | 30 | $\sim 1$ | $0.5\ 10^{-3}$ |
| Sig.-2 | 20 | 3,3 | 365.4 | 45 | $\sim 1$ | 0.05 |
| Sig.-3 | 1 | 5,6 | 506.2 | 4 | $\sim 1$ | 0.05 |
| Sig.-4 | 100 | 6,6 | 250.2 | 35 | $\sim -1$ | 0.005 |
| Sig.-5 | 10 | 4,5 | 350.0 | 20 | $\sim -1$ | 0.04 |
| Sig.-6 | 50 | 5,5 | 450.0 | 25 | $\sim -1$ | 0.04 |

extensions of the SM includes a charged Higgs boson state. We consider as a prototype of these models the 2-Higgs Doublet Model of type II (2HDM-II). $H^-$ decays to the right handed $\tau^-$ through the $\tau$ Yukawa coupling: $H^- \to \tau_R^- \bar{\nu}$. The $H^-$ decay to left handed $\tau^-$ is completely suppressed in MSSM. However, in the scenario of singlet neutrinos in large extra dimensions, $H^-$ can decay to both right handed and left handed $\tau^-$ depending on the parameters $M_*$, $m_D$, $\delta$, $m_{H^\pm}$ and $\tan \beta$, due to the large number of Kaluza-Klein states of the right handed bulk neutrino: $H^- \to \tau_R^- \bar{\nu} + \tau_L^- \psi$, where $\psi$ is a bulk neutrino and $\nu$ is dominantly a light neutrino with a small admixture of the Kaluza-Klein modes of the order $m_D R/|n|$. The measurement of the polarization asymmetry

$$A_{LR} = \frac{\Gamma(H^- \to \tau_L^- \psi) - \Gamma(H^- \to \tau_R^- \bar{\nu})}{\Gamma(H^- \to \tau_L^- \psi) + \Gamma(H^- \to \tau_R^- \bar{\nu})}, \tag{13}$$

can be used to distinguish between the ordinary 2HDM-II and the scenario of singlet neutrinos in large extra dimensions.

The singlet neutrino may propagate into a subset $\delta_\nu$ ($\delta_\nu \leq \delta$) of the $\delta$ additional spatial dimensions, in which case the formalism for the generation of small Dirac neutrino masses is merely a generalization of the case $\delta_\nu = \delta$ [213].

The charged Higgs boson decay to right handed $\tau$, $H^- \to \tau_R^- \bar{\nu}$ has been extensively studied for the LHC [190, 193]. Here we discuss the possibility to observe $H^- \to \tau_L^- \psi$ at the LHC above the top-quark mass. Table 4 shows the parameters selected for the current analysis. The cases where the asymmetry is $+1$ are discussed in details. We assume a heavy SUSY spectrum with maximal stop mixing. The present analysis is conducted in the framework of PYTHIA6.1 and ATLFAST [100, 138], and the Higgs boson masses and couplings are calculated to 1-loop with FeynHiggsFast [214].

## 4.2 Analysis

We consider the $2 \rightarrow 2$ production process where the charged Higgs boson is produced with a top-quark, $gb \rightarrow tH^{\pm}$ as shown in Figure 1. Further, we require the hadronic decay of the top-quark, $t \rightarrow Wb \rightarrow jjb$ and the charged Higgs boson decay to $\tau$-leptons. The major backgrounds are the single

Table 5: The expected rates ($\sigma \times$ BR), for the signal $gb \rightarrow tH^{\pm}$ with $H^{-} \rightarrow \tau_R^{-} \bar{\nu} + \tau_L^{-} \psi$ and $t \rightarrow jjb$, and for the backgrounds: $Wt$ and $t\bar{t}$ with $W^{-} \rightarrow \tau_L^{-} \bar{\nu}$ and $W^{+} \rightarrow jj$. We assume an inclusive $t\bar{t}$ production cross section of 590 pb. Other cross sections are taken from PYTHIA 6.1 with CTEQ5L parton distribution function. See Table 4 for the parameters used for Sig.-1, Sig.-2 and Sig.-3. In the last columns, we compare the $H^{-} \rightarrow \tau_R^{-} \bar{\nu}$ branching ratios in this model to the corresponding MSSM branching ratios from HDECAY [80].

| Process | $\sigma \times$ BR (pb) | BR | BR(MSSM) |
|---|---|---|---|
| Sig.-1 | 1.56 | 0.73 | 0.37 |
| Sig.-2 | 0.15 | 1.0 | 0.15 |
| Sig.-3 | 0.04 | 1.0 | 0.01 |
| $t\bar{t}$ | 84.11 | | |
| $gb \rightarrow Wt$ ($p_T > 30$ GeV) | 47.56 | | |

top production $gb \rightarrow Wt$, and $t\bar{t}$ production with one $W^{+} \rightarrow jj$ and the other $W^{-} \rightarrow \tau_L^{-} \bar{\nu}$[17]. Depending on the polarization asymmetry, $H^{-} \rightarrow \tau_R^{-} \bar{\nu}$ will contribute as an additional background. In Table 5, we list the rates for the signal and for the backgrounds. The polarization of the $\tau^{\pm}$-lepton is included in this analysis through TAUOLA [45]. We consider the hadronic one-prong decays of the $\tau^{\pm}$-lepton — see the relations (2) — which are believed to carry a better imprint of the $\tau^{\pm}$ polarization [191].

For the signal in MSSM, right handed $\tau_R^{-}$'s come from the charged Higgs boson decay, $H^{-} \rightarrow \tau_R^{-} \bar{\nu}$, while in the backgrounds, left handed $\tau_L^{-}$'s come from the decay of the $W^{-}(\rightarrow \tau_L^{-} \bar{\nu})$. Because of the neutrino in the final state, only the transverse mass, Equation (4), can be reconstructed. In the framework of large extra dimensions, we are interested in $H^{-} \rightarrow \tau_L^{-} \psi$ where the polarization of the $\tau$-lepton would be identical to the background case but opposite to the MSSM case. Therefore, the polarization of the $\tau$-lepton would not help in suppressing the backgrounds. Nevertheless, there are still some differences in the kinematics of the signal and of the backgrounds: the different transverse mass bounds and the increasingly harder $\tau$-jet and missing transverse momenta as the Higgs boson mass increases. The reconstructed transverse mass for the signal and the backgrounds are shown in Figure 8

Table 6: The expected signal-to-background ratios and significances calculated for an integrated luminosity of 100 fb$^{-1}$ (one experiment). See Table 4 for the parameters used for Sig.-1, Sig.-2 and Sig.-3. In all the cases considered, the signal can be observed at the LHC with significances in excess of 5-$\sigma$ at high luminosity.

| | Sig.-1 | Sig.-2 | Sig.-3 |
|---|---|---|---|
| Signal events | 41 | 215 | 16 |
| $t\bar{t}$ | 7 | 7 | 7 |
| $Wt$ | 3 | 3 | 3 |
| Total background | 10 | 10 | 10 |
| $S/B$ | 4.1 | 21.5 | 1.6 |
| $S/\sqrt{B}$ | 13.0 | 68.0 | 5.1 |

and the expected signal-to-background ratios and the signal significances in Table 6. The reconstruction

---

[17]There is no enhancement in the background rate from the contribution $W^{-} \rightarrow \tau_L^{-} \psi$.
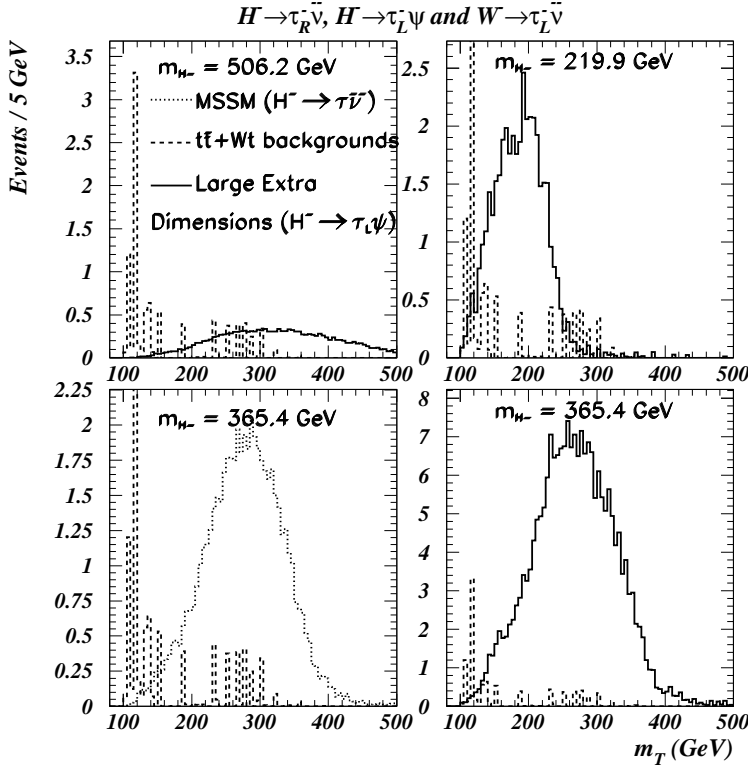
Fig. 8: The reconstructions of the transverse mass of the signal in MSSM, the signal in models with a singlet neutrino in large extra dimensions and of the backgrounds, for an integrated luminosity of 100 fb$^{-1}$. The observation of the signal in the transverse mass distribution would not be sufficient to identify the model: the $\tau^{\pm}$ polarization effects must be explored further.

of the transverse mass is not enough to distinguish between the MSSM and the singlet neutrinos in large extra dimensions. The differences in these two scenarios are best seen in the distribution of $p^{\pi}/E^{\tau-jet}$, the fraction of the energy carried by the charged track which is shown in Figure 9. In the MSSM, this distribution peaks near 0 and 1 while in $H^{-} \rightarrow \tau_{L}^{-}\psi$ from large extra dimensions and in the backgrounds, this distribution peaks in the center. The backgrounds are relatively very small, and as concluded in [190, 193], the discovery reach is limited by the signal size itself. Therefore the observation of a signal in the transverse mass distribution and in the distribution of the fraction of the energy carried by the charged track should help determine whether the scenario is MSSM or not.

## 4.3 Conclusions

We studied the observability of the channel $H^{-} \rightarrow \tau_{L}^{-}\nu$ in models with a singlet neutrino in large extra dimensions at the LHC. Although the observation of a signal in the transverse mass distribution can be used to claim discovery of the charged Higgs boson, it is insufficient to pin down the scenario that is realized. Additionally, by reconstructing the fraction of the energy carried by the charged track in the one-prong $\tau^{\pm}$ decay, it is possible to claim whether the scenario is the ordinary 2HDM or not. The further measurement of the polarization asymmetry might provide a distinctive evidence for models with singlet neutrinos in large extra dimensions.
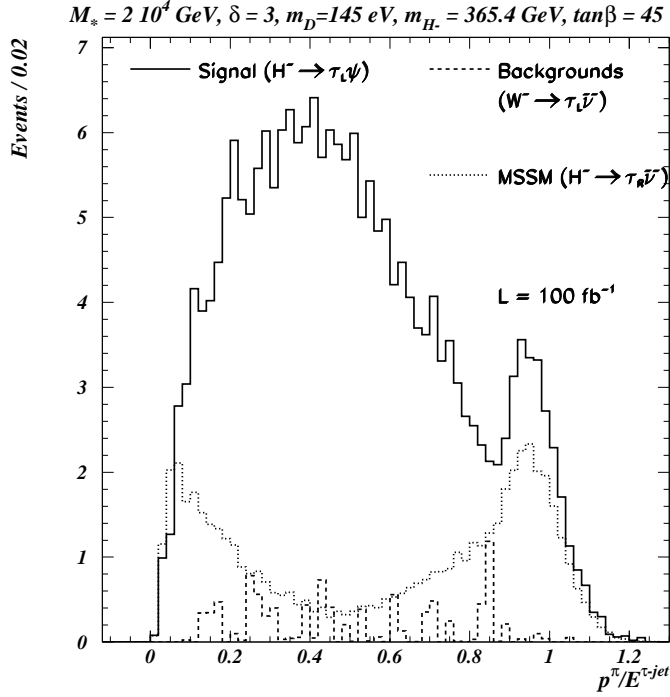
Fig. 9: The distribution of the ratio of the charged pion track momentum in one prong $\tau$ decay to the $\tau$-jet energy for $m_A = 350$ GeV, $\tan\beta = 45$, $M_* = 20$ TeV, $\delta = 3$ and $m_\nu = 0.05$ eV, and for an integrated luminosity of 100 fb$^{-1}$. In the 2HDM-II, this ratio would peak near 0 and 1 as shown while in other models, the actual distribution of this ratio would depend on the polarization asymmetry since both left and right handed $\tau$'s would contribute. In the case shown, the asymmetry is $\sim 1$ and the ratio peaks near the center of the distribution.

## 5. H$^{\pm}$ Decays into SUSY Particles

Thus far, all analyzes have implicitly assumed that the SUSY counterparts of ordinary particles had masses much higher than $m_{H\pm}$. However, lowering the typical SUSY mass scale may induce new interactions among $H^{\pm}$ bosons and several of the sparticles, so that the former may be abundantly produced in the decay of the latter (e.g., from gluinos and squarks, see [223]) or, alternatively, new Higgs boson decay channels into SUSY particles may well open at a profitable rate [215]. We will defer the study of the first scenario to section 6.. Here, we will investigate in some depth the second possibility, focusing on the 'intermediate' $\tan\beta$ region (say, between 3 and 10) left uncovered by the SM decay channels (see Figure 2)[18].

### 5.1 Motivation

It was demonstrated in [215] that the decays of a charged Higgs boson into a chargino and a neutralino could probe regions of the MSSM parameter space where decays to SM particles, such as $b\bar{t}$ or $\tau^-\bar{\nu}_\tau$ yield no significant signal — see Figure 2. In particular, intermediate values of $\tan\beta$ between $\sim 3$ and $\sim 10$ were in part accessible via $H^{\pm} \to \tilde{\chi}_1^{\pm}\tilde{\chi}_{\{2,3\}}^0$ modes resulting in three lepton final states (where leptons mean electrons or muons), a hadronically reconstructed top quark (from $gg \to \bar{b}tH^-$, $gb \to tH^-$

[18]Depending on the actual rate of the new SUSY decay channels in the complementary $\tan\beta$ areas (less than three or larger than ten), some rescaling to the discovery reaches via the SM modes of Figure 2 may be needed. This will be addressed in Ref. [227].

and their charge conjugate production processes) plus substantial missing transverse momentum (from neutralino and chargino decays to the stable lightest neutralino, i.e., the lightest supersymmetric particle or LSP).

We refer to the charginos and neutralinos collectively as "inos", which are the mass eigenstate mixtures of the electroweak (EW) gauginos and higgsinos. We expand on the parton level analysis of [215]: firstly, by studying the signal in a full event generator environment with an improved background analysis that includes potential MSSM background processes (the previous study considered only SM backgrounds); secondly, by further investigating the possible role of on-shell or off-shell sleptons (the supersymmetric partners of the leptons) in the signals. As noted in the previous study, if there is a light slepton, then the leptonic branching ratios (BRs) of the inos can be significantly enhanced (especially those of $\widetilde{\chi}_2^0$, $\widetilde{\chi}_3^0$). Since both inos and sleptons play key roles in the signal process, a considerable number of MSSM input parameters are relevant. We seek to scan this expanse of parameter space, at least at the parton level, identifying parameter points or series of points that merit dedicated event generator analyzes.

To correctly delineate the portions of parameter space that can potentially yield viable signals, it is necessary first to know where experimental constraints cut off otherwise favorable zones. LEP 2 experiments have yielded a number of bounds on MSSM particles and parameters that impinge directly on our preferred signal regions. Among these, the most crucial are [216]: the mass limit on the lighter chargino, taken as $m_{\widetilde{\chi}_1^\pm} > 103\,\text{GeV}$ (which allows for the possibility of a light sneutrino resulting in negative interference from the then-significant $t$-channel in chargino pair production); the mass limits on the sleptons, taken as $m_{\tilde{e}_1} \geq 99.0\,\text{GeV}$, $m_{\tilde{\mu}_1} \geq 91.0\,\text{GeV}$, $m_{\tilde{\tau}_1} \geq 85.0\,\text{GeV}$ and $m_{\tilde{\nu}} \geq 43.7\,\text{GeV}$ (the last being from studies at the $Z^0$ pole); and the regions excluded by searches for signals of the type $e^+e^- \to Z^{0*}h$ and $e^+e^- \to Ah$. For the numerical limits just given, it is assumed that $m_{\widetilde{\chi}_1^\pm} - m_{\widetilde{\chi}_1^0}$, $m_{\tilde{\ell}_1} - m_{\widetilde{\chi}_1^0} \geq 5\,\text{GeV}$. The constraint from Higgs boson production is somewhat vague owing to an estimated uncertainty in the expected mass of the light Higgs boson of 2–3 GeV from un-calculated higher order corrections [217] and up to 5 GeV from the error in the measurement of the top quark mass, $m_t = 174.3 \pm 3.2 \pm 4.0\,\text{GeV}$ [218]. A small shift in the light Higgs boson mass translates into a substantial shift in the location of the bound seen in the $\tan\beta$ versus $m_A$ plane. Other LEP 2 limits which generally should be less restrictive than those just mentioned are also incorporated into our analysis.

There are also other processes where charged Higgs bosons (or $A$, to whose mass that of the $H^\pm$ is closely tied) enter as virtual particles at the one-loop level. These include neutral meson mixing ($K^0\bar{K}^0$, $D^0\bar{D}^0$, or $B^0\bar{B}^0$) [219,220], $Z^0 \to b\bar{b}$ ($R_b$) [220,221], and $b \to s\gamma$ decays [219–222], the last of which, where restrictions on $m_{H^\pm}$ are linked to a number of MSSM variables, notably including the masses of the lighter chargino and the stops, is generally thought to be the most constraining [221]. This constraint may well disqualify regions of the parameter space where our signal is strong and otherwise allowed; however, the applicability of these low energy constraints is unclear due to a variety of factors (see [215]) and thus they will not be included in this analysis (though we do choose our stop parameters with an eye towards attempting to evade potential $b \to s\gamma$ bounds).

## 5.2 Parameter Space Exploration

We begin in Figure 10 (top plot) with a look at the raw cross-section for $gg \to \bar{b}tH^-$, $gb \to tH^-$ and their charge conjugate production processes in the $\tan\beta$ vs $m_A$ plane. Other MSSM parameters are fixed at the values noted in the figure caption. Here we correctly take into account the subtraction needed to avoid double counting between the $2 \to 2$ and the $2 \to 3$ production processes [204, 205]. The charged Higgs boson mass is calculated including radiative corrections as contained in ISAJET [182] and the CTEQ4L [197] structure function set is employed.

In Figure 10 (bottom plot), we fold in the BRs of a charged Higgs boson into an ino pair (restricted here to either $\widetilde{\chi}_1^\pm\widetilde{\chi}_2^0$ or $\widetilde{\chi}_1^\pm\widetilde{\chi}_3^0$) multiplied by the BR of the ino pair into a trio of charged leptons $\ell^+\ell^-\ell'^\pm$

(recall that "$\ell$" herein denotes either an electron or a muon), where $\ell$ and $\ell'$ may or may not be of the same flavor. In calculating the leptonic BRs of the inos all conceivable decay chains are taken into
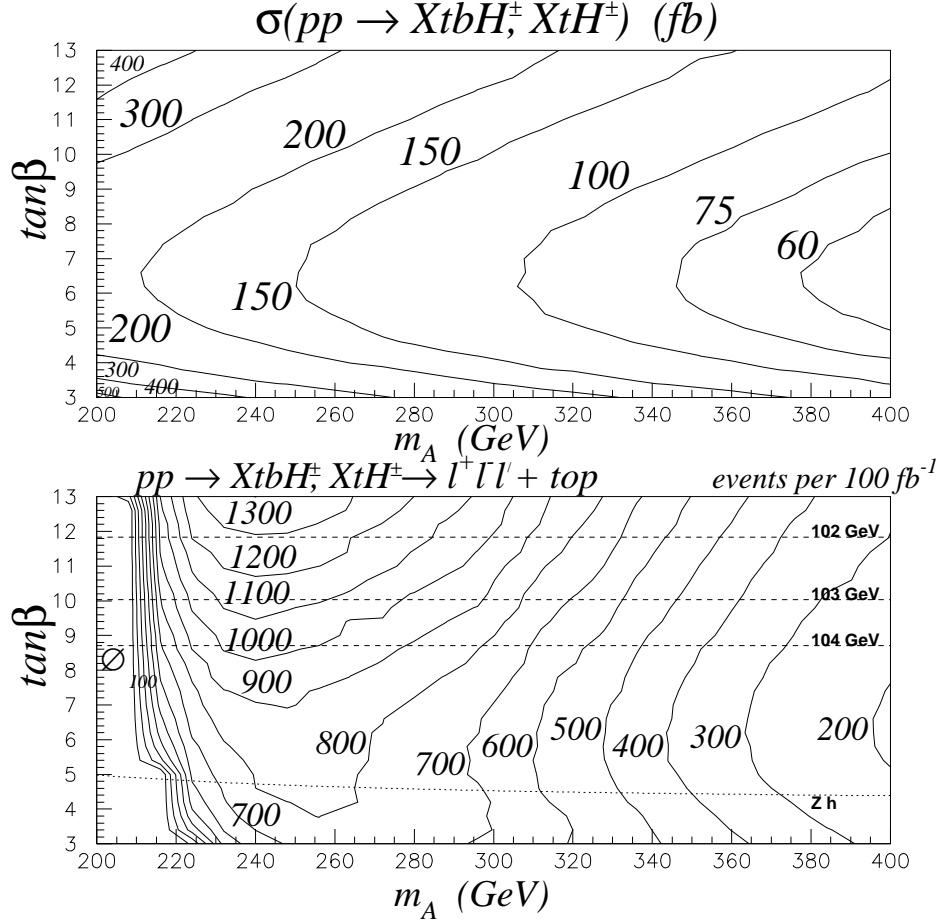


Fig. 10: (top plot) Raw cross-section (in fb) for $gg \to \bar{b}tH^-$, $gb \to tH^-$ and their charge conjugate production processes in the $\tan\beta$ versus $m_A$ plane. The proper subtraction factor to avoid double counting between the $2 \to 2$ and the $2 \to 3$ production processes is included. (bottom plot) Expected number of $pp \to XtbH^\pm, XtH^\pm \to \ell^+\ell^-\ell'^\pm + t$ events per $100\,\mathrm{fb}^{-1}$ at the LHC (with no cuts), assuming the charged Higgs boson decays into $\widetilde{\chi}_1^\pm \widetilde{\chi}_2^0$ or $\widetilde{\chi}_1^\pm \widetilde{\chi}_3^0$. Here $M_2 = 200\,\mathrm{GeV}$ and $\mu = -115\,\mathrm{GeV}$. One-loop formulæ as found in [182, 228] are used to relate $m_{H^\pm}$ to $m_A$. $m_t = 175\,\mathrm{GeV}$ and $m_b = 4.25\,\mathrm{GeV}$. Other MSSM input parameters are: $m_{\tilde{q}} = 1\,\mathrm{TeV}$ for the first two generations, $m_{\tilde{t}_L} = 600\,\mathrm{GeV}$, $m_{\tilde{t}_R} = 500\,\mathrm{GeV}$, $m_{\tilde{b}_R} = 800\,\mathrm{GeV}$, $A_t = 500\,\mathrm{GeV}$, $A_b = 0$; $m_{\tilde{\ell}_R} = 150\,\mathrm{GeV}$, $m_{\tilde{\ell}_L} = m_{\tilde{\nu}}^{soft} = 200\,\mathrm{GeV}$ and $A_\ell = 0$ for all three generations.

account[19]. The plot shows that, assuming an integrated luminosity of $100\,\mathrm{fb}^{-1}$, hundreds to thousands of events are expected for $m_A \leq 400\,\mathrm{GeV}$. The possibility of extracting the SUSY signal exists across the full range of allowed $\tan\beta$ values and for $m_A$ (and $m_{H^\pm}$) $\lesssim 400\,\mathrm{GeV}$ provided the threshold for the $H^\pm \to \widetilde{\chi}_1^\pm \widetilde{\chi}_{\{2,3\}}^0$ decay is exceeded. Higher values of $\tan\beta$ and $m_A \simeq 240\,\mathrm{GeV}$ are optimal choices (quite different than when only the raw production rate is considered). The region from the top of the plot down to the dashed curve marked as '103 GeV' is excluded by the LEP 2 limit on the chargino mass,

[19]Including possible extra minor contributions arising when a neutralino decays into a $\widetilde{\chi}_1^\pm$ (or a $W^\pm$) and one lepton and the $\widetilde{\chi}_1^\pm$ then decays into $\widetilde{\chi}_1^0$ along with the second lepton (or $W^\pm$ decays leptonically). These decay modes yield extra neutrinos in addition to the final products of the main decay modes, but should be experimentally indistinguishable. Possible modes with $\widetilde{\chi}_3^0 \to \widetilde{\chi}_2^0 X$ are also taken into account.

and the region below the dotted curve is excluded by Higgs boson production. As shown on the plot, the upper bound is fairly sensitive to the $m_{\tilde{\chi}_1^\pm}$ limit; and thus in turn very dependent on the values chosen for other MSSM parameters, in particular the higgsino mixing parameter $\mu$ and $M_2$[20], which are chosen to be favorable to our signal in the plot. Also, as mentioned in the previous section, the exact location of the latter bound is fairly loose due to uncertainty in the mass of the light Higgs boson.

The expected number of events is shown again in Figure 11, this time in the $M_2$ versus $\mu$ plane with $\tan\beta$ fixed at 8 and $m_A = 290\,\text{GeV}$ $(m_{H^\pm} \simeq 300\,\text{GeV})$. The shaded region is excluded by the LEP 2 bound on the chargino mass. Again we see that hundreds to thousands of events are possible in un-excluded regions of the parameter space; but it is also apparent that small values of $|\mu|$ are strongly preferred. This is a serious restriction which means that the preferred and un-excluded signal region is just beyond that region probed by LEP 2 (and thus also the region expected to be searched in the first phase of a future $e^+e^-$ linear collider).
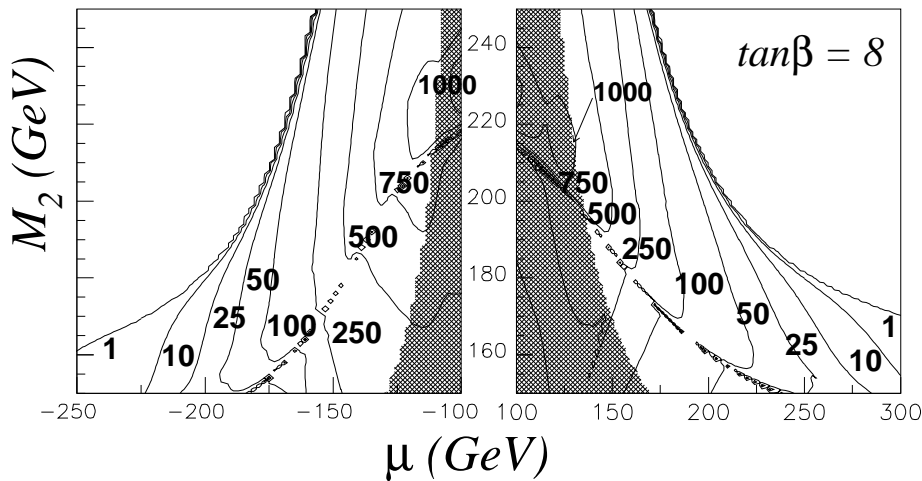


Fig. 11: Expected number of $pp \to XtbH^\pm, XtH^\pm \to \ell^+\ell^-\ell'^\pm + t$ events per $100\,\text{fb}^{-1}$ at the LHC (with no cuts), seen in the $M_2$ versus $\mu$ plane. Here $\tan\beta = 8$ and $m_A = 290\,\text{GeV}$ $(m_{H^\pm} \simeq 300\,\text{GeV})$. Other inputs as in Figure 10.

Figure 12 shows contours for the raw number of three-lepton events $(\ell^\pm\ell^-\ell^+ + p_T^{miss} + t)$ expected at the LHC for $\sqrt{s} = 14\,\text{TeV}$ and $\mathcal{L} = 100\,\text{fb}^{-1}$ in the $M_2$ versus $m_{\tilde{\ell}_R}$ plane before any selection cuts are applied. The soft slepton mass spectrum is fixed by $m_{\tilde{\ell}_L} = m_{\tilde{\nu}}^{soft} = m_{\tilde{\ell}_R} + 50\,\text{GeV}$ (soft slepton masses are assumed to be degenerate for all three generations; the $A_\ell$'s are still kept equal to zero) and $\mu$ is set to $-115\,\text{GeV}$. All other inputs are as in the previous figures. The shaded region is excluded by LEP 2 limits on $m_{\tilde{\chi}_1^\pm}$ (below) and $m_{\tilde{\ell}}$ (left)[21]. We see that over a thousand events are possible. The optimal spot (excluding the sliver region) is at $(m_{\tilde{\ell}_R}, M_2) \approx (110.0\,\text{GeV}, 195.5\,\text{GeV})$ which boasts well over a thousand events.

---

[20]$M_1$ and $M_2$ are the $U(1)_Y$ and $SU(2)_L$ gaugino masses, respectively; Grand Unified Theories (GUTs) predict gaugino unification and $M_1 = \frac{5}{3}\tan^2\theta_W M_2 \approx 0.5032\,M_2 \simeq \frac{1}{2}M_2$, as will be assumed in all numerical calculations.

[21]There is a small "sliver" of allowed parameter space that slices through the excluded region to the left. This is where the charged sleptons are only slightly more massive than the LSP (taken as within 5 GeV) and thus can evade the LEP 2 searches. Note though that then we expect to get soft leptons from the slepton decay and so our signal probably disappears here.
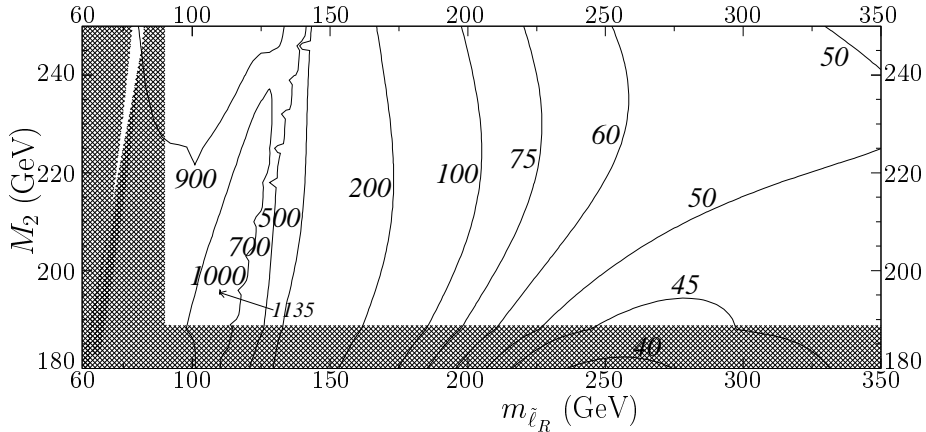
Fig. 12: Expected number of $pp \to XtbH^{\pm}, XtH^{\pm} \to \ell^+\ell^-\ell'^{\pm} + t$ events per $100\,\text{fb}^{-1}$ at the LHC (with no cuts), seen in the $M_2$ versus $m_{\tilde{\ell}_R}$ plane with $\mu$ fixed at $-115\,\text{GeV}$. Other inputs as in Figure 11.

## 5.3 Analysis

Here, we will show how all SM backgrounds can be completely removed, leaving only MSSM processes as irreducible backgrounds in the $3\ell + p_T^{miss} + t$ channel. The relevant SM noise is constituted by $WZ^0$, $Z^0Z^0$, $b\bar{b}Z^0$, $t\bar{t}$, $t\bar{t}\ell^+\ell^-$ (consisting of both $t\bar{t}Z^0$ and $t\bar{t}\gamma^*$, but not their interference), $t\bar{b}W$ and $t\bar{b}W\ell^+\ell^-$ (again, via $Z^0$ and $\gamma^*$) production and decay. As for the MSSM backgrounds, one has to deal with pair production of sleptons, gauginos or squarks/gluinos and with neutral MSSM Higgs bosons produced in association with heavy quark pairs (SM-like $t\bar{t}h$ production is found to merit attention while associated production of the heavier neutral Higgs bosons is negligible).

We simulated the inclusive $H^{\pm} \to 3l$ signal and the MSSM backgrounds at the 5 points in the intermediate $\tan\beta$ region of the MSSM parameter space listed in Table 7. These points were chosen in the favorable regions obtained in the previous section. In each case we have also chosen $m_{\tilde{g}} = 700\,\text{GeV}$, $m_{\tilde{q}} = 1000\,\text{GeV}$, $m_{\tilde{b}_R} = 800\,\text{GeV}$, $m_{\tilde{t}_L} = 600\,\text{GeV}$, $m_{\tilde{t}_R} = 500\,\text{GeV}$ and $A_t = 500\,\text{GeV}$. Rather large gluino and squark masses are chosen to preclude large charged Higgs boson production rate from MSSM cascade decays [223], thus leaving the 'direct' production modes of the previous section as the only numerical relevant contributors at the LHC [224]. Sleptons are chosen to be light in accordance with the discussion in the last section.

Table 7: Simulated MSSM parameter points. All masses in GeV. The event number is the parton-level result $H^{\pm} \to \chi_1^{\pm}\chi_{\{2,3\}}^0 \to 3\ell X$ per $100\,\text{fb}^{-1}$. $M_1 = \frac{1}{2}M_2$ is assumed.

| Point | $\tan\beta$ | $m_{H^{\pm}}$ | $\mu$ | $M_2$ | $m_{\tilde{\ell}_R}$ | $m_{\tilde{\ell}_L}$ | events |
|-------|-------------|---------------|-------|-------|----------------------|----------------------|--------|
| A | 8 | 250 | $-115$ | 200 | 120 | 170 | 1243 |
| B | 10 | 250 | $-115$ | 200 | 120 | 170 | 1521 |
| C | 10 | 300 | $-115$ | 200 | 120 | 170 | 1245 |
| D | 10 | 250 | $+130$ | 210 | 125 | 175 | 1288 |
| E | 10 | 300 | $+130$ | 210 | 125 | 175 | 1183 |

HERWIG 6.3 [181] is used to generate all hard processes[22], fragmentation and showering, with adoption of the default settings [181]. The SUSY spectrum was obtained from ISASUSY 7.58 [182]

---
[22]An exception is the $t\bar{t}\gamma^*$ process, which uses a set of separate subroutines [225].

through the ISAWIG interface [226]. The detector aspects were simulated using CMSJET 4.801 [135], which contains a parameterized description of the CMS detector response; however, since none of our selection cuts depend strongly on unique performance factors of the CMS detector, we expect the analysis here to roughly coincide with what the ATLAS detector environment would yield. The effects of pile-up at high luminosity running of the LHC have not been included.

In order to distinguish between signal and background events, the following selection criteria are applied:

**1.** We require exactly three isolated leptons ($\ell = e,\ \mu$), with $p_T > 20$, 7 and 7 GeV, respectively, all within $|\eta| < 2.4$. The isolation criterion demands that there are no charged particles with $p_T > 1.5$ GeV in a cone of radius $R = 0.3$ radians centered around each lepton track and that the sum of the transverse energy in the ECAL (Electromagnetic Calorimeter of CMS) crystal towers between $R = 0.05$ and $R = 0.3$ radians is smaller than 3 GeV.

**2.** We impose a $Z^0$-veto, i.e., rejection of all di-lepton pairs with opposite charge and same flavor that have an invariant mass in the range $m_Z \pm 10$ GeV.

**3.** We select only events with three or four jets, all with $p_T > 20$ GeV and $|\eta| < 4.5$.

**4.** Among these jets, we look for the combination of three that are most probably coming from a top decay, by minimizing the difference $m_{jjj} - m_t$, $m_{jjj}$ being the invariant mass of the three-jet system. These three jets must have $m_{jjj}$ in the range $m_t \pm 35$ GeV.

**5.** One of the jets must be $b$-tagged (the signed significance of the transverse impact parameter must be $\sigma(ip) = \frac{ip_{xy}}{\Delta ip_{xy}} > 2.5$). The two other jets must have their invariant mass, $M_{jj}$, in the range $m_W \pm 20$ GeV.

**6.** The $p_T$ of the hardest lepton must be less than 80 GeV[23].

**7.** The transverse missing momentum is in the following interval: $50\,\text{GeV} < \not{p}_T < 200\,\text{GeV}$.

**8.** The $p_T$ of the hardest jet is $< 180$ GeV.

**9.** We exploit the 'effective' transverse mass of Ref. [215], by imposing
$$M_{\text{eff}} = \sqrt{2 p_T^{3\ell} \not{p}_T (1 - \cos \Delta\phi)} < 140\,\text{GeV}$$
(where $p_T^{3\ell}$ is the three lepton transverse momentum and $\Delta\phi$ the azimuthal angle between $p_T^{3\ell}$ and $\not{p}_T$).

**10.** In addition, the three-lepton invariant mass, $m_{3\ell}$, must be $< 120$ GeV.

In Table 8 we summarize the signal and background events that remain after applying these criteria, assuming a luminosity of $100\,\text{fb}^{-1}$ and optimizing the selection using the $m_A = 250$ GeV signal. Due to the aforementioned small mass differences in the ino sector, leptons coming from the signal events will often be soft, which explains much of the difference between the numbers in the "$3\ell$ events" column of Table 8 and those from the parton-level analysis in Table 7. Clearly, it is vital to have a low $p_T$ threshold for accepting leptons. Conservatively, here we have set this to 7 GeV for both electrons and muons.

Requiring three tightly isolated leptons in addition to a hadronically reconstructed top quark allows us to eliminate most of the SM backgrounds: $W^\pm Z^0$, $Z^0 Z^0$, $b\bar{b} Z^0$ as well as the initially large $t\bar{t}$ channel. The $t\bar{t}\ell^+\ell^-$ background, resulting from $t\bar{t}Z^0$, $t\bar{t}\gamma^*$ and $t\bar{t}h^0$ production can easily mimic the signature of the signal. However, after applying the $Z^0$-veto, the previously dominant $t\bar{t}Z^0$ component of this background becomes negligible compared to the intrinsic MSSM backgrounds[24]. Among the latter, the channels that survive the selection are squark/gluino and gaugino pair-production (in which we include $\tilde{\chi}\tilde{g}$ too) as well as the associated production of a light Higgs boson with a $t\bar{t}$ pair. In gaugino-gaugino production, a gluon jet can fake one of the three jets from the top decay, but in the next stage of the top reconstruction these events will always be rejected (see Table 8). On the other hand, squark/gluino and

---

[23]This reflects the relatively small mass difference between the parent ino and the daughter ino (the latter is typically the LSP).

[24]The single-top counterparts, $t\bar{b}W^-\ell^+\ell^-$, are sub-leading, as they amount to a $\sim 25\%$ correction to the double-top rates.

Table 8: Number of events after the cuts mentioned in the text at a luminosity of $100\,\mathrm{fb}^{-1}$.

| Process | $3\ell$ events | $Z^0$-veto | 3,4 jets | $m_{jjj} \sim m_t$ | $M_{jj} \sim m_W^\dagger$ | others |
|---|---|---|---|---|---|---|
| $t\bar{t}$ | 847 | 622 | 90 | 30 | 0 | 0 |
| $t\bar{t}Z^0$ | 244 | 34 | 13 | 5 | 0 | 0 |
| $t\bar{t}\gamma^*$ | 18 | 18 | 10 | 3 | 1 | 0 |
| $t\bar{t}h$ | 66 | 52 | 33 | 9 | 3 | 1 |
| $\tilde{\ell}\tilde{\ell}$ | 5007 | 4430 | 475 | 112 | 2 | 0 |
| $\tilde{\chi}\tilde{\chi}$ | 8674 | 7047 | 1203 | 365 | 19 | 3 |
| $\tilde{q}, \tilde{g}$ | 37955 | 29484 | 3507 | 487 | 100 | 0 |
| $tH^+$ (point A) | 251 | 241 | 80 | 23 | 6 | 5 |
| $tH^+$ (point B) | 321 | 298 | 118 | 42 | 13 | 9 |
| $tH^+$ (point C) | 279 | 258 | 100 | 36 | 11 | 7 |
| $tH^+$ (point D) | 339 | 323 | 121 | 48 | 13 | 9 |
| $tH^+$ (point E) | 291 | 278 | 114 | 40 | 10 | 5 |

$^\dagger$Includes $b$-tagging efficiency for the third jet

squark-gaugino background events that pass the top reconstruction cut are likely to have a real top in the final state, or else a $bW^+$ pair.

The events that pass the top reconstruction cut can be distinguished from the signal by noticing that MSSM cascade decays will typically produce harder leptons, more and harder jets, as well as a larger amount of missing $p_T$, with respect to the signal. Also, one can further suppress these backgrounds by putting an upper limit on the three lepton invariant mass and on the mass made up from the $p_T$ of the three leptons and the $\not{p}_T$. In particular, these last two variables are very effective if the mass of the Higgs boson is just above the chargino+neutralino threshold, i.e., for $m_A \simeq 250\,\mathrm{GeV}$. For larger charged Higgs boson masses, the lepton $p_T$ cut-off increases and the discriminative power of this variable is reduced.

### 5.4 Conclusions

The inability to cover the intermediate $\tan\beta$ region by exploiting charged Higgs boson decays into SM particles prompted us to carefully investigate the potential offered by other channels. In SUSY models such as the MSSM, it is natural to explore to this end the interactions between charged Higgs bosons and the inos. Assuming that squarks and gluinos are heavy enough so that the production rates of $H^\pm$ states via cascade decays of sparticles are negligible, the obvious place to look is the decay of a charged Higgs boson itself into a chargino-neutralino pair.

The limited $XtH^-$ (and the charge conjugate) production rate precludes exploration for large values of $m_{H^\pm}$; however, for $m_{H^\pm} \stackrel{<}{\sim} 300\,\mathrm{GeV}$, a signal could well be observed above the background, provided that: (1) $\mu$ and $M_2$ are not much above the current LEP restrictions from ino searches; (2) sleptons are sufficiently light. We are thus guided to a region of parameter space where both the ino and the Higgs boson spectra will be accessible at the LHC, making it a quite reasonable choice for initial phenomenological studies. (A more refined analysis encompassing a wider span of the MSSM parameter space will be ready in due course [227].)

Before closing, we would like to remark on possible improvements in our analysis. One such improvement would be the inclusion of the leptonic decays of the top, in which case one can look for a signature with four leptons and a $b$-jet in the final state [228][25]. After applying a reasonable set of

---

[25]In fact, it should be noted that both leptonic and hadronic decays of top quarks (and of inos) have been allowed in the generated events of the present analysis, although the former have negligible impact because of the enforced top mass reconstruction procedure.

cuts on the lepton momenta, we find the SM noise can be completely eliminated. Furthermore, rejecting events with more than two jets and limiting the $E_T^{miss}$ eliminate the background from squark/gluino pair production. Ino (again, including $\widetilde{\chi}\widetilde{g}$) and slepton pair production as well as associated production of a light neutral Higgs boson with a heavy quark pair then constitute the principal backgrounds, though the former are largely reduced by requiring one $b$-tagged jet.

Another extension under development is the study of charged Higgs boson decays including the higher ino mass eigenstates ($\widetilde{\chi}_2^\pm$ and $\widetilde{\chi}_4^0$) for $m_{H^\pm} \gtrsim 300\,\text{GeV}$. For the highest mass inos, the number of possible decay chains ending in the LSP can quickly multiply. Such decay modes may have preferred regions of parameter space for $\mu$ and $M_2$ quite different from the cases presented here.

Although limited to some restricted region of parameter space, we have managed with our present analysis to cover some portion of the elusive intermediate $\tan\beta$ region in the MSSM; and we regard our results thus far as encouraging enough to look further into these more exotic charged Higgs boson decay modes [227].

## 6. $H^\pm$ from SUSY Cascade Decays at the LHC

In this section, we analyze the cascade decays of the scalar quarks and gluinos of the MSSM, which are abundantly produced at the LHC, into heavier charginos and neutralinos which then decay into the lighter ones and charged Higgs particles. We show that these decays can have substantial branching fractions. The production rates of these Higgs bosons can be much larger than those from the direct production mechanisms, in particular for intermediate values of $\tan\beta$. An event generator analysis shows that the detection of $H^\pm$ bosons produced through this mechanism is possible.

### 6.1 Motivation

As previously recalled, for masses $m_{H^\pm} > m_t$, the two production mechanisms with potentially sizeable cross sections at the LHC are the $2 \to 3$ and $2 \to 2$ processes — shown in Figure 1 — which have to be properly combined to avoid double counting [204–207]. However, the cross sections are rather small: even for the extreme values, $\tan\beta = 2$ and 40, they hardly reach the level of a picobarn for a charged Higgs boson mass $m_{H^\pm} = 200\,\text{GeV}$. For intermediate values of $\tan\beta$ and/or larger $H^\pm$ masses, the cross sections are too small for these processes to be useful. For instance, for $\tan\beta = 10$, the cross section is below the level of a few femtobarn for $m_{H^\pm} \gtrsim 250\,\text{GeV}$. The other mechanisms for $H^\pm$ production at hadron colliders give even smaller cross sections [206, 224].

In a recent paper, Ref. [223], it has been shown that there is a potentially large source of the $H^\pm$ bosons of the MSSM at the LHC: the cascade decays of squarks and gluinos, which are abundantly produced in $pp$ collisions, thanks to their strong interactions. These squarks and gluinos can decay into the heavy charginos and neutralinos and if enough phase space is available, the latter particles could then decay into the lighter charginos/neutralinos, and $H^\pm$ bosons, with substantial branching ratios.

In this section, we summarize the production of $H^\pm$ particles through these cascade decays at the LHC and describe a Monte Carlo simulation which shows that these final states can be possibly detected in some regions of the MSSM parameter space.

### 6.2 $H^\pm$ Bosons from Cascade Decays in the MSSM

At the LHC the total squark and gluino production cross section is $\sigma(\tilde{q} + \tilde{g}) \sim 110\,(3)\,\text{pb}$ for $m_{\tilde{g}} \sim m_{\tilde{q}} \sim 0.5\,(1)\,\text{TeV}$ leading to a large, $\sim 3 \cdot 10^7$ to $10^6$, number of events with an accumulated luminosity of $\mathcal{L} \sim 300\,\text{fb}^{-1}$. These squarks and gluinos can decay into the heavy charginos and neutralinos, $\chi_2^\pm, \chi_3^0$ and $\chi_4^0$ with significant branching fractions, a few ten percent. If enough phase space is available, the latter particles could then decay into the lighter charginos/neutralinos, $\chi_1^\pm, \chi_1^0$ and $\chi_2^0$, and $H^\pm$ bosons, with branching ratios of the order of a few ten percent, again. A key point here, is that the coupling of the Higgs bosons to chargino and neutralino states is maximal for higgsino–gaugino mixed states [229],

while the gauge boson couplings to neutralinos are maximal for higgsino–like states. In the gaugino–like or higgsino–like regions, this results into the dominance of the decays of the heavier charginos and neutralinos into the lighter ones and Higgs bosons compared to the same decays with gauge boson final states.

The total number of charged Higgs particles produced at the end of the chain

$$pp \to \tilde{g}\tilde{g}, \tilde{q}\tilde{q}, \tilde{q}\tilde{g} \to \chi_2^{\pm}, \chi_3^0, \chi_4^0 + X \to \chi_1^{\pm}, \chi_2^0, \chi_1^0 + H^{\pm} + X \tag{14}$$

could be rather large (of the order of a few 10.000 to a few 100.000 events for the high–luminosity option) in favorable regions of the parameter space. The interesting and important point to note is that the rate of $H^{\pm}$ production does not depend very crucially on $\tan\beta$ unlike in the other mechanisms mentioned above — Note also that $H^{\pm}$ bosons could be searched for, if kinematically possible, in the direct decays of heavy third generation squarks into their lighter partners or in direct gluino three–body decays. This is illustrated below, in two scenarii with the intermediate value $\tan\beta = 10$ and where the universality of the gaugino masses has been assumed at the GUT scale, leading to the relation $M_2 \simeq 2M_1 \simeq M_3/3 \simeq m_{\tilde{g}}/3$ at the weak scale.
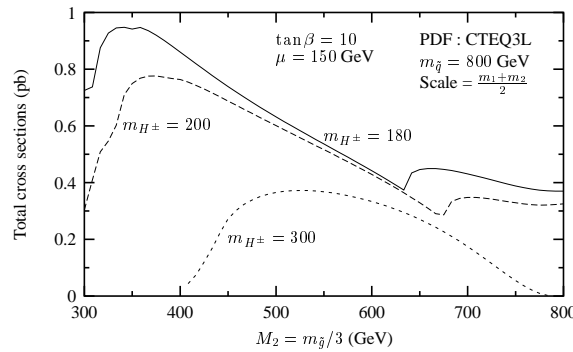


Fig. 13: Cross sections times branching ratios for gluinos decaying into squarks and squarks decaying through cascades into $H^{\pm}$ bosons as functions of $M_2$ with $\mu = 150$ GeV and $\tan\beta = 10$. $m_{\tilde{q}} = 900$ GeV and $m_{\tilde{g}} = 3M_2$.

Scenario 1 (Figure 13): Here gluinos (with $m_{\tilde{g}} = 3M_2$) are heavier than squarks ($m_{\tilde{q}} = 900$ GeV) and therefore $\tilde{g} \to \tilde{q}q$ occurs 100% of the time. The higgsino mass parameter has been chosen to be small, $\mu = 150$ GeV, so that all squarks — in particular those of the first two generations — will mainly decay into the heavier charginos and neutralinos which are gaugino like with masses $m_{\chi_2^+} \sim m_{\chi_4^0} \sim 2m_{\chi_3^0} \sim M_2$. For large enough $M_2$, there is then enough phase space for the decay of the heavier gauginos into the lighter higgsino states, with masses $m_{\chi_1^+} \sim m_{\chi_1^0} \sim m_{\chi_2^0} \sim |\mu|$, and $H^{\pm}$ bosons to occur. For small $M_2$ values, the states $\chi_{3,4}^0$ and $\chi_2^+$ are not heavy enough for the decays into $H^{\pm}$ bosons to occur, in particular for large $m_{H^{\pm}}$. When these decays are allowed, $\sigma \times \text{BR}(\to H^{\pm})$ values of the order of 1 pb for $m_{H^{\pm}} \sim 180$ GeV and 0.3 pb for $m_{H^{\pm}} \sim 300$ GeV can be reached. For increasing values of $M_2$, the gluino mass increases and the cross sections for associated squark and gluino and gluino pair production drop and $\sigma \times \text{BR}(\to H^{\pm})$ decreases accordingly; at some stage, only the cross section for squark production survives $m_{\tilde{q}}$ being fixed. The decrease of $\sigma \times \text{BR}(\to H^{\pm})$ with increasing $M_2$ is also due to the more suppressed phase space for $\tilde{q} \to q'\chi_2^{\pm}, q\chi_4^0$ since for large $M_2$, $m_{\chi_4^0}, m_{\chi_2^{\pm}} \sim M_2$. For even larger $M_2$ values, $M_2 \gtrsim 650$ GeV, the channel $\chi_3^0 \to H^{\pm}\chi_1^{\mp}$ opens up, and since the phase space is more favorable, because $m_{\chi_3^0} \sim M_2/2$, $\sigma \times \text{BR}(\to H^{\pm})$ increases again.

Scenario 2 (Figure 14): Here the scalar partners of light quarks are heavier than stops which are heavier than gluinos, $m_{\tilde{q}} = 1.2m_{\tilde{g}}$ with $m_{\tilde{g}} \sim 3M_2 = 800$ GeV. Gluinos will decay mainly into three–body final states mediated by the exchange of top squarks which have a smaller virtuality. Note that the cross sections for squark and gluino production are constant and the variation of $\sigma \times \text{BR}(H^{\pm})$ is only due
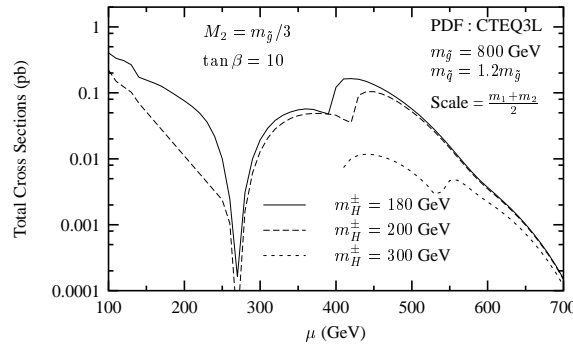
Fig. 14: Cross sections times branching ratios for squarks decaying into gluinos with the gluinos decaying through cascades into $H^\pm$ bosons, as as functions of $\mu$ for $\tan\beta = 10$. $m_{\tilde{g}} = 800$ GeV and $m_{\tilde{q}} = 1.2 m_{\tilde{g}}$.

to the variation of the branching ratios $\mathrm{BR}(\tilde{g} \to \chi^0_{3,4}qq, \chi^\pm_2 qq')$ and $\mathrm{BR}(\chi^0_{3,4}, \chi^\pm_2 \to \chi^\pm_1 H^\mp, \chi^0_{1,2}H^\pm)$. One sees that $\sigma \times \mathrm{BR}(H^\pm)$ is relatively large for small values of $\mu$ and $m_{H^\pm}$, when the gaugino–like heavy $\chi$ states are light enough for the decays $\chi^0_4 \to \chi^\pm_1 H^\mp$ and $\chi^\pm_2 \to \chi^0_{1,2}H^\pm$ to occur. In the mixed region, $\mu \sim M_2$, the mass difference between the heavy and light $\chi$ states are too small to allow for decays in $H^\pm$ bosons. For large values of $\mu$, $\sigma \times \mathrm{BR}(H^\pm)$ increases to reach values of the order of $\sim 0.1$ pb for $m_{H^\pm} \sim 200$ GeV (in particular when the additional channels $\chi^0_3 \to \chi^\pm_1 H^\mp$ open up) before it drops out because of the gradually closing phase space for the decays $\tilde{g} \to q\bar{q}\chi^0_{3,4}, qq'\chi^\pm_2$.

Thus, large samples of $H^\pm$ bosons can be produced in these SUSY cascade decays. In the regions of $m_{H^\pm}$ and $\tan\beta$ values that we are interested in, the dominant decay modes of the charged Higgs bosons are [80, 230] $H^+ \to t\bar{b}$ ($\sim 90\%$ sufficiently above the $tb$ threshold) followed by $H^+ \to \tau^+\nu_\tau$ ($\sim 10\%$). In the simulation which we present below, we will focus on the latter decays which are easier to detect in the jet environment of the LHC.

### 6.3  An Event Generator Analysis

Selecting the one-prong hadronic decays of these tau leptons will allow us to exploit the tau polarization effects in our analysis. Therefore, the signature of $H^\pm$ bosons produced in SUSY cascade decays consists of one hard $\tau$–jet plus additional hard jets (often $b$-jets) accompanied by a large amount of missing energy due to the presence of the lightest neutralinos and the neutrinos.

The main SM processes leading to the same signature are top pair production, $pp \to t\bar{t}$, with one top decaying hadronically and the other one decaying leptonically, and QCD $W^\pm + jets$ production with $W^\pm \to \tau^\pm\nu_\tau$. As we will argue below, these SM backgrounds can be efficiently suppressed. However, a more difficult task will be to distinguish the $H^\pm$ signal from other SUSY cascade decay processes. As was discussed above, all squark and gluino production in colliders will end up in lightest neutralinos and fermions through cascade decays via gauginos and sleptons. Events in which these fermions are taus will mimic the signal. Hence, a good understanding of the nature of these SUSY backgrounds will be needed prior to a search for charged Higgs bosons in cascade decays.

We performed a Monte Carlo simulation of the production signal and the main backgrounds for the following scenario: $m_{H^\pm} = 200$ GeV, $\tan\beta = 10$, $\mu = 450$ GeV, $M_2 = 2M_1 = 200$ GeV, $m_{\tilde{g}} = 800$ GeV, $m_{\tilde{q}} = 1.2 m_{\tilde{g}}$ and $m_{\tilde{l}} = 300$ GeV. The signal and background events were generated with PYTHIA 6.152 [100]. To account for the tau polarization, PYTHIA was interfaced with the TAUOLA [45] package. The detector aspects were simulated using CMSJET 4.801 [135], which contains a parameterized description of the CMS detector response. The effects of pile–up at high luminosity running of the LHC have not been included. The features that will allow to distinguish the $H^\pm$ signal from the SM and SUSY backgrounds are summarized below.
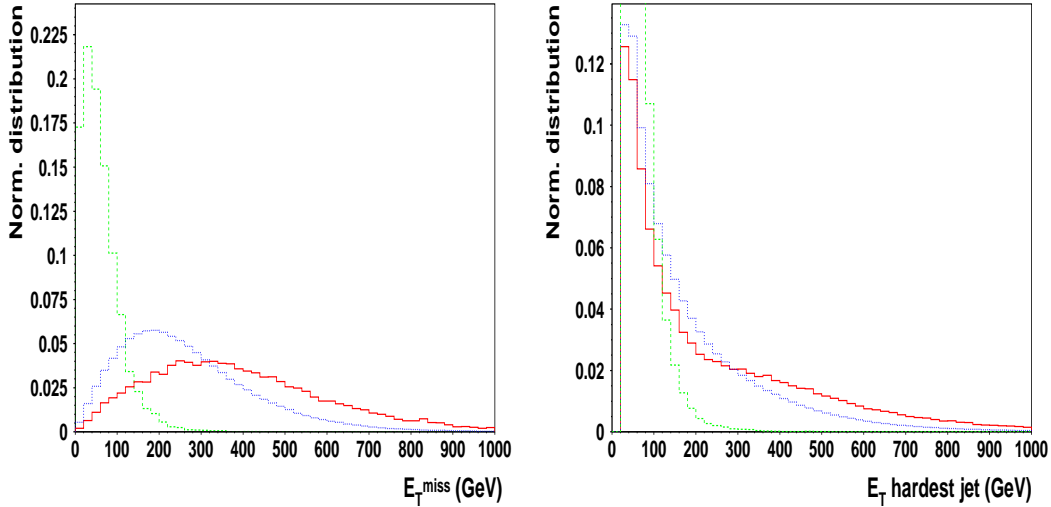
Fig. 15: Normalized distribution of $E_T^{miss}$ (left) and normalized $E_T$ distribution of the hardest jet in the event (right) for the $t\bar{t}$ background (green–light dashed line), the SUSY cascade background (blue–medium line) and the charged Higgs signal (red–dark line).

In the left–hand panel of Figure 15, the $E_T^{\text{miss}}$ distribution, normalized to the number of events, is shown for the $t\bar{t}$ background, the SUSY cascade background and the charged Higgs boson signal. Demanding a very large $E_T^{\text{miss}}$ in the events allows us to eliminate the $t\bar{t}$ background. Also part of the SUSY cascade background can be suppressed relative to the signal due to a slight excess of missing energy in cascade decays including charged Higgs bosons. Similarly, making a hard requirement on the $E_T$ of the hardest jet in the event will help in the background rejection. In the right–hand panel of Fig. 15, this $E_T$ distribution is shown and it is clear that the SM processes can be efficiently suppressed.

After eliminating the SM backgrounds, the more difficult task remains to discriminate the $H^{\pm}$ bosons from the other particles in the SUSY cascade decays. $\tau$–leptons in the cascade backgrounds originate from charginos and neutralinos in the intermediate state. In our scenario, charginos decay predominantly into $W^{\pm}$ bosons and neutralinos into $Z^0$ bosons. Taus coming from these particles will typically have a softer spectrum than the ones coming from a 200 GeV charged Higgs boson. Therefore we impose a lower limit on the transverse energy of the $\tau$-jet, $E_T^{\tau-\text{jet}} > 120$ GeV, which is well above the mass of the $W^{\pm}$ and $Z^0$ bosons. As an upper limit on $E_T^{\tau-\text{jet}}$, we chose the mass of the charged Higgs boson.

The significant presence of $W^{\pm}$'s in the SUSY cascade background also needs to exploit the tau polarization effects [191] explained in section 2.: by selecting events in which the fraction of the $\tau$-jet transverse momentum carried by the charged pion is large, the SUSY background involving $W^{\pm}$ bosons can be suppressed relative to the signal. The tau leptons in the background coming from either $\tilde{\tau}$ and $Z^0$ decays or MSSM neutral Higgs boson (in particular $H$ and $A$) decays cannot be suppressed this way.

These considerations lead us to the following selection criteria in order to distinguish between signal and background events:

*i)* The transverse missing energy $E_T^{miss}$ in the event should be larger than 300 GeV.

*ii)* The hardest jet in the event should have $E_T > 400$ GeV.

*iii)* Events with more than five jets are rejected.

*iv)* We require exactly one hadronically decaying tau (1-prong) i.e. we demand a narrow jet within $|\eta| < 2.5$ which should contain a hard charged track with $p_T > 5$ GeV in a cone of $\Delta R = 0.15$ radians around the calorimeter jet axis, and it should be isolated i.e. no charged tracks with $p_T > 2$ GeV are allowed in a cone of $\Delta R = 0.4$ radians around the axis.

*v*) The $E_T$ of the $\tau$-jet, defined as the $E_T$ reconstructed in a cone of $\Delta R = 0.4$ radians around the jet axis, should be in the interval: $120\,\text{GeV} < E_T^{\tau-jet} < 200\,\text{GeV}$.

*vi*) More than 80% of the $\tau$-jet transverse energy should be carried by the charged track: see the requirement (3) in section 2..

Events that satisfy conditions (*i*) and (*ii*) can be efficiently triggered on using the jet and missing energy triggers. If the above selection criteria are applied, we obtain the following numbers for an integrated luminosity of 100 fb$^{-1}$: 17 events for the $H^\pm$ boson signal and 21 events for the SUSY cascade background, while the $t\bar{t}$ background is completely suppressed. This results in a significance $S/\sqrt{B}$ of 3.5, meaning that a $5\sigma$-observation of $H^\pm$ bosons produced in SUSY cascade decays could be made with about 2 years of high luminosity data of the LHC, assuming the above physics scenario and provided the SUSY background processes are well understood.

## 6.4  Conclusions

We have shown that charged Higgs boson production from cascade decays of strongly interacting SUSY particles can occur with large rates, in favorable domains of the MSSM parameter space. This is true, in particular for intermediate values of $\tan\beta$ where the standard production processes are disfavored because of the smallness of the $H^-tb$ Yukawa coupling. We have shown that the SM background to the cascade production can be efficiently suppressed. By exploiting the characteristics of the $\tau$-jet in the final state, the $H^\pm$ signal can be made visible above the other SUSY cascade decays.

Our strategy to distinguish the $H^\pm$ bosons from other cascade processes depends on prior knowledge of the properties of the SUSY background. Therefore, before any reasonable search for charged Higgs bosons in cascade decays can take place, the general nature of SUSY cascade decays should be sufficiently understood in order to select the kinematical region in which the signal is enhanced with respect to the SUSY background. Due to the complexity of the signature and the dependence on calorimetric energy resolutions, these results would need to be confirmed by a more detailed simulation. However, our current findings point towards the conclusion that there exists a potential for observing charged Higgs bosons produced in SUSY cascade decays at the LHC, provided the nature of the SUSY background is well understood.

A similar analysis, dealing with the production of the neutral Higgs particles of the MSSM through the cascade decays of squarks and gluinos is under way [231].

## 7.  Summary

We have investigated the feasibility of detecting various signatures of the charged Higgs boson in order to provide a complete coverage for $H^\pm$ searches in upcoming experiments at the Tevatron and at the LHC.

In the threshold region, i.e., for $m_{H^\pm} \sim m_t$, the $gg \to tbH^\pm$ process has been used to correctly account for the $H^\pm$ production and decay phenomenology in this region of parameter space instead of the usual narrow width approximation. It is found that a significant charged Higgs boson signal can be extracted in the channel $H^\pm \to \tau^\pm\nu_\tau$ after an integrated luminosity of 15 fb$^{-1}$ at the Tevatron Run 2 while the factorization approach used in the narrow with approximation would not predict such a favorable signal. The case of the LHC, which is further complicated by the potential problem of double counting when calculating the inclusive cross section, is currently being studied.

In models with singlet neutrinos in large extra dimensions, the process $H^- \to \tau_L^- \psi + c.c.$ — which is completely suppressed in the 2HDM — can be enhanced thanks to the large number of Kaluza-Klein states of the right handed bulk neutrino. Such a signal can be observed at the LHC with significances exceeding 5-$\sigma$. However, in order to identify the scenario that is realized (2HDM-II or large extra dimensions) both the transverse charged Higgs mass and the fraction of the energy carried away by charged

tracks in the one-prong $\tau$ decays must be reconstructed. Further evidence for large extra dimensions would come the measurement of the polarization asymmetry.

In the intermediate $\tan\beta$ region, the charged Higgs boson decays to SM particles do not yield any significant discovery potential. To cover this region of the parameter space, charged Higgs decays into chargino-neutralino pairs have been studied. It is demonstrated that, by searching for a three-lepton final state with a top quark and a large missing energy resulting from the $gg \to tbH^\pm$ where the charged Higgs decays to $\tilde{\chi}_1^\pm \tilde{\chi}_2^0$ or $\tilde{\chi}_1^\pm \tilde{\chi}_3^0$, a significant charged Higgs signal could be extracted for intermediate $\tan\beta$ values and $m_{H^\pm} \stackrel{<}{\sim} 300$ GeV. Further analysis is in progress aiming to extend the coverage to higher charged Higgs boson masses.

A significant source of charged Higgs boson production is the cascade decays of SUSY particles (squarks and gluinos) also sensitive to the intermediate $\tan\beta$ region where, as previously mentioned, the SM charged Higgs boson productions and decays yield no discovery potential. The subsequent decay of the charged Higgs boson into the $\tau$-lepton has been studied taking advantage of the polarization effects in the $\tau$-jet final state. It is determined that a significant charged Higgs boson signal can be observed through these cascade decays of SUSY particles provided the SUSY background is well understood.

The charged Higgs boson mass can be determined in $H^\pm \to tb$ and $H^\pm \to \tau^\pm \nu_\tau$ where the precisions range from 0.5% at $\sim 200$ GeV to 1.8% at $\sim 500$ GeV for an integrated luminosity of 300 fb$^{-1}$. By measuring the rate of $H^\pm \to \tau^\pm \nu_\tau$, $\tan\beta$ can be determined with precisions ranging from 7.4% at $\tan\beta = 20$ to 5.4% at $\tan\beta = 50$ for an integrated luminosity of 300 fb$^{-1}$ and assuming a 10% uncertainty on the luminosity.

The studies discussed here are the necessary continuation of previous work and in the process, reveal the enormous potential of the charged Higgs boson:

- To understand the structure of the Higgs sector through the determination of $m_{H^\pm}$ and $\tan\beta$ and to probe the decoupling limit of the MSSM, thus distinguishing between the SM and the MSSM, particularly in the $H^\pm \to \tau^\pm \nu_\tau$ channel. Indeed, the scope of the parameter space covered by this channel is comparable to the reach of the $A/H \to \tau\tau$ channel in the neutral Higgs sector.

- To provide evidence — or not — of large extra dimensions, the existence of which, especially at the electroweak scale, would constitute the solution to the outstanding hierarchy problem.

- To explore the SUSY particle arena and thus providing various signatures whose detection will constitute evidence of the existence of these exotic particles.

## References

[1] P. W. Higgs, Phys. Lett. **12** (1964) 132 and Phys. Rev. **145** (1966) 1156; F. Englert and R. Brout, Phys. Rev. Lett. **13** (1964) 321; G. S. Guralnik, C. R. Hagen and T. W. Kibble, Phys. Rev. Lett. **13** (1964) 585.

[2] For reviews on the Higgs sector in the Standard Model and in its supersymmetric extensions, see J.F. Gunion, H.E. Haber, G.L. Kane, S. Dawson, The Higgs Hunter's Guide (Addison-Wesley, Reading, MA 1990), Erratum: hep-ph/9302272.

[3] LEP Collaborations, CERN-EP/2001-055 (2001), hep-ex/0107029.

[4] LEP Higgs Working Group, hep-ex/0107030.

[5] See e.g. T. Hambye and K. Riesselmann, Phys. Rev. **D55** (1997) 7255.

[6] M. Carena, M. Quirós and C. Wagner, Nucl. Phys. **B461** (1996) 407; H. Haber, R. Hempfling and A. Hoang, Z. Phys. **C75** (1997) 539.

[7] S. Heinemeyer, W. Hollik and G. Weiglein, Phys. Rev. **D58** (1998) 091701, hep-ph/9806250, Phys. Lett. **B440** (1998) 296, Phys. Lett.**B455** (1999) 179.

[8] R.-J. Zhang, Phys. Lett. **B447** (1999) 89; J. R. Espinosa and R. J. Zhang, JHEP **0003**, 026 (2000), Nucl. Phys. **B586** (2000) 3.

[9] A. Brignole, G. Degrassi, P. Slavich and F. Zwirner, hep-ph/0112177.

[10] M. Carena *et al.*, Report of the Tevatron Higgs Working Group, hep-ph/0010338.

[11] CMS Coll., Technical Proposal, report CERN/LHCC/94-38 (1994).

[12] ATLAS Coll., ATLAS Detector and Physics Performance: Technical Design Report, Volume 2, report CERN/LHCC/99-15 (1999).

[13] D. Zeppenfeld, R. Kinnunen, A. Nikitenko and E. Richter-Was, Phys. Rev. **D62** (2000) 013009.

[14] A. Bialas and P. V. Landshoff, Phys. Lett. **B256** (1991) 540; J.-R. Cudell and O.F. Hernandez, Nucl. Phys. **B471** (1996) 471; V. A. Khoze, A. D. Martin and M. G. Ryskin, hep-ph/0111078 and references therein.

[15] M. Spira, Fortschr. Phys. **46** (1998) 203.

[16] S. Dawson, A. Djouadi and M. Spira, Phys. Rev. Lett. **77** (1996) 16.

[17] A. Djouadi, M. Spira and P.M. Zerwas, Phys. Lett. **B264** (1991) 440; S. Dawson, Nucl. Phys. **B359** (1991) 283; D. Graudenz, M. Spira and P.M. Zerwas, Phys. Rev. Lett. **70** (1993) 1372; S. Dawson and R.P. Kauffman, Phys. Rev. **D49** (1994) 2298; M. Spira, A. Djouadi, D. Graudenz and P.M. Zerwas, Phys. Lett. **B318** (1993) 347, Nucl. Phys. **B453** (1995) 17.

[18] R.V. Harlander, Phys. Lett. **B492** (2000) 74.

[19] R. V. Harlander and W. B. Kilgore, hep-ph/0201206.

[20] M. Krämer, E. Laenen and M. Spira, Nucl. Phys. **B511** (1998) 523.

[21] S. Catani, D. de Florian and M. Grazzini, JHEP **0105** (2001) 025.

[22] R. V. Harlander and W. B. Kilgore, Phys. Rev. **D64** (2001) 013015.

[23] S. Catani, D. de Florian, M. Grazzini and P. Nason, these proceedings.

[24] V. Drollinger, T. Muller and D. Denegri, hep-ph/0111312.

[25] T. Binoth, J.P. Guillet, E. Pilon and M. Werlen, Eur. Phys. J. **C16** (2000) 311.

[26] Z. Bern, A. De Freitas and L.J. Dixon, JHEP **09** (2001) 037.

[27] S. Catani, D. de Florian and M. Grazzini, JHEP **0201** (2002) 015.

[28] S. Frixione, P. Nason and G. Ridolfi, Nucl. Phys. **B383** (1992) 3; S. Frixione, Nucl. Phys. **B410** (1993) 280; U. Baur, T. Han and J. Ohnemus, Phys. Rev. **D48** (1993) 5140, Phys. Rev. **D51** (1995) 3381, Phys. Rev. **D48** (1996) 1098, Phys. Rev. **D57** (1998) 2823.

[29] L.J. Dixon, Z. Kunszt and A. Signer, Phys. Rev. **D60** (1999) 114037.

[30] T.G. Rizzo, Phys. Rev. **D22** (1980) 389; W.-Y. Keung and W.J. Marciano, Phys. Rev. **D30** (1984) 248; R.N. Cahn, Rep. Prog. Phys. **52** (1989) 389 V. Barger et al., Phys. Rev. **D49** (1994) 79.

[31] M. Dittmar and H. Dreiner, the LHC," Phys. Rev. **D55** (1997) 167.

[32] N. Kauer and D. Zeppenfeld, Phys. Rev. **D65** (2002) 014021.

[33] R.K. Ellis and S. Veseli, Phys. Rev. **D60** (1999) 011501 and Nucl. Phys. **B511** (1998) 649; J.M. Campbell and R.K. Ellis, Phys. Rev. **D62** (2000) 114012.

[34] T. Han, G. Valencia and S. Willenbrock, Phys. Rev. Lett. **69** (1992) 3274.

[35] A. Djouadi and M. Spira, Phys. Rev. **D62** (2000) 014004.

[36] D. Rainwater and D. Zeppenfeld, JHEP **9712** (1997) 005.

[37] D. Rainwater, D. Zeppenfeld and K. Hagiwara, Phys. Rev. **D59** (1999) 014037; T. Plehn, D. Rainwater and D. Zeppenfeld, Phys. Rev. **D61** (2000) 093005.

[38] D. Rainwater and D. Zeppenfeld, Phys. Rev. **D60** (1999) 113004, (E) *ibid.* **D61** (1999) 099901.

[39] N. Kauer, T. Plehn, D. Rainwater and D. Zeppenfeld, Phys. Lett. **B503** (2001) 113.

[40] T. Plehn, D. Rainwater and D. Zeppenfeld, Phys. Lett. **B454** (1999) 297.

[41] V. Del Duca, W. Kilgore, C. Oleari, C. Schmidt and D. Zeppenfeld, Phys. Rev. Lett. **87** (2001) 122001, Nucl. Phys. **B616** (2001) 367.

[42] G. Azuelos et al., section D of these proceedings.

[43] S. Dawson, R.P. Kauffman, Phys. Rev. Lett. **68** (1992) 2273; R.P. Kauffman, S.V. Desai, D. Risal, Phys. Rev. **D55** (1997) 4005, (E) *ibid.* **D58** (1998) 119901, Phys. Rev. **D59** (1999) 057504.

[44] J. Campbell and R. K. Ellis, hep-ph/0202176.

[45] R. Decker, S. Jadach, M. Jezabek, J.H. Kühn and Z. Was, Comp. Phys. Comm. **76** (1993) 361, *ibid* **70** (1992) 69; *ibid.* **64** (1991) 275; CERN-TH-6195 (1991) and CERN-TH-5856 (1990).

[46] H. Chehime and D. Zeppenfeld, Phys. Rev. **D47** (1993) 3898; D. Rainwater, R. Szalapski and D. Zeppenfeld, Phys. Rev. **D54** (1996) 6680.

[47] J. Campbell and R.K. Ellis, http://theory.fnal.gov/people/ellis/Programs/mcfm.html

[48] M. Sapinski and D. Cavalli, Acta Phys. Polon. **B32** (2001) 1317; E. Richter-Was and M. Sapinski, Acta Phys. Polon. **B30** (1999) 1001.

[49] D. Green, K. Maeshima, R. Vidal, W. Wu and S. Kunori, FERMILAB-FN-0705.

[50] F. Maltoni, D. Rainwater and S. Willenbrock, hep-ph/0202205.

[51] W. Beenakker, S. Dittmaier, M. Krämer, B. Plümper, M. Spira and P.M. Zerwas, Phys. Rev. Lett. **87** (2001) 201805.

[52] L. Reina and S. Dawson, Phys. Rev. Lett. **87** (2001) 201804.

[53] D.A. Dicus and S. Willenbrock, Phys. Rev. **D39** (1989) 751.

[54] J. Kwiecinski, A.D. Martin and A.M. Stasto, Phys. Rev. **D56** (1997) 3991; M.A. Kimber, A.D. Martin and M.G. Ryskin, Eur. Phys. J. **C12** (2000) 655.

[55] T. Han and S. Willenbrock, Phys. Lett. **B273** (1991) 167.

[56] T. Han and R. Zhang, Phys. Rev. Lett. **82** (1999) 25; T. Han, A. S. Turcot and R. Zhang, Phys. Rev. **D59** (1999) 093001.

[57] D. de Florian, M. Grazzini and Z. Kunszt, Phys. Rev. Lett. **82** (1999) 5209.

[58] A. D. Martin, R. G. Roberts, W. J. Stirling and R. S. Thorne, Eur. Phys. J. **C18** (2000) 117.

[59] G. L. Bayatian *et al.*, CMS Technical Proposal, report CERN/LHCC/94-38x (1994); R. Kinnunen and D. Denegri, CMS NOTE 1997/057; R. Kinnunen and A. Nikitenko, CMS TN/97-106; R. Kinnunen and D. Denegri, hep-ph/9907291.

[60] Y. L. Dokshitzer, S. I. Troian and V. A. Khoze, Sov. J. Nucl. Phys. **46** (1987) 712; J. D. Bjorken, Phys. Rev. **D47** (1993) 101.

[61] M. A. Shifman, A. I. Vainshtein, M. B. Voloshin and V. I. Zakharov, Sov. J. Nucl. Phys. **30** (1979) 711; J. Ellis, M. K. Gaillard and D. V. Nanopoulos, Nucl. Phys. **B106** (1976) 292.

[62] V. Del Duca, W. Kilgore, C. Oleari, C. Schmidt and D. Zeppenfeld, in preparation.

[63] V. Del Duca, A. Frizzo and F. Maltoni, Nucl. Phys. **B568** (2000) 211.

[64] B. L. Combridge and C. J. Maxwell, Nucl. Phys. **B239** (1984) 429.

[65] S. Heinemeyer, W. Hollik and G. Weiglein, Comp. Phys. Comm. **124** (2000) 76; hep-ph/0002213;

[66] S. Heinemeyer, W. Hollik and G. Weiglein, Eur. Phys. Jour. **C9** (1999) 343.

[67] A. Dabelstein, Z. Phys. **C67** (1995) 495, Nucl. Phys. **B456** (1995) 25.

[68] P. Chankowski, S. Pokorski and J. Rosiek, Nucl. Phys. **B423** (1994) 437; S. Heinemeyer, W. Hollik, J. Rosiek and G. Weiglein, Eur. Phys. Jour. **C19** (2001) 535.

[69] M. Frank, S. Heinemeyer, W. Hollik and G. Weiglein, hep-ph/0202166

[70] M. Carena, S. Heinemeyer, C.E.M. Wagner and G. Weiglein, hep-ph/9912223.

[71] S. Heinemeyer and G. Weiglein, hep-ph/0102117.

[72] G. Degrassi et al., *in preparation* .

[73] M. Carena, J. Espinosa, M. Quirós and C. Wagner, Phys. Lett. **B355** (1995) 209.

[74] S. Heinemeyer, W. Hollik and G. Weiglein, JHEP **0006** (2000) 009.

[75] B.C. Allanach et al., hep-ph/0202233, to appear in the Snowmass 2001 proceedings.

[76] M. Carena, H.E. Haber, S. Heinemeyer, W. Hollik, C.E.M. Wagner, and G. Weiglein, Nucl. Phys. **B580** (2000) 29.

[77] C. Balazs, J. L. Diaz-Cruz, H. J. He, T. Tait and C. P. Yuan, Phys. Rev. D **59**, 055016 (1999) J. Guasch, R. A. Jimenez and J. Sola, Eur. Phys. J. C **2**, 373 (1998).

[78] G. Degrassi, P. Gambino and G. F. Giudice, JHEP **0012**, 009 (2000); M. Carena, D. Garcia, U. Nierste and C. E. M. Wagner, Phys. Lett. B **499**, 141 (2001).

[79] M. Carena, S. Heinemeyer, C.E.M. Wagner and G. Weiglein, hep-ph/0202167

[80] A. Djouadi, J. Kalinowski and M. Spira, Comp. Phys. Comm. **108** (1998) 56.

[81] R. Hempfling, Phys. Rev. **D49** (1994) 6168; LJ. Hall, R. Rattazzi and U. Sarid, Phys. Rev. **D50** (1994) 7048; M. Carena, M. Olechowski, S. Pokorski, C. Wagner, Nucl. Phys. **B426** (1994) 269.

[82] M. Carena, S. Mrenna and C. Wagner, Phys. Rev. **D60** (1999) 075010; *ibid* **D62** (2000) 055008.

[83] S. Heinemeyer, W. Hollik and G. Weiglein, Eur. Phys. Jour. **C16** (2000) 139.

[84] A. Djouadi, Phys. Lett. **B435** (1998) 101.

[85] K. Jakobs, talk at the *XXXVIth Rencontres de Moriond*, 2001.

[86] S. G. Frederiksen, N. Johnson, G. Kane and J. Reid, Phys. Rev. **D50** (1994) 4244; S.P. Martin, J. D. Wells, Phys.Rev. **D60** (1999) 035006.

[87] D. Choudhury and DP. Roy, Phys. Lett. **B322** (1994) 368; J. Gunion, Phys. Rev. Lett. **72** (1994) 199.

[88] O.J.P. Eboli and D. Zeppenfeld, Phys. Lett. **B495** (2000) 147.

[89] G. Bélanger *et al*, Nucl.Phys. **B581** (2000) 3; G. Bélanger *et al*, Phys. Lett. **B519** (2001) 93.

[90] A. Djouadi, Mod. Phys. Lett. **A14** (1999) 359; A. Djouadi, M. Drees, P. Fileviez Perez, M. Muhlleitner, hep-ph/0109283.

[91] G. Bélanger, F. Boudjema, A. Pukhov and A. Semenov, hep-ph/0112278.

[92] A. Pukhov, E. Boos, M. Dubinin, V. Edneral, V. Ilyin, D. Kovalenko, A. Kryukov, V. Savrin, S. Shichanin and A. Semenov, INP-MSU 98-41/542, hep-ph/9908288.

[93] For reviews, see W.L. Freedman, R. Kirshner and C. Lineweaver, talks given at the International Conference of Cosmology and Particle Physics (CAPP98), CERN, June 1998.

[94] J. Ellis, K. Enqvist, D.V. Nanopoulos and K. Tamvakis, Phys. Lett. **B155** (1985) 381; M. Drees, Phys. Lett. **B158** (1985) 409, Phys. Rev. **D33** (1986) 1486.

[95] G. Anderson, H. Baer, C.H. Chen and X. Tata, Phys. Rev. **D61** (2000) 095005.

[96] For a review see A. Brignole, L.E. Ibáñez, C. Muñoz, hep-ph/9707209; L. Randall and R. Sundrum, Nucl. Phys. **B557** (1999) 79.

[97] G. Bélanger, F. Boudjema and K. Sridhar, Nucl. Phys. **B568** (2000) 3.

[98] G. Bélanger, F. Boudjema and S. Rosier-Lees, in preparation.

[99] M. Knecht, A. Nyffeler, M. Perrottet and E. de Rafael, hep-ph/0111059.

[100] T. Sjöstrand, Comp. Phys. Comm. **82** (1994) 74; T. Sjöstrand, P. Edén, C. Friberg, L. Lönnblad, G. Miu, S. Mrenna and E. Norrbin, Comp. Phys. Commun. **135** (2001) 238; T. Sjöstrand, L. Lönnblad and S. Mrenna, preprint LU TP 01-21, August 2001, hep-ph/0108264, http://www.thep.lu.se/~torbjorn/Pythia.html.

[101] T. Plehn, M. Spira and P.M. Zerwas, Nucl. Phys. **B479** (1996) 46, (E) *ibid.* **531** (1998) 655; S. Dawson, S. Dittmaier and M. Spira. Phys. Rev. **D58** 115012, 1998, Acta Phys. Polon. **B29** (1998) 2875; M. Spira, Web page and program list at http://mspira.home.cern.ch/~mspira/proglist.html

[102] A. Djouadi, W. Killian, M. Mühlleitner and P.M. Zerwas, Eur. Phys. J. **C10** (1999) 45.

[103] R. Lafaye, D.J. Miller, M. Mühlleitner and S. Moretti, DESY-99-192, hep-ph/0002238.

[104] E. Richter-Was and D. Froidevaux, ATLAS-NOTE-PHYS-104 1997.

[105] U. Ellwanger, J.F. Gunion and C. Hugonie, preprint UCD-2001-13, `hep-ph/0111179`.

[106] H.P. Nilles, M. Srednicki and D. Wyler, Phys. Lett. **120B** (1983) 346; M. Drees, Int. J. Mod. Phys. **A4** (1989) 3635; J. Ellis, J.F. Gunion, H.E. Haber, L. Roszkowski and F. Zwirner, Phys. Rev. **D39** (1989) 844; U. Ellwanger and M. Rausch de Traubenberg, Z. Phys. **C53** (1992) 521; P.N. Pandita, Z. Phys. **C59** (1993) 575, Phys. Lett. **B318** (1993) 338; T. Elliot, S.F. King and P.L. White, Phys. Rev. **D49** (1994) 2435, *ibid.* **D52** (1995) 4183, *ibid.* **D53** (1996) 4049.

[107] Z. Kunszt, S. Moretti and W.J. Stirling, Z. Phys. **C74** (1997) 479.

[108] H. Baer, M. Bisset, X. Tata and J. Woodside, Phys. Rev. **D46** (1992) 303;A. Dedes and S. Moretti, hep-ph/9909526, Eur. Phys. J. **C10** (1999) 515,Phys. Rev. **D60** (1999) 015007;A. Datta, A. Djouadi, M. Guchait and Y. Mambrini, hep-ph/0107271.

[109] A. Djouadi, J.L. Kneur, G. Moultaka, Phys. Rev. Lett. **80** (1998) 1830 and Nucl. Phys. **B569** (2000) 53; G. Bélanger, F. Boudjema, T. Kon, V. Lafage, Eur. Phys. J. **C9** (1999) 511; A. Dedes and S. Moretti, Eur. Phys. J. **C10** (1999) 515.

[110] U. Ellwanger, M. Rausch de Traubenberg and C. Savoy, Nucl. Phys. **B492** (1997) 21;U. Ellwanger and C. Hugonie, Eur. Phys. J. **C5** (1998) 723.

[111] ALEPH, DELPHI, L3, OPAL Collaborations and LEPHIGGS working group, EP/2000-055.

[112] A bibliography can be found at `http://www.cern.ch/lephiggs/`.

[113] A. Dedes, C. Hugonie, S. Moretti and K. Tamvakis, Phys. Rev. **D63** (2001) 055009.

[114] C. Hugonie and S. Moretti, `hep-ph/0110241`.

[115] CDF Run II TDR, Fermilab-Pub-96/390-E; D0 Run II TDR, Fermilab-Pub-96/357-E.

[116] CDF (D0) Run IIb TDR in preparation.

[117] P. Bhat, R. Gilmartin and H. Prosper, Phys. Rev. **D62** (2000) 074022.

[118] H. Baer, D.Dicus, M.Drees and X.Tata, Phys.Rev. **D37**, (1987) 1367; "J.F.Gunion and H.E.Haber, Nucl.Phys. **B307**, (1988) 445, K.Griest and H.E.Haber, Phys. Rev. **D37**, (1988) 719; A. Djouadi, et. al., Phys. Lett. **B376** (1996) 220; A. Djouadi and M. Drees, Phys. Lett. **B407** (1997) 243.

[119] R.E.Shrock and M.Suzuki, Phys.Lett. **B10** (1982) 250; L.F. Li, Y.Liu and L. Wolfenstein, Phys.Lett. **B159** (1985) 45.

[120] A.S. Joshipura and J.W.F.Walle, Nucl. Phys. **B397** (1993) 105.

[121] L. Randall and R. Sundrum, Phys. Rev. Lett. **83** (1999) 3370.

[122] G. F. Giudice, R. Rattazzi and J. D. Wells, Nucl. Phys. B **595** (2001) 250.

[123] For a recent discussion see J. Gunion, hep-ph/0110362.

[124] LEP Higgs Working Group, hep-ex/0107032.

[125] J.F. Gunion, Phys. Rev. Lett. **72** (1994) 199.

[126] The TriDAS Project. Technical Design Report. CERN/LHCC 2000-38, CMS TDR 6.1, 15 December 2000.

[127] A. Nikitenko "L1 and HLT for SUSY and Higgs", talk on Jet/MET meeting 5 Dec. 2001, http://cmsdoc.cern.ch/~anikiten/hlt-talk/talk.pdf.

[128] P. Chumney, S. Dasu, W. H. Smith, CMS Note 2000/074.

[129] P. Chumney, private communication.

[130] http://cmsdoc.cern.ch/cmsim/cmsim.html

[131] http://cmsdoc.cern.ch/orca/

[132] A.S.Belyaev et al., hep-ph/0101232.

[133] K. Cranmer, T. Figy, W. Quayle, D. Rainwater and D. Zeppenfeld, http://pheno.physics.wisc.edu/Software/MadCUP/

[134] K.Hagiwara and D.Zeppenfeld, Nucl. Phys. **B313** (1989) 560.

[135] S. Abdullin, A. Khanov and N. Stepanov, CMSJET, CMS TN/94-180; http://cmsdoc.cern.ch/~abdullin/cmsjet.html

[136] D. Rainwater, PhD thesis, report hep-ph/9908378.

[137] I. Vardanian, O. Kodolova, S. Kunori and A. Nikitenko, CMS Note in preparation.

[138] E. Richter-Was, D. Froidevaux, L. Poggioli, ATLAS Internal Note ATL-PHYS-98-131 (1998).

[139] M. Spira, VV2H programme, home.cern.ch/m/mspira/www/proglist.html.

[140] H.L. Lai et al., Eur. Phys. J. **C12** (2000) 375.

[141] F.Berends, H.Kuijf, B.Tausk, W.Giele, Nucl. Phys. **B357** (1991) 32; W. Giele, E. Glover, D. Kosover, Nucl. Phys. **B403** (1993) 603.

[142] G.Azuelos and R.Mazini, ATLAS internal note, in preparation.

[143] C.Buttar, K.Jakobs and R.Harper, ATLAS internal note, in preparation.

[144] V.Cavasinni, D.Costanzo, I.Vivarelli, ATLAS communication ATL-COM-CAL-2001-001 (2001).

[145] K.Jakobs and Th.Trefzger, ATLAS internal note ATL-PHYS-2000-015 (2000); D.Green et al., J. Phys. G: Nucl. Part. Phys. **26** (2000) 1751.

[146] V.Cavasinni, D.Costanzo, E.Mazzoni, I.Vivarelli, ATLAS internal note, in preparation.

[147] M.Klute, ATLAS internal note, in preparation.

[148] R.Mazini, ATLAS internal note, in preparation.

[149] D. Cavalli, L. Cozzi, L. Perini, S. Resconi, ATL-PHYS-1994-051 (1994).

[150] D. Cavalli, G. Negri, ATLAS Note in preparation (2002).

[151] J. Thomas, ATLAS Note in preparation (2002); J. Thomas, Ph.D. Thesis, Johannes Gutenberg-Universität Mainz (2002).

[152] D. Cavalli, S. Resconi, ATL-PHYS-1998-118 (1998)

[153] D. Cavalli, ATL-PHYS-1996-080 (1996).

[154] D. Cavalli and S. Resconi, ATL-PHYS-2000-005 (2000).

[155] M. Spira, Programs for SM and MSSM Higgs boson production at hadron colliders, Code and documentaion for HIGLU, HQQ and HDECAY, http://mspira.home.cern.ch/mspira/proglist.html

[156] Z. Kunszt, Nucl. Phys. **B247** (1984) 339; J.F. Gunion, Phys. Lett. **B253** (1991) 269; W.J. Marciano and F.E. Paige, Phys. Rev. Lett. **66** (1991) 2433; D.A. Dicus and S. Willenbrock, Phys. Rev. **D39** (1989) 751; M. Spira, Fortschr. Phys. **46** (1998) 203.

[157] S. Gonzalez de la Hoz, E. Ros, M. Vos, ATL-COM-PHYS-2001-029 (2001); D. Dicus et al., Phys. Rev. **D59** (1999) 094016.

[158] K. Mahboubi et. al., http://butler.physik.uni-mainz.de/∼mahboubi

[159] K. Mahboubi, Ph.D. Thesis, http://www.ub.uni-heidelberg.de/archiv/1577.

[160] The ATLAS Collaboration ATLAS First Level Trigger, Technical Design Report, ATLAS TDR 12, CERN/LHCC 98-14, (1998)

[161] R. Dubitzky, K. Jakobs, E. Bagheri, K. Mahboubi, M. Wunsch, Atlas Internal Note ATL-DAQ-99-011, (1999).

[162] R. Kinnunen and D. Denegri, CMS NOTE 1999/037.

[163] S. Eno, W. Smith, S. Dasu, R. Kinnunen and A. Nikitenko, CMS NOTE 2000/055.

[164] D. Kotlinski, A. Nikitenko and R. Kinnunen, CMS NOTE 2001/017.

[165] A. Nikitenko, CMS NOTE in preparation.

[166] Sami Lehti, Dissertation, University of Helsinki, Report Series in Physics, HU-P-D93, 2001.

[167] A. Nikitenko and L. Wendland, Talk in the btau Meeting, 21 August, 2001.

[168] A. Nikitenko, S. Kunori and R. Kinnunen, CMS NOTE 2001/040.

[169] R. Kinnunen and A. Nikitenko, CMS NOTE 1997/106.

[170] D. Denegri, V. Drollinger, R. Kinnunen, K. Lassila-Perini, S. Lehti, F. Moortgat, A. Nikitenko, S. Slabospitsky, N. Stepanov, CMS NOTE 2001/032.

[171] V. Drollinger, IEKP-KA/01-16.

[172] H. Plothow-Besch, Comput. Phys. Commun. **75** (1993) 396.

[173] A. S. Belyaev, E. E. Boos, A. N. Vologdin, M. N. Dubinin, V. A. Ilyin, A. P. Kryukov, A. E. Pukhov, A. N. Skachkova, V. I. Savrin, A. V. Sherstnev and S. A. Shichanin, hep-ph/0101232.

[174] T. Sjostrand "PYTHIA 5.7 and JETSET 7.4 Physics and manual", CERN-TH.7112/93.

[175] V. Drollinger, V. Karimaki, S. Lehti, N. Stepanov and A. Khanov, CMS IN 2000/034.

[176] V. Drollinger, CMS NOTE-1999/066.

[177] V. Drollinger, Ph. Gras and Th. Muller, CMS NOTE-2000/073.

[178] P. H. Nilles, Phys. Rev. **110** (1984) 1; H. Haber and G. Kane, Phys. Rev. **115** (1985) 75.

[179] ALEPH, DELPHI, L3 and OPAL Collaborations, CERN-EP/2000-055; ALEPH Coll., Phys. Lett. B487 (2000) 253; DELPHI Coll., M. Ellert et al., Nucl. Phys. B. Proc. Sup. 98 (2001), 336; L3 Coll., Phys. Lett. B496 (2000) 34; OPAL Coll., CERN-EP/98-173.

[180] CDF Collaboration, hep-ex/9912013, Phys. Rev. **D62** (2000) 012004; DØ Collaboration, FermiLab-Conf-2000-294-E, hep-ex/0102039, FermiLab-Pub-2001-022-E.

[181] G. Marchesini, B.R. Webber, G. Abbiendi, I.G. Knowles, M.H. Seymour and L. Stanco, Comp. Phys. Commun. **67** (1992) 465; G. Corcella, I.G. Knowles, G. Marchesini, S. Moretti, K. Odagiri, P. Richardson, M.H. Seymour and B.R. Webber, preprint Cavendish-HEP-99/17, hep-ph/9912396; JHEP **0101** (2001) 010; hep-ph/0201201.

[182] H. Baer, F.E. Paige, S.D. Protopopescu and X. Tata, preprint BNL-HET-99-43, FSU-HEP-991218, UH-511-952-00, hep-ph/0001086 (Higgs mass calculations and code by M. Bisset, whose private programs were used in the work on charged Higgs decays to SUSY).

[183] D. Cavalli et al., ATLAS Internal note ATL-PHYS-94-053 (1994).

[184] M. Dress, M. Guchait and D.P. Roy, hep-ph/9909266 and references therein.

[185] K.A. Assamagan, Acta Phys. Pol. **B31** (2000) 881, ATLAS Internal Note ATL-PHYS-99-025.

[186] K.A. Assamagan, Acta Phys. Pol. **B31** (2000) 863, ATLAS Internal Note ATL-PHYS-99-013.

[187] K.A. Assamagan and Y. Coadou, ATLAS Internal Note ATL-PHYS-2000-031 (2000).

[188] M. Guchait and S. Moretti, JHEP **01** (2002) 001.

[189] D.J. Miller, S. Moretti, D.P.Roy and W.J. Stirling, Phys. Rev. **D61** (2000) 055011.

[190] K.A. Assamagan and Y. Coadou, ATLAS Internal Note ATL-PHYS-2001-017 (2001).

[191] D.P. Roy, Phys. Lett. **B459** (2000) 607.

[192] B.K. Bullock, K. Hagiwara and A.D. Martin, Nucl. Phys. **B395** (1993) 499; J.H. Kühn and A. Santamaria, Z. Phys. **C48** (1990) 445; S. Raychaudhuri and D.P. Roy, Phys. Rev. **D52** (1995) 1556.

[193] R. Kinnunen, CMS Note 2000/045.

[194] M. Hohlfeld, ATLAS Internal Note ATL-PHYS-2001-004 (2001).

[195] J.F. Gunion et al, 'Higgs boson discovery and properties', Snowmass 1996, hep-ph/9703330.

[196] See, e.g.: M. Antonelli and S. Moretti, in Proc. of the '13th Convegno sulla Fisica al LEP (LEP-TRE 2001)', Rome 18-20 April 2001, hep-ph/0106332 and references therein.

[197] H.L. Lai, J. Huston, S. Kuhlmann, F. Olness, J. Owens, D. Soper, W.K. Tung and H. Weerts, Phys. Rev. **D55** (1997) 1280.

[198] D. Chakraborty, in Proc. of the 'Tevatron Run II SUSY/Higgs' Workshop, Fermilab, hep-ph/0010338.

[199] J.F. Gunion, Phys. Lett. **B322** (1994) 125; J.L. Diaz-Cruz and O.A. Sampayo, Phys. Rev. **D50** (1994) 6820.

[200] CDF Collaboration: F. Abe et al., Phys. Rev. Lett. **79** (1997) 357; D0 Collaboration: T. Affolder et al., Phys. Rev. **D62** (2000) 012004; D0 Collaboration: B. Abbott et al., Phys. Rev. Lett. **82** (1999) 4975; D. Chakraborty (on behalf of the D0 and CDF Collaborations), presented at the '13th Hadron Collider Physics Conference', preprint FERMILAB-Conf-99/143-E.

[201] S. Moretti and W.J. Stirling, Phys. Lett. **B347** (1995) 291; Erratum, ibidem B366 (1996) 451; A. Djouadi, J. Kalinowski and P.M. Zerwas, Z. Phys. **C70** (1996) 435; E. Ma, D.P. Roy and J. Wudka, Phys. Rev. Lett. **80** (1998) 1162; F.M. Borzumati and A. Djouadi, [hep-ph/9806301.

[202] CDF Collaboration: F. Abe et al., Phys. Rev. Lett. **79** (1997) 3585.

[203] S. Moretti, M.H. Seymour, K. Odagiri, P. Richardson and B.R. Webber, preprint Cavendish-HEP-98/06.

[204] J.F. Gunion, Phys. Lett. **B322** (1994) 125; F. Borzumati, J.-L. Kneur and N. Polonsky, Phys. Rev. **D60** (1999) 115011.

[205] S. Moretti and D.P. Roy, Phys. Lett. **B470** (1999) 209.

[206] K.A. Assamagan, A. Djouadi, M. Drees, M. Guchait, R. Kinnunen, J.-L. Kneur, D.J. Miller, S. Moretti, K. Odagiri and D.P. Roy, in Proceedings of the Workshop 'Physics at TeV Colliders', Les Houches, France, 8-18 June 1999, hep-ph/0002258.

[207] A. Belyaev, D. Garcia, J. Guasch and J. Solá, hep-ph/0105053.

[208] K. Odagiri, hep-ph/9901432; D.P. Roy, Phys. Lett. B459 (1999) 607; A. Tricomi, hep-ph/0105199.

[209] K. A. Assamagan and A. Deandrea, hep-ph/0111256, Phys. Rev. **D** (in press).

[210] N. Arkani-Hamed, S. Dimopoulos, G. R. Dvali and J. March-Russell, Phys. Rev. **D65** (2002) 024032; K. R. Dienes, E. Dudas and T. Gherghetta, Nucl. Phys. **B557** (1999) 25; K. Agashe, N. G. Deshpande and G. H. Wu, Phys. Lett. **B489** (2000) 367.

[211] C. D. Hoyle, U. Schmidt, B. R. Heckel, E. G. Adelberger, J. H. Gundlach, D. J. Kapner and H. E. Swanson, Phys. Rev. Lett. **86** (2001) 1418.

[212] Y. Fukuda et al. [SuperKamiokande Collaboration], Phys. Rev. Lett. **82** (1999) 2644; **85** (2000) 3999; **86** (2001) 5656; A. Ioannisian and A. Pilaftsis, Phys. Rev. **D62** (2000) 066001; R. N. Mohapatra and A. Perez-Lorenzana, Nucl. Phys. **B576** (2000) 466; A. S. Dighe and A. S. Joshipura, Phys. Rev. **D64** (2001) 073012; A. De Gouvea, G. F. Giudice, A. Strumia and K. Tobe, hep-ph/0107156.

[213] N. Arkani-Hamed, S. Dimopoulos and G. R. Dvali, Phys. Lett. **B429** (1998) 263; Phys. Rev. **D59** (1999) 086004; I. Antoniadis, N. Arkani-Hamed, S. Dimopoulos and G. R. Dvali, Phys. Lett. **B436** (1998) 257; G. F. Giudice, R. Rattazzi and J. D. Wells, Nucl. Phys. **B544** (1999) 3; E. A. Mirabelli, M. Perelstein and M. E. Peskin, Phys. Rev. Lett. **82** (1999) 2236; T. Han, J. D. Lykken and R. J. Zhang, Phys. Rev. **D59** (1999) 105006 (1999).

[214] S. Heinemeyer, W. Hollik and G. Weiglein, hep-ph/0002213.

[215] M. Bisset, M. Guchait and S. Moretti, Eur. Phys. J. **C19** (2001) 143.

[216] See, e.g., LEP SUSY Working Group web page, http://www.cern.ch/LEPSUSY/.

[217] M. Carena, P.H. Chankowski, S. Pokorski, and C.E.M. Wagner, Phys. Lett. **B441** (1998) 205.

[218] L. Demortier et al. (CDF/D0), FNAL-TM-2084; D.E. Groom et al., Eur. Phys. J. **C15** 1.

[219] M. Misiak, S. Pokorski, and J. Rosiek, hep-ph/9703442.

[220] P.H. Chankowski and S. Pokorski, hep-ph/9707497.

[221] J. Erler and D.M. Pierce, Nucl. Phys. **B526** (1998) 53.

[222] See Ref. [13] of [215] for a cross-section of MSSM $b \rightarrow s\gamma$ literature; for discussion of the current status of $b \rightarrow s\gamma$ calculations, see M. Misiak, hep-ph/0009033.

[223] A. Datta, A. Djouadi, M. Guchait and Y. Mambrini, Phys. Rev. **D65** (2002) 015007; H. Baer, M. Bisset, X. Tata and J. Woodside, Phys. Rev. **D46** (1992) 303.

[224] S. Moretti, preprint RAL-TR-2000-038, CERN-TH/2001-036, hep-ph/0102116.

[225] S. Moretti, private communication.

[226] See: http://www-thphys.physics.ox.ac.uk/users/PeterRichardson/HERWIG/isawig.html.

[227] M. Bisset, F. Moortgat and S. Moretti, in preparation.

[228] M. Bisset, Univ. of Hawaii at Manoa Ph.D. Dissertation, UH-511-813-94 (1994).

[229] See e.g., J.F. Gunion and H.E. Haber, Phys. Rev. **D37** (1988) 2515; A. Djouadi, J. Kalinowski and P.M. Zerwas, Z. Phys. **C57** (1993) 569; A. Djouadi, J. Kalinowski, P. Ohmann and P.M. Zerwas, Z. Phys. **C74** (1997) 93; P.M. Zerwas (ed.) et al., hep-ph/9605437.

[230] A. Djouadi and P. Gambino, Phys. Rev. **D51** (1995) 218.

[231] A. K. Datta, A. Djouadi, M. Guchait, Y. Mambrini and F. Moortgat, in preparation.